

**Nanostructured, Electroactive and Bioapplicable Materials**

A Thesis

Submitted to the Faculty

of

Drexel University

by

Shan Cheng

in partial fulfillment of the

requirements for the degree

of

Doctor of Philosophy

September 2002

## Thesis Approval Form

This thesis, entitled Nanostructured, Electroactive and Bioapplicable Materials

\_\_\_\_\_ and authored  
by Shan Cheng, is hereby accepted and approved.

### Signatures:

Chairman, Examining Committee:



Supervising Professor:

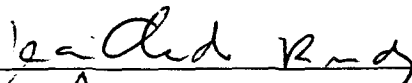


Committee Members:



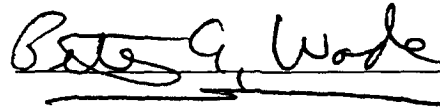
M. A. Whattery



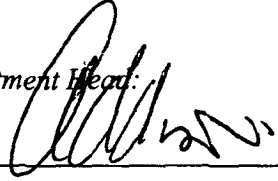




Graduate Advisor:



Department Head:



© Copyright 2002  
Shan Cheng. All Rights Reserved.

### **Dedications**

This dissertation is dedicated to my husband Yunkai Zhou, my parents, Mr. and Mrs. Hai Cheng and Linmeng Wang, for their encouragement, support and love.

## Acknowledgments

In retrospect of my past few years, I have always realized that there are many people who have directed, assisted and supported me during my Ph.D. study. Without them I would never be able to make to this point. Although it would be impossible to name each of them, I would like to express my deep gratitude to all of them.

First, I would like to thank my advisor, Dr. Yen Wei, for his tremendous effort in guiding, helping and encouraging me during the last five years. His broad knowledge, insightful thoughts and sparkling ideas have significantly widened my horizons and inspired my research. Personally, I have also greatly benefited from his devoted, energetic and enthusiastic manner towards science.

I also thank the members of my candidacy exam and/or dissertation committees, Dr. Jean-Claude Bradley, Dr. Franklin A. Davis, Dr. Joe P. Foley, Dr. Amar Nath, Dr. Sally Solomon, and Dr. Margaret A. Wheatley, for their time and valuable suggestions. Special thanks are due to the committee chair, Dr. Anthony W. Addison for insightful discussions on many topics, including my oral proposal and research collaboration. I am also grateful to Dr. Sally Solomon for her detailed comments on my oral proposal.

I would like to thank many of my collaborators. I specially thank Dr. Shuxi Li for his valuable guidance and assistance when I first started my research at Drexel University and all along thereafter. Many thanks are due to Dr. Qiuwei Feng, who has provided generous help in my research, especially in the sol-gel projects, and also in my personal life as my best friend. I also thank Ms. Elizabeth Guterman and Dr. Peter Lelkes of the

School of Biomedical Engineering, Science and Health Systems for collaborations in bioapplicable electroactive materials.

I am grateful to many people for their selfless support in many areas. I especially acknowledge Mr. David von Rohr for his help in electron microscopies measurements, Dr. Jeffrey Honovich for mass spectral measurements, Dr. Guoliang Yang for AFM studies, Mr. Prithwiraj Maitra of Temple University for some TGA measurements, and Ms. Edith Smith for her kindly help and coordination in obtaining the chemicals and instruments for our research work.

I thank Dr. Jigeng Xu, Dr. Hua Dong, Dr. Homayoun Jamasbi, Mr. Muduo Lin, Ms. Houping Yin, Mr. Zhengfei Sun, Ms. Kate Ong, Ms. Alpa Patel and Mr. Subhabrata Bhattacharyya, in Dr. Yen Wei's group, either previously or currently. They have greatly enriched my experience at Drexel, and brought me many cherishable memories. I also want to thank the people in the Department of Chemistry, including all professors, staff and my fellow graduates, for providing such a joyful studying and working environment.

I am grateful to my parents, Mr. and Mrs. Hai Cheng and Linmeng Wang, and my sister, Ms. Gung Cheng, for their continuous encouragement and unconditional love throughout. I shall be indebted to them forever. Finally, I want to thank my husband, Yunkai Zhou, who is now also a Ph.D. candidate majoring in computer networking -- "polymers of computers" as he always described. Discussion with him has always been amazingly helpful, even though we are not in the same field. It is him always being there lighting my spirit up, keeping my heart warm, and showing me the sunshine on the road.

## Table of Contents

List of Tables.....	xii
List of Figures .....	xiii
Abstract .....	xxi
Preface .....	1
Chapter 1. An Overview to Nanostructured Porous Sol-Gel Materials.....	5
1.1. Introduction .....	5
1.2. Fundamental Sol-Gel Process .....	7
1.2.1. Inorganic Salt Precursors .....	7
1.2.2. Alkoxide Precursors .....	8
1.3. Mesoporous Materials from Surfactant Templated Sol-Gel Methods .....	9
1.4. Mesoporous Materials from Nonsurfactant Templated Sol-Gel Methods .....	13
1.5. Characterization Methods for Porous Materials.....	15
1.5.1. Gas Sorption Measurement.....	18
1.5.1.1. Classification of Adsorption Isotherms.....	18
1.5.1.2. Adsorption Hysteresis .....	20
1.6. References .....	21
Chapter 2. Mesoporous Sol-Gel Material Prepared Using Thermal Sensitive Templates: New Opportunities to Convenient Synthesis.....	30
2.1. Introduction .....	30
2.1.1. Surfactant Templates and Their Removal.....	31
2.1.2. Nonsurfactant Templates and Their Removal.....	34
2.1.3. Thermal Sensitive Templates .....	34

2.2. Experimental .....	36
2.2.1. Materials.....	36
2.2.2. Synthesis of Mesoporous Silica Materials with Thermal Sensitive Nonsurfactant Templates.....	36
2.2.3. Instrumentation and Characterization .....	38
2.3. Results and Discussion.....	39
2.4. Conclusions and Remarks .....	46
2.5. Acknowledgments.....	47
2.6. References .....	47
Chapter 3. Synthesis of Mesoporous Silica Nanospheres through a Nonsurfactant Templated Base Catalyzed Sol-Gel Reaction .....	66
3.1. Introduction .....	66
3.1.1. Silica Sphere from Sol-Gel Process .....	67
3.1.2. Porous Spheres from Surfactant Templated Sol-Gel Pathway .....	68
3.1.3. Morphology Studied of Nonsurfactant Templated Sol-Gel Pathway .....	70
3.2. Experimental .....	72
3.2.1. Materials.....	72
3.2.2. Synthesis of Mesoporous Spherical Silica Particles through a Nonsurfactant Templated Pathway .....	72
3.2.3. Synthesis of Mesoporous Spherical Silica Particles through a Two- Step Water-in-Oil Method.....	74
3.2.4. Instrumentation and Characterization .....	74
3.3. Results and Discussion.....	75
3.4. Conclusions and Remarks .....	82



3.5. Acknowledgments .....	83
3.6. References .....	83
Chapter 4. Synthesis of Mesoporous Gold-Silica Nanocomposite Materials via Sol-Gel Process with Nonsurfactant Templates.....	96
4.1. Introduction .....	96
4.1.1. Gold Nanoparticles in Sol-Gel Matrices: Properties.....	97
4.1.2. Gold Nanoparticles in Sol-Gel Matrices: Synthesis.....	99
4.2. Experimental .....	101
4.2.1. Materials.....	101
4.2.2. Synthesis of Mesoporous Gold-Silica Nanocomposites .....	101
4.2.3. Instrumentation and Characterization .....	103
4.3. Results and Discussion.....	104
4.4. Conclusions .....	111
4.5. Acknowledgments.....	112
4.6. References .....	112
Chapter 5. Organic-Inorganic Nanocomposite Thin Films Based on Arrays of Vinyl Modified Silica Nanoparticles.....	125
5.1. Introduction .....	125
5.1.1. Organic-Inorganic Nanocomposite: Opportunities to Advanced Materials.....	126
5.1.2. Organic-Inorganic Nanocomposite Based on Core-Shell Nanoparticle Arrays .....	127
5.2. Experimental .....	129
5.2.1. Materials.....	129

5.2.2. Treatment of Substrate Surface .....	129
5.2.3. Arrays of Vinyl Monomer Modified Silica Nanoparticles and Preparation of Nanocomposite Thin Films .....	130
5.2.4. Arrays of Porous and Nonporous Silica Nanoparticles.....	131
5.2.5. Instrumentation and Characterization .....	131
5.3. Results and Discussion.....	132
5.3.1. Organic-Inorganic Nanocomposite Thin Films Based on Vinyl Modified Nanoparticle Arrays .....	132
5.3.2. An Extended Study: Assembly of Monolayer Mesoporous Nanospheres .....	136
5.4. Conclusions .....	137
5.5. Acknowledgments.....	138
5.6. References .....	138
Chapter 6. Bioapplicable Conducting Polymers based on a Biological Template Guided Synthesis.....	149
6.1. Introduction .....	149
6.1.1. Conducting Polymers with Improved Biocompatibility and Solubility.....	150
6.1.2. Conducting Polymer: Polyaniline .....	153
6.1.3. Biological Template: Collagen .....	154
6.2 Experimental .....	155
6.2.1. Materials.....	155
6.2.2. Synthesis of Polyaniline-Collagen (PANI-Colla) Complex Materials.....	156
6.2.3. Cell Growth Studies on PANI-Colla Films.....	157

6.2.4. Instrument and Characterization .....	158
6.3. Results and Discussion.....	158
6.4. Conclusions .....	163
6.5. Acknowledgments.....	165
6.6. References .....	165
Chapter 7. Synthesis and Characterization of Aniline Derivative Modified 8-Hydroxyquinoline Ligands and Their Metal Complexes.....	179
7.1. Introduction .....	179
7.1.1. Light Emitting Diodes.....	180
7.1.2. Structure of Organic Light Emitting Diodes.....	182
7.1.3. 8-Hydroxyquinoline-Metal Complexes.....	184
7.2. Experimental .....	186
7.2.1. Materials.....	186
7.2.2. Synthesis of N,N'-bis(N,N-dimethyl-4'-aminophenyl)-5-imino-7-amino-8-ketoquinoline (1a) and N,N'-bis(4'-aminophenyl)-5-imino-7-amino-8-ketoquinoline (2a).....	187
7.2.3. Syntheses of Complexes.....	188
7.2.4. Instrumentation and Characterization .....	190
7.3. Results and Discussion.....	190
7.4. Conclusions .....	196
7.5. Acknowledgments.....	197
7.6. References .....	197
Chapter 8. Concluding Remarks.....	216
8.1. Nanostructured Materials .....	216

8.2. Electroactive, Bioapplicable Materials .....	221
Appendix A. Stimuli-Responsive Polyphosphazenes as Controlled Drug Delivery Matrix Materials.....	223
A.1. Abstract .....	223
A.2. Introduction .....	224
A.2.1. Controlled Drug Delivery.....	224
A.2.2. Polyphosphazene.....	226
A.2.2.1. Synthesis of Polyphosphazenes.....	226
A.2.2.2. Applications of Polyphosphazenes in Controlled Drug Delivery.....	228
A.2.3. Stimuli-Responsive Polymers .....	229
A.3. Proposed Research .....	229
A.3.1. Theoretical Considerations.....	230
A.3.1.1. Signal .....	231
A.3.1.2. Proposed Intelligent Drug Delivery Systems.....	231
A.3.2. Experimental .....	235
A.3.2.1. Modification.....	235
A.3.2.2. Formulation.....	235
A.3.2.3. Degradation Study.....	236
A.3.2.4. Release Study.....	236
A.3.2.5. Instrumentation and Characterizations.....	237
A.4. Ph.D. Thesis Research.....	238
A.5. Acknowledgments.....	239

A.6. References .....	239
Appendix B Electrochemistry Measurements of Aniline Derivative Modified 8-Hydroxyquinoline Ligands.....	247
B.1. Experimental .....	247
B.2. Results .....	247
B.3. Acknowledgments.....	248
Vita .....	257

### List of Tables

Table 2-1.	Composition and pore parameters of the sol-gel silica samples prepared in the presence of 20-60 wt % benzoin template and heated at 150 °C (i.e., SB -150 samples).....	50
Table 2-2.	Weight loss and pore parameters of the sol-gel silica sample prepared with 40 wt % benzoin template (i.e., SB40-) heated at different temperatures. ....	51
Table 3-1.	Composition of the sol-gel spherical silica samples prepared in the presence of 30-70 wt % fructose templates and the pore parameters of the porous silica nanospheres after template removal of fructose by water extraction. ....	87
Table 4-1.	Compositions and pore parameters of the gold-silica composite samples prepared in the presence of 50 wt % DBTA template (i.e., GS50- samples) or without DBTA template (i.e., GS0-50 sample).....	117
Table 7-1.	The UV absorbance at 600 nm of a series of <b>1a</b> solutions at different concentration. ....	202

### List of Figures

Figure 1-1.	Three structure types proposed for silica-surfactant mesophases and the X-ray diffraction patterns: (a) MCM-41 (hexagonal); (b) MCM-48 (Cubic); (c) MCM-50 (Lamellar).....	26
Figure 1-2.	Proposed schematics of the liquid-crystal templating (LCT) mechanism.....	27
Figure 1-3.	IUPAC classification of physisorption isotherms. ....	28
Figure 1-4.	IUPAC classification of hysteresis loops.....	29
Figure 2-1.	Typical patterns for the weight loss and its derivative over temperature during the pyrolysis of benzoin.....	52
Figure 2-2.	Typical patterns for the weight loss and its derivative over temperature during the pyrolysis of composite sample prepared with 20 wt % of benzoin (SB20).....	53
Figure 2-3.	Typical patterns for the weight loss and its derivative over temperature during the pyrolysis of composite sample prepared with 30 wt % of benzoin (SB30).....	54
Figure 2-4.	Typical patterns for the weight loss and its derivative over temperature during the pyrolysis of composite sample prepared with 40 wt % of benzoin (SB40).....	55
Figure 2-5.	Typical patterns for the weight loss and its derivative over temperature during the pyrolysis of composite sample prepared with 50 wt % of benzoin (SB50).....	56
Figure 2-6.	Typical patterns for the weight loss and its derivative over temperature during the pyrolysis of composite sample prepared with 60 wt % of benzoin (SB60).....	57
Figure 2-7.	Representative IR spectra of benzoin containing silica (SB40): (a) before template removal by heating at 150 °C; (b) after template removal by heating at 150 °C; (c) IR spectrum of pure silica gel.....	58
Figure 2-8.	Nitrogen adsorption-desorption isotherms at -196 °C for porous silica samples prepared with varied concentration of benzoin after template removal by heating at 150 °C.....	59

Figure 2-9.	BJH pore size distributions obtained from the desorption branches of nitrogen sorption isotherms at -196 °C for the porous silica samples prepared with varied concentration of benzoin after heated at 150 °C.....	60
Figure 2-10.	Nitrogen adsorption-desorption isotherms at -196 °C for porous silica samples prepared with 40 wt % benzoin after template removal by heating at various temperatures.....	61
Figure 2-11.	BJH pore size distributions obtained from the desorption branches of nitrogen sorption isotherms at -196 °C for the porous silica samples prepared with 40 wt % of benzoin after template removal by heating at various temperatures.....	62
Figure 2-12.	Relationship between the net BET surface area and the amount of template being removed from Sample SB40 at different heating temperatures. ....	63
Figure 2-13.	Relationship between the net pore volume and the amount of template being removed from Sample SB40 at different heating temperatures. ....	64
Figure 2-14.	Representative transmission electron micrograph (TEM) for the porous silica sample prepared with 40 wt % benzoin after template removal by heating at 150 °C. The gray wormlike features are interconnected pores randomly distributed throughout silica matrix. (a) A low magnification image. (b) A high magnification image. ....	65
Figure 3-1.	Typical SEM images of the silica spheres (SF50). (a) Before the template removal by water extraction. (b) After the template removal by water extraction.....	88
Figure 3-2.	Representative IR spectra of silica spheres (SF50). (a) Before template removal by water extraction. (b) After template removal by water extraction. (c) IR spectrum of pure silica gel. ....	89
Figure 3-3.	Nitrogen adsorption-desorption isotherms at -196 °C for the water extracted silica spheres prepared with fructose concentration ranging from 30 to 70 wt %. ....	90



Figure 3-4.	BJH pore size distributions obtained from the nitrogen desorption isotherms at -196 °C for the water extracted silica spheres prepared with fructose concentration ranging from 30 to 70 wt %.....	91
Figure 3-5.	Representative TEM images for the porous silica spheres: Low magnification TEM showing the uniform spheres with average diameter of 420 nm. ....	92
Figure 3-6.	Representative TEM images for the porous silica spheres. (a) High magnification TEM of one silica sphere revealing the low density core. (b) TEM picture of an ultra-thin section of a ground silica sphere showing the overall porous structure. (c) High resolution TEM image of the edge area of the sphere shown in (b). The sample exhibits interconnected wormlike pores with diameter of ~3-5 nm. ....	93
Figure 3-7.	Typical SEM images of the silica spheres prepared with 50 wt % of fructose and TEOS/EtOH (v/v) ratio of 1:10. (a) Particles aggregated into clusters. (b) Broken particles exhibit hollow cores. ....	94
Figure 3-8.	Typical SEM images of the silica spheres prepared with 50 wt % of fructose through a two-step water in oil method. (a) Particles without breakage. (b) Particle with broken pieces around. (c) Broken particles from a cluster showing the hollow core.....	95
Figure 4-1.	Representative X-ray energy dispersive spectra for gold-silica nanocomposite.....	118
Figure 4-2.	N <sub>2</sub> adsorption–desorption isotherms at –196 °C for the annealed gold-silica nanocomposite samples with varied gold content after removal of DBTA template.....	119
Figure 4-3.	BJH pore size distribution curves of the mesoporous gold-silica nanocomposite derived from desorption isotherm branches.....	120
Figure 4-4.	Powder XRD patterns for the mesoporous gold-silica nanocomposite sample GS50-10.....	121
Figure 4-5.	(a) Representative TEM image of mesoporous gold-silica nanocomposite sample (GS50-10). The darkest round spots are gold nanoparticles. The gray framework feature is silica matrix with inter-connected wormlike pores. Insert: an electron diffraction	

	pattern of gold nanoparticles in the same sample. (b) Size distribution histogram of the gold particles dispersed in the mesoporous composite sample shown in (a) with Gaussian curve fitted to the data. About 300 particles sampled from 5 different areas based on TEM images were employed for this estimation. The presence of some gold particles (less than 0.3%) with apparent diameters greater than 8 nm might be attributed to aggregation of gold nanoparticles or overlapping images of particles because of the sample thickness.....	122
Figure 4-6.	A series of X-ray mapping images of mesoporous gold-silica nanocomposite containing 25 wt % gold (GS50-25). (a) As-made nanocomposite. (b) Gold mapping. (c) Silicon mapping. (d) Oxygen mapping.....	123
Figure 4-7.	Typical solid state UV-Vis reflectance spectrum of mesoporous gold-silica nanocomposite.....	124
Figure 5-1.	Fabrication schematics of organic-inorganic nanocomposite based on self-array of vinyl modified silica nanoparticles.....	141
Figure 5-2.	Representative AFM images of vinyl modified nanoparticles assembled on mica surface. (a) Interconnected island domains. (b) An edge area with monolayer particle arrays.....	142
Figure 5-3.	Representative AFM image of thin film of monolayer array of vinyl modified silica nanoparticles with short range ordering and the corresponding depth analysis plot.....	143
Figure 5-4.	Representative AFM image of PHEMA-silica nanocomposite thin film obtained after a photo-initiated polymerization of pre-arrayed vinyl modified silica nanoparticles in HEMA suspension on mica surface.....	144
Figure 5-5.	Representative AFM images of vinyl-modified silica nanoparticles arrayed on hydrophobic graphite surface.....	145
Figure 5-6.	Representative IR spectra of nanocomposite thin films polymerized at different time interval: (a) 0 h, (b) 6 h, and (c) 12 h. ....	146
Figure 5-7.	Representative energy dispersive X-ray spectrum for organic-inorganic nanocomposite thin film.....	147

Figure 5-8.	Representative SEM images of mesoporous nanoparticles arrayed on glass slide by solvent casting at (a) a low magnification, and (b) a high magnification.....	148
Figure 6-1.	Schematics of biologically templated synthesis of PANI-Colla complex. ....	170
Figure 6-2.	The protonation and redox reactions between the various forms of polyaniline.....	171
Figure 6-3.	UV-Vis absorption spectra of chemical polymerized PANI-Colla complex reaction mixture at day 2 to day 5 (a)-(d), in comparison with UV-Vis absorption spectrum of PANI polymerized for 5 days (e). ....	172
Figure 6-4.	Comparison photographs of (a) PANI as-synthesized suspension and (b) Redispersed PANI in 0.01 M acidic acid <i>vs.</i> (c) PANI-Colla as-synthesized suspension and (d) PANI redispersed in 0.01 M acidic acid. The PANI as-synthesized reaction mixture (a) is a slightly brownish green color solution with dark green precipitate. Dispersion of precipitate of (a) in acidic acid aqueous solution forms a suspension, which settles in a few minutes. In contrast, the as-synthesized PANI-Colla (c) is green solution with dark green precipitate. Re-dispersed in acidic acid aqueous solution under sonicating, PANI-Colla complex forms green color solution (d). ....	173
Figure 6-5.	FT-IR spectra of (a) collagen, (b) PANI and (c) PANI-Colla complex.....	174
Figure 6-6.	FT-IR comparison spectra of (a) a physical mixture of polyaniline and collagen <i>vs.</i> (b) PANI-Colla complex. ....	175
Figure 6-7.	UV-Vis absorption spectra of PANI-Colla complex in aqueous solution at various pH: (a) 13.0 (b) 10.5 (c) 6.6 (d) 4.7, and (e) UV-Vis absorption spectrum of aniline collagen mixture in water at pH 4.7.....	176
Figure 6-8.	Comparison AFM images of (a) collagen and (b) PANI-Colla complex.....	177
Figure 6-9.	Comparison images of attachment and differentiation of PC-12 cells on tissue culture dishes coated with (a) PANI-Colla and (b)	

	PANI under culturing conditions for 72 h. The bright globular features in the pictures are cells poorly attached on substrate surface and suspending in the medium. In comparison with PANI coated surface (b), PANI-Colla coated substrate (a) exhibit significantly improved cell affinitive property with less globular features observed. Precursor neuron cells adhered on PANI-Colla surface also showed vivid differentiation and network formation tendencies, evidenced by the formation of prolonged interconnected neurites after cultured for 72 h. In contrast, the cell differentiation on PANI occurred but rarely under the same conditions. ....	178
Figure 7-1.	Structures of new ligands and their metal complexes. ....	203
Figure 7-2.	Schematic cross-sectional diagram of an OLED. ....	204
Figure 7-3.	Synthetic scheme for ligand <b>1a</b> and hydrogenation reaction of ligand <b>1a</b> to ligand <b>1b</b> . ....	205
Figure 7-4.	NMR Spectra of ligand <b>1a</b> . Inserts: (a) H <sub>2</sub> and H <sub>4</sub> irradiated, (b) H <sub>3</sub> irradiated. ....	206
Figure 7-5.	NMR Spectrum of ligand <b>2a</b> . ....	207
Figure 7-6.	FT-IR spectra of (a) ligand <b>1a</b> and (b) ligand <b>2a</b> . ....	208
Figure 7-7.	Representative UV-Vis spectra for ligand <b>1b</b> in toluene after oxidation with air for various reaction periods: (a) 1, (b) 4, (c) 7, (d) 10, (e) 13, (f) 16 min. ....	209
Figure 7-8.	During air oxidation: <b>1b</b> → <b>1a</b> , UV absorbance at (a) 330 nm, (b) 420 nm and (c) 600 nm measured as a function of time. ....	210
Figure 7-9.	Molar absorptivity calculation curve plotted based on UV absorbance at 600 nm of ligand <b>1a</b> at different concentrations. ....	211
Figure 7-10.	Plot of concentration of <b>1b</b> versus reaction time (a) based on UV measurement, (b) for first-order reaction with the same initial concentration. Insert: linear plot for a first-order reaction - natural logarithm of concentration of <b>1b</b> versus reaction time. ....	212
Figure 7-11.	Mass spectrum of aluminum complex <b>3a</b> . ....	213

Figure 7-12.	Mass spectrum of aluminum complex <b>3b</b> .	214
Figure 7-13.	Mass spectra of aluminum complex sample, <b>3a</b> , stored under different conditions. Top: dissolved in acetone for 2 h; Bottom: powder under nitrogen for 2 weeks.	215
Figure A-1.	Repeating unit in polyphosphazenes.	242
Figure A-2.	Two fundamental routes to synthesize substituted polyphosphazenes.	243
Figure A-3.	Applications of materials modified with stimuli-responsive polymers for separation/purification, membrane valves, and bioactive molecules.	244
Figure A-4.	Release mechanism for grafted stimuli-sensitive polyphosphazene matrices.	245
Figure A-5.	Preparation of poly(N-isopropylacrylamide) modified polyphosphazene as temperature sensitive delivery matrix material.	246
Figure B-1.	Rotating disk (Hg on Au) polarogram (2400 rpm) of ligand <b>1a</b> in MeCN. Scan Rate = 50 mV/s.	249
Figure B-2.	Cyclic voltammogram (Hg on Au, negative potential region) vs. Ag/Ag <sup>+</sup> of ligand <b>1a</b> in MeCN. Scan Rate = 100 mV/s.	250
Figure B-3.	Cyclic voltammogram (Pt wire, negative region) vs. Ag/Ag <sup>+</sup> of ligand <b>1a</b> in MeCN. Scan Rate = 100 mV/s.	251
Figure B-4.	Cyclic voltammogram (Pt wire, positive region) vs. Ag/Ag <sup>+</sup> of ligand <b>1a</b> in MeCN. Scan Rate = 100 mV/s.	252
Figure B-5.	Rotating disk (Hg on Au) polarogram (2400 rpm) of ligand <b>2a</b> in MeCN. Scan Rate = 40 mV/s.	253
Figure B-6.	Cyclic voltammogram (Hg on Au, negative region) vs. Ag/Ag <sup>+</sup> of ligand <b>2a</b> in MeCN. Scan Rate = 100 mV/s.	254
Figure B-7.	Cyclic voltammogram (Pt wire, negative region) vs. Ag/Ag <sup>+</sup> of ligand <b>2a</b> in MeCN. Scan Rate = 100 mV/s.	255

Figure B-8. Cyclic voltammogram (Pt wire, positive region) vs. Ag/Ag<sup>+</sup> of ligand **2a** in MeCN. Scan Rate = 100 mV/s.....256

**Abstract**

Nanostructured, Electroactive and Bioapplicable Materials

Shan Cheng

Advisor: Yen Wei

Novel nanostructured porous sol-gel materials, nanocomposites, electroactive and bioapplicable materials have been successfully developed for a wide range of perceivable applications. Several versatile nonsurfactant templated sol-gel pathways have been developed to prepare nanostructured porous materials and composites with different morphologies (e.g., monoliths, nanospheres, nanoparticles, and thin films), structures, compositions and properties. The synthetic conditions were systematically studied and optimized. The template effects on pore structure as well as synthetic process, especially template removal steps, have been investigated. The composition and pore structures were thoroughly studied with various spectroscopic and microscopic methods such as IR, TGA, SEM, TEM, BET and XRD. The obtained mesoporous materials usually exhibit high surface area, large pore volume and narrowly distributed pore diameter. The porosity can be fine tuned simply by adjusting the template concentration. The convenient synthesis as well as the distinctive structure and physical-chemical properties render these sol-gel materials great suitability for a wide range of potential applications, such as chemical and biological sensors, catalysts, drug delivery and functional coatings.

Biocompatible and electroactive nanocomposites have been prepared through a biological agent (i.e., collagen) templated chemical polymerization of aniline monomers.

The resultant polyaniline-collagen complexes exhibit well controlled doping-dedoping electroactivity and much enhanced solubility. Demonstrated with cell growth studies, the polyaniline-collagen complexes show improved biocompatibility in comparison to polyaniline. The new materials can be used to fabricate scaffolds, with which the effect of electrical stimuli on cell growth and differentiation can be evaluated with the hope of ultimately using electrical signal to stimulate controllable cell and tissue regeneration.

Aniline derivative substituted quinoline ligand compounds and their complexes have been prepared and investigated as potential electroluminescent materials.





## Preface

The overall objective of this dissertation is to develop new advanced materials, more specifically, nanostructured porous materials, nanocomposites and electroactive materials, for potential applications in electrooptical devices, biosensors, drug delivery and tissue engineering. Among others, two main considerations are present throughout this research work. Firstly, it is always desirable to have versatile and controllable synthesis processes and products. Of our special interest is the versatility of the newly developed nonsurfactant templating sol-gel pathway. Aiming at a variety of potential applications, it is desired that a broad selection of templates can be used, materials with different morphologies and compositions can be produced, and the entire process can be fine-tuned. Secondly, due to the special requirement of bio-applications, these materials and/or their synthetic reagents and conditions need to do no harm to biomolecules and cells, and this property is described as “biofriendly” in this dissertation.

The organization of the dissertation is as follows.

Chapter 1 is an overview of nanostructured porous sol-gel materials. Based on an introduction of fundamental sol-gel chemistry, mesoporous materials (i.e., with pore diameter of 2-50 nm) obtained from both surfactant and nonsurfactant templated sol-gel methods are described in detail. Discussions include the template species, templating mechanisms, reaction conditions and the characteristic microstructures of porous materials. Description of general characterization and testing methods for porous materials is provided with an emphasis on gas sorption measurement.

Chapter 2 presents a study focused on the synthesis of mesoporous materials with a new category of nonsurfactant template, i.e., thermal decomposable compounds. With this new class of templates, conventional high temperature (i.e., 500-600 °C) calcination template removal process can be avoided. The materials with typical nonsurfactant templated mesoporous structure are prepared with a template removal process at a relatively low temperature (e.g., 150 °C). The materials synthesis and characterization are described. The template removal process is discussed in detail.

Chapter 3 describes the development of a synthetic route to prepare mesoporous nanospheres with uniform size and shape. The study demonstrates the morphological controllability of the nonsurfactant templating method. The experimental method, material characterization and template effect on pore structures are discussed. In this work, fructose was selected as the nonsurfactant template because it has been proven by our group previously a very effective and biofriendly template, among over one hundred other nonsurfactant molecules examined (e.g., glucose, maltose, soluble starch, cyclodextrins, glycerol, oligopeptides, tartaric acid, etc.). With well-defined morphology and nanostructure, the nanospheres are potentially useful for a variety of applications, such as drug delivery, bio-sensor and catalyst.

Chapter 4 presents the studies on gold nanoparticle dispersion in mesoporous silica matrices for the perceivable chemical and biological sensing applications. The gold-silica nanocomposites were prepared through a nonsurfactant templated sol-gel pathway with a gold sol as the source of metal particles. The obtained nanocomposites

exhibit mesoporosity of the silica framework as well as the unique size dependent optical properties of the second material phase, i.e., gold nanoparticles. The characteristics of the materials such as composition, morphology, porosity, and optical properties are discussed.

An effort to fabricate organic-inorganic nanocomposite thin films with ordered nanostructured domains is reported in Chapter 5. The nanocomposite thin films were studied for their composition, morphology and layer ordering behavior. The studies involved the use of both spectroscopic and microscopic methods, such as IR spectroscopy and atomic force microscopy (AFM). The self-assembling of two-dimensional ordered array of mesoporous nanospheres is also described.

Chapter 6 is devoted to the development of electroactive and biocompatible materials. The background introduction of conductive polymers as well as a review of applications of conducting polymers in biotechnology is provided. Using the preparation of polyaniline-collagen complex as an example, the bio-templated synthetic route is demonstrated, which aims at simultaneously improving both biocompatibility and water solubility of conductive polymers. The properties of the complex material (e.g., solubility, electroactivity, and morphology) are evaluated and reported based on comparison with the component materials. The improved biocompatibility is demonstrated with cell growth studies. With improved processability, biocompatibility and controlled electroactivity, the materials will be used as a scaffold material for tissue engineering applications.

Chapter 7 is focused on the synthesis and characterization of two aniline derivative substituted quinoline ligand compounds and their metal complexes, as potential electroluminescent materials. The feasibility of obtaining new ligands and metaloquinolates through molecular design was demonstrated.

Finally, Chapter 8 concludes this dissertation with summaries of the results and outlook for future work. It should be noted that although this thesis work is a continuation of Dr. Wei's research effort, I have been involved in planning, formulating and conducting the experiments. As an example of my independent discoveries in this thesis, in the pursuit of making mesoporous nanoparticles, I developed a novel method to make mesoporous nanospheres. In addition, I am the first to explore the use of thermally sensitive compounds as nonsurfactant templates and to obtain gold-silica mesoporous nanocomposite materials by the nonsurfactant templating pathway.

## **Chapter 1. An Overview to Nanostructured Porous Sol-Gel Materials**

### **1.1. Introduction**

The discovery in 1930s of the synthetic microporous zeolites, a series of aluminosilicate materials with frameworks analogous to those formed geologically, has brought up tremendous opportunities in many areas of advanced materials, from fundamental scientific research to diverse industrial applications.<sup>1-4</sup> In the past few decades, considerable efforts have been devoted to developing nanostructured (i.e., structures roughly in the 1-100 nm size range) porous materials with a wide range of porosity, morphology and composition. The chemical and mechanical mechanisms that influence porosity during and after the synthesis process have been extensively studied. Advanced characterization methods and instruments have been developed, which greatly facilitate the research in the field. With their unique structural properties, nanostructured porous materials have been widely used as catalysts,<sup>5,6</sup> separation media,<sup>7,8</sup> sorption materials,<sup>9</sup> ion-exchangers and bioreactors.<sup>10</sup>

In the early 1990s, a surfactant templated synthetic route has been developed by researchers at Mobil Corporations.<sup>11,12</sup> Known as M41S, silicon and other metal oxides with periodic nanoporous structures have been obtained. While M41S has tunable pore diameters of 1.5-10 nm, this was the first time that the pore size of synthetic porous materials was expanded to the mesoscopic range. This breakthrough discovery created an innovative strategy for the synthesis of nanostructured porous materials. Soon after, this

surfactant templated method was extended to the synthesis of a wide range of porous silica materials, as well as many other metal oxide species.

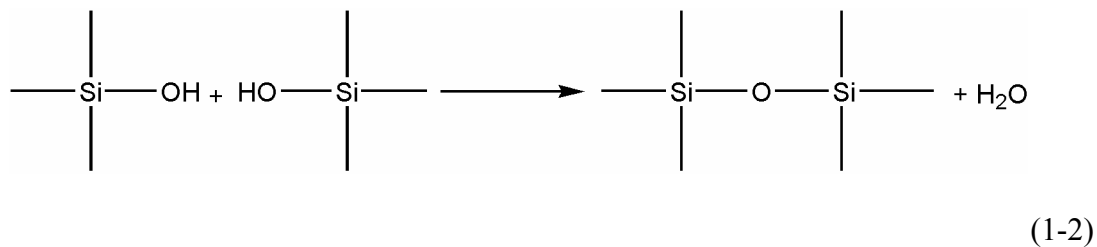
In 1998, our group reported a general nonsurfactant templated sol-gel pathway.<sup>13</sup> The syntheses of bulk mesoporous silica materials have been achieved through sol-gel reactions in the presence of nonsurfactant organic compounds. This exciting discovery conceptually expended the categories of the template compounds available for the sol-gel synthesis of porous materials. The process has been demonstrated to be convenient, mild and biofriendly. The mesoporous materials prepared with nonsurfactant templates have been successfully used for enzyme and protein immobilizations.<sup>14</sup> A major part of my research work has been focused on further developing this nonsurfactant templated pathway, and exploring new opportunities to tailor the structure-morphology and properties-function relations of the new nanostructured porous materials and composites for a range of potential applications. For the convenience of further discussion, it is necessary for us to briefly introduce the sol-gel chemistry, clarify some terminologies and review the templated sol-gel methods. Due to their importance to reveal and verify the structural properties of synthesized porous products, major porosity characterization methods will be discussed in a separate section with an emphasis on gas adsorption measurements.

## 1.2. Fundamental Sol-Gel Process

The overall sol-gel process, as the name implies, usually involves two stages: precursors initially form high molecular weight but still soluble poly-intermediates, a sol, and the intermediates further link together to form a three-dimensional network, a gel.<sup>15</sup> The precursors for a sol-gel reaction could be either inorganic salts or organic compounds, known as metal alkoxides. The formation of a gel from both types of precursors will be illustrated in the following with silica as the primary example, since most of our understanding of the sol-gel process is derived from silica composition.

### 1.2.1. Inorganic Salt Precursors

Porous silica gels can be prepared with inorganic salts, such as sodium silicates or potassium silicates.<sup>16</sup> In this method, two types of chemical reactions are involved: soluble silicates hydrolyze to monomeric  $\text{Si(OH)}_4$  under acidic conditions, reaction 1-1, followed by polymeric condensation of the silicic acid, reaction 1-2.

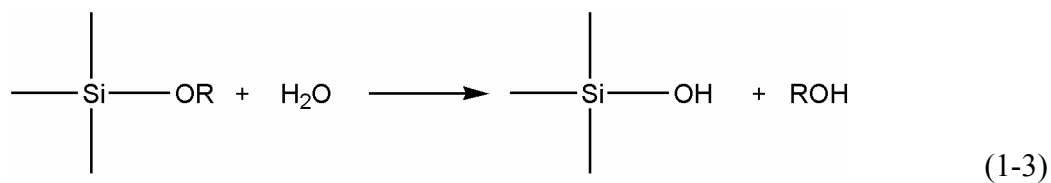


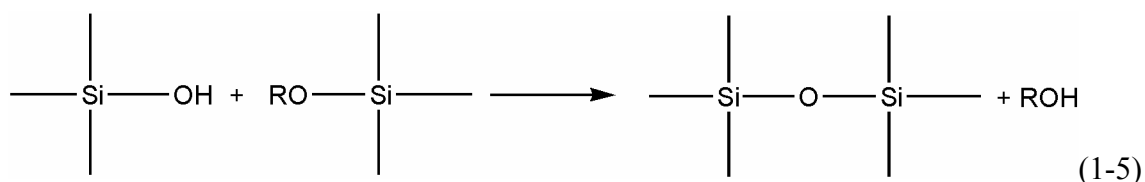
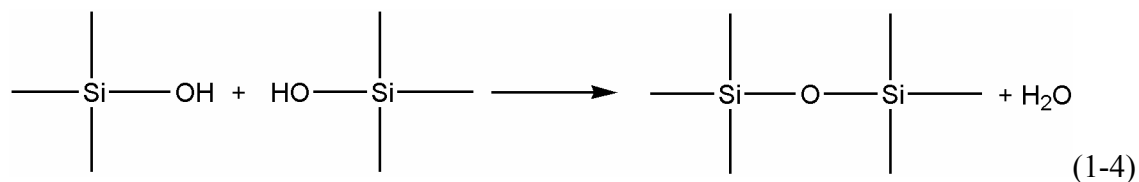


The porous structure of the silica gel prepared with this method is affected by the composition of the silicate precursor, temperature, pH, aging and drying conditions, among which pH and the drying condition are the most important ones.

### 1.2.2. Alkoxide Precursors

An alternative method to silica gel involves the hydrolysis and condensation reactions of tetraalkoxysilanes in the presence of water and appropriate catalysts.<sup>15,17</sup> Firstly, silicic acids are produced by hydrolysis of an alkoxysilanes, as in reaction 1-3. The silicic acids then undergo either self-condensation, reaction 1-4, or condensation with an alkoxide as in reaction 1-5. Tetraethoxysilane (TEOS) and tetramethoxysilane (TMOS) are the most commonly used alkoxide precursors in the preparation of silica containing gels due to their controllability in reaction kinetics. In the case of inorganic silicate precursors, salts such as NaCl or KCl are formed as by products, and it is quite difficult to completely remove these salts from the gels. In contrast, the gelation reactions of alkoxysilanes lead to the release of alcohol and water molecules, which can be readily removed by drying process. Therefore, the alkoxide precursors are preferred for making porous materials with high purity, and in most of our syntheses, metal alkoxide precursors are used.





According to the application demands, sol-gel products can be prepared under appropriate conditions into various forms, such as monoliths,<sup>18-20</sup> particles,<sup>21,22</sup> thin films<sup>23-25</sup> and fibers.<sup>26,27</sup> Besides product versatility, the sol-gel process also offers many other advantages such as the simplicity and convenience of the synthesis procedure, flexibility of solution chemistry, low cost in starting materials, and good product purity.<sup>28</sup>

### 1.3. Mesoporous Materials from Surfactant Templated Sol-Gel Methods

Based on pore size, the International Union of Pure and Applied Chemistry (IUPAC) classifies porous materials into the following categories:<sup>29</sup>

- Microporous: with pore diameter less than 2 nm
- Mesoporous: with pore diameter between 2 and 50 nm
- Macroporous: with pore diameter greater than 50 nm

Before early 1990s, with a pore or channel diameter of 0.7-1.2 nm, there seems a natural limit for the synthetic porous solid. Most of the zeolites and sol-gel materials are microporous.<sup>15,30</sup> A breakthrough point has been reached in 1992 when Kresge *et al.* announced the surfactant templated synthesis of a series of periodic mesoporous silica and aluminosilica oxides, known as M41S family.<sup>11</sup> Using alkyltrimethylammonium cationic surfactants as pore structure directing agents, porous materials were obtained with a hexagonal arrangement of uniform mesopores in the range of ~1.5-10 nm. The pore size is controllable by varying the length of the alkyl chain of the template molecules or with the aid of auxiliary organic compound as additives, spacers and pore fillers. Three typical periodical mesophase structures of M41S family are illustrated in Figure 1-1: hexagonal phase, a one-dimensional system of hexagonally arranged cylindrical channels; cubic phase, a three-dimensional bicontinuous porous frame structure; and lamellar phase, a two dimensional system of layered sheets structure.<sup>12,31</sup> Other structures with random array of pores were also observed. All of these mesoporous materials are characterized by high surface area, large pore volume and narrow pore size distributions as compared to microporous materials.

The formation mechanism of this mesoporous family of molecular sieves was proposed as liquid-crystal templating (LCT).<sup>32,33</sup> The so-called “templating” here is a process during which an organic species functions as a central structure, surrounded by inorganic oxides forming a framework. As illustrated in Figure 1-2,<sup>32</sup> long chain surfactant molecules arrange themselves through micelle self-assembly to form liquid-

crystalline phases. Silicate species deposit between surfactant “rods” and then condense to form the inorganic network. The interaction of the surfactant and silicate species mediates the hexagonal ordering. After removing the surfactant templates from the as-synthesized sample, materials exhibit mesoporosity with pore size of 2-10 nm. In general, the overall LCT mechanism is directed by two features. One is the dynamics of surfactant molecules to form assemblies, micelle, and ultimately crystalline structure, which functions as template. The other is the ability of the inorganic oxide to undergo hydrolysis and polycondensation reactions to form network around the organic template.

Since the discovery of M41S family, the surfactant template hydrothermal pathway has been extensively studied and expanded to sol-gel process.<sup>32,33</sup> A wide variety of surfactant molecules with different sizes, shapes, functionalities and charges have been subsequently demonstrated to be able to effectively function as pore structure directing agents. These surfactant molecules can be classified based on their head group chemistry and charge as follows.

- Cationic surfactants: the hydrophilic group carries a positive charge, e.g., tetraalkylammonium salts<sup>34</sup>  $(C_nH_{2n+1})(CH_3)_3NX$ ,  $n = 6, 8, 9, 10, 12, 14, 16, 18, 20, 22$ ;  $X = OH, Cl, Br, HSO_4$ ; and  $(C_nH_{2n+1})(C_2H_5)_3N$ ,  $n = 12, 14, 16, 18$ ).
- Anionic surfactants: the hydrophilic group carries a negative charge, e.g., sulfates<sup>35</sup>  $(C_nH_{2n+1}OSO_3^-)$  ( $n = 12, 14, 16, 18$ ), sulfonates<sup>36</sup>  $(C_{16}H_{33}SO_3H$  and  $C_{12}H_{25}C_6H_4SO_3Na)$ , and phosphates  $(C_{12}H_{25}OPO_3H_2, C_{14}H_{29}OPO_3K)$ .

- Neutral surfactants: the hydrophilic group is not charged, e.g., primary amines<sup>37</sup> ( $C_nH_{2n+1}NH_2$ ) and poly(ethylene oxides)<sup>38,39</sup> (PEO).

It is necessary to point out that in neutral surfactant templating systems where strong electrostatic interactions are absent, LCT mechanism may not be suitable to describe the mesophase formation. Instead, neutral surfactants have much stronger tendency to form aggregations in solution.<sup>40</sup> Those aggregations of surfactant molecules and the hydrogen bonding interactions may play an important role in directing the mesophase formation in the case of neutral surfactant templates.

The surfactant templated approach has also been extended from silicates and aluminosilicates<sup>41-44</sup> to a wide range of metal oxides. With this method, a variety of mesoporous inorganic oxide frameworks, some of which may have important technological applications, have been achieved, including: titanium oxide,<sup>45,46</sup> zirconium oxide,<sup>47,48</sup> vanadium oxide,<sup>49</sup> tungsten oxide,<sup>50</sup> and so forth.

Porosity control during the surfactant templated sol-gel synthesis has been considerably studied. The pore geometry is controlled primarily by the template concentration, charge of the surfactant and the processing conditions.<sup>32</sup> For example, mesoporous materials prepared with charged surfactants usually exhibit ordered hexagonal porous structure, while the materials obtained with neutral surfactants sometimes lack a long range ordered channel arrangement and exhibit both complementary textural and framework-confined mesoporosity.<sup>37</sup> Pore size, recently being expanded up to 30 nm,<sup>51</sup> can be controlled by the size of the surfactant, addition of

auxiliary organics, aging conditions and template removal method.<sup>32,33,52</sup> The wall thickness, which greatly affects the thermal stability of the material, is controlled by the charge of the surfactant and the formation mechanism. Materials prepared with neutral surfactants usually exhibit a greater wall thickness and furthermore a higher thermal stability than that obtained with ionic surfactants, due to the absence of electrostatic or charge-matching effects.<sup>37</sup>

#### **1.4. Mesoporous Materials from Nonsurfactant Templated Sol-Gel Methods**

A novel nonsurfactant templated sol-gel route to mesoporous materials has been developed by our group.<sup>53,54</sup> Unlike the surfactant template pathway, the non-surfactant organic compounds, such as glucose, maltose, and dibenzoyltartaric acid, were employed as templates or pore structure directing agents during a sol-gel process under room temperature. The template can be easily removed by solvent extraction. The obtained materials exhibit mesoporosity with pore diameter of ~2-6 nm, which is controllable by simply varying the nonsurfactant content in the solution. The materials show high surface area of ~1000 m<sup>2</sup>g<sup>-1</sup> and large pore volume of ~1.0 cm<sup>3</sup>g<sup>-1</sup>. The pore structure is not highly ordered, which is similar to that of some neutral surfactant templated mesoporous materials. A framework filled with interconnected wormlike pores is observed. The initial study of the nonsurfactant template pathway involved the formation of silica mesophases under acidic conditions. Subsequent efforts have shown these structures can also be formed in basic or near neutral media.<sup>53</sup>

The mechanism of nonsurfactant templating to mesophase formation was not yet fully understood. It was proposed that during the nonsurfactant templated sol-gel process, nonsurfactant aggregates and the aggregate assemblies may function as the organic templates. The interactions between the organic templates and the silicate intermediates, such as hydrogen bonding, may also play an important role in directing the mesophase formation prior to and/or during the gelation.

Through the nonsurfactant templated sol-gel pathway, mesoporous silica oxide, alumina oxide and titanium oxide have been successfully prepared.<sup>55</sup> Mesoporous zinc phosphate has been obtained with the glucosamine molecules as nonsurfactant template.<sup>56</sup> The process has been extended to prepare various advanced materials including organic-inorganic hybrid materials<sup>57</sup> and mesoporous bio-composites with enzyme/protein immobilized.<sup>14</sup>

In comparison to the surfactant templated sol-gel method to mesoporous materials, the nonsurfactant templated pathway is mild, less expensive, environmentally friendly and biofriendly. In this method, easy removal of template by solvent extraction can avoid the structure damage by calcination. The framework thickness from the non-surfactant route (~4 nm) is much larger than that of M41S (0.8-1.5 nm), which contributes to superior thermal stability. Porous silica by the non-surfactant route exhibits much fewer defects than that from neutral surfactants. Moreover, a vast diversity of organic compounds provides possibilities to form macroscopic nanostructured sol-gel materials.

## 1.5. Characterization Methods for Porous Materials

Reliable porosity characterization methods are important for developing porous materials. To evaluate exact pore parameters such as pore size, size distribution and surface area, the most commonly used methods include, among others, gas sorption measurement, mercury porosimetry, small angle X-ray scattering, fluid flow methods (permeation and diffusion), flow microcalorimetry and electron microscopy.

The gas sorption measurement is a widely used nondestructive method to analyze pore size and distribution. Its best working range is from micropores up to 200 nm pore width.<sup>58</sup> Gas sorption measurement is one of the most applicable methods for sol-gel silica materials which are either mesoporous or microporous. This method will be reviewed later in more detail.

Mercury porosimetry<sup>59</sup> is a method of measuring pore size and pore size distribution by injecting mercury into pores. Due to the high pressure involved (up to 400 MPa) and the limiting size of pores for penetration by pressurized mercury (~2 nm), this method is more suitable to characterize mesoporous or macroporous materials. Safety requirement and sample disposal are major concerns for this technique.

In small angle X-ray scattering measurement, X-rays from a source are focused into a fine beam and directed on to the sample. A small fraction of the beam is scattered and detected. The intensity and the way the intensity varies with the scattering angle are determined by the variations of electron density within a sample, which originate from the structure of the sample. The electron density is high in the solid wall area and falls to



zero in a pore. Structural information can therefore be deduced from the knowledge of scattering intensity and angle.<sup>60,61</sup> For example, approximated as the repeating distance in the porous materials, the sum of a pore diameter and a pore wall thickness can be estimated base on the  $d$  spacing calculated from the Bragg equation (1-6). The measurement obtained with this method reflects all interfacial situations, including closed porosity which is not accessible to adsorption techniques.



(1-6)

A fluid flow method<sup>59</sup> can be used to measure the pore size of porous materials. The size of penetrating pores can be evaluate by flow rate and pressure drop across porous materials. The result measured by this method is strongly affected by pore shape and the tortuosity of the network.<sup>62</sup>

The operational principle for the flow microcalorimeter used to characterize the surface porosity is that gas or liquid adsorption occurring on the solid surface is associated with the evolution or absorption of heat.<sup>63</sup> The usefulness of this method greatly depends on the availability of a correlation between the porosity and the heat of adsorption of certain adsorbate molecules on the porous surface. For example, preferential heats of adsorption of *n*-butanol from *n*-heptane solution have been successfully used to measure polar surface areas. It is found that for polar surfaces, 1 joule of the adsorption heat of *n*-butanol corresponds to 6.7 m<sup>2</sup> of the surface areas obtained from the polar sites in graphite.<sup>64</sup>

To analyze and interpret data, most of the porosity characterization methods adapt structural model assumptions and mathematical approximations. As a result, sometimes they may not be able to reveal the real pore structure of porous materials. Based on image analysis,<sup>65</sup> microscopic observation provides a straightforward evaluation of pore size, shape and distribution.<sup>66,67</sup> The major advantage of microscopic characterization is that a pore model is not necessary. The method allows a direct observation of the pore structures. To ensure statistically representative results, sufficient samples must be analyzed with this method.

Each of these analytical methods has its own advantages as well as suitable working conditions. In general, the selection of the approaches should be dependent upon the properties and the microstructures of the material under investigation. For the same reason, it is normally insufficient for a single method to qualify for a confirmative analysis of pore parameters. Therefore multiple analyses should be carried out to facilitate a comprehensive understanding of the porosity. In our studies, the major approaches used to study the porosity of mesoporous sol-gel silica are gas adsorption measurement, small angle X-ray scattering and electron microscopy image analysis. Due to its relative complexity and its considerable usage in our experiments, a brief discussion on gas adsorption measurement is provided next as a subsection.

### **1.5.1. Gas Sorption Measurement**

As aforementioned, gas sorption measurement is a common nondestructive method to analyze microporous and mesoporous materials. The following is a brief description of its working rationale.

In an adsorption process, the amount of adsorbed gas (i.e., adsorbate) at the surface of a porous material (i.e., adsorbent) depends on its microstructure, pressure and temperature.<sup>68</sup> Therefore, the pore structure of the adsorbent can be quantitatively evaluated from the gas sorption isotherm. The gas sorption isotherm is a plot of the amount of adsorbed gas as a function of gas pressure at a constant temperature, usually liquid nitrogen temperature ( $-196\text{ }^{\circ}\text{C}$ ). The pressure is expressed as relative pressure, a fraction of saturated pressure. The amount of the adsorbed gas is expressed in volume at standard temperature and pressure (STP) relative to the weight of the sample. During the measurement, the pressure of the gas increases from vacuum to saturation pressure, and then gradually decreases back to vacuum. Along with the pressure variation, two branches of the isotherm are obtained, namely adsorption branch and desorption branch.

#### **1.5.1.1. Classification of Adsorption Isotherms**

Depending on the relative strength of the interactions among adsorbate molecules and the structure of the adsorbent, the adsorbate-adsorbent system may exhibit monolayer adsorption, multilayer adsorption, capillary condensation or a combination. The shape of an isotherm indicates the occurrence of these phenomena, and furthermore, reveals the

porosity of the adsorbent. According to the IUPAC classification, the majority of the adsorption isotherms may be categorized into six types as shown in Figure 1-3.<sup>29</sup>

Type I reversible isotherms are typical in microporous solids with relatively small external surfaces. Monolayer adsorption occurs significantly at relatively low partial pressures  $< 0.5 P/P_0$ .

Type II reversible isotherms describe the gas sorption with a non-porous or macroporous solid in which multi-layer adsorption forms due to a strong interaction between adsorbed molecules.

Type III reversible isotherms are convex towards the relative pressure axis. This type of isotherm originates from both non-porous and microporous solid. These isotherms are characteristic of weak adsorbate-adsorbent interactions.

Type IV isotherms exhibit a plateau with a characteristic hysteresis loop. The presence of hysteresis loops is associated with mesoporous solid, where capillary condensation occurs.

Type V isotherms are related to the Type III isotherms in that the adsorbate-adsorbent interactions are weak. Type V isotherms are usually obtained from microporous or mesoporous solids.

Type VI isotherms are stepwise, which represent multilayer adsorption on a uniform non-porous surface.

Gas adsorption measurements of most of mesoporous sol-gel silica materials we studied present type IV isotherms with a characteristic hysteresis loop at around  $0.5 P/P_0$ ,

which is usually associated with capillary condensation in mesoporous structure. In general, the hysteresis loops may exhibit a variety of shapes and sizes, which are affected by pore shape, size of the network and degree of interconnection.

#### **1.5.1.2. Adsorption Hysteresis**

Classified by IUPAC, there are four typical types of isotherms, which are shown in Figure 1-4.<sup>29</sup>

Type H1 loop is often associated with pores with regular shape and narrow size distribution.

Type H2 loop used to be attributed to ink-bottle pores, which have narrow necks and wide body. Now it has been well recognized that network effect also play an important role in the loop formation.

Type H3 loop is observed with aggregates of plate-like particle giving rise to slit-shape pores.

Type H4 loop is usually associated with narrow slit-like pores.

Additional network structural information can be also revealed by the shape and the size of the isotherm hysteresis loops.<sup>69</sup> For example, a narrower hysteresis loop can be observed with materials with higher connectivity. Another example can be found in observations that; for porous solids with bidispersed structure, the sharpness of desorption isotherm knee describes the size of the solid particles.

## 1.6. References

1. Dyer, A. *An Introduction to Zeolite Molecular Sieves*; Wiley: Chichester, 1998.
2. Weitkamp, J.; Puppe, L. *Catalysis and Zeolites: Fundamentals and Applications*; Springer: Berlin, 1999.
3. De Boer, R. *Theory of Porous Media: Highlights in Historical Development and Current state*; Springer: Berlin, New York, 2000.
4. Ishizaki, K.; Komarneni, S.; Nanko, M. *Porous Materials –Process, Technology and Application*; Kluwer Academic: Netherlands, Chapter 5, 1998.
5. Thomas, J. M.; Raja, R. *Austr. J. Chem.* **2001**, *54*, 551.
6. Doesburg, E. B. M.; De Jong, K. P.; Van Hooff, J. H. C. *Stud. Surf. Sci. Cataly.* **1999**, *123*, 433.
7. Tsuru, T. *Separation and Purification Methods* **2001**, *30*, 191.
8. Nair, B. N.; Okubo, T.; Nakao, S.-I. *Maku* **2000**, *25*, 73.
9. Misaelides, P.; Godelitsas, A. *NATO Sci. Seri., Seri. E: Appl. Sci.* **1999**, *362*, 193.
10. Stewart, M. P.; Buriak, J. M. *Adv. Mater.* **2000**, *12*, 859.
11. Kresge, C. T.; Leonowicz, M. E.; Roth, W. J.; Vartuli, J. C.; Beck, J. S. *Nature* **1992**, *359*, 710.
12. Beck, J. S.; Vartuli, J. C.; Roth W. J.; Leonowicz, M E.; Kresge, C. T.; Schmitt, K. D.; Chu, T-W.; Olson, D. H.; Sheppard, E. W.; McCullen, S. B.; Higgins, J. B.; Schlenker, J. L. *J. Am. Chem. Soc.* **1992**, *114*, 10834.
13. Wei, Y.; Jin, D.; Ding, T.; Shin, W.-H.; Liu, X.; Cheng, S. Z. D.; Fu, Q. *Adv. Mater.*, **1998**, *4*, 313.
14. (a) Wei, Y. Xu, J. Feng, Q.; Dong, H.; Lin, M. *Mater. Lett.* **2000**, *44*, 6. (b) Wei, Y.; Xu, J.; Feng, Q.; Lin, M.; Dong, H.; Zhang, W.; Wang, C. *J. Nanosci. Nanotechno.* **2001**, *1*, 83.
15. Brinker, C. J.; Scherer, G. W. *Sol-Gel Science: The Physics and Chemistry of Sol-Gel Processing*; Academic: New York, 1990.

16. Iler, R. K. *The Chemistry of Silica*; Wiley: New York, 1979.
17. Jones, R. W. *Fundamental Principles of Sol-Gel Technology*; The Institute of Metals: London, 1989.
18. Klein, L. C.; Garvey, G. J. *J. Non-Cryst. Solid* **1982**, *48*, 97.
19. Hench, L. L.; West, J. K. *Adv. Mater. Opt. Electron.* **1993**, *2*, 149.
20. Okazaki, H.; Kitagawa, T.; Shibata, S.; Kimura, T. *J. Non-Cryst. Solids* **1990**, *116*, 87.
21. Kim, K.; Jang, K. Y.; Upadhye, R. S. *J. Am. Ceram. Soc.* **1991**, *74*, 1987.
22. Titulaer, M. K.; Jansen, J. B. H.; Geus, J. W. *J. Non-Cryst. Solids* **1994**, *168*, 1.
23. Brinker, C. J.; Frye, G. C.; Hurd, A. J.; Ward, K. J.; Ashley, C. S. *Ultra Structure Processing of Advanced Materials*, Uhlmann, D. R.; Ulrich, D. R., eds., John Wiley & Sons, New York, p211, 1992.
24. Langlet, M.; Wals, D.; Marage, P.; Joubert, J. C. *J. Non-Cryst. Solids* **1992**, *147*, 488.
25. Yamane, M.; Shibata, S.; Yasumori, A.; Yano, T.; Uchihiro, S. *J. Sol-Gel Sci. Technol.* **1994**, *2*, 247.
26. Brichall, J. D.; Bradbury, J. A. A.; Dinwoodie, J. *Handbook of Composites, Vol. 1*; Watt, W.; Perov, B. V.; Eds.; **1985**, Elsevier: Amsterdam, p115.
27. Selvaraj, U.; Prasada Rao, A. V.; Komatneni, S.; Brooks, S.; Kurtz, S. *J. Mater. Res.* **1992**, *7*, 992.
28. Klein, L. C.; Woodman, R. H. *Key Engineering Materials* **1996**, *115*, 109.
29. Sing, K. S. W.; Everett, D. H.; Haul R. A. W.; Moscou, L.; Pierotti, R. A.; Rouquérol, J.; Siemieniewska, T. *Pure Appl. Chem.* **1985**, *57*, 603.
30. Breck, D. W. *Zeolite Molecular Sieves*; Kieger, Malabar, 1984.
31. Barton, T. J.; Bull, L. M.; Klemperper, W. G.; Loy, D. A.; McEnaney, B.; Misono, M.; Monson, P. A.; Pez, G.; Scherer, G. W.; Vartuli, J. C.; Yaghi, O. M. *Chem. Mater.* **1999**, *11*, 2656.
32. Raman, N. K.; Anderson, M. T.; Brinker, C. J. *Chem. Mater.* **1996**, *8*, 1682.

33. Soten, I.; Ozin, G. A. *Supramolecular Organization and Materials Design*, Jones, W., Rao, C. N. R., eds., Cambridge University Press: Cambridge, UK, 2002, p 34.
34. Karra, V. R.; Moudrakovski, I. K.; Sayari, A. *J. Porous Mater.* **1996**, *3*, 77.
35. Huo, Q.; Margolese, D. I.; Ciesla, U.; Demuth, D. G.; Feng, P.; Gier, T. E.; Sieger, P.; Firouzi, A.; Chmelka, B. F.; Schuth, F.; Stucky, G. D. *Chem. Mater.* **1994**, *6*, 1176.
36. Antonelli, D. M.; Ying, J. Y. *Angew. Chem., Int. Ed. Engl.* **1995**, *34*, 2014.
37. Tanev, P. T.; Pinnavaia, T. J. *Science* **1995**, *267*, 865.
38. Bagshaw, S. A.; Prouzet, E.; Pinnavaia, T. J. *Science*, **1995**, *269*, 1242.
39. Bagshaw, S. A.; Pinnavaia, T. J. *Angew. Chem., Int. Ed. Engl.* **1996**, *35*, 1102.
40. Rosen, M. J. *Surfactants and Interfacial Phenomena*, 2<sup>nd</sup> ed., Wiley: New York. 1989.
41. Corma, A.; Navarro, M. T.; Perez-Pariente, J. *J. Catal.* **1994**, *148*, 569.
42. Janicke, M. T.; Landry, C. C.; Christiansen, S. C.; Birtalan, S.; Stucky, G. D.; Chmelka, B. F. *Chem. Mater.* **1999**, *11*, 1342.
43. Serrano, D. P.; Aguado, J.; Escola, J. M.; Garagorri, E. *Chem. Comm.* **2000**, *20*, 2041.
44. Roziere, J.; Brandhorst, M.; Dutartre, R.; Jacquin, M.; Jones, D. J.; Vitse, P.; Zajac, J. *J. Mater. Chem.* **2001**, *11*, 3264.
45. Antonelli, D. M.; Ying, J. Y. *Process. Prop. Nanocryst. Mater., Proc. Symp.* **1996**, 59.
46. Yun, H.-S.; Miyazawa, K.; Zhou, H.; Honma, I.; Kuwabara, M. *Adv. Mater.* **2001**, *13*, 1377.
47. Schuth, F. *Ber. Bunsen. -Ges. Phys. Chem.* **1995**, *99*, 1306.
48. Wong, M. S.; Antonelli, D. M.; Ying, J. Y. *Nano. Mater.* **1997**, *9*, 165.
49. Luca, V.; MacLachlan, D. J.; Hook, J. M.; Withers, R. *Chem. Mater.* **1995**, *7*, 2220.
50. Orel, B.; Groselj, N.; Krasovec, U. O.; Jese, R.; Georg, A. *J. Sol-Gel Sci. Tech.* **2002**, *24*, 5.
51. Zhao, D.; Huo, Q.; Feng, J.; Chmelka, B. F.; Stucky, G. D. *J. Am. Chem. Soc.* **1998**, *120*, 6024.



52. Sayari, A.; Danumah, C.; Moudrakovski, I. L. *Chem. Mater.* **1995**, *7*, 813.
53. Wei, Y.; Xu, J.; Dong, H.; Dong, J.; Qiu, K.; Jansen-Varnum, S. A. *Chem. Mater.* **1999**, *11*, 2023.
54. (a) Pang, J. B.; Qiu, K. Y.; Wei, Y.; Lei, X.; Liu, Z. F. *Chem. Comm.* **2000**, *6*, 477. (b) Pang, J. B.; Qiu, K. Y.; Wei, Y. *Chem. Mater.* **2001**, *14*, 2361.
55. (a) Zheng, J.-Y.; Pang, J.-B.; Qiu, K.-Y.; Wei, Y. *J. Mater. Chem.* **2001**, *11*, 336. (b) Zheng, J.-Y.; Pang, J.-B.; Qiu, K.-Y.; Wei, Y. *Microporous Mesoporous Mater.* **2001**, *49*, 189.
56. Nenoff, T. M.; Thoma, S. G.; Provencio, P.; Maxwell, R. S. *Chem. Mater.* **1998**, *10*, 3077.
57. (a) Feng, Q. *Novel Organic-Inorganic Hybrid Mesoporous Materials and Nanocomposites*; Ph.D. Dissertation, Drexel University, 2001. (b) Y. Wei; Q. Feng; S. Cheng; K.-Y. Qiu; J.-B. Pang; R. Yin; K. Ong, *Macromolecules*, submitted.
58. Mikijeli, B.; Varela, J. A. Whittmore, O. *J. Am. Ceram. Bull.* **1991**, *70*, 829.
59. MaEnaney, B.; Mays, T. *Porosity in Carbons*, Patrick, J. W., ed., Halsted Press: New York, p93, 1995.
60. Stoeckli, H. F. *J. Collo. Inter. Sci.* **1977**, *59*, 184.
61. Huber, U.; Stoeckli, H. F.; Houriet, J.-P. *J. Collo. Inter. Sci.* **1978**, *67*, 195.
62. Brow, L. F. Travis, B. J. *Chem. Eng. Sci.* **1983**, *38*, 843.
63. Groszek, A. J. *Mate. Sci. Foru.* **1988**, *25*, 483.
64. Groszek, A. J. *Carbon* **1987**, *25*, 717.
65. Tsuchinari, A. Hokii, T.; Shimobayashi, O.; Kanaoka, C. *J. Ceram. So. Jpn.* **1991**, *99*, 561.
66. Patrick, J. *J. Microscopy* **1983**, *132*, 333.
67. Innes, R. W.; Fryer, J. R.; Stoeckli, H. F. *Carbon* **1989**, *27*, 71.
68. Gregg, S. J.; Sing, K. S. W. *Adsorption, Surface Area and Porosity*, 2<sup>nd</sup> ed.; Academic: London, 1982.

69. Lee, C. K.; Chiang, A. S. T.; Tsay, C. S. *Key Eng. Mater.* **1996**, *115*, 21.

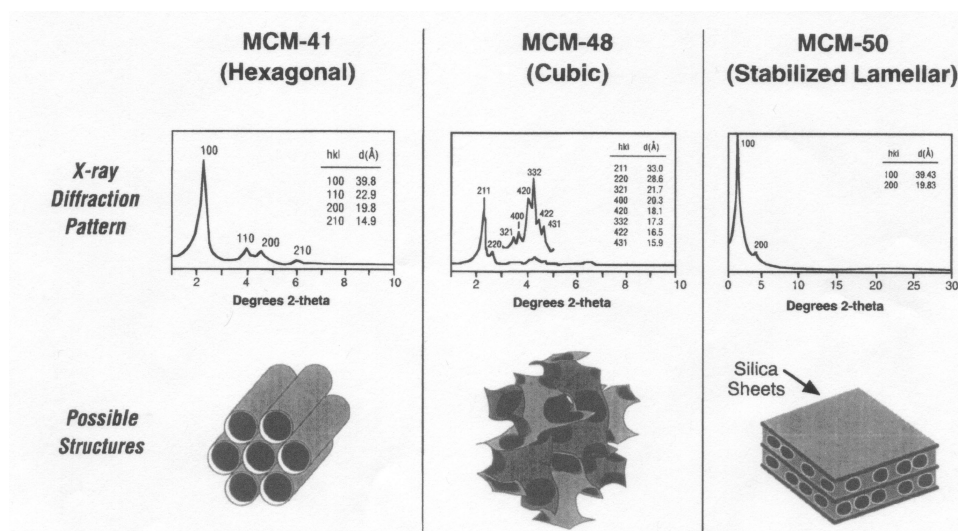


Figure 1-1. Three structure types proposed for silica-surfactant mesophases and the X-ray diffraction patterns: (a) MCM-41 (hexagonal); (b) MCM-48 (Cubic); (c) MCM-50 (Lamellar).

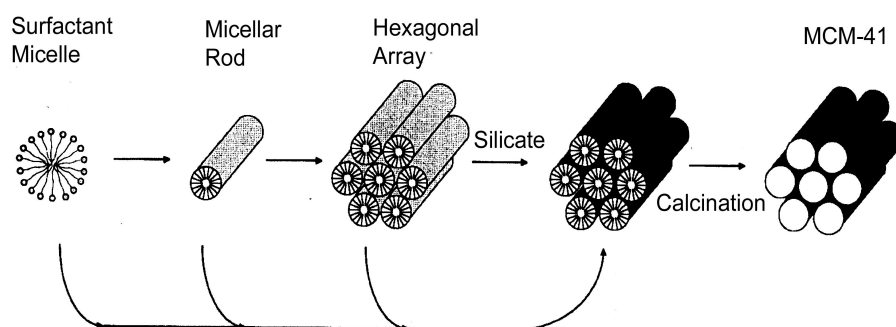


Figure 1-2. Proposed schematics of the liquid-crystal templating (LCT) mechanism.

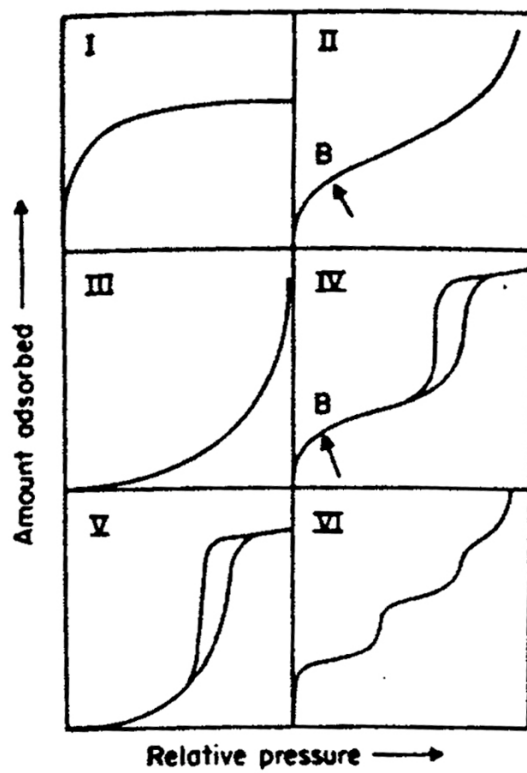


Figure 1-3. IUPAC classification of physisorption isotherms.

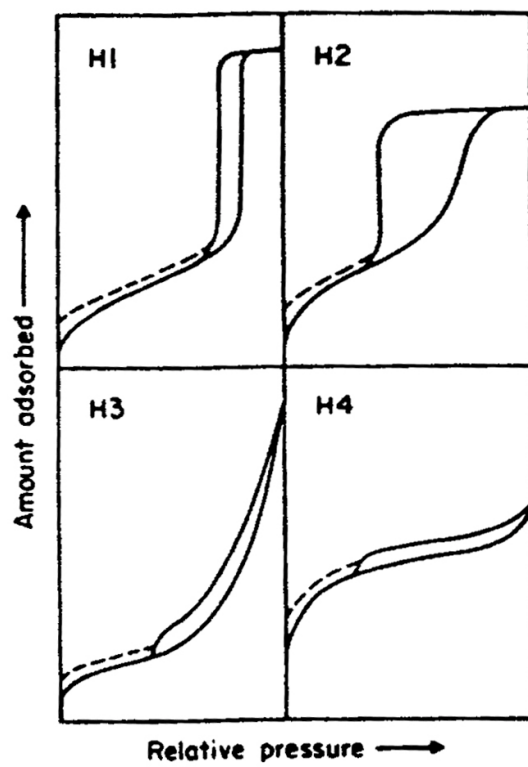


Figure 1-4. IUPAC classification of hysteresis loops.

## Chapter 2. Mesoporous Sol-Gel Material Prepared Using Thermal Sensitive Templates: New Opportunities to Convenient Synthesis

### 2.1. Introduction

The concept of template has been introduced into the synthesis of porous materials since the successful discovery of MCM-41 family of mesoporous silicate and aluminosilicate molecular sieves by Kresge *et al.*<sup>1,2</sup> In their method, using surfactants as a pore structure directing agent (i.e., template), porous materials have been synthesized, for the first time, with cavity, channel size or layer spaces in the mesoscale under hydrothermal conditions. The templated sol-gel pathway has then been extensively studied to test various template species, reaction conditions and mechanisms.<sup>3</sup> As a general templated sol-gel process, organic molecules are introduced into a sol mixture. Following the typical sol-gel process (i.e., gelling, aging and drying) under appropriate conditions, organic molecules are incorporated into inorganic matrix, forming a template containing gel. After removing the template from the as-synthesized organic-inorganic composite, the spaces previously occupied by the organic molecules are left behind as pores in sol-gel matrices. In contrast to conventional gels which usually have microporous structure with wide pore size distributions, porous materials obtained with templates usually are mesoporous. The selection of the template, along with its removal, plays an important role in the templating method, and specifically, provides controllability of porosity and microstructure of the materials. In this chapter, we present a sol-gel synthesis using a new category of template, thermal sensitive compounds, to

prepare mesoporous silica materials. We show for the first time that with readily thermal decomposable templates, mesoporous materials can be obtained after a relatively low temperature thermal template removal at around 150 °C. In the following sections, we proceed to briefly overview the templating process and removal of templates based on two classes of templates, surfactant and nonsurfactant.

### **2.1.1. Surfactant Templates and Their Removal**

Most mesoporous materials have been synthesized using ionic<sup>1,2,4-9</sup> or neutral surfactants<sup>10-16</sup> as templates. Depending on the hydrophobic character of the surfactant and the interaction between the organic template and the inorganic precursor, surfactant molecules can either direct the formation of liquid-crystal-like inorganic-surfactant nanostructures through micelle self-arrays, or be incorporated into amorphous inorganic frameworks based on hydrogen bonding interactions. The detailed mechanisms have been discussed in Chapter 1, and therefore here we will focus on the reaction process. In general, using different charged surfactant molecules and inorganic solution species, the mesophase structure can be synthesized by either direct or mediated pathways under certain pH conditions. Six surfactant templating pathways have been identified:  $S^+I$ ,  $S^-I$ ,  $S^+XI^+$ ,  $S^-XI^+$ ,  $S-I$ , and  $S^0I^0$ , where S is the surfactant, I is the inorganic phase, and X is the mediating ion. Silicates have been synthesized by  $S^+I$ ,  $S^+XI^+$ ,  $S^0I^0$  pathways. For  $S^+I$  synthesis, a cationic surfactant is selected and the pH is adjusted to 9-14, such that the silica precursors will be negatively charged. For the  $S^+XI^+$  approach, the mesophase is



well formed below the isoelectric point of silica when pH is lower than 2. M41S silicates have been prepared through both of these methods.<sup>5,17</sup> For S<sup>o</sup>T<sup>o</sup> the reaction is carried out at near neutral pH, which means the silicate ions are partially charged, but the surfactant molecules are neutral. For example, mesoporous silicates have been obtained using TEOS and polyethylene oxide or primary amines (e.g., dodecyl amine) as neutral surfactant templates.<sup>10,12,13,18,19</sup>

To provide mesoporous materials, surfactant templates need to be selectively removed from mesostructured organic-inorganic precursors. Due to the strong electrostatic interaction between the template and the inorganic precursors, especially in the case of ionic surfactant templates, the surfactant molecules are usually removed by calcination<sup>1,2</sup> or hot solvent extraction.<sup>18,19</sup>

When being calcined, template containing samples are heated in flowing nitrogen, oxygen, or air at temperatures above 500 °C. During the pyrolysis, the organic molecules thermalchemically decompose to simple gaseous molecules and escape from the inorganic matrices. The templates can be removed completely with this method. However, such an aggressive thermal treatment, to some extent, results in an undesirable loss of porosity and pore regularity due to pore contraction and pore collapse. The studies of the effect of calcination conditions on porosity show that when calcined at 540 °C in air for 10 h, MCM-41 samples exhibit 10-25 % volume shrinkage depending on synthetic conditions.<sup>20</sup>

Hot solvent extraction provides another approach to remove organic groups from ionic or neutral surfactant templated materials. Chen et al. reported that almost 100 % of the surfactant templates can be removed by extracting MCM-41 with a 1 M HCl solution at 70 °C for about 30 h.<sup>19</sup> In some other studies, hot ethanol has been used to extract neutral surfactant template from silica samples.<sup>18,19</sup> In comparison to calcination, hot solvent extraction does not appreciably affect the pore volume. However the harsh hydrothermal conditions in most synthesis of mesoporous materials still limit the usefulness of the process in applications wherein the materials involved are temperature-sensitive, such as enzymes immobilization and thin film coatings on polymer or metal substrates.

Some synthetic routes with template removal at lower temperature have been explored, such as UV-ozone treatment,<sup>21-23</sup> ion exchange,<sup>24,25</sup> oxygen plasma treatment<sup>26,27</sup> and supercritical fluid extraction.<sup>28</sup> Keene and coworkers reported that with an extended exposure to ozone, which is produced by in-situ photochemical reaction or by an electric arc, surfactant templates can be removed from bulk MCM-41 type materials.<sup>21</sup> More recently, Clark *et al.* extended this room temperature ozone treatment to remove the template surfactant from thin film mesophases on various substrates. Selective area template removal was demonstrated to afford patterned porous thin film.<sup>22</sup>

### **2.1.2. Nonsurfactant Templates and Their Removal**

It was recently reported by our group that with nonsurfactant small molecules as template, mesoporous materials can be prepared with template removal by solvent extraction at room temperature.<sup>29-31</sup> Most of the nonsurfactant molecules that have been studied are water soluble small organic compounds, including glucose, fructose, hydroxyl carboxylic acid, urea, glycerol, hydroxyethylmethacrylate and so forth. To remove these organic species, the aged template containing samples are usually ground into fine powder or smaller pieces and then extracted with water at room temperature. The template molecules gradually dissolve in water and diffuse out from the inorganic matrices. Template molecules can be removed up to about 100 % by repeatedly replacing the soaking medium with fresh water.<sup>29,30</sup>

From the materials processing point of view, the use of water soluble nonsurfactant templates provides a mild low temperature synthetic route to prepare mesoporous sol-gel materials. The versatility of nonsurfactant template compounds should allow us to further explore other types of templates aiming at designing synthesis processes suitable for various applications.

### **2.1.3. Thermal Sensitive Templates**

To the best of our knowledge, there has been no report on using thermal sensitive compounds as templates to synthesize mesoporous materials. Here, thermal sensitive compounds entitle a category of compounds that dissociate or decompose to small

gaseous molecules with an increased environmental temperature. In this study, we use such thermal sensitive compounds as templates to prepare mesoporous silica materials. Due to the thermal instability, this new type of template may offer the opportunities to become a useful alternative for efficient template removal at relatively low temperature. In addition, the study should expand the range of organic compounds that can act as a template, and provide further understanding of the mechanism of non-surfactant compound directed mesoporosity formation.

Benzoin was selected as a sample compound for this study. With a melting point of 135 °C and a boiling point of 194 °C at 12 mmHg, benzoin dissociates thermally as well as photolytically.<sup>32</sup> When being heated, benzoin decomposes and generates gaseous products such as carbon dioxide and carbon monoxide. The synthesis method is based on the newly developed nonsurfactant template sol-gel pathway.<sup>22-24</sup> The reaction involves an acid catalyst sol-gel reaction of tetraethyl orthosilicate (TEOS) in the presence of benzoin at different concentration. The thermal-chemical template removal at varied temperatures was studied in detail. We showed that, for the first time, with a thermal sensitive template mesoporous materials can be obtained after a thermal template removal at around 150 °C. The materials exhibit typical mesoporosity with high surface areas and large pore volume, adjustable by simply varying the template concentration. The pore parameters are also tunable by controlling the heating temperature and time. As an extended study of mesoporous materials via the nonsurfactant template pathway, we further discussed the correlation of extent of template removal and materials porosity

since controllable partial removal of the template is permitted with this thermal sensitive template.

## **2.2. Experimental**

The synthesis approach of making mesoporous silica materials with thermal sensitive compound as template was developed based on the protocol of nonsurfactant templated sol-gel pathway developed in our laboratory. Special care is required during the drying process due to the large amount of solvent presented in the reactions. Template removal was achieved at relatively low temperatures (~150 °C) under a reduced pressure.

### **2.2.1. Materials**

Tetraethyl orthosilicate (TEOS, Aldrich), benzoin (98 %, Aldrich), benzil (98 %, Aldrich), benzoyl peroxide (BPO, 97 %, Aldrich), hydrochloric acid (HCl, Fisher), ethyl alcohol (EtOH, Pharmco), pyridine (99 %, Aldrich), ethyl ether (anhydrous, Fisher) were all used as received without further purification.

### **2.2.2. Synthesis of Mesoporous Silica Materials with Thermal Sensitive Nonsurfactant Templates**

As a general procedure, TEOS was prehydrolyzed with distilled deionized H<sub>2</sub>O in EtOH using HCl as catalyst. The molar ratio of [TEOS]:[H<sub>2</sub>O]:[EtOH]:[HCl] was used as 1:4:2:0.01. The prehydrolyzed sol was then mixed with a template solution, which was

pre-prepared by dissolving a designed amount of benzoin in pyridine. Following the typical sol-gel process, transparent and monolithic template-containing silica disks were obtained after slow drying at room temperature. A series of samples were prepared with template content ranging from 20 wt % to 60 wt %, which was calculated based on the weight of the final dry product. As a typical procedure to prepare the prehydrolyzed TEOS sol, 41.60 g TEOS (0.2 mol), 14.4 g H<sub>2</sub>O (0.8 mol), 27.60 g EtOH (0.4 mol) and 1.00 ml 2M HCl (2.0 mmol) were mixed in a 250 ml round bottom flask and refluxed at 60 °C for 4 h. The sol mixture was prepared in a relatively large quantity for the convenience of preparing a series of samples with different concentrations. Upon cooling down to room temperature, the sol mixture was mixed with template solution. To prepare a sample containing with 40 wt % benzoin (SB40), the template solution was prepared by dissolving 1.0 g benzoin (40 wt % based on the weight of silica dioxide and the template in the final dry product) in 6.00 g pyridine and then was added into 10.56 g hydrolyzed sol mixture, which originally contains TEOS 0.025 mol. The beaker was then sealed with a piece of paraffin film. The sol mixture was kept stirred for an additional 1~2 h. Then, 2~4 pinholes were punched on the paraffin film to allow the evaporation of the solvent and volatile byproduct of the sol-gel reaction, such as ethonal and H<sub>2</sub>O. The sol mixture started to gel in ~4 h. Transparent and monolithic template-containing silica disks were obtained after the gelation and drying at room temperature up to 2 months. It should be pointed out that a fast drying process resulted in phase separation, especially for the high template content samples. To obtain mesoporous materials, the as-synthesized samples

were ground manually into fine powder and heated in a vacuum oven for 6 h at 150 °C.

We also investigated other possible thermal decomposable templates, such as BPO and benzil. Template solutions were prepared with BPO and benzyl, using ethyl ether and EtOH as solvent, respectively. Similar procedures were adapted from the preparation of benzoin containing samples to prepared silica samples templated with BPO and benzil. However, phase separations observed as precipitates occurred during the sol-gel process (usually within 24 h) for both BPO and benzil templated samples, even at a template concentration of 30 wt %. This may be attributed to the volatility of the solvent employed to prepare the template solutions.

### **2.2.3. Instrumentation and Characterization**

The N<sub>2</sub> adsorption-desorption characterization was conducted on a Micromeritics ASAP 2010 surface area and pore size analyzer at -196 °C. Prior to the measurements, the samples were degassed at the corresponding calcination temperature and 1 Pa for 6-7 h. Transmission electron microscopy (TEM) images were obtained on a JEOL 2000 FX TEM with an accelerating voltage of 200 kV. The samples were prepared by allowing an ethyl alcohol suspension of the finely ground powder to evaporate on a copper grid coated with a holey carbon film. The copper grids were obtained from SPI Supplies. Infrared spectra of KBr powder-pressed pellets were recorded on a Perkin-Elmer Model 1600 FTIR spectrophotometer. Thermal gravimetric analysis (TGA) was carried out with

a TA Instruments Hi-Res TGA 2950 (Temple University) under oxygen atmosphere with a heating rate of 1 °C/min. Before TGA measurement, the samples were dried in a vacuum oven at room temperature until a constant mass was obtained.

### **2.3. Results and Discussion**

Using a thermal sensitive nonsurfactant compound, benzoin, as a pore structure directing template, the mesoporous silica materials have been successfully prepared through the sol-gel reactions followed by removal of the template with thermal treatment at a relatively low temperature.

To study the thermal stability of benzoin when confined in silica matrices, TGA measurements of the as-synthesized samples were compared with that of pure benzoin. Figures 2-1 to 2-6 show typical patterns for the weight loss and their derivative over temperature during the pyrolysis of pure benzoin and benzoin containing (20-60 wt %) silica composite samples. The TGA of pure benzoin exhibits a weight loss close to 100 % between 130 °C and 160 °C, which is associated with the pyrolysis of the compound. Representing the decomposition rate, the derivative curve of the weight loss with respect to temperature shows a relatively sharp peak centered at 150 °C, the decomposition temperature of the compound. TGA of the benzoin-containing silica sample demonstrates three stages of weight losses: two major ones at around 110 °C and 200 °C, respectively, and a minor one at around 340 °C. The weight loss occurring at around 110 °C could be associated with the decomposition of surface bonded benzoin and the elimination of the



volatile sol-gel reaction byproducts, such as EtOH and water molecules. The second major weight loss at around 200 °C arises from the burn-off of the template benzoin. Compared to pure benzoin, the template benzoin decomposes at a broader temperature range and the maximum decomposition rate appears at a higher temperature due to the confinement of the silica matrix. During the calcination, more than 90 wt % of the total weight loss occurs below 250 °C. A slight weight loss observed around 340 °C could be attributed to the phenomenon that some benzoin molecules are completely wrapped by the silica matrix and isolated from other template molecules. Therefore, the decomposition products cannot escape until the gaseous pyrolysis products burst out from “silica cage” at a higher temperature. This is evidenced by the fact that this minor weight loss at around 340 °C is not observed for high benzoin content (i.e., 60 wt %) sample (Figure 2-6). In a high benzoin concentration system, template and silica form a bicontinuous mesophase structure, and therefore the gaseous decomposition products are able to get out from silica matrices easily through interconnected pores or channels. The presence of small amount of ethyloxy groups resulted from the incomplete sol-gel reactions may also contribute to the slight weight loss at 340 °C. For all the samples, above 400 °C, the weight loss becomes insignificant.

From the TGA data, it is noticed that at around 150 °C, the decomposition temperature of pure benzoin, the derivative curve of the weight loss of the benzoin-containing silica composite reaches a local minimum. This is undesirable since the removal of the template at 150 °C would then take a long period of time. Our experiment

data show that about 70 wt % of weight loss (calculated based on the total weight loss at 550 °C) occurred after being heated at 150 °C for 6 h. To ensure a faster and more effective template removal at 150 °C, a vacuum pump was employed to continuously remove the gaseous pyrolysis product from the silica matrix. Moreover, benzoin vaporizes at a lower temperature under a lower pressure. The isothermal TGA data indicate that under a reduced pressure (<1 mmHg), more than 90 wt % of the weight loss can be achieved after heating the samples at 150 °C for 6 h, indicating an effective removal of benzoin from the silica matrix. After heating at 150 °C for 6 h, the samples were measured with TGA again up to 550 °C. The weight loss was less than 10 wt %. As previously mentioned, this may be attributed to incomplete decomposition of benzoin or to incomplete sol-gel reactions, where some ethoxy groups remained in the samples. Hence, the benzoin removed at 150 °C for 6 h was much greater than 90 wt %.

The removal of the template compound from the silica composites was also monitored by FT-IR analysis. Figure 2-7 exemplifies the IR spectra of the sample SB-40 before (a) and after (b) the thermal treatment at 150 °C with IR spectrum of pure silica (c) as a reference. The strong peaks at 1100-1200  $\text{cm}^{-1}$  are attributed to Si-O bond. The spectrum of benzoin-containing sample exhibits two series of characteristic absorption bands in the ranges of 1500-1600  $\text{cm}^{-1}$  and 600-700  $\text{cm}^{-1}$ , which correspond to aromatic C=C stretch vibrations and C-H bend vibrations, respectively. The intensity of these peaks decreases dramatically after the template removal by heating at 150 °C. The spectrum of obtained porous silica shows the typical absorption bands as pure silica gel.

After the thermal treatment at 150 °C, a few aromatic ring C-H absorption bands such as 708 cm<sup>-1</sup> and 640 cm<sup>-1</sup> did not disappear completely. This may be attributed to the residue benzoin molecules wrapped in the closed silica pores with less accessibility to the template removal process.

The composition of the benzoin containing silica materials prepared with template content varied from 20 to 60 % and the pore parameters of the porous silica after the template removal by thermal treatment at 150 °C are summarized in Table 2-1. As represented by the benzoin concentrations in the as-synthesized materials, the compositions measured based on the total weight loss at 550 °C from TGA are comparable with the designed feeding concentrations. The discrepancies could be attributed to the EtOH and the water molecules tightly bounded to the silica matrix, particularly in the case where the sample is prepared at a low benzoin concentration. As the benzoin concentration increases, the discrepancy becomes smaller and relatively negligible.

After the template was removed by heating at 150 °C under a reduced pressure, the silica materials exhibit a high Brunauer-Emmett-Teller (BET) surface area up to 780 m<sup>2</sup>/g, a large pore volume of about 0.5 cm<sup>3</sup>/g, and a relatively narrow pore size distribution with a pore diameter of ~3 nm. Representative nitrogen adsorption-desorption isotherms at -196 °C for the mesoporous silica samples after the thermal treatment are shown in Figure 2-8. With increasing concentration of benzoin, the isotherms gradually transform from reversible type I to typical type IV ones with H2

hysteresis loop at relative pressure ( $P/P_0$ ) of  $\sim 0.4-0.8$ . At a higher template concentration, the H2 hysteresis loop becomes greater in magnitude and shifts to higher  $P/P_0$ . As shown in Figure 2-9, the Barrett-Joyner-Halenda (BJH) pore size distribution curves from the desorption branch of the samples exhibit relatively narrow distributions with peak pore diameter at 3-5 nm. A larger pore size is observed for a sample with higher benzoin content. The effects of template concentrations on pore parameters resemble those we observed for other nonsurfactant template compounds.<sup>29-31</sup> As the benzoin concentration increases, the pore volume and pore diameter of the material tend to increase. As the benzoin content increase up to 50 wt %, surface area increases; and after that the surface area tends to decrease. As reported earlier, this is a result of competition of the effect of increased pore diameter over the effect of increased pore volume.<sup>31</sup>

To study the influence of the thermal treatment on the pore parameters, the benzoin containing silica materials were, stepwisely, heated at different temperatures for the same duration (i.e., 6 h). Table 2-2 summarizes the weight loss of the silica composites and the pore parameters of the obtained porous materials after the thermal treatments at different temperature under a reduced pressure (i.e.,  $< 1$  mmHg), represented by the silica sample containing 40 wt % benzoin (i.e., SB40). The TGA study shows that, the weight loss can be observed with a thermal treatment temperature as low as 50 °C. Furthermore, the extent of template removal increases as the heating temperature does, and more than 90 wt % of weight loss occurred after a heating at 150 °C. A further increasing of heating temperate to 200 °C, which is much higher than the

boiling point of benzoin (i.e., 194 °C , 12 mmHg), did not appreciably increase the weight loss. These observations confirm that most (~100 %) of benzoin was effectively removed from the silica matrices with a thermal treatment at 150 °C. The slight weight loss (< 10 %) at higher temperature is mainly due to the incomplete sol-gel reaction. It was noticed that the samples exhibited slightly decreased pore surface area and pore volume with an increased heating temperature after 150 °C. This may be attributed to the pore contractions and collapse during the thermal treatments.

Figure 2-10 illustrates the typical N<sub>2</sub> adsorption-desorption isotherms at -196 °C for the as-synthesized sample SB40 and porous silica materials obtained by heating SB40 at different temperatures. The isotherms show a pattern that resembles type IV with an H2 hysteresis at P/P<sub>0</sub> of ~0.4-0.6. With increasing heating temperature, the well-defined H2 hysteresis loop tends to become larger while still remaining at P/P<sub>0</sub> of ~0.4-0.6, and the isotherms shift up to higher adsorbed volume. Revealed by N<sub>2</sub> sorption measurements, the as-synthesized benzoin-containing sample before the thermal treatment shows slight porosity with small surface area of ~100 m<sup>2</sup>/g and small pore volume of ~0.09 cm<sup>3</sup>/g, which are typical of nonporous solid. Upon heating, benzoin is gradually removed from the silica matrix. After a thermal treatment at 150 °C for 6 h, the obtained porous material shows high surface areas (~780 m<sup>2</sup> g<sup>-1</sup>) and large pore volume (>0.5 m<sup>3</sup> g<sup>-1</sup>). At about 3 nm, the pore diameters of the silica matrices appear to be relatively unchanged with the extent of the template removal. Figure 2-11 shows the BJH pore size distributions from

the desorption branch of the samples heated at different temperatures. The porous silica matrices possess narrowly distributed mesopores centered at about 3.7 nm.

The trend of porosity change with the extent of template removal within the samples has been studied in an effort to reveal the mesoscale template distribution inside the silica-template composites. The results show that upon a gradual removal of the template from silica matrix, the average pore diameter is relatively unaffected and remains at around 3 nm, while both BET surface area and pore volume increase along with the amount of template being removed. The net BET surface area is defined as the difference of the surface area between the as-synthesized sample and the one with the template partially removed. The net BET pore volume is similarly defined as the pore volume difference between these two samples. It is revealed in Figures 2-12 and 2-13 that the net BET surface area and the net BET pore volume are, with good correlation coefficients of  $R^2 = 0.93-0.94$ , linearly dependent on the amount of template removed. This further confirms that the pores or the channels observed in the silica materials after removing the template come from the space previously occupied by the template molecules. This partial template removal and porosity correlation study provides us a better perception on the real picture of mesophase distribution inside the template-silica samples.

The pore diameter values determined from the BJH method have been found in favorable agreement with those obtained from TEM image. A representative TEM image for the sample SB40-150 is shown in Figure 2-14. There are numerous wormhole-like

interconnected pores or channels with a regular diameter of about 3-5 nm. This image is quite similar to that of the mesoporous materials prepared by using other nonsurfactant templates.<sup>29,31</sup>

#### **2.4. Conclusions and Remarks**

In summary, we have described the convenient synthesis of mesoporous silica materials using benzoin as a thermal sensitive nonsurfactant template. In contrast to the conventional high temperature calcination for template removal, which employs temperature of 400-500 °C, in this synthesis route, the template can be efficiently removed from silica gels with a low temperature treatment at about 150 °C. Removal of the template provides silica matrices well-defined mesoscopic morphology with large surface area (ca. 780 m<sup>2</sup>/g) and pore volume (ca. 0.5 cm<sup>3</sup>/g). The pore structure can be fine-tuned by the template concentration. The amount of template being removed is well controllable by the heating temperature and heating time.

This study expanded the range of nonsurfactant templates to a new type of compound, thermal sensitive compounds that can function as pore structure directing agents as well as provide opportunities for a convenient template removal with low temperature thermal treatment. By carefully selecting template compounds, a variety of convenient and efficient template removal process may be developed. For example, using light decomposable compounds as templates, template removal may be achieved by a photo-chemical process. This would allow for possible photolytic patterning of the

mesoporous materials. We have carried out preliminary experiment using UV light to remove the benzoin template. However, the results are not conclusive yet. Further experiments are ongoing in our lab.

The versatility of nonsurfactant compounds allows further explorations on designing diverse and convenient synthesis of mesoporous materials for a wide range of potential applications, especially for biological applications wherein the mild synthetic conditions are desirable, such as protein immobilizations, biosensors, and drug delivery, etc.

## 2.5. Acknowledgments

I would like to thank Mr. Prithwiraj Maitra at Temple University for his assistance with some of the TGA measurements.

## 2.6. References

1. Kresge, C. T.; Leonowicz, M. E.; Roth, W. J.; Vartuli, J. C.; Beck, J. S. *Nature*, **1992**, 359, 710.
2. Beck, J. S.; Vartuli, J. C.; Roth, W. J.; Leonowicz, M. E.; Kresge, C. T.; Schmitt, K. D.; Chu, C. T.-W.; Olson, D. H.; Sheppard, E. W.; McCullen, S. B.; Higgins, J. B.; Schlenker, J. L. *J. Am. Chem. Soc.* **1992**, 114, 10834.
3. For reviews: (a) Sotgiu, I.; Ozin, G. A. *Supramolecular Organization and Materials Design*, Jones, W., Rao, C. N. R., eds; Cambridge University Press: Cambridge, UK, p34, 2002. (b) Raman, N. K.; Anderson, M. T.; Brinker, C. J. *Chem. Mater.* **1996**, 8, 1682.
4. Chen, C.-Y.; Li, H.-X.; Davis, M. E. *Microporous Mater.* **1993**, 2, 17
5. Huo, Q.; Margolese, D. I.; Ciesla, U.; Demuth, D. G.; Feng, P.; Gier, T. E.; Sieger, P.; Firouzi, A.; Chmelka, B. F.; Schüth, F.; Stucky, G. D. *Chem. Mater.* **1994**, 6, 1176.



6. Huo, Q.; Magargolese, D. I.; Ciesla, U.; Feng, P.; Gier, T. E.; Sieger, P.; Leon, R.; Petroff, P. M.; Schüth, F.; Stucky, G. D. *Nature* **1994**, *368*, 317.
7. Luan, Z.; Cheng, C. F.; Zhou, W.; Klinowski, J. *J. Phys. Chem.* **1995**, *99*, 1018.
8. Antonelli, D. M.; Ying, J. Y. *Chem. Mater.* **1996**, *8*, 874.
9. Yang, H.; Coombs, N.; Ozin, G. A. *Nature* **1997**, *386*, 692.
10. Tanev, P. T.; Chibwe, M.; Pinnavaia, T. J. *Nature* **1994**, *368*, 321.
11. Attard, G. S.; Glyde, J. C.; Göltner, C. G.; *Nature* **1995**, *378*, 366.
12. Bagshaw, S. A. Prouzet, E.; Pinnavaia, T. J. *Science* **1995**, *269*, 1242.
13. Bagshaw, S. A.; Pinnavaia, T. J. *Angew. Chem. Int. Ed. Eng.* **1996**, *35*, 1102.
14. Zhao, D.; Feng, J.; Huo, Q.; Melosh, N.; Fredrickson, G. H.; Chmelka, B. F.; Stucky, G. D. *Science* **1998**, *279*, 548.
15. Prouzet, E.; Cot, F.; Nabias, G.; Larbot, A.; Kooyman, P.; Pinnavaia, T. J. *Chem. Mater.* **1999**, *11*, 1498.
16. Kluson, P.; Kacer, P.; Cajthaml, T.; Kalaji, M. *J. Mater. Chem.* **2001**, *11*, 644.
17. Behrens, P. *Angew. Chem., Int. Ed. Eng.* **1996**, *35*, 515.
18. Tenev, P. T.; Pinnavaia, T. J.; *Chem. Mater.* **1996**, *8*, 2068.
19. Tanev, P. T.; Pinnavaia, T. J.; *Science* **1995**, *267*, 865.
20. Chen, C.-Y.; Li, H.-X.; Davis, M. E.; *Micropor. Mater.* **1993**, *2*, 17.
21. Keene, M. T. J.; Denaud, R.; Llewellyn, P. L. *Chem. Commun.* **1998**, *20*, 2203.
22. Clark, T. Jr.; Ruiz, J. D.; Fan, H.; Brinker, C. J.; Swanson, B. I.; Parikh, A. N. *Chem. Mater.* **2000**, *12*, 3879.
23. Yu, J. J.; Boyd, I. W. *Appl. Phys.* **2002**, *74*, 143.
24. Whitehurst, D. D. U. S. Pat. 5,143,879, 1992.
25. Suda, S.-I.; Tashiro, T.; Umegaki, T. *J. Non-Cryst. Solids* **1999**, *255*, 178.

26. Schuth, F.; *Ber. Bunsen.-Ges. Phys. Chem.* **1995**, *99*, 1306.
27. Huang, J.; Ichinose, I.; Kunitake, T.; Nakao, A. *Nano Lett.* **2002**, *2*, 669.
28. Kawi, S.; Lai, M. W. *Chem. Commun.* **1998**, 1407.
29. Wei, Y.; Jin, D.; Ding, T.; Shih, W.-H.; Liu, X.; Cheng, S. Z. D.; Fu, Q. *Adv. Mater.* **1998**, *3*, 313.
30. Wei, Y.; Xu, J.; Dong, H.; Dong, J.; Qiu, K.; Jansen-Varnum, S. A. *Chem. Mater.* **1999**, *11*, 2023.
31. (a) Pang, J. B.; Qiu, K. Y.; Wei, Y.; Lei, X.; Liu, Z. F. *Chem. Commun.* **2000**, *6*, 477.  
(b) Pang, J. B.; Qiu, K. Y.; Wei, Y. *Chem. Mater.* **2001**, *14*, 2361.
32. Stevens, M. P. *Polymer Chemistry- An Introduction*, 2<sup>nd</sup> ed, Oxford University Press, Inc.: New York, 1990, p 195.

Table 2-1. Composition and pore parameters of the sol-gel silica samples prepared in the presence of 20-60 wt % benzoin template and heated at 150 °C (i.e., SB -150 samples).

sample code <sup>a</sup>	Benzoin (wt %)		S <sub>BET</sub> (m <sup>2</sup> g <sup>-1</sup> )	V <sub>PORE</sub> (cm <sup>3</sup> g <sup>-1</sup> )	D <sub>BET</sub> <sup>c</sup> (Å)	D <sub>BJH</sub> <sup>d</sup> (Å)	micropore <sup>e</sup>	
	calcd.	found <sup>b</sup>					surface area (m <sup>2</sup> g <sup>-1</sup> )	vol. (cm <sup>3</sup> g <sup>-1</sup> )
SB20-150	20	30	568	0.341	24	24	55.287	0.03
SB30-150	30	36	684	0.460	27	28	-	-
SB40-150	40	42	783	0.586	30	28	-	0.02
SB50-150	50	51	727	0.666	37	31	-	-
SB60-150	60	59	523	0.733	53	43	-	-

<sup>a</sup> The numerical figure in the sample code denotes respectively the benzoin concentration (wt %) in the materials before thermal treatment and the heating temperature. <sup>b</sup> Values from the weight loss of the samples, which represent total content of volatile compounds, at 550 °C based on TGA measurement. <sup>c</sup> The sample average pore diameter calculated from  $4 V/S_{BET}$  by the BET method. <sup>d</sup> Determined from the maxima of the BJH desorption pore size distribution curve with the Halsey equation. <sup>e</sup> Values determined from the *t*-plot analysis.

Table 2-2. Weight loss and pore parameters of the sol-gel silica sample prepared with 40 wt % benzoin template (i.e., SB40-) heated at different temperatures.

sample code <sup>a</sup>	weight loss <sup>b</sup> (%)	S <sub>BET</sub> (m <sup>2</sup> g <sup>-1</sup> )	V <sub>PORE</sub> (cm <sup>3</sup> g <sup>-1</sup> )	D <sub>BET</sub> <sup>c</sup> (Å)	D <sub>BJH</sub> <sup>d</sup> (Å)	micropore <sup>e</sup>	
						surface area (m <sup>2</sup> g <sup>-1</sup> )	vol. (cm <sup>3</sup> g <sup>-1</sup> )
SB40-RT	-	102	0.088	32	28	-	-
SB40-50	6	274	0.218	32	30	-	-
SB40-75	13	402	0.313	31	32	-	-
SB40-100	26	480	0.364	30	29	-	-
SB40-125	29	596	0.452	30	32	-	-
SB40-150	37	783	0.586	30	30	-	0.02
SB40-175	38	681	0.513	30	30	-	-
SB40-200	38	653	0.473	28	29	-	-
SB40-550	42	510	0.284	28	26	107.84	0.11

<sup>a</sup>The first numerical figure in the sample code denotes the benzoin concentration (wt %) and the second figure denotes the heating temperature. <sup>b</sup> Values from the weight loss of the samples, which represent content of volatile compounds based on isothermal TGA measurement by heating the samples at pre-set temperature for 6 h under reduced pressure. <sup>c</sup> The sample average pore diameter calculated from  $4 V/S_{BET}$  by the BET method. <sup>d</sup> Determined from the maxima of the BJH desorption pore size distribution curve with the Halsey equation. <sup>e</sup> Values determined from the *t*-plot analysis.

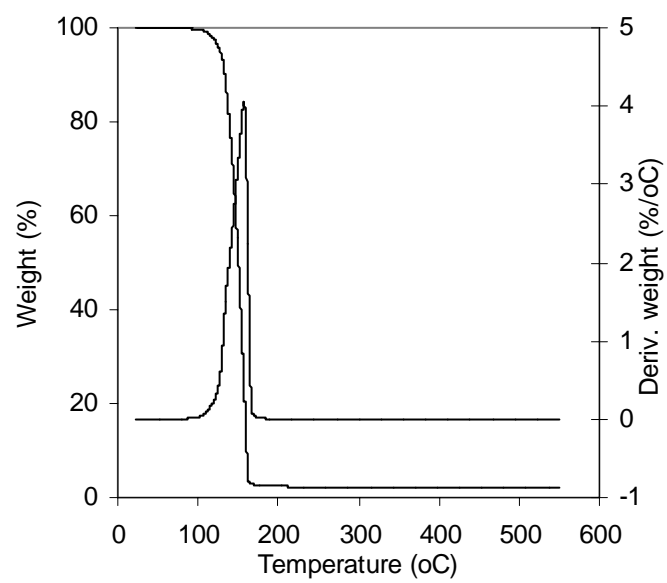


Figure 2-1. Typical patterns for the weight loss and its derivative over temperature during the pyrolysis of benzoic acid.

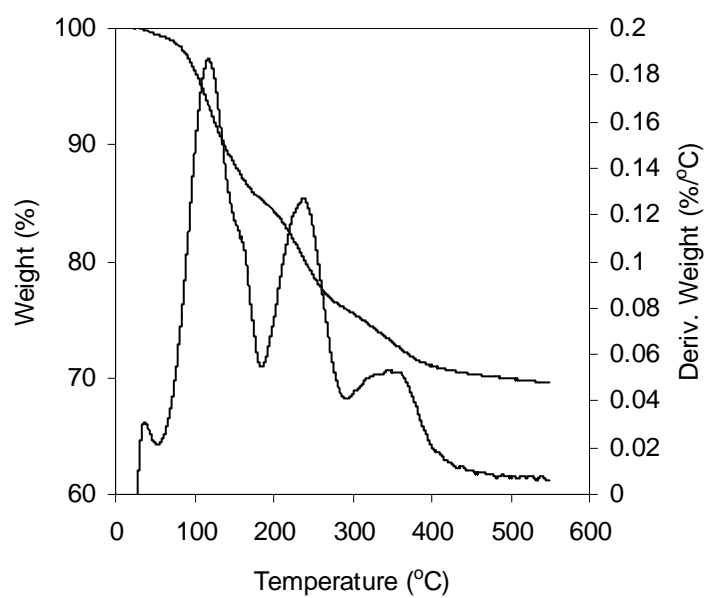


Figure 2-2. Typical patterns for the weight loss and its derivative over temperature during the pyrolysis of composite sample prepared with 20 wt % of benzoin (SB20).

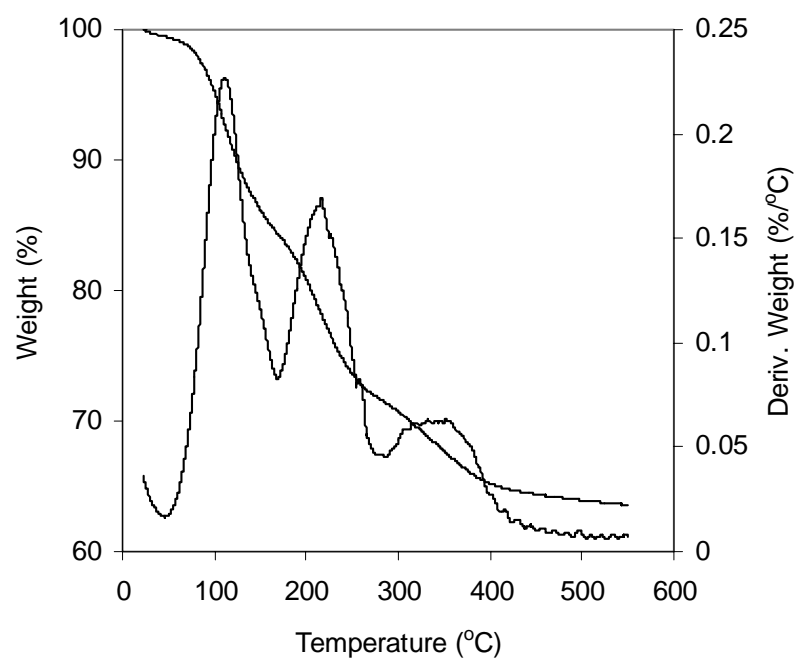


Figure 2-3. Typical patterns for the weight loss and its derivative over temperature during the pyrolysis of composite sample prepared with 30 wt % of benzoin (SB30).

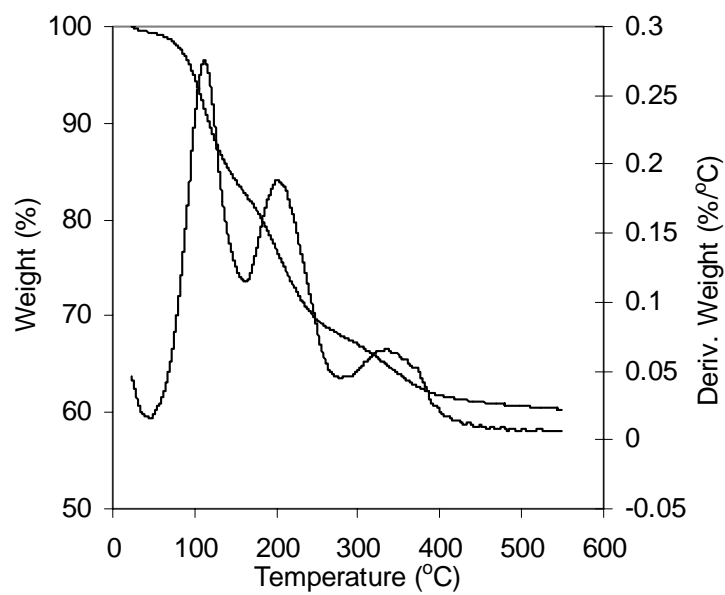


Figure 2-4. Typical patterns for the weight loss and its derivative over temperature during the pyrolysis of composite sample prepared with 40 wt % of benzoin (SB40).



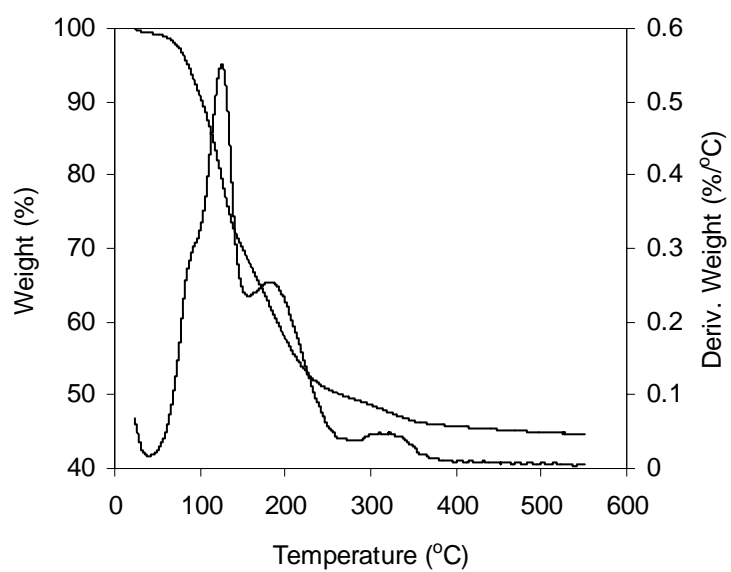


Figure 2-5. Typical patterns for the weight loss and its derivative over temperature during the pyrolysis of composite sample prepared with 50 wt % of benzoin (SB50).

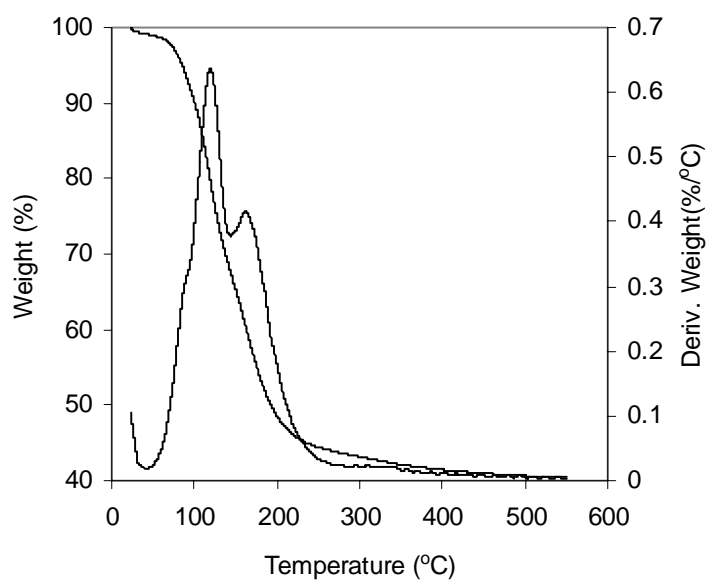


Figure 2-6. Typical patterns for the weight loss and its derivative over temperature during the pyrolysis of composite sample prepared with 60 wt % of benzoin (SB60).

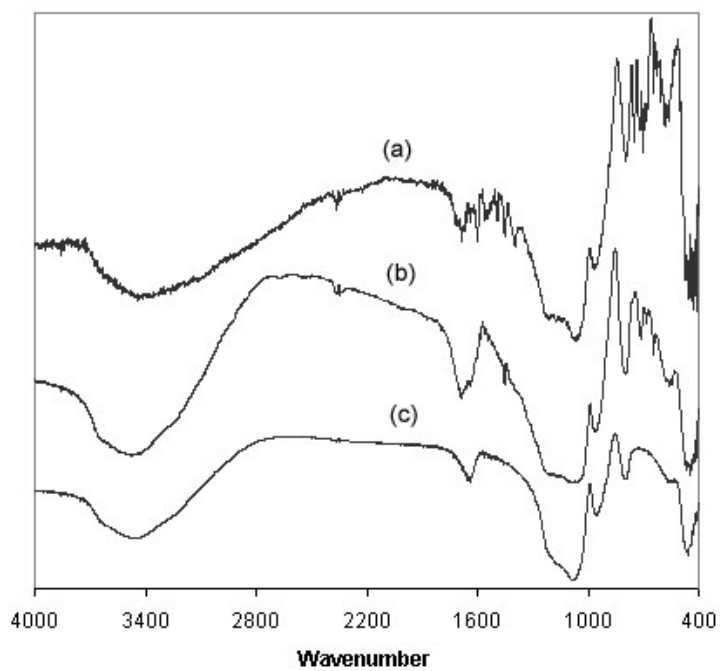


Figure 2-7. Representative IR spectra of benzoin containing silica (SB40): (a) before template removal by heating at 150 °C; (b) after template removal by heating at 150 °C; (c) IR spectrum of pure silica gel.

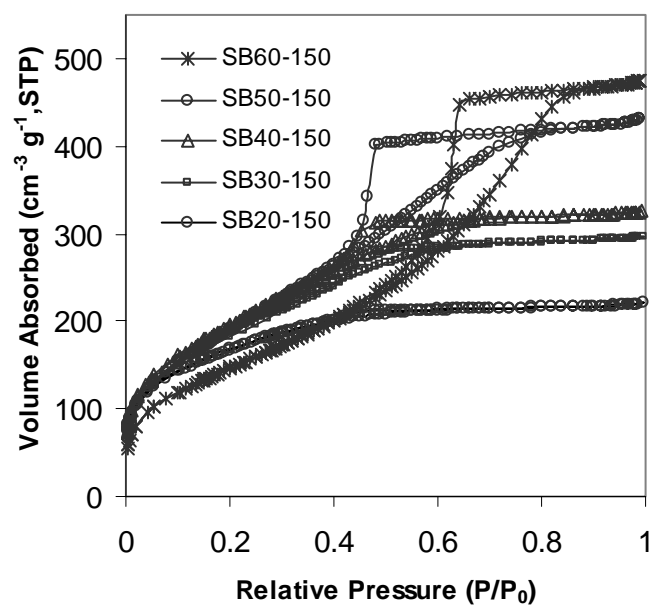


Figure 2-8. Nitrogen adsorption-desorption isotherms at -196 °C for porous silica samples prepared with varied concentration of benzoin after template removal by heating at 150 °C.

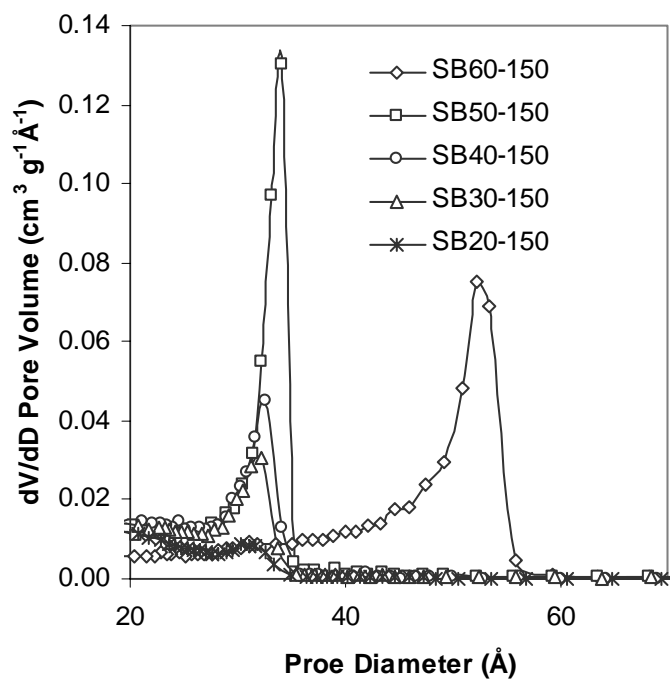


Figure 2-9. BJH pore size distributions obtained from the desorption branches of nitrogen sorption isotherms at -196 °C for the porous silica samples prepared with varied concentration of benzoin after heated at 150 °C.

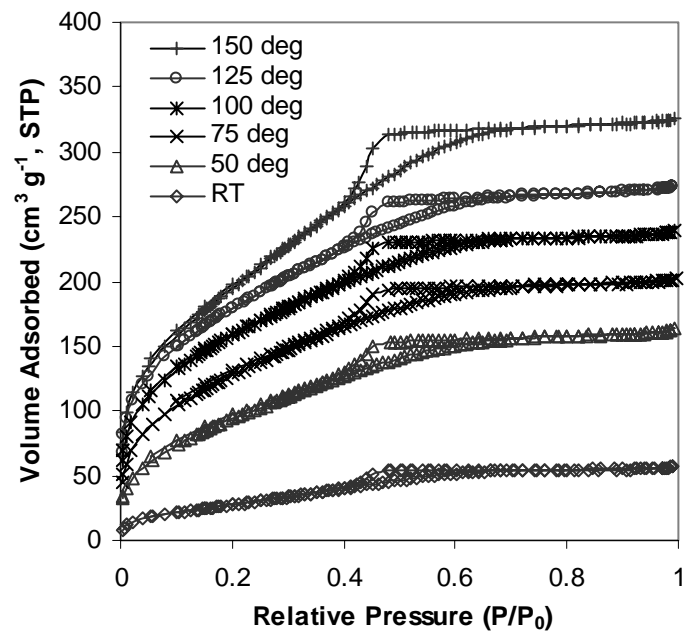


Figure 2-10. Nitrogen adsorption-desorption isotherms at -196 °C for porous silica samples prepared with 40 wt % benzoin after template removal by heating at various temperatures.

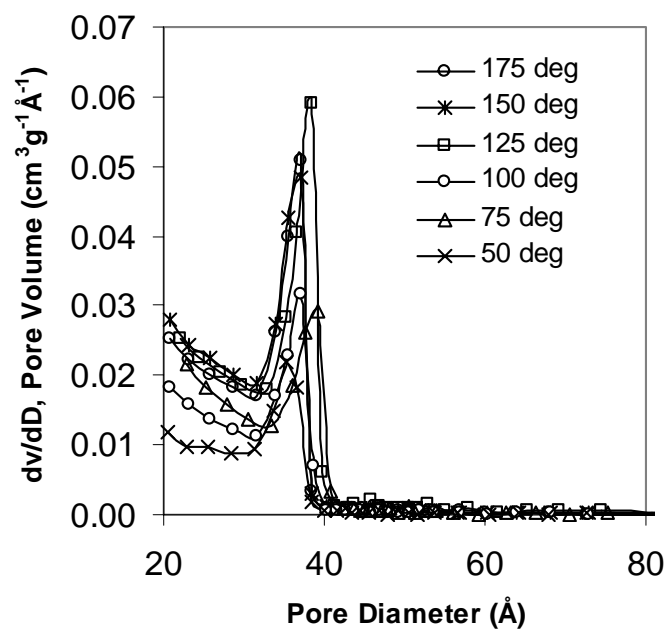


Figure 2-11. BJH pore size distributions obtained from the desorption branches of nitrogen sorption isotherms at -196 °C for the porous silica samples prepared with 40 wt % of benzoin after template removal by heating at various temperatures.

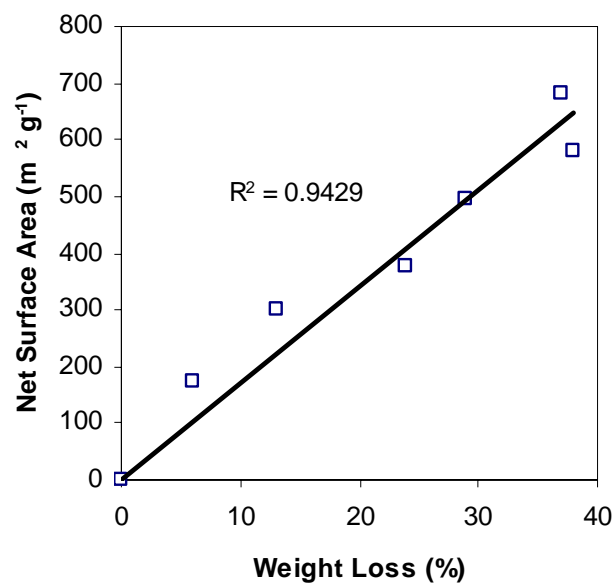


Figure 2-12. Relationship between the net BET surface area and the amount of template being removed from Sample SB40 at different heating temperatures.



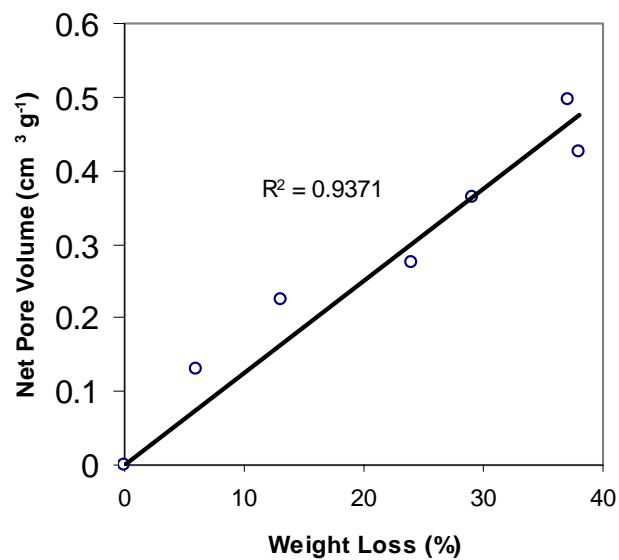


Figure 2-13. Relationship between the net pore volume and the amount of template being removed from Sample SB40 at different heating temperatures.

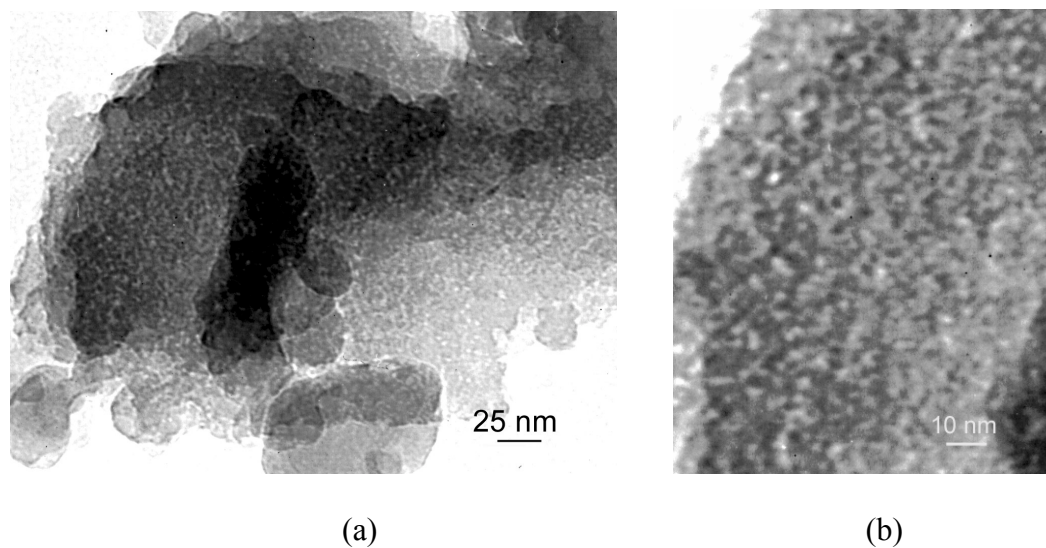


Figure 2-14. Representative transmission electron micrograph (TEM) for the porous silica sample prepared with 40 wt % benzoin after template removal by heating at 150 °C. The gray wormlike features are interconnected pores randomly distributed throughout silica matrix. (a) A low magnification image. (b) A high magnification image.

## **Chapter 3. Synthesis of Mesoporous Silica Nanospheres through a Nonsurfactant Templated Base Catalyzed Sol-Gel Reaction**

### **3.1. Introduction**

The design of porous materials with desired structure is of ever increasing technological importance. Through surfactant templating synthesis, mesoporous materials have been prepared with diverse forms and remarkable morphologies under carefully controlled conditions.<sup>1-3</sup> These technologically important forms of porous materials include monoliths or bulk materials, spheres,<sup>4</sup> films,<sup>5-7</sup> and fibers.<sup>8,9</sup> Porous spheres have attracted a lot of research interests due to their widespread applications, especially in the fields of sensing, catalysis, separation, and controlled drug delivery.<sup>1,2</sup> In this chapter we present the synthesis of mesoporous silica spheres through the newly developed nonsurfactant templated sol-gel pathway.<sup>10</sup> This approach is not only defined as a new example of the versatility of the nonsurfactant route, but also a new concept that illustrates that morphology control can be achieved by adjusting some synthetic parameters such as pH. Both the convenient synthetic method along with the possibility to control the microstructure, and the well defined morphology of the resulting spheres open up the opportunities for nonsurfactant templated preparation for a wide range of new mesoporous materials.

### 3.1.1. Silica Sphere from Sol-Gel Process

Porous silica gel particles have been used as catalyst supports and as packing materials for chromatographic separation. The performance of the particles strongly depends on their size, texture and porosity. Pore structures of commercial particles commonly consist of interstices of secondary silica particles, which are packed and annealed at high temperature. However, for better chemical stability and mechanical strength, particles with interconnected pore structure are preferred.

Many fine silica spheres have been prepared by the sol-gel method using different techniques.<sup>11</sup> A commonly used one is spray drying small droplets of pre-prepared sol solution.<sup>12</sup> Silica spheres with diameter of 0.1-5 mm can be obtained by varying the size of the droplets. As an alternative, silica sol droplets can be also sprayed into an immiscible liquid and gelled by heating or chemical methods.<sup>13,14</sup> The silica source can be either an alkylorthosilicate such as TEOS or a concentrated sodium silicate solution.<sup>15</sup> The gelled silica particles are collected, washed, and dried. Then a high-temperature (i.e., 450 °C) calcination is applied to tune the porous structure.

Solid silica spheres can be also made by the controlled hydrolysis and gelation of alkylorthosilicates in an emulsion medium.<sup>16,17</sup> For example, in the presence of water and alcohol, poly(ethoxysiloxane) is pre-hydrolyzed under acidic condition forming an emulsion, and the pH is then adjusted by adding NaOH or NH<sub>4</sub>OH to afford gelled silica particles. The obtained silica spheres have tunable pore diameters ranging from 3 to 80 nm. The porosity and size of particles are critically dependent on careful control of

preparation conditions. In general, the silica spheres prepared by the above methods have an irregular shape, a broad pore size distribution and relatively low specific surface areas (30-690 m<sup>2</sup>/g).<sup>18</sup>

### 3.1.2. Porous Spheres from Surfactant Templated Sol-Gel Pathway

Templating with surfactant compounds, which could be ionic, nonionic or mixed ionic-nonionic, spherical or near spherical silica spheres with meso/macro-pores have been prepared with the size ranging from submicrometer to millimeter.<sup>19-21</sup> The control over the size and porosity of the porous spheres has been demonstrated under various synthesis conditions, such as template concentration, pH, and stirring/static condition. Hirose *et al.* reported a polyethyleneglycol (PEG) templated sol-gel synthesis of spherical porous silica by the reaction of tetramethoxysilane (TMOS) in water/oil (W/O) emulsions.<sup>22</sup> The interconnected pore structure was made by thermally eliminating PEG from gel particles at 500 °C. By changing the molecular weight or the concentration of PEG, the pore size can be controlled in the region from mesopore to macropore. Since the discovery of ionic surfactant micelle templated monolithic mesoporous molecular sieves,<sup>23,24</sup> many groups have succeeded in expanding this new method to other material forms such as spheres. Using quaternary ammonium surfactants, good structure directing agents for the formation of MCM-41 and MCM-48 silicas, hard mesoporous silica spheres were prepared.<sup>20,25-27</sup> The process was found to be pH dependent with a low

acidity environment favoring the sphere formation. The pore size of the obtained silica spheres is dependent on the alkyl chain length of the surfactants employed.

The possibility of using non-ionic surfactants such as polyethylene oxide-based ones to prepare porous silica spheres was also demonstrated. The syntheses led to agglomeration of particles with wormhole mesoporous structure.<sup>28,29</sup> Most of these syntheses were performed at neutral pH. A double step non-ionic surfactant templated process was developed by Boissière *et al.* with utilization of a mild acidic medium as intermediate step.<sup>30</sup> With this approach, the hydrolysis step and assembly step were clearly separated as two distinct steps. Mesoporous silica particles with perfectly spherical shape and relatively wide particle size distributions were obtained.

In an effort to prepare mesoporous spheres with modified morphology, a mixed ionic-nonionic surfactant templating route was developed by Qi and coworkers.<sup>31</sup> Mesoporous silica spheres ranging from 2 to 6  $\mu\text{m}$  in size were prepared under static acidic conditions. Through this method, the pore structure can be adjusted from hexagonallike to more wormlike disordered structure by varying the nonionic/cationic surfactant ratio, while severe aggregation of spherical particles was observed at high nonionic/cationic surfactant ratios. A more generalized aerosol-based process for solid, well-ordered spherical particles was established by Lu *et al.*<sup>32</sup> The method relies on evaporation-induced interfacial self-assembly confined to spherical aerosol droplets. The surfactant templates, which could be cationic, nonionic, or copolymers, were successfully employed in this method to prepare silica spheres with stable mesoporous hexagonal,

cubic, as well as vesicular structures. These various pathways to the preparation of mesoporous spheres so far all involve a severe calcination step for the purpose of removing surfactant templates.

In addition to the solid mesoporous silica spheres, some research groups reported the strategies to develop mesoporous spheres with core/shell structures. By a delayed-neutralized surfactant templated sol-gel process<sup>33</sup> or templating the sol-gel precursors against organic polymer colloidal particles,<sup>34</sup> hollow mesoporous spheres have been obtained with a controllable wall thickness ranging from 30 to 100 nm. On the other hand, the synthesis of particles with solid core/mesoporous shell structure has also been achieved by a sol-gel reaction involving sequential seed growth and surfactant templating process.<sup>35</sup>

### **3.1.3. Morphology Studied of Nonsurfactant Templated Sol-Gel Pathway**

With the possibility to remove template by solvent extraction, the nonsurfactant route offers the advantage of mild synthetic conditions.<sup>36,37</sup> As a newly developed synthetic pathway, the research efforts devoted to the nonsurfactant templating sol-gel route have been mainly focused on controlling the porosity and varying the composition of the mesoporous materials. Few studies have been carried out to tailor material morphologies. With nonsurfactant templated method, materials are typically prepared as monolithic disks through a sol-gel reaction under acidic or near neutral conditions. The dried template containing monoliths, usually transparent, are then ground into fine

powders and subjected to solvent extraction or calcination to remove the template. So far, most porous materials prepared through nonsurfactant templated sol-gel pathway are in the form of fine powders. Pang *et al.* reported a preparation of monolithic mesoporous silica with dimensions in millimeter scale.<sup>38</sup> In their synthesis, instead of being ground to fine powder, the template containing samples were directly subjected to an extensive solvent extraction to afford monolithic mesoporous materials with high surface area and large pore volume. Izutsu and coworkers synthesized millimeter-sized mesoporous silica spheres from the reactions of TEOS with tartaric acid in cyclohexanol by the sol-gel process.<sup>39</sup> An emulsion polymerization mechanism was proposed for sphere formation.

In this chapter, we present a successful synthesis of mesoporous spheres using a nonsurfactant compound, fructose, as template. The template can be easily removed from as-synthesized fructose-silica composites by water extraction at ambient temperature. The obtained silica particles exhibit well-defined spherical shape and uniform size with a diameter of around 420 nm. After the removal of template, the silica spheres show mesoporosity with a relatively narrowly distributed pore size at around 3 nm, a surface area of greater than 470 m<sup>2</sup>/g, and a pore volume at about 0.4 cm<sup>3</sup>/g. The porosity of the obtained silica spheres can be fine-tuned by adjusting the template concentration in the starting sol mixture.



## **3.2 Experimental**

The synthesis approach of making mesoporous spherical silica particles was developed based on the nonsurfactant templated sol-gel pathway to mesoporous bulk materials. Fructose was used as template due to its demonstrated templating ability and biofriendly properties in the synthesis of enzyme immobilized bulk porous silica materials.<sup>40</sup>

### **3.2.1. Materials**

Tetraethyl orthosilicate (TEOS, 98 %, Aldrich), fructose (98 %, Aldrich), ethyl alcohol (EtOH, 200 proof, absolute, Pharmco), Kerosene (Aldrich), sorbitan monooleate (Span 80, Aldrich), aqueous ammonia (NH<sub>4</sub>OH, 29.2 wt %, Fisher) and hydrochloric acid (HCl, Fisher) were all used as received without further purification.

### **3.2.2. Synthesis of Mesoporous Spherical Silica Particles through a Nonsurfactant Templated Pathway**

In general, the mesoporous spherical silica particles were prepared through a cohydrolysis and subsequent condensation of TEOS and a nonsurfactant template, fructose, in a mixture of EtOH, H<sub>2</sub>O and NH<sub>4</sub>OH. To prevent the formation of particle clusters, a TEOS/solvent (v/v) ratio of 1:40 was employed. By adding various amount of fructose aqueous solution into the starting sol mixture, a series of samples were prepared with different template concentrations. As a typical procedure to prepare mesoporous

spherical silica particles with 50 wt % template in the starting sol, TEOS (5.2 g, 0.025 mol) and EtOH (200 ml) were mixed in a 400-ml beaker at room temperature under magnetic stirring. Into the TEOS/EtOH solution, was added 7.5 g fructose aqueous solution (30 wt %), which contains 2.25 g of fructose. The mixture was stirred for additional 30 min till a homogeneous clear solution was obtained. As catalyst,  $\text{NH}_4\text{OH}$  (29.2 wt %, 4.0 ml) was added. The pH of the mixture was  $\sim 8$  (tested by pH paper). The beaker was then covered with a piece of paraffin film. In about 30 min, a white colloidal suspension appeared progressively, which was indicative of the particle formation. The reaction mixture was kept stirred at room temperature overnight. Wet silica product was separated from the mixture by centrifugation. After washing with EtOH, the product was dried in vacuum oven at ambient temperature for 3 days. Fructose containing silica spheres were obtained as yellowish fine powder with a yield of 50 % (calculated based on the sum of the theoretical weight of silica and the weight of fructose). To remove the template, the as-synthesized composite was extracted with water. About 0.5 g of sample was immersed in 15 ml of distilled deionized water under agitation for 2-3 h. The mixture was then centrifuged and the water was decanted. The sample was repeatedly washed in the same manner for 10 times. Upon drying in a vacuum oven for 3 days porous silica spheres were obtained as white powder.

For the purpose of comparison, a control sample was also synthesized in the absence of template under otherwise identical conditions.

### **3.2.3. Synthesis of Mesoporous Spherical Silica Particles through a Two- Step Water-in-Oil Method**

Mesoporous silica spheres with large size were prepared through a two-step water in oil method. The template containing sol mixture was pre-hydrolyzed first and the emulsifier was introduced to form a water in oil system. As a typical procedure to prepare spheres with 50 wt % template, TEOS (2.6 g, 0.0125 mol) and EtOH (5 ml) were mixed in a 50-ml beaker at room temperature under magnetic stirring. Into the TEOS/EtOH solution, was added 3.75 g fructose aqueous solution (30 wt %), which contains 1.125 g of fructose. The 0.0625 ml of 2M HCl (0.125 mmol) was added to catalyze the pre-hydrolysis. The beaker was then covered with a piece of paraffin film. The mixture was stirred for additional 45 min followed by the addition of pre-mixed Kerosene (26.1 g) and Span 80 (11.2 g). The mixture was then heated up and maintained to 40 °C for 3 days, during which white precipitate was gradually formed. Wet silica product was separated from the mixture by centrifugation. After washing with acetone, the product was dried in a vacuum oven at ambient temperature for 3 days. Fructose containing silica spheres were obtained as a yellow cream colored fine powder with a yield of 46 %. The template was removed with water extraction follow the procedures described in section 3.2.2.

### **3.2.4. Instrumentation and Characterization**

The nitrogen adsorption-desorption characterization was conducted on a Micromeritics ASAP 2010 surface area and pore size analyzer (Micromeritics, Inc.

Norcross, GA) at  $-196\text{ }^{\circ}\text{C}$ . Prior to the measurements, the samples were degassed at  $100\text{ }^{\circ}\text{C}$  and  $1\text{ Pa}$  for 6-7 h. Scanning electron microscopy (SEM) was performed on an AMRAY 1830 (Bedford, MA) microscope, with an accelerating voltage of  $20\text{ kV}$ . The samples were deposited on double sided carbon tape supported with a sample holder. The samples were gold-coated before the SEM characterization. The IR spectra of KBr powder-pressed pellets were recorded on a Perkin-Elmer 1600 FTIR spectrometer. Transmission electron microscopy (TEM) images were obtained from a JEOL-2000FX electron microscope operated at an accelerating voltage of  $200\text{ kV}$  (Lehigh University). The samples were prepared by evaporation of ethyl alcohol suspensions of the sample powder on copper grids coated with holey carbon film. The copper grids were obtained from SPI Supplies. Both as-synthesized silica spheres and finely ground samples were characterized with TEM.

### **3.3. Results and Discussion**

Mesoporous silica spheres have been prepared with the sol-gel reaction of TEOS in the presence of fructose as a template followed by the template removal through water extraction. The synthesis route is closely related to the nonsurfactant template sol-gel pathway to prepare mesoporous silica monoliths.<sup>9,10</sup> The major difference is that a proper amount of basic catalyst,  $\text{NH}_4\text{OH}$ , is introduced to the sol-template mixture to obtain the desired morphology. During the hydrolysis and condensation of the sol-gel reactions,

fructose is incorporated into the spherical silica matrix and directs the mesophase formation within the spherical fructose-silica composite.

The shape and the size of silica spheres (a) before and (b) after template removal were investigated with SEM and typical images are shown in Figure 3-1. The as-synthesized template containing silica particles show regular spherical shape. With a mean diameter of  $\sim 420$  nm, the spheres present a uniform size, which is not appreciably affected by the template concentration. After template removal with water extraction, the product retains the spherical shape with little evidence of fracture and breakage (Figure 3-1(b)).

The template removal from the as-synthesized composite sample was monitored with FT-IR spectroscopy. Figure 3-2 shows the representative IR spectra of the silica spheres (a) before and (b) after water extraction. The IR spectrum of pure silica gel (c) is displayed as a reference. The spectrum of fructose containing sample exhibits a characteristic strong absorption band at  $1400\text{ cm}^{-1}$  and a broad one at  $2940\text{ cm}^{-1}$ , which correspond to aliphatic C-H bending and stretching vibrations respectively. After water extraction, these two bands disappear and the spectrum shows the typical absorption bands as those in pure silica gel, which indicates that the template has been completely removed from porous silica matrix. The complete removal of fructose from silica matrix is also evidenced by the fact that calcination of the extracted sample to  $600\text{ }^{\circ}\text{C}$  showed no appreciable weight loss in the TGA measurement.

Table 3-1 summarizes the composition of the fructose-containing silica particles prepared with a variety of template concentrations and the pore parameters of the porous silica nanospheres upon template removal by water extraction. In the final dried template-containing silica samples, the fructose content determined from TGA experiments increases as the feed concentration of the fructose is increased in the starting reaction solution. It is noted that the final template content is generally lower than that in the feed concentration. The discrepancies could be attributed to the fact that in addition to being incorporated into the silica particles upon the phase separation, partial amount of the fructose still remains in the solvent during the sol-gel reactions. This phenomenon also serves as evidence of the existence of certain interactions between the template molecules and the sol-gel intermediates, so that even in the presence of a good solvent, the template can still be incorporated into silica beads upon a phase separation.

After the template removal by water extraction, mesoporous silica nanospheres were obtained. Nitrogen adsorption-desorption measurements were used to characterize the porosity of the extracted spheres. The pore parameters were found to be comparable with those of the mesoporous silica bulk materials prepared with acid catalyzed nonsurfactant templated sol-gel reactions. Representative nitrogen adsorption-desorption isotherms at  $-196\text{ }^{\circ}\text{C}$  for the mesoporous silica spheres are shown in Figure 3-3. At a fructose content ranging from 19 to 45 wt %, all the isotherms resemble type IV isotherms with H2 hysteresis loops at a relative pressure ( $P/P_0$ ) of  $\sim 0.5$ , which is indicative of mesoporosity.<sup>11</sup> The initial part of the type VI isotherm at low  $P/P_0$  ( $< 0.4$ ) is

mainly attributed to the monolayer-multilayer adsorption occurring on the pore surface. The adsorption isotherm goes up drastically after  $P/P_0$  of  $\sim 0.4$ , which suggests the occurrence of the pore filling by capillary condensation of nitrogen in the framework confined mesopores. The small H3 hysteresis loop observed at high  $P/P_0$  is indicative of the presence of narrow slit-like pores, which could be attributed to the exterior pores of the particles and the voids among the porous spheres. With increasing concentration of fructose, the H2 hysteresis loop becomes greater in magnitude and the isotherms exhibit larger final adsorbed volumes at  $P/P_0 \approx 1$ , indicating the increasing pore volumes. The Brunauer-Emmett-Teller (BET) surface areas calculated according to the Kelvin equation are also found to increase with template concentration (Table 3-1). At the fructose content of 45 wt %, the extracted silica spheres show a relatively large BET surface area of  $630 \text{ m}^2/\text{g}$ , a pore volume of around  $0.5 \text{ cm}^3/\text{g}$ . Based on the t-plot analysis data, the contributions from the micropores to the total surface area and pore volume are almost negligible.

Revealed by type IV nitrogen isotherms with H2 hysteresis loops, the mesopores inside the spheres most likely have a structure similar to interconnected narrow-necked ink bottle shape, in which the nitrogen adsorption and desorption processes can be deciphered as follows. The adsorption starts on the surface of the wide part inside the bottle and followed by a pore filling-up process. The desorption process occurs through the narrow neck of the bottle. Therefore the pore size distribution derived from the desorption branch of the isotherm may be attributed to the size of the neck due to this

bottle neck blocking effect. The representative Barrett-Joyner-Halenda (BJH) pore size distribution curves from the desorption branch of the nitrogen sorption isotherms are shown in Figure 3-4. Prepared with the fructose content of 30-70 wt %, the extracted silica spheres possess narrowly distributed mesopores in the range of 3-5 nm. The pore size distribution curves seem not significantly affected by the template concentration. Despite of the complexity and the uncertainty in using the gas sorption measurement to determine the pore size and distribution, this method still provides us a good indication of the pore structures of the samples. The pore diameters determined from the BJH method have been found in favorable agreement with those values obtained from the TEM images.

A representative low magnification TEM micrograph for the as-synthesized porous spheres is shown in Figure 3-5. Particles exhibit regular spherical shape with a relatively uniform size. These observations are consistent with SEM measurements. The morphology and porous structure are further revealed by high magnification TEM. The typical micrographs of an as-synthesized particle and a finely ground one are displayed in Figure 3-6 (a) and (b). From the image of a thin section of ground sample, Figure 3-6 (c), interconnected worm like channels and pores can be clearly observed. By image analysis, the average pore/channel diameter is about 3-4 nm, which is well in agreement with the value calculated from nitrogen sorption measurements. Revealed by the nitrogen sorption measurements and TEM characterization, the pore structures of silica spheres are comparable with those of the mesoporous silica monoliths prepared



with nonsurfactant templates at different pH (normally around 7 or lower).<sup>36,37</sup> This further indicates that the pore structure formation mainly depends on the characteristics of the nonsurfactant template and the template/silica interactions, but is not obviously affected by the sol-gel process. Yet we do not completely understand the function of nonsurfactant compound in directing the mesophase formation in the silica spheres. It might be similar to the case wherein monoliths are produced with the nonsurfactant templates, template aggregation and hydrogen bonding between the template and intermediate silicates play important roles.<sup>36,41</sup>

It is of particular interest that the TEM images of the as-synthesized spheres (Figure 3-5 and Figure 3-6(a)) show relatively bright centers, which may suggest a low silica density in the center part of the spheres, or most likely a hollow core. The similar structural inhomogeneities have been previously reported in the preparation of large size spheres with a surfactant template.<sup>1,33</sup> Such a hollow center structure was also observed in other experiments to synthesize porous silica spheres with varied sizes under different conditions.

Shown in Figure 3-7, are the typical SEM micrographs of particles prepared with 50 wt % fructose and a TEOS/solvent (v/v) of 1:10 ratio. The sample consists of spherical particles with diameters of  $\sim 1$   $\mu\text{m}$ . In comparison to the well separated particles obtained with TEOS/solvent (v/v) of 1:40 ratio, most of the particles in this sample had agglomerated into clusters (Figure 3-7(a)). This aggregation was probably due to condensation of hydrolyzed surface groups of different spheres when they had a higher

possibility to come into contact with each other in a lower solvent content system. These particles are in fact hollow in the core. The void center can be clearly observed From the SEM image of some broken particles (Figure 3-7 (b)). The shell of the particles possesses a uniformed thickness of  $\sim 200$  nm. Hollow spheres with large size (i.e.,  $\sim 30$   $\mu\text{m}$ ) were obtained through a two-step water in oil synthesis. The typical SEM images of the sample consisted of thin-walled large spheres are shown in Figure 3-8. Most of particles were popped open during the drying and washing steps or during introduction into the high vacuum of SEM. The hollow core structure is evidenced by broken particles, as well as pieces of bowl shaped fragments throughout the sample.

We suggested the formation of such a hollow/low-density center structure is the result of incomplete hydrolysis/condensation reaction inside the spheres. During the phase separation of the sol-gel process, the intermediate silicate droplets formed. The hydrolysis and condensation of the droplet proceed rapidly from the surface due to the sufficient contact with water and basic catalyst. The gradually gelled and hardened shell causes a slow feeding of water into the spheres as well as a slow release of the organic byproduct from the inner part, which in turn results in an incompletely hydrolyzed core. In the case of water in oil synthesis, the presence of surfactant may contribute to the stabilization of large prehydrolyzed sol droplets.

### 3.4. Conclusions and Remarks

In the presence of a nonsurfactant small molecule, fructose, nanometer-sized mesoporous silica spheres were prepared with a base-catalyzed sol-gel reaction from the mixture of tetraethoxysilane, ethanol and water. As the pore structure directing template, fructose can be conveniently removed from the spherical silica matrices by water extraction under mild conditions. After the template removal, the silica spheres exhibit mesoporosity with a high surface area up to  $630 \text{ m}^2/\text{g}$ , a pore volume of around  $0.5 \text{ cm}^3/\text{g}$  and narrowly distributed pore size with a peak pore diameter at  $\sim 3\text{-}4 \text{ nm}$ . The pore structure, such as surface area and pore volume, can be fine-tuned by simply changing the template concentration in the starting sol mixture. The characteristics of pore structures of the silica nanospheres are similar to those observed for the porous bulk materials prepared via nonsurfactant templating pathway under acidic or near neutral conditions. The spheres have a low density core which could be attributed to the incomplete hydrolysis/condensation reactions inside the particles. As an alternative to prepare mesoporous silica spheres, the base catalyzed nonsurfactant templating pathway is environment-friendly, low cost and easy in template removal. With various nonsurfactant template compounds or different metal alkoxides, the versatility of this synthetic route could further be extensively demonstrated. With both the mild, convenient synthetic process and the well defined morphology and nanostructure, the obtained mesoporous spheres are suitable for further investigation as the matrix materials for sensor and

catalyst development. The hollow core/porous shell structure are of special interests for drug delivery applications.

### 3.5. Acknowledgments

I would like to acknowledge Mr. David J. von Rohr in Department of Materials Engineering at Drexel University for his assistance in obtaining SEM images. I also want to thank Mr. Patrick Ndungu in Department of Chemistry at Drexel University for the discussions on TEM measurements.

### 3.6. References

1. Schacht, S.; Huo, Q.; Voigt-Martin, I. G.; Stucky, G. D., Schüth, F. *Science*, **1996**, 273, 768.
2. Yang, H.; Coombs, N.; Ozin, G. A. *Nature* **1997**, 386, 692.
3. Renzo, F. Di; Testa, F.; Chen, J. D.; Cambon, H.; Galarneau, A.; Plee, D.; Fajula, F. *Micro. Meso. Mater.* **1999**, 28, 437.
4. Unger, K. K.; Kumar, D.; Grun, M.; Buchel, G.; Ludtke, S.; Adam, T.; Schumacher, K.; Renker, S. *J. Chroma.* **2000**, 892, 47.
5. Edler, K. J.; Roser, S. J. *Int. Revi. Phys. Chem.* **2001**, 20, 387.
6. Yang, H.; Vovk, G.; Coombs, N.; Sokolov, I.; Ozin, G. *Nature* **1996**, 381, 589.
7. Aksay, I. et al. *Science* **1996**, 273, 892.
8. Bruinsma, P. J.; Kim, A. Y.; Liu, J.; Baskaran, S. *Chem. Mater.* **1997**, 9, 2507.
9. Yang, P.; Zhao, D.; Chmelka, B. F.; Stucky, G. D. *Chem. Mater.* **1998**, 10, 2033.
10. Cheng, S.; Wei, Y. *Poly. Mater. Sci. Eng.* **2002**, 87, 302.

11. Matijević, E.; Gheradi, P. *Transformation of Organometallics into Common and Exotic Materials: Design and Activation*, NATO ASI series E, No. 141, Laine, R. M., ed, Martinus Nijhoff: Dordrecht, 1988, p 279.
12. Iler, R. K. *The chemistry of Silica*; John Wiley: New York, 1979.
13. Titulaer, M. K.; Jansen, J. B. H.; Geus, J. W. *J. Non-Cryst. Solids* **1994**, *168*, 1.
14. Van der Grift, C. J. G.; Boon, A. Q. M.; Van Veldhuizen, A. J. W.; Trommar, H. G. J.; Geus, J. W.; Quinson, J. F.; Brun, M. *Apply. Catal.* **1990**, *65*, 225.
15. Titulaer, M. K.; Jansen, J. B. H.; Geus, J. W. *J. Non-Cryst. Solids* **1994**, *168*, 1.
16. Unger, K.; Schick-Kalb, J.; Krebs, K. F. *J. Chromatogr.* **1973**, *83*, 5.
17. Kohlschutter, H. W.; Mihm, U. *Kolloid Z. Z. Polym.* **1971**, *243*, 148.
18. Van der Grift, C. J. G.; Geus, J. W.; Barten, H.; Laferink, R. G. I.; Van Milterburg, J. C.; Den Ouden, A. T. Characterization of Porous Solids, Stud. Surf. Sci. Catal., Unger, K. K., Rouqueroel, J., Sing, K. S. W., Kral, H., eds, Elsevier: Amsterdam, 1988, vol. 39, p 619.
19. Boissiere, C; vander Lee, A.; Mansouri, A. E.; Larbot, A.; Prouzet, E. *Chem Commun.* **1999**, 2047.
20. Huo, Q.; Feng, J.; Schuth, F.; Stucky, G. D. *Chem. Mater.* **1997**, *9*, 14.
21. Grun, M.; Lauer, I.; Unger, K. K. *Adv. Mater.* **1997**, *9*, 254.
22. (a) Hirose, A.; Yamashita, H.; Maekawa, T. *Anal. Sci.* **1994**, *10*, 737. (b) Yamashita, H.; Maekawa, T. *Ceram. Trans.* **1995**, *51*, 39.
23. Kresge, C. T.; Leonowicz, M. E.; Roth, W. J.; Vartuli, J. C.; Beck, J. S. *Nature* **1992**, *359*, 710.
24. Beck, J. S.; Vartuli, J. C.; Roth W. J.; Leonowicz, M E.; Kresge, C. T.; Schmitt, K. D.; Chu, T-W.; Olson, D. H.; Sheppard, E. W.; McCullen, S. B.; Higgins, J. B.; Schlenker, J. L. *J. Am. Chem. Soc.* **1992**, *114*, 10834.
25. Grun, M.; Lauer, I.; Unger, K. K. *Adv. Mater.* **1997**, *9*, 254.
26. Yang, H; Vovk, G.; Coombs, N.; Sokolov, I.; Ozin, G. A. *J. Mate. Chem.* **1998**, *8*, 743.

27. Hunter, H. M. A.; Garcia-Bennett, A. E.; Shannon, I. J.; Zhou, W.; Wright, P. A. *J. Mater. Chem.* **2002**, *12*, 20.
28. Cot, F., Kooyman, P. J., Larbot, A., Prouzet, E. *Mesoporous Molecular Sieves 1998*, Bonneviot, L., Beland, F., Danumah, C., Giasson, S., Kaliaguine, S., eds, Elsevier Science: Amsterdam, Lausanne, New York, Oxford, Shannon, Singapore, Tokyo, vol. 177, 1998.
29. Prouzet, E.; Frederic, Cot, Georges, N.; Larbot, A.; Kooyman, P.; Pinnavaia, T. J. *Chem. Mater.* **1999**, *11*, 1498.
30. Boissière, C.; van der Lee, A.; Mansouri, A. E.; Larbot, A.; Prouzet, E. *Chem. Commun.* **1999**, 2047.
31. Qi, L.; Ma, J.; Cheng, H.; Zhao, Z. *Chem. Mater.* **1998**, *10*, 1623.
32. Lu, Y.; Fan, H.; Stump, A.; Ward, T.; Rieker, T.; Brinker, C. J. *Nature* **1999**, 398, 223.
33. (a) Lin, H. P.; Mou, Z. Y. *Science* **1996**, *273*, 765. (b) Lin, H. P.; Mou, C. Y.; Liu, S. B.; Tang, C. Y. *Chem. Commun.* **2001**, 1970.
34. (a) Zhong, Z.; Yin, Y.; Gate, B.; Xia, Y. *Adv. Mater.* **2000**, *12*, 206. (b) Yin, Y.; Lu, Y.; Gates, B.; Xia, Y. *J. Am. Chem. Soc.* **2001**, *13*, 1146.
35. Büchel, G.; Unger, K. K.; Matsumoto, A.; Tsutsumi, K. *Adv. Mater.* **1998**, *10*, 1036.
36. Wei, Y.; Jin, D.; Ding, T.; Shih, W.-H.; Liu, X.; Cheng, S. Z. D.; Fu, Q. *Adv. Mater.* **1998**, *3*, 313.
37. (a) Pang, J. B.; Qiu, K. Y.; Wei, Y.; Lei, X.; Liu, Z. F. *Chem. Commun.* **2000**, 6, 477. (b) Pang, J. B.; Qiu, K. Y.; Wei, Y. *Chem. Mater.* **2001**, *14*, 2361.
38. Pnag, J.-B., Qiu, K.-Y.; Wei, Y.; Lei, X.-J.; Liu, Z.-F. *Chem. Commun.* **2000**, 477.
39. Izutsu, H.; Mizukami, F.; Nair, P. K.; Kiyozumi, Y.; Meada, K. *J. Mater. Chem.* **1997**, *7*, 767.
40. Dong, H. *Organic-Inorganic Hybrid Mesoporous Silica Materials and Their Applications as Host Matrix for Protein Molecules*, Ph.D dissertation, Drexel University, 2002.

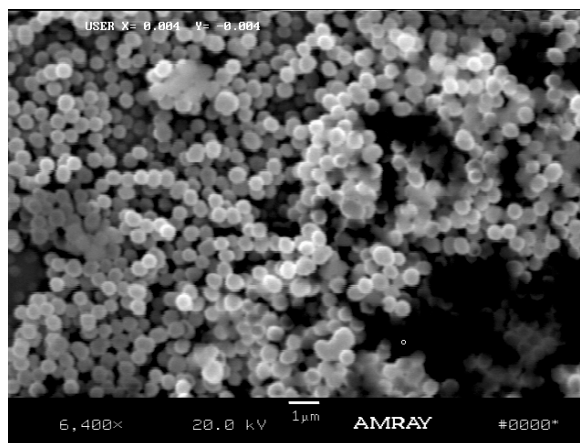
41. Polarz, S.; Smarsly, B.; Bronstein, L.; Antonietti, M. *Angew. Chem. Int. Ed.* **2001**, *40*, 4417.

Table 3-1. Composition of the sol-gel spherical silica samples prepared in the presence of 30-70 wt % fructose templates and the pore parameters of the porous silica nanospheres after template removal of fructose by water extraction.

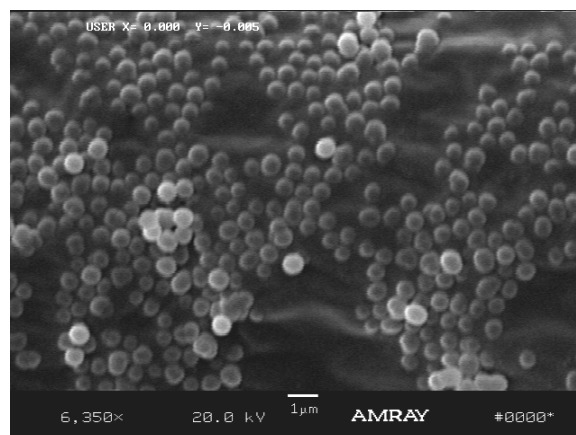
Sample code	Fructose (wt %)		Surface area $S_{\text{BET}}$ , ( $\text{m}^2\text{g}^{-1}$ )	Pore Vol. $V$ , ( $\text{cm}^3\text{g}^{-1}$ )	BET pore diameter( $\text{\AA}$ ) <sup>c</sup>	BJH pore diameter( $\text{\AA}$ ) <sup>d</sup>	Micropore	
	calcd <sup>a</sup>	found <sup>b</sup>					surface area ( $\text{m}^2\text{g}^{-1}$ )	Vol. ( $\text{cm}^3\text{g}^{-1}$ ) <sup>e</sup>
SF30	30	19	114	0.127	44	44	6.79	0.004
SF50	50	31	340	0.270	32	34	25.97	0.015
SF60	60	40	472	0.422	35	37	16.46	0.085
SF70	70	45	627	0.516	32	35	29.24	0.016

<sup>a</sup> Designed fructose content in the template containing silica, as calculated from the feed composition based on the assumptions that TEOS transformed into  $\text{SiO}_2$  with a 100% yield and fructose was completely confined in the  $\text{SiO}_2$  matrices. <sup>b</sup> Values from weight loss at 550 °C based on TGA measurement. <sup>c</sup> The average pore diameters calculated from  $4V/S_{\text{BET}}$  by the BET method. <sup>d</sup> Determined from the maxima of the BJH desorption pore size distribution curves with the Halsey equation. <sup>e</sup> Values determined from the  $t$ -plot analysis.





(a)



(b)

Figure 3-1. Typical SEM images of the silica spheres (SF50). (a) Before the template removal by water extraction. (b) After the template removal by water extraction.



Figure 3-2. Representative IR spectra of silica spheres (SF50). (a) Before template removal by water extraction. (b) After template removal by water extraction. (c) IR spectrum of pure silica gel.

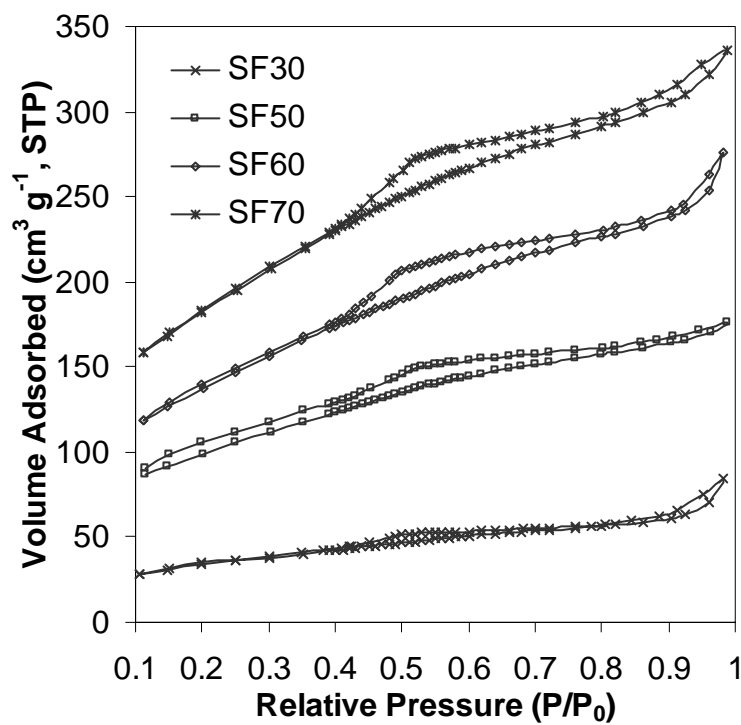


Figure 3-3. Nitrogen adsorption-desorption isotherms at -196 °C for the water extracted silica spheres prepared with fructose concentration ranging from 30 to 70 wt %.

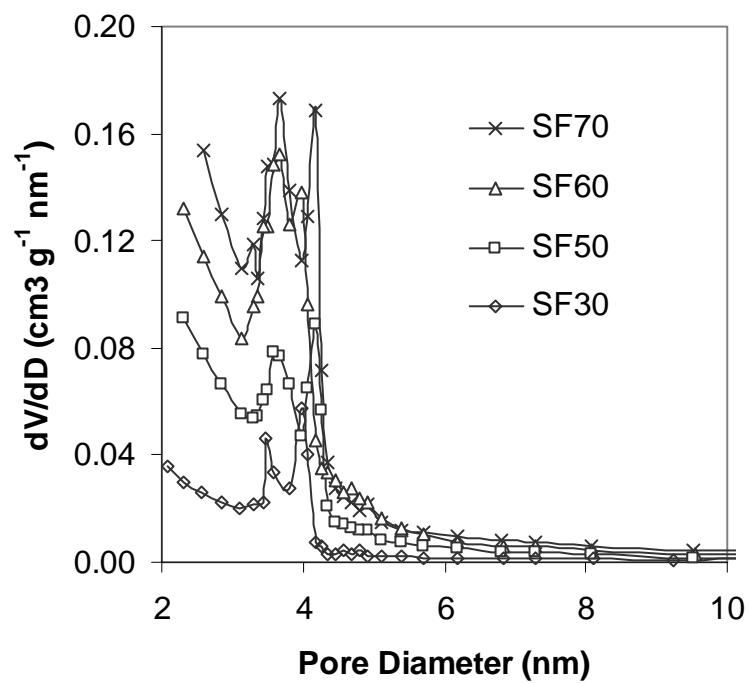


Figure 3-4. BJH pore size distributions obtained from the nitrogen desorption isotherms at  $-196\text{ }^\circ\text{C}$  for the water extracted silica spheres prepared with fructose concentration ranging from 30 to 70 wt %.

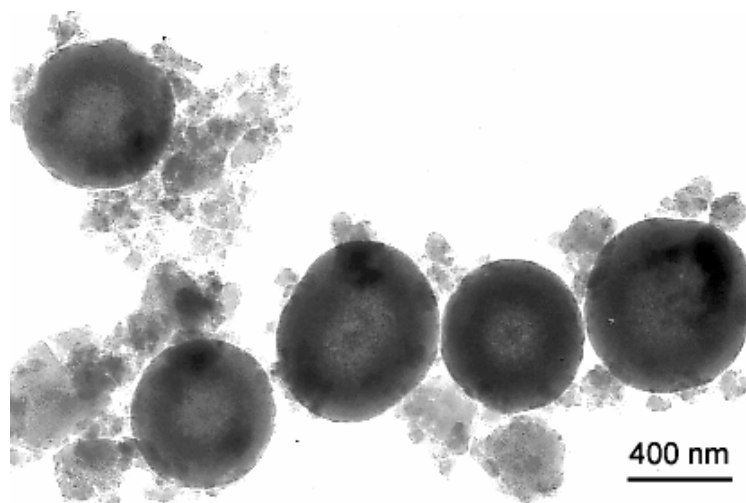


Figure 3-5. Representative TEM images for the porous silica spheres: Low magnification TEM showing the uniform spheres with average diameter of 420 nm.

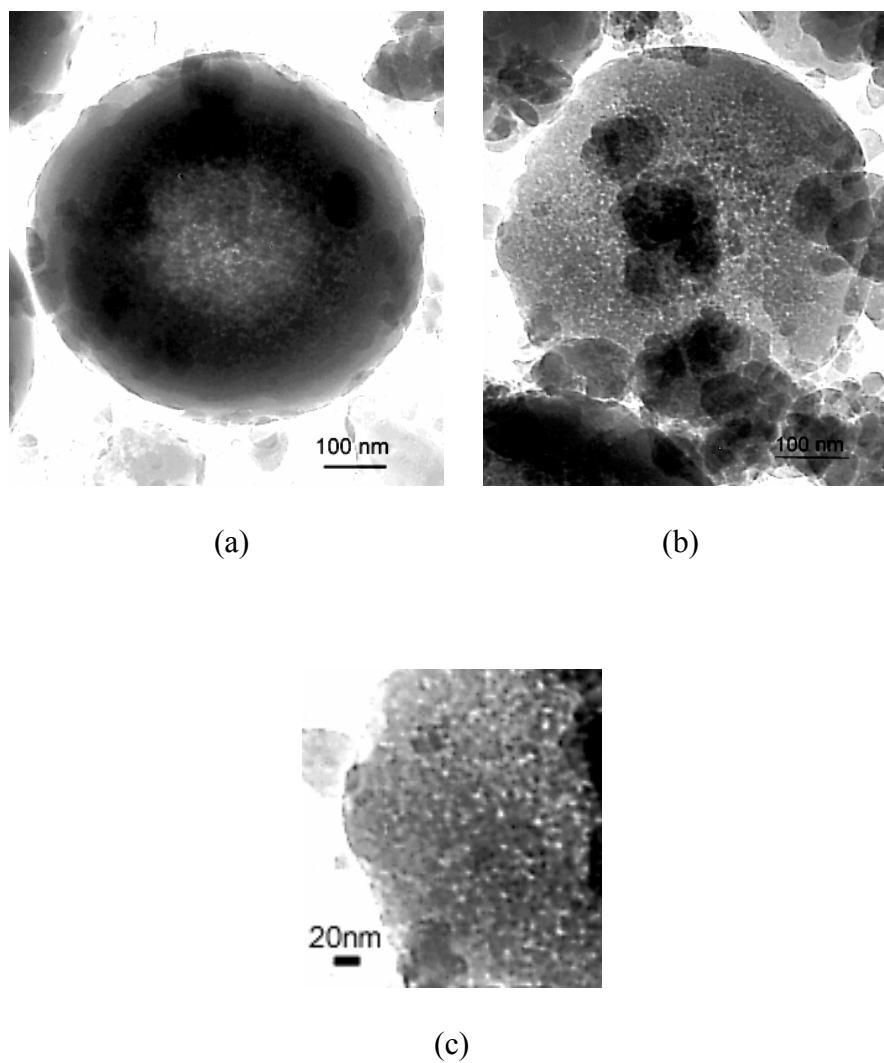
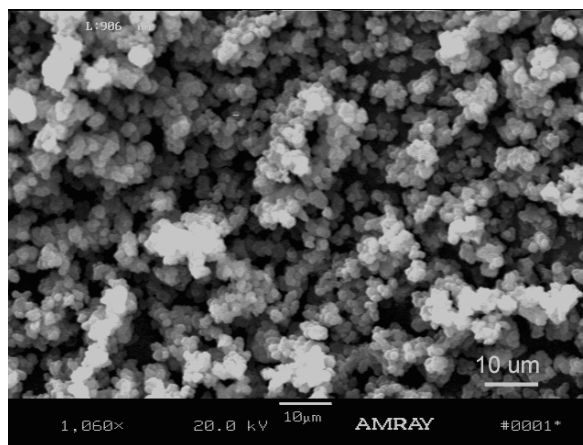
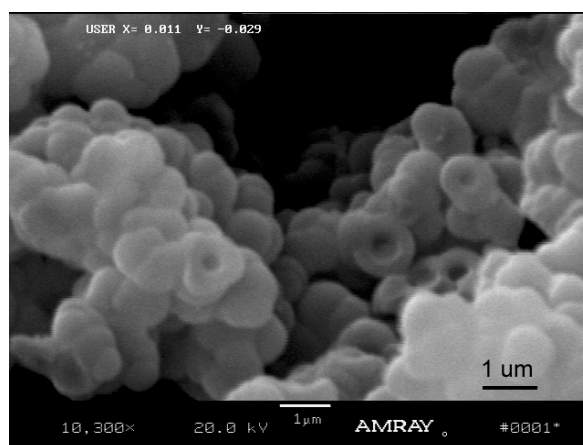


Figure 3-6. Representative TEM images for the porous silica spheres. (a) High magnification TEM of one silica sphere revealing the low density core. (b) TEM picture of an ultra-thin section of a ground silica sphere showing the overall porous structure. (c) High resolution TEM image of the edge area of the sphere shown in (b). The sample exhibits interconnected wormlike pores with diameter of  $\sim 3-5$  nm.

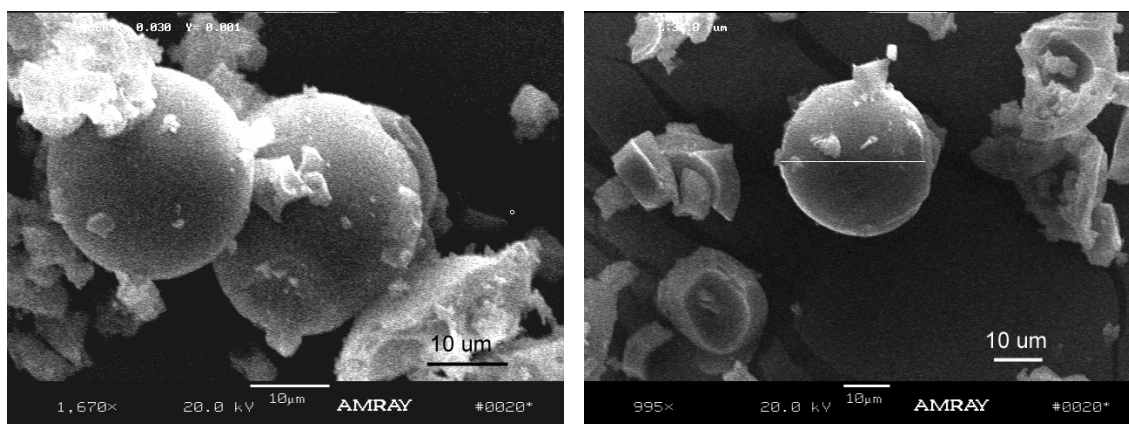


(a)



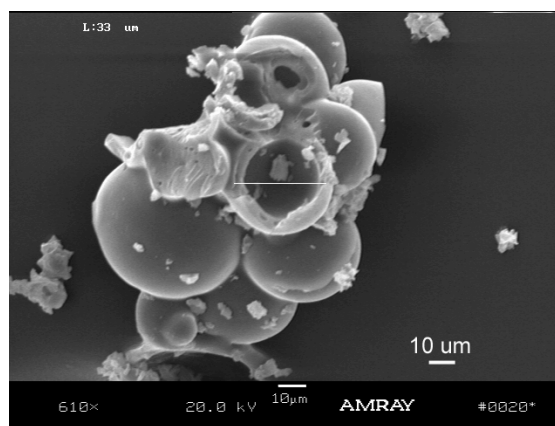
(b)

Figure 3-7. Typical SEM images of the silica spheres prepared with 50 wt % of fructose and TEOS/EtOH (v/v) ratio of 1:10. (a) Particles aggregated into clusters. (b) Broken particles exhibit hollow cores.



(a)

(b)



(c)

Figure 3-8. Typical SEM images of the silica spheres prepared with 50 wt % of fructose through a two-step water in oil method. (a) Particles without breakage. (b) Particle with broken pieces around. (c) Broken particles from a cluster showing the hollow core.



## **Chapter 4. Synthesis of Mesoporous Gold-Silica Nanocomposite Materials via Sol-Gel Process with Nonsurfactant Templates**

### **4.1. Introduction**

In addition to being successfully applied to prepare porous sol-gel materials with different morphologies, the nonsurfactant templating pathway also provides a convenient synthetic route to the preparation of composite materials. It has been well demonstrated that using polymerizable compounds such as vinyl monomers as template, polymer-silica nanocomposite can be prepared with the nonsurfactant templating sol-gel process followed by a post polymerization.<sup>1,2</sup> As the results of the fine morphology obtained from the sol-gel method, the composite materials exhibit excellent mechanical and optical properties. In this study, we explored the application of the nonsurfactant templating route from another point of view: using this method to prepare mesoporous metal-silica nanocomposite. By introducing a second sol component such as metal colloidal solution into the silica precursor solution, metal-silica nanocomposite materials were obtained through a one-step sol-gel reaction in the presence of nonsurfactant compound as pore structure directing agent. After the template removal, the composite materials exhibit mesoporosity. In this study we are particularly interested in gold nanoparticles, and next we proceed to describe the rationale behind it, beginning from the overview of some unique characteristics of gold.

#### 4.1.1. Gold Nanoparticles in Sol-Gel Matrices: Properties

Gold is widely recognized for its usefulness in modern technologies due to some of its unique physical and chemical properties, such as excellent conduction of electricity ( $\sigma = 446.4 \text{ S/cm}$ ), malleability, ductility, and excellent resistance to corrosion and tarnish.<sup>3,4</sup> More recently, nanoscale dispersed gold particles in metal oxide sol-gel matrices have attracted great research interests due to their distinctive optical,<sup>5-7</sup> electrical<sup>8</sup> and chemical properties<sup>9</sup>, which are dramatically different from bulk gold materials.<sup>10-15</sup>

In comparison to other noble metals such as platinum (Pt) and palladium (Pd), gold was found to be less catalytically active. This phenomenon was theoretically illustrated by its high ionization energy and the low chemical adsorption energy on the surface.<sup>16</sup> Haruta *et al.* discovered that when supported on metal oxides such as titanium oxides, gold ultrafine powder with diameter in nanometer scale may function as an extraordinarily active catalyst for low-temperature combustion, partial oxidation of hydrocarbons, hydrogenation of unsaturated hydrocarbons and reduction of nitrogen oxide.<sup>17</sup> The activity and selectivity of gold catalysts are tunable by varying the support materials, the preparation methods, and particularly the size of the gold particles.<sup>18</sup> For example, at a critical diameter of 2 nm, the product in the reaction of propylene with oxygen and hydrogen catalyzed by supported gold particles switches from propylene oxide to propane.<sup>19</sup> In the low-temperature oxidation of CO on supported gold particles, the reaction rate increases notably as the diameter of the gold particles decreases to  $\sim 3.5$

nm, and the reaction reaches the highest rate at ~3 nm. A further decrease in particle diameter below 3 nm leads to a decrease in gold activity.<sup>20</sup> Not yet fully understood on the atomic level, the wide range of tunability of catalytic properties of nanodispersed gold particles in sol-gel metal oxide matrices opens opportunities in the chemical industry and environmental applications.

The linear and nonlinear optical behavior of nanoscale gold particles dispersed in sol-gel silica matrices are strongly depends on the particles size. These properties have been extensively studied and applied for sensing applications.<sup>21,22</sup> Surface plasmon resonance (SPR) is characteristic of mesoscale (2-50 nm) particle surfaces.<sup>23,24</sup> At this dimension, the electron cloud can oscillate on the particle surfaces and absorb electromagnetic radiation at a particular level of energy.<sup>25</sup> However smaller nanoparticles (< 1-2 nm) do not display this phenomenon since their electrons exist in discrete energy levels, and bulk gold has a continuous absorbance in the UV/Vis/IR region. SPR of gold nanoparticles usually exhibit a spectral peak at about 500–550 nm, which can be used to determine the particle size as well as to rapidly monitor changes in environment.<sup>26</sup> For example, with methyl-orange-modified 50 nm gold particles supported in silica matrices, the presence of HCl vapor can be observed by the SPR spectrum change within a few seconds.<sup>27</sup> Samples cast as thin films exhibit even faster response time. Surface enhanced Raman radiation is also an important characteristic for gold nanoparticles,<sup>28,29</sup> which is extraordinarily useful in optical sensing.<sup>30,31</sup> The Raman scattering of the molecules

absorbed on a nanoparticle surface can be usually enhanced by a factor of  $10^3$  to  $10^6$ , which consequently lowers the detection limits.

Not only interesting from the size-dependent properties of gold nanoparticles, the sol-gel derived supporting matrix materials also exhibit distinctive advantages for practical sensing<sup>32,33</sup> and catalysis applications.<sup>34-36</sup> Some of the reasons are as follows. 1) The high porosity of sol-gel matrix (silica, titania, and zirconia) allows for a fast mass exchange between active sites and surroundings. 2) The optical properties of the nanocrystalline dispersant are only slightly affected by the transparent matrix. 3) Materials may be readily cast as a variety of forms (e.g., monolith, thin film, coating, and so forth) due to the convenient sol-gel process.<sup>37,38</sup>

We have been interested in the dispersions of noble metal (Au or Ag) nanoparticles in mesoporous sol-gel materials. With a pore size range of 2-50 nm, the mesopores permit ingress by molecules and guests physically excluded from microporous materials, and provide a high surface area available for sensing and catalysis. In comparison to macroporous materials, the pore size can be made small enough to prevent the active species (i.e., nanosized particles) from leaking out of the matrices.

#### **4.1.2. Gold Nanoparticles in Sol-Gel Matrices: Synthesis**

Several general strategies were reported for the encapsulation of metallic colloids in sol-gel matrices. Using an inverse micelle technique, spherical nanosized metal-silica composite particles were prepared via a sol-gel reaction within the metal alkoxide

microemulsion.<sup>39</sup> Martino *et al.* reported the synthesis of metal nanocluster dispersed silica monoliths, by diffusing the metal clusters into pre-existing wet monoliths formed through a sol-gel reaction.<sup>40</sup> Silica thin films and bulk materials containing metal colloids were also prepared by diffusing metal salt solution into silica matrices, followed by a reduction of the metal salt, which could be chemical, photo-chemical or sono-chemical reduction.<sup>41,42</sup> Using a two-step sol-gel procedure, Whilton *et al.*<sup>43</sup> synthesized porous silica-supported metal nanoparticles. Prefabricated metal-polymer microgel hybrids were incorporated in a silica matrix. In this method, the spherical functionalized polymer microgels function as both nanosized exo-templates for controlled growth of metal colloids, and endo-templates for porous sol-gel silica. It has been noticed that the morphology and properties of the metal-silica composite were greatly affected by the preparation methods.

In this work, we have successfully applied the convenient nonsurfactant-templating approach to the synthesis of mesoporous gold-silica nanocomposites. Composite monoliths were synthesized through a one-step sol-gel reaction in the presence of a colloidal gold sol and a nonsurfactant template in the starting precursor sol mixtures. After the template was removed through calcinations, the materials exhibited mesoporosity with a high surface area up to 600 m<sup>2</sup>/g, a pore volume of ~ 0.5 cm<sup>3</sup>/g and relatively narrow pore size distributions with a pore diameter of 3-4 nm. Gold particles ranging in diameters of 2-8 nm were homogeneously dispersed throughout the silica matrix. The gold-silica composites are nanoscopic materials in which the optical and

physical/chemical properties of gold nanoparticles are coupled with the high surface area and the high porosity of the silica framework.

## **4.2. Experimental**

The synthesis approach of making mesoporous gold-silica nanocomposite materials was developed based on the protocol of nonsurfactant templated sol-gel pathway developed in our laboratory. A gold sol was introduced into the sol mixture as the source for gold particles.

### **4.2.1. Materials**

Tetraethyl orthosilicate (TEOS, Aldrich), tetrahydrofuran (THF, Aldrich), dibenzoyl tartaric acid (DBTA, Aldrich), hydrochloric acid (HCl, Fisher), Liquid Bright Gold 5154<sup>TM</sup> (Engelhard Corporation) were all used as received without further purification.

### **4.2.2. Synthesis of Mesoporous Gold-Silica Nanocomposites**

Mesoporous gold-silica nanocomposites were synthesized through a simple one-step sol-gel process in the presence of DBTA as a nonsurfactant template. With a stabilizing agent, Liquid Bright Gold 5154<sup>TM</sup> is a colloidal gold solution, which contains 5 wt % metallo-organic gold compound in cyclohexanone. It is widely used for gold coating on glass and ceramics with good adhesion properties. To prepare the composite,

the colloidal gold sol was combined with a pre-hydrolyzed silica sol and the template solution. As the sol mixture gelled, the gold sol was incorporated into the three-dimensional silica network. After being aged and dried at room temperature, the resulting material was subjected to calcination to remove the template and to anneal the gold-silica composite. By fixing the DBTA template concentration at 50 wt %, which is calculated based on the weight of silicon dioxide and the template in the final dry product (excluding gold content), a series of samples with different gold contents were prepared. In this work the DBTA template content was fixed at 50 wt % since the effect of nonsurfactant template on pore structure of silica matrix has been established and previously reported.<sup>21,22</sup> The amount of gold sol used was varied from 10 to 25 wt %, based on the weight of TEOS employed. The exact gold content of the final composite materials was determined by elemental analysis with energy dispersive X-ray (EDX). As a typical procedure to prepare the sample GS50-10 containing with 10 wt % gold-sol, 4.16 g TEOS (0.02 mol), 8.79 g THF (0.12 mol), 1.44 g H<sub>2</sub>O (0.08 mol) and 0.100 ml 2M HCl (0.20 mmol) were mixed in a 50 ml beaker and magnetically stirred at room temperature for 4 h. The template solution was prepared by dissolving 1.20 g DBTA (50 wt % based on the weight of silica dioxide and the template in the final dry product) in 1.00 g THF and then was added into the hydrolyzed TEOS sol. After 30 minutes under gentle stirring, 0.42 g Liquid Bright Gold 5154<sup>TM</sup> (10 wt % based on TEOS) was added. The resulting dark brown mixture was homogeneous and slightly translucent. The beaker was then covered with a piece of paraffin film. After 1-2 hours, the beaker was removed

from the stirring plate. Approximately 15-20 pinholes were punched on the paraffin film to allow the evaporation of the solvent and volatile byproducts of the sol-gel reactions, e.g., ethanol and water. The sol-gel reaction proceeded at room temperature for about 8 days. On drying, dark-brown opaque and monolithic DBTA-containing gold-silica gel was obtained. The sample was further dried under vacuum for 10 days, during which it broke into smaller, but crack-free, pieces. Two control samples were prepared in the absence of either gold-sol or DBTA template under otherwise identical conditions.

To get mesoporous gold-silica composites, the as-synthesized samples were ground into a fine powder and subjected to calcination in air for a period of 16 h at 550 °C, with a heating rate of 0.5 °C/min. After the calcination, the sample turned a wine-red color because of the surface plasmon resonance of gold nanoparticles.

#### **4.2.3. Instrumentation and Characterization**

The N<sub>2</sub> sorption characterization was conducted on a Micromeritics ASAP 2010 surface area and pore size analyzer (Micromeritics Inc., Norcross, GA) at -196 °C. All samples were degassed at 200 °C and 1 Pa for at least 6 h prior to N<sub>2</sub> adsorption-desorption isotherm measurement. Powder XRD patterns were recorded on a Siemens D500 diffractometer equipped with a rotating anode and using Cu K $\alpha$  radiation ( $\lambda = 0.15418$  nm). EDX elemental analysis and X-ray mapping were conducted on an EDX interfaced AMRAY 1830 scanning electron microscope (SEM). The instrument was operated at an accelerating voltage of 5 kV. The samples were deposited on sample



holders with adhesive carbon tape. TEM images of the gold-silica nanocomposites were obtained with Hitachi H-9000 HRTEM operated at an accelerating voltage of 300 kV. The TEM samples were prepared by evaporation of ethyl alcohol suspensions of the finely ground sample powder on a copper grid coated with holey carbon film. The copper grids were obtained from SPI Supplies. Solid state UV-visible reflectance spectra of the as-synthesized samples were measured with a Perkin Elmer-330 Spectrophotometer. The baseline of the instrument was calibrated with magnesium carbonate powder. The samples were prepared by spreading a layer of silica-gold nanocomposite fine powder on the top of a layer of magnesium carbonate in a quartz sample holder. All the spectra were obtained at a scanning rate of 180 nm/min.

### **4.3. Results and Discussion**

In the presence of DBTA as a nonsurfactant template, mesoporous gold-silica nanocomposite materials were prepared using a sol-gel process, combining a gold sol and a pre-hydrolyzed silica sol. As nano-sized gold phases dispersed in the three-dimensional mesoporous silica network, the composites were prepared with various gold contents. The compositions and pore parameters of porous gold-silica composites are summarized in Table 4-1. The compositions were determined by elemental analysis with the EDX technique (Figure 4-1). The results show that in the final composite materials the gold content is increased from 6.9 to 11.4 (wt %), which is consistent with the trend of gold sol stoichiometry in the starting sol mixture. To examine the confining ability of the

porous silica matrices over the gold particles, the gold contents of the composites were investigated after extracting the mesoporous gold-silica samples with tetrahydrofuran in a Soxhlet apparatus for 5 h. The results are also summarized in Table 4-1. For all the gold-containing samples, after solvent extraction, more than 85 % of the gold particles are not washed out and are still retained in the porous composite. This indicates a good confinement of active species (i.e., gold nanoparticles) in the mesoporous silica matrices with a low leaking level.

Representative nitrogen adsorption-desorption isotherms at  $-196\text{ }^{\circ}\text{C}$  for the porous gold-silica nanocomposite samples after the calcinations are shown in Figure 4-2. All the samples show type IV like isotherms with H2 hysteresis loops at  $P/P_0$  of  $\sim 0.4-0.8$ . The isotherm of the control sample in the absence of gold (i.e., SG50-0) containing 50 wt % DBTA is similar to that of typical nonsurfactant templated mesoporous silica materials, which we reported earlier.<sup>44</sup> With the gold content at 10.1 wt % or lower, the pore structures of the composite samples are comparable to the control sample in the absence of gold. These materials exhibit mesoporosity with a pore diameter of 3-4 nm, a high Brunauer-Emmett-Teller (BET) surface area up to  $600\text{ m}^2/\text{g}$  and a large pore volume of  $\sim 0.5\text{ cm}^3/\text{g}$ . Based on the t-plot analysis, the contributions from micropores to the pore volume are relatively small (Table 4-1). It should be noticed that with the gold content as low as 6.9 wt %, the composite sample (i.e., GS50-10) shows a higher BET surface area than the gold-free control sample (i.e., GS50-0). This phenomenon is not unexpected. During the sol-gel process, the organic moieties in the starting liquid gold sol might be

trapped in the gold-silica matrix, and function as “co-templates” with DBTA. As gold concentration increases, the BET surface area of the composite samples is found to fluctuate around 500-600 m<sup>2</sup>/g. When the gold content is further increased to 11.4 wt %, the pore diameter remains at 3.5 nm. However, the surface area decreases to ~200 m<sup>2</sup>/g, and a smaller value of pore volume (~ 0.17 cm<sup>3</sup>/g) is observed. This indicates that in the presence of larger number of gold particles, less number of pores or pore channels is formed or preserved in the composite matrix. Besides the effect of gold particle occupation of the interior pore space, some other factors may also contribute to this phenomenon. A relatively weak interaction between the gold particles and template (i.e., DBTA) molecules/aggregations might be one of the reasons. In the nonsurfactant templating sol-gel pathway, hydrogen bonding between the template and intermediate silicates plays an important role in directing the mesophase formation.<sup>44-46</sup> In the presence of gold particles, the template-silica intermediate interface is partially replaced by template-gold particle interface, which has less interaction between the two phases. As a result, less mesophase is formed by template directing during the sol-gel reaction and final material exhibits a smaller surface area and pore volume. In addition, the introduction of gold into the silica matrix also brings complexities in porosity measurement with nitrogen sorption, among which two major ones are electrostatic forces between adsorbate (i.e., nitrogen) and metallic surface, and increased material density. These two factors also lead to a lower measured surface area and pore volume with BET measurement.<sup>47</sup>

In all, with the introduction of gold sol, there simultaneously exist two factors affecting, in an opposite way, the porosity of the composite materials. One, as described above, results from co-templates, which increase the total pore surface area. The other factor is “the presence of gold” that reduces the surface area. The outcome depends on the compromise of these two factors: at low gold content, the pore surface area reduced by the gold coating is compensated, or even overcome, by the co-templating effect. As a result, the composite materials persist in a relatively high surface area and pore volume. While as gold content increases, the co-template effect gradually becomes negligible, giving rise to decreased surface area. To confirm the co-templating effect, a control sample without DBTA, GS0-50, was prepared only with the gold sol (50 wt % of the weight of TEOS, corresponding to 17.4 wt % gold in composite) and a pre-hydrolyzed silica sol. The nitrogen sorption measurement shows that in spite of shifting to a lower adsorbed volume, the isotherm of GS0-50 (Figure 4-2) still resembles a type IV pattern with a small H2 hysteresis loops at  $P/P_0$  of  $\sim 0.7$ , which is indicative of certain porosity. Compared with sample prepared only using DBTA as template (i.e., GS50-0), this control sample templated only by gold-sol (i.e., GS0-50) shows a slightly larger pore diameter. This explains the trend that the pore diameter for all nanocomposites tend to increase as the gold sol concentration is increased, even though with the introduction of gold particles pore diameter of the composites is over all smaller than the gold-free sample (GS50-0).

The Barrett-Joyner-Halenda (BJH) pore size distribution curves derived from desorption branches of the nitrogen isotherms are shown in Figure 4-3. With differential volumes plotted against pore diameter, the curves indicate a relatively narrow pore size distributions with a peak pore diameter centered at 3-4 nm for all DBTA templated samples. The control sample prepared only with gold sol exhibit a broad pore size distribution ranging from 3 to 7 nm. The pore size distribution derived from the desorption branch of a type IV isotherm with a H2 hysteresis loop is usually believed to be associated with the size distribution of the narrow neck of pores with “ink bottle” shape. It is now more recognized that this may be over-simplified and the role of network effect should be taken into consideration when interpreting the pore shape and size derived from isotherm measurement.<sup>48</sup> Despite of the complexity and the uncertainty in using the gas sorption measurement to determine the pore size and distribution, this method still provides us a good perception of the pore structures of the sample materials. The pore diameter derived from the BJH method has been found in favorable agreement with those values obtained from XRD and the TEM images.

With some variation in the peak intensity, all the mesoporous gold-silica samples exhibit similar powder XRD profile, which is exemplified by sample GS50-10 in Figure 4-4. The XRD pattern shows an intense peak at a  $d$  spacing of 6.3 nm along with a broad shoulder at low angle range. A broad diffraction peak centered at  $2\theta$  of  $21^\circ$  was observed at high angle range. This pattern is characteristic of a mesophase with a porous structure lacking long-range order, which is reminiscent of the disordered worm-like mesoporous

silicas prepared by nonsurfactant templating.<sup>44-46,49</sup> The analogous XRD patterns were also observed from some mesoporous materials obtained with neutral and cationic surfactant templates.<sup>50-54</sup> In the worm-like porous structure,  $d$  spacing obtained from XRD could be approximated as the repeating distance from one layer of silica wall to the next layer of silica wall crossing a mesopore space. From the difference of the repeating distance (6.3 nm) and the pore diameter (3.0 nm), the thickness of pore wall can be estimated as 3.3 nm, which is comparable with those of the mesoporous materials prepared by non-ionic surfactant templating route,<sup>55,56</sup> or cationic surfactant templated multi precursors sol-gel method.<sup>54</sup> The presence of a single broad peak at  $2\theta$  value of  $21^\circ$  in high angle range is associated with the amorphous structure of sol-gel.<sup>44</sup>

The porous structure of the silica matrices and the morphology of the gold particles within the mesoporous composites were further studied using transmission electron microscopy (TEM). As shown in Figure 4-5(a), nearly spherical gold particles with the size varying from 2 to 8 nm in diameter were randomly scattered in the silica porous matrix. In some area the gold particles co-form the pore wall by partially extruding into the pores or by penetrating the pores. The overall composite matrix exhibit a disordered, interconnected, worm-hole like pore structure with an average pore diameter of 3-5 nm. The observed pore structure is similar to those of the mesoporous silica materials prepared with nonsurfactant templates reported in the literature.<sup>44,45,49</sup> As shown in the insert of Figure 4-5(a), the electron diffraction of the gold nanoparticle shows a series of spots symmetrically distributed along concentric rings, which is

indicative of a well-defined crystalline structure. Base on the TEM images analysis, the diameters of most of the gold particles are estimated to be less than 8 nm. The histogram of the gold particle size (Figure 4-5(b)) can be well fit by Gaussian function with a mean particle diameter of 3.8 nm. The gold cluster distributions in the bulk composite materials were studied using an X-ray mapping technique. A series of X-ray elemental mapping images (Figure 4-6) of the as-synthesized samples show that, from a macroscopic view, the gold particles are evenly distributed throughout the composite samples. More densified gold distributions are observed for higher gold content samples. The microscopic studies reveal the porous structure of the composite from a more direct point of view.

The annealed gold-silica nanocomposites retain a distinctive wine red color, which arises from the surface plasmon resonance (SPR) of gold particles. The UV-visible spectra of as-synthesized composite samples show broad plasmon absorbance peaks at around 520 nm with full width at half max (FWHM) of 160 nm (Figure 4-7). All the spectra are found to be similar. The peak position and the shape are not significantly affected by the gold concentration. The absorption maxima obtained in this work are comparable with reported spectra of nanosized gold particles dispersed in silica aerogel prepared with other methods.<sup>57,58</sup> Though dominated by the particle size, the exact wavelength and shape of the plasmon absorbance maximum are also known to be affected by particle shape, orientation and the environment.<sup>38-42,59-63</sup> Therefore, the presence of such a well-defined plasmon absorption not only reveals the size scale of

gold particles in the nanocomposites, but also contributes to some other morphological information: the colloidal gold particles in the composites are more likely to be confined in the pore cages, or if co-forming the pore wall with silica, they are more likely to be exposed to the pore surface rather than embedded in the silica matrices.<sup>37</sup>

#### **4.4. Conclusions**

In this paper we have presented a facile synthesis of mesoporous gold-silica nanocomposites through a one-step sol-gel reaction. Using nonsurfactant compound DBTA as pore structure directing template, the synthesis process is environment friendly and convenient. The versatility of this method for preparing nanocomposite can be demonstrated with a various selection of nonsurfactant compounds and colloidal nanoparticles. The pore size and pore structure of the nanocomposite are able to be fine-tuned by varying the amount of template or using different template compounds. Here, with DBTA as a nonsurfactant template and a gold sol as the source of metal nanoparticles, mesoporous gold-silica nanocomposites have been successfully prepared with this method. Gold particles with the size of 2-8 nm were dispersed throughout the porous silica matrices. With a gold load as high as up to 10 wt %, the composite materials exhibit mesoporosity with a large surface area, a big pore volume, and relatively narrow pore size distributions. The mesoporous silica matrices show little effect upon the optical characteristics of gold nanoparticles. Surface plasmon resonance spectra of the gold-silica nanocomposites resemble typical plasmon absorption of gold particles with similar size



(i.e., 2-50 nm). Combining both high porosity of the silica framework and the unique physical/chemical properties (such as conductivity, optical behavior and so forth) of the second material phase, nanosized gold particles, the mesoporous gold-silica nanocomposite materials are potentially useful for sensors and catalysts. The promising application of using these novel nanocomposites to detect the chemical contaminant cyanide and other agents with surface-enhanced Raman spectroscopy is currently under active investigation. The preliminary results show that with the gold nanoparticles containing silica samples, the limiting detected concentration of cyanide ion in aqueous solution can go down to 10 ppm. The systematic results of this chemical sensing application study will be reported separately.

#### **4.5. Acknowledgments**

I am grateful to US Army Research Office (ARO) and Army Research Laboratory (ARL) for the support of this project. I thank Mr. David J. von Rohr of Drexel University for his assistance in energy dispersive X-ray elemental analysis and X-ray mappings. I also acknowledge Dr. Jiebin Pang at Peking University for his help with some of the TEM measurements.

#### **4.6. References**

1. Feng, Q. *Novel Organic-Inorganic Hybrid Mesoporous Materials and Nanocomposites*; Ph.D. Dissertation, Drexel University, 2001.

2. Y. Wei; Q. Feng; S. Cheng; K.-Y. Qiu; J.-B. Pang; R. Yin; K. Ong, *Macromolecules* submitted.
3. Green T, and Russell R. *The Gold Companion - The A-Z of Mining, Marketing, Trading and Technology*. Rosendale Press Ltd: Great Britain, 1991.
4. World Wide Web presentation of Chemicool Periodic Table is © Copyright 1996-99 by David D. Hsu.
5. Kozuka, H.; Hashimoto, T.; Uchino, T.; Yoko, T. *ICR Annu. Rep.* **1996**, 1995/2, 22.
6. Takahiro, K.; Kunitatsu, A.; Nagata, S.; Yamaguchi, S.; Yamamoto, S.; Aoki, Y.; Naramoto, H. *Nuclear Instruments & Methods in Physics Research, Section B: Beam Interactions with Materials and Atoms* **1999**, 152, 314.
7. El-Kouedi, M.; Foss, C. A. Jr. *J Phys Chem B* **2000**, 104, 4031.
8. Voisin, C.; Del Fatti, N; Christofilos, D.; Vallee, F. *J Phys Chem. B* **2001**, 105, 2264.
9. Haruta, M. *Catalysis Surveys from Japan* **1997**, 1, 61.
10. (a) Bharathi, S.; Nogami, M.; Lev, O. *Langmuir* **2001**, 17, 2602, (b) Nogami, M. *Ceram. Trans.* **1998**, 81, 255.
11. Epifani, M.; Carlino, E.; Blasi, C.; Giannini, C.; Tapfer, L.; Vasanelli, L. *Chem. Mater*, **2001**, 13, 1533.
12. Bronstein, L. M.; Polarz, S.; Smarsly, B.; Antonietti, M. *Adv. Mater.* **2001**, 13, 1333.
13. Khushalani, D.; Hasenzahl, S.; Mann, S. J. *Nanosci. Nanotech.* **2001**, 1, 129.
14. Hayakawa, T.; Ono, Y.; Nogami, M. *Proc. SPIE-Int. Soc. Opt. Eng.* **2000**, 3943, 102.
15. Anderson, M. L.; Morris, C. A.; Stroud, R. M.; Merzbacher, C. I.; Rolison, D. R. *Langmuir*, **1999**, 15, 674.
16. Hammer, B.; Nørskov, J. K. *Nature*, **1995**, 376, 238.
17. (a) Haruta, M.; Yamada, N.; Kobayashi, T.; Iijima, S. *J. Catal.* **1989**, 115, 301. (b) Haruta, M. *Catal. Today* **1997**, 36, 153.
18. Haruta, M. *Physics and Chemistry of Clusters, Proceedings of Nobel Symposium*, **2000**, 117, 99.

19. Hayashi, T.; Tanaka, K.; Haruta, M. *J. Catal.* **1998**, *178*, 566.
20. Bamwenda, G. R.; Tsubota, S.; Nakamura, T.; Haruta, M. *Cata. Lett.* **1997**, *44*, 83.
21. Tsujino, T.; Kawazu, M.; Maeda, K. *J. Sol-Gel Sci. Technol.* **2000**, *19*, 825.
22. Hayakawa, T.; Ono, Y.; Nogami, M. *Proc SPIE-Int. Soc. Optic. Eng.* **2000**, *3943*, 102.
23. Perner, M.; Bost, P.; Lemmer, U.; von Plessen, G.; Feldmann, J.; Becker, U.; Menning, M.; Schmitt, M.; Schmidt, H. *Phys. Rev. Lett.* **1997**, *78*, 2192.
24. Chen, W.; Cai, W. P.; Liang, C. H.; Zhang, L. D. *Mate. Res. Bull.* **2001**, *36*, 335.
25. Shipway, A. N.; Katz, E.; Willner, I. *Chem. Phys. Chem.* **2000**, *1*, 18.
26. Tanahashi, I.; Tohda, T. *J. Am. Ceram. Soc.* **1996**, *79*, 796.
27. Anderson, M. L.; Rolison, D. R.; Merzbacher, C. I. *Proc. SPIE-Int. Soc. Opt. Eng.* **1999**, *3790*, 38.
28. Lombardi, J. R.; Birke, R. L. *Surface Enhanced Raman Spectroscopy, In Techniques for Characterization of Electrodes and Electrochemical Processes*, Varma, R.; Selman, J. R., ed., John Wiley & Sons, New York, 1991.
29. García-Vidal, F. J.; Pendry, J. B.; *Phys. Rev. Lett.* **1996**, *77*, 1163.
30. (a) Akbarian, F.; Dunn, B. S.; Zink, J. I. *J. Raman Spec.* **1996**, *27*, 775. (b) Akbarian, F.; Dunn, B. S.; Zink, J. I. *J. Phys. Chem.* **1995**, *99*, 3892.
31. Murphy, T.; Schmidt, H.; Kronfeldt, H.-D. *Proc. SPIE-Int. Soc. Opt. Eng.* **1997**, *3107*, 281.
32. Bharathi, S.; Nogami, M. *Analyst* **2001**, *126*, 1919.
33. Lee, Y.-H.; Farquharson, S.; Kwon, H.; Shahriari, M.; Rainey, P. *SPIE-Int. Soc. Opt. Eng.* **1999**, *3537*, 252.
34. Claus, P.; Brueckner, A.; Mohr, C.; Hofmeister, H. *J. Am. Chem. Soci.* **2000**, *122*, 11430.
35. Rath, A.; Aceves, E.; Mitome, J.; Liu, J.; Ozkan, U. S.; Shore, S. G. *J. Molecular Catalysis A: Chemical* **2100**, *165*, 103.

36. Valden, M.; Lai, X.; Goodman, D. W. *Science* **1998**, *11*, 1647.
37. De, G. J. *Sol-Gel Sci. Technol.* **1998**, *1*, 289.
38. (a) Scott, B. J.; Wirnsberger, G.; Stucky, G. D. *Chem. Mater.* **2001**, *13*, 3140. (b) Innocenzi, P.; Brusatin, G.; Martucci, A.; Urabe, K. *Thin Solid Films* **1996**, *279*, 23.
39. Li, T.; Moon, J.; Morrone, A. A.; Mecholsky, J. J.; Talham, D. R.; Adair, J. H. *Langmuir* **1999**, *15*, 4328.
40. Martino, A.; Yamamaka, S. A.; Kawola, J. S.; Loy, D. L. *Chem. Mater.* **1997**, *9*, 423.
41. Sakka, S.; Kozuka, H. *J. Sol-Gel Sci. Technol.* **1998**, *13*, 701.
42. Chen, W.; Cai, W. P.; Liang, C. H.; Zhang, L. D. *Mater. Res. Bull.* **2001**, *36*, 335.
43. Whilton, N. T.; Berton, B.; Bronstein, L.; Hentze, H. P.; Antonietti, M. *Adv. Mater.* **1999**, *11*, 1014.
44. Wei, Y.; Jin, D.; Ding, T.; Shih, W.-H.; Liu, X.; Cheng, S. Z. D.; Fu, Q. *Adv. Mater.* **1998**, *4*, 313.
45. Wei, Y.; Xu, J.; Dong, H.; Dong, J.; Qiu, K.; Jansen-Varnum, S. A. *Chem. Mater.* **1999**, *11*, 2023.
46. (a) Pang, J. B.; Qiu, K. Y.; Wei, Y.; Lei, X.; Liu, Z. F. *Chem. Comm.* **2000**, *6*, 477. (b) Pang, J. B.; Qiu, K. Y.; Wei, Y. *Chem. Mater.* **2001**, *14*, 2361.
47. Gregg, S. J.; Sing, K. S. W. *Adsorption, Surface Area and Porosity*, 2<sup>nd</sup> ed.; Academic: London, 1982.
48. (a) Lee, C. K.; Chiang, A. S. T.; Tsay, C. S. *Key Engineering Materials* **1995**, *115*, 21. (b) Sing, K. S. W.; Everett D. H.; Haul, R. A. W.; Moscou, L.; Pierotti, R. A.; Rouqu erol, J.; Siemieniewska, T. *Pure & Appl. Chem.* **1995**, *57*, 603.
49. Polarz, S.; Smarsly, B.; Bronstein, L.; Antonietti, M. *Angew. Chem. Int. Ed.* **2001**, *40*, 4417.
50. Tanev, P. T.; Pinnavaia, T. J. *Science* **1995**, *267*, 865.
51. Bagshaw, S. A.; Prouzet, E.; Pinnavaia, T. J. *Science* **1995**, *269*, 1242.
52. Ryoo, R.; Kim, J. M.; Ko, C. H.; Shin, C. H. *J. Phys. Chem.* **1996**, *100*, 17718

53. Qi, L.; Ma, J.; Cheng, H.; Zhao, Z. *Chem. Mater.* **1998**, *10*, 1623.
54. Joo, J.; Hyeon, T.; Hyeon-Lee, J. *Chem. Comm.* **2000**, *16*, 1487.
55. Prouzet, E.; Pinnavaia, T. J. *Angrw. Chem. Int. Ed.* **1997**, *36*, 516.
56. Zhao, D.; Huo, Q.; Feng, Chmelka, B. F.; Stucky, G. D. *J. Am. Chem. Soc.* **1998**, *120*, 6024.
57. Smith, D. D.; Sibille, L. *J. Poro. Mater.* **2000**, *7*, 499.
58. Anderson, M. L.; Rolison, D. R. *Proc. SPIE-Int. Soc. Opt. Eng.* **1999**, *3790*, 38.
59. Doremus, R. H.; Rao, P. *J. Mater. Res.* **1996**, *11*, 2834.
60. Heilweil, E. J.; Hochstrasser, R. M. *J. Chem. Phys.* **1985**, *82*, 4762.
61. Khlebtsov, N. G.; Bogatyrev, V. A.; Dykman, L. A.; Mellnikov, A. G. *Optics and Spectroscopy* **1996**, *80*, 113.
62. Kozuka, H. *Proc. SPIE-Int. Soc. Opt. Eng.* **1997**, *3136*, 304.
63. Bloemer, M. J.; Haus, J. W.; Ashley, P. R. *J. Opt. Soc. Am.* **1990**, *B7*, 790.

Table 4-1. Compositions and pore parameters of the gold-silica composite samples prepared in the presence of 50 wt % DBTA template (i.e., GS50- samples) or without DBTA template (i.e., GS0-50 sample).

sample code <sup>a</sup>	Gold (wt %) <sup>b</sup>		S <sub>BET</sub> (m <sup>2</sup> /g)	V <sub>PORE</sub> (cm <sup>3</sup> /g)	D <sub>BJH</sub> (nm)	micropore vol. (cm <sup>3</sup> /g) <sup>c</sup>
	Before extrac.	After extrac.				
GS50-0	0.0	0.0	596	0.48	3.6	0.08
GS50-10	6.9	5.9	629	0.42	3.0	0.07
GS50-20	10.1	7.8	573	0.39	3.1	0.09
GS50-25	11.4	11.4	212	0.17	3.5	0.03
GS0-50	17.4	15.8	108	0.13	4.2	-

<sup>a</sup> The numerical figure in the sample code denotes the DBTA template concentration (wt % of silica dioxide and template in the final dry product, excluding gold content) and gold sol content (wt % of TEOS) in the starting materials, respectively. <sup>b</sup> Average values calculated based on EDX elemental analysis taken at 4 different areas of each sample after the calcination. <sup>c</sup> Values determined from the *t*-plot analysis.

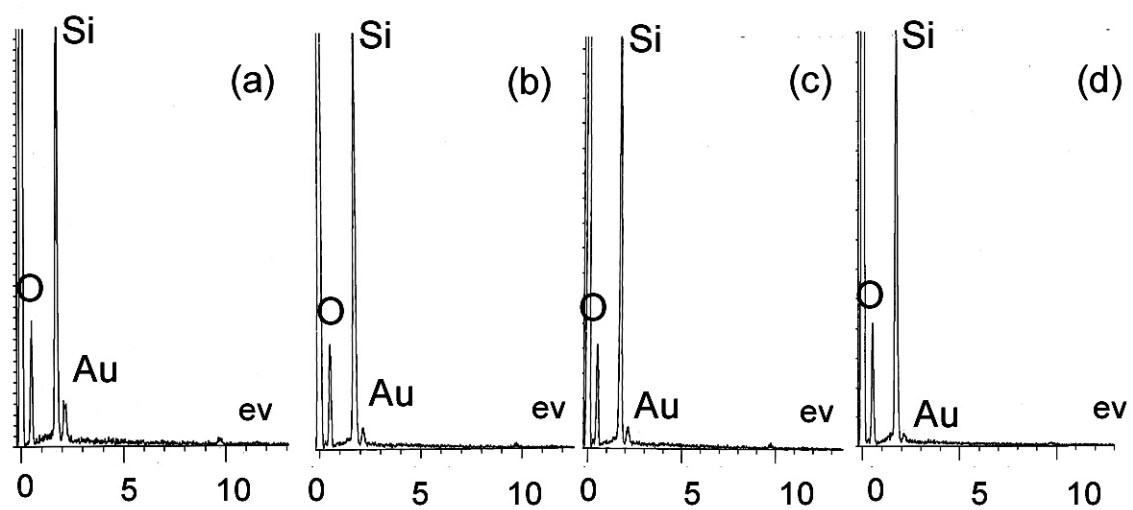


Figure 4-1. Representative X-ray energy dispersive spectra for gold-silica nanocomposite.

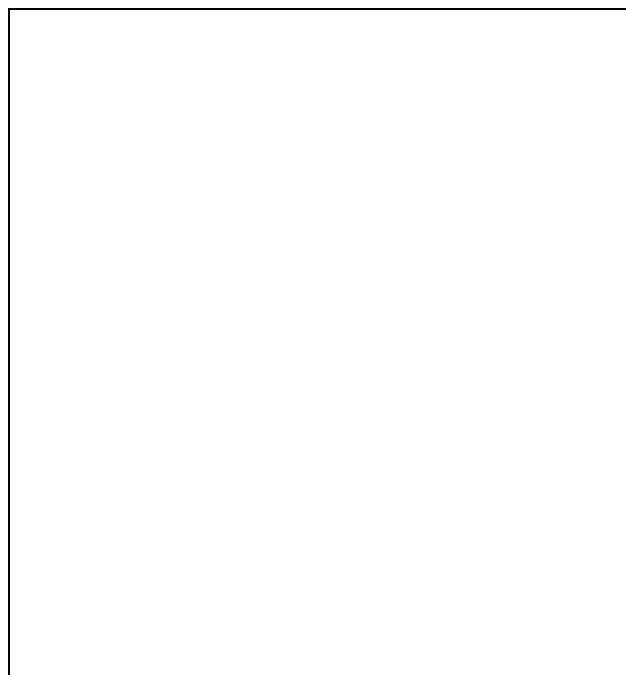


Figure 4-2. N<sub>2</sub> adsorption–desorption isotherms at –196 °C for the annealed gold-silica nanocomposite samples with varied gold content after removal of DBTA template.



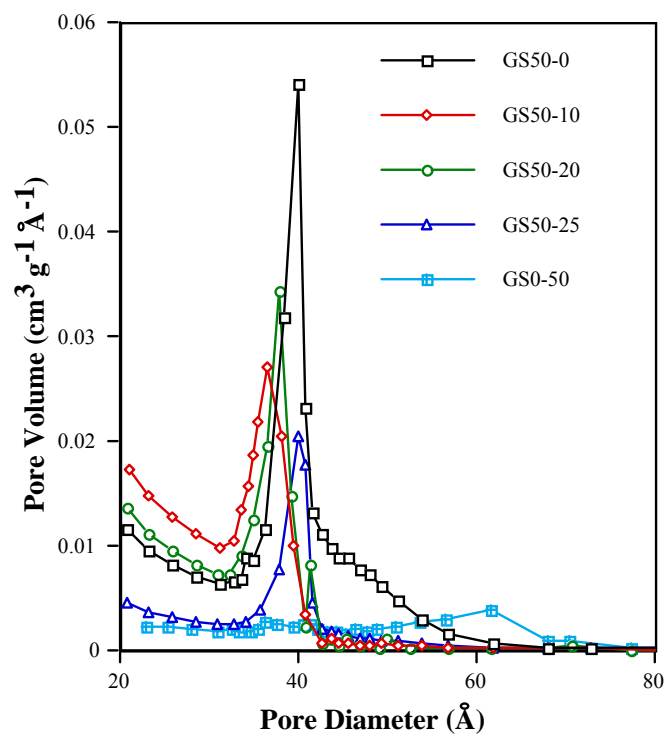


Figure 4-3. BJH pore size distribution curves of the mesoporous gold-silica nanocomposite derived from desorption isotherm branches.

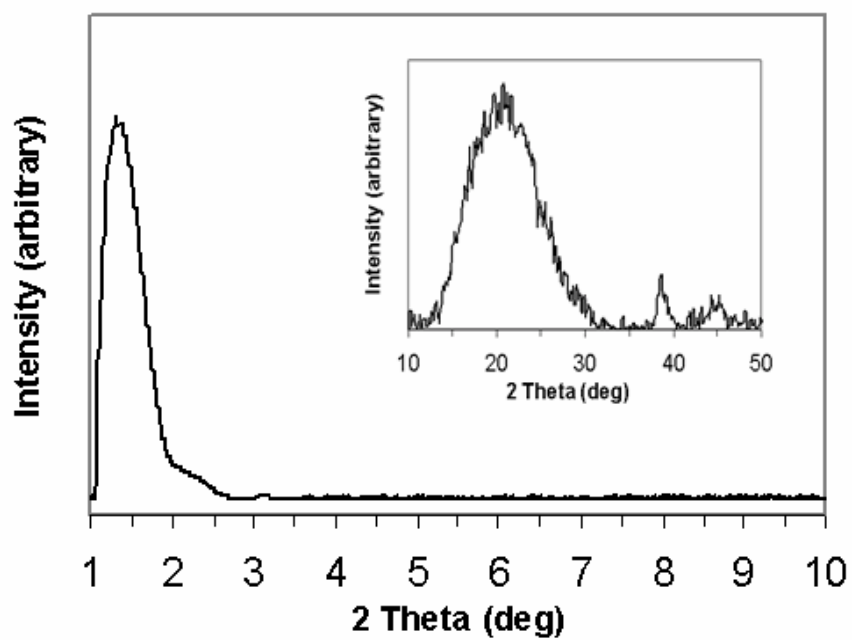


Figure 4-4. Powder XRD patterns for the mesoporous gold-silica nanocomposite sample GS50-10.

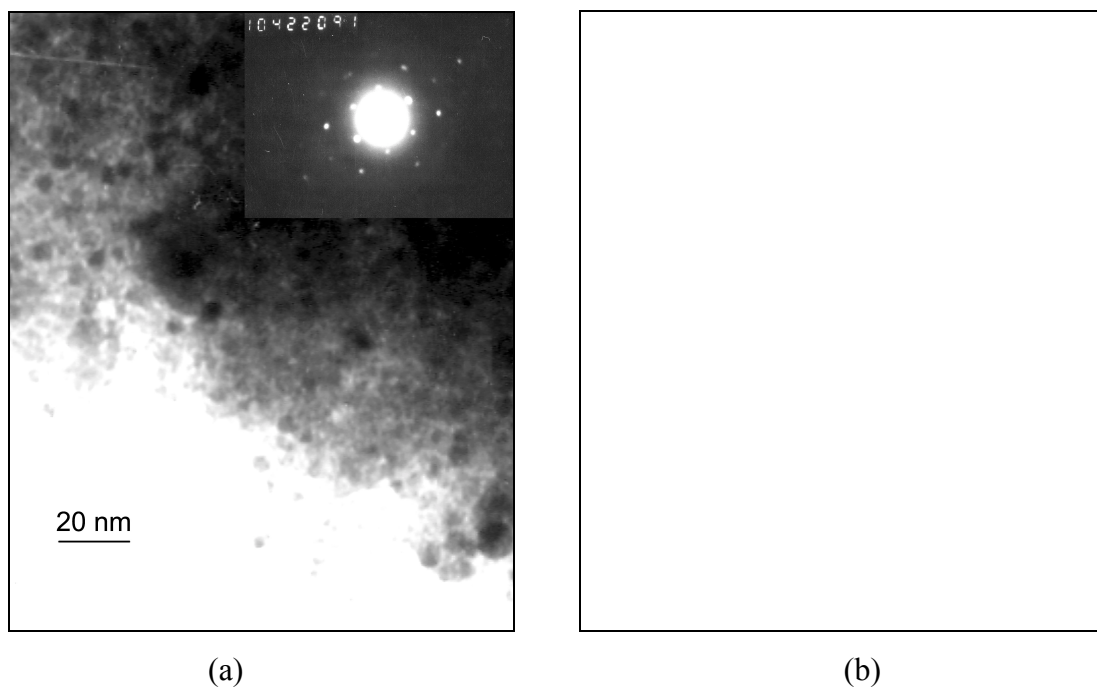


Figure 4-5. (a) Representative TEM image of mesoporous gold-silica nanocomposite sample (GS50-10). The darkest round spots are gold nanoparticles. The gray framework feature is silica matrix with inter-connected wormlike pores. Insert: an electron diffraction pattern of gold nanoparticles in the same sample. (b) Size distribution histogram of the gold particles dispersed in the mesoporous composite sample shown in (a) with Gaussian curve fitted to the data. About 300 particles sampled from 5 different areas based on TEM images were employed for this estimation. The presence of some gold particles (less than 0.3%) with apparent diameters greater than 8 nm might be attributed to aggregation of gold nanoparticles or overlapping images of particles because of the sample thickness.

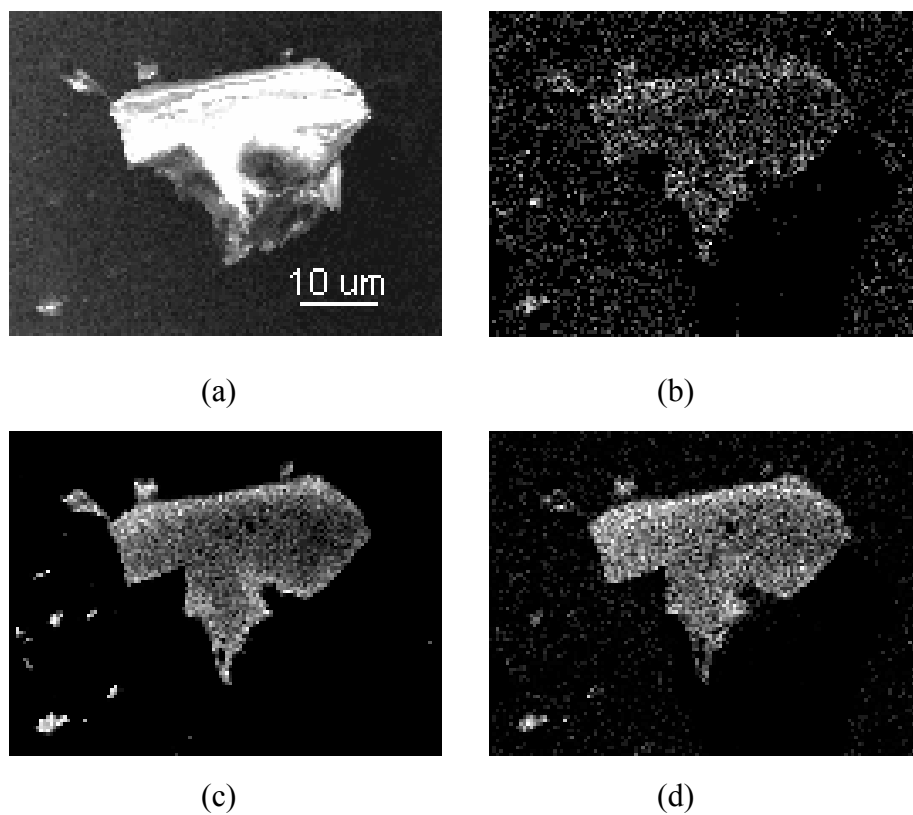


Figure 4-6. A series of X-ray mapping images of mesoporous gold-silica nanocomposite containing 25 wt % gold (GS50-25). (a) As-made nanocomposite. (b) Gold mapping. (c) Silicon mapping. (d) Oxygen mapping.

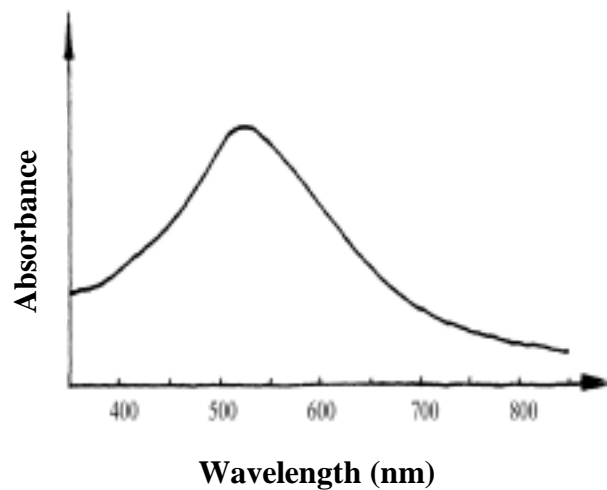


Figure 4-7. Typical solid state UV-Vis reflectance spectrum of mesoporous gold-silica nanocomposite.

## **Chapter 5. Organic-Inorganic Nanocomposite Thin Films Based on Arrays of Vinyl Modified Silica Nanoparticles**

### **5.1. Introduction**

Organic-inorganic nanocomposite synthesis, developed based on combining both organic and inorganic components at the nanometer scale, is an innovative route to advanced materials.<sup>1-3</sup> More recently, using specially designed functional organic or inorganic materials, organized nanocomposite films have been fabricated for novel electronics and optics applications.<sup>4,5</sup> In this study, organic-inorganic nanocomposite thin films have been fabricated on mica, glass slides and graphite surfaces by solution casting and self-assembly of vinyl modified silica nanoparticles followed by an in-situ photo-initiated free radical polymerization. The obtained nanocomposite thin films were studied for their composition, morphology and layer ordering behavior. The studies involved the use of spectroscopic and microscopic methods, such as IR spectroscopy, electron microscopy and atomic force microscopy (AFM). These films are of interest because of their possible optics and barrier coating applications. Also, knowledge of arrangement of organic functionalized inorganic nanoparticles on the substrate provides us insight of fundamental mechanisms involved in the formation of the nanostructured composite and has practical importance for engineering the materials with advanced interfacial properties.

### **5.1.1. Organic-Inorganic Nanocomposite: Opportunities to Advanced Materials**

Conventionally, organic-inorganic composite materials are frequently prepared by the mechanical blending of polymers and glass fibers or other inorganic materials to improve mechanical and optical properties, or compensate the unfavorable properties of each other.<sup>6</sup> For example, the properties of a gas barrier of weather proofing of organic materials will be improved by adding inorganic fillers,<sup>7</sup> and the flexibility and impact strength of an inorganic material can be enhanced when hybridized with polymers.<sup>8</sup> The overall properties of a composite material depend not only on the nature of each component, but also on the interfacial phase morphology of the composite. In the classical physically blended composites, the organic and inorganic components are not dispersed homogeneously at the microscopic level. Due to the organic-inorganic thermodynamic incompatibility, mechanical failure occurs often at macroscopic interfaces between the inorganic filler and organic matrices. In addition, optical properties such as transparency of either inorganic component or polymers may not be maintained due to the large domain size. Nanocomposites have attracted more and more attention in the field of advanced materials research, due to their potentials to solve these interfacial problems, as well as to develop innovative materials for promising applications including optics, electronics, mechanics, biology and others. This new class of materials has been developed based on organic and inorganic species combined at a nanoscale level. Usually, the composite materials with at least one phase below 100 nm are considered as nanocomposites.<sup>9</sup>

Nanometer scale phases provide materials with increased interfacial interactions. The materials have a high degree of interpenetration between the two dissimilar phases. As a result of this high degree of mixing, the ordinarily sharp interfacial zone will be blurred and a continuum of the structure and the properties of organic and inorganic components could be achieved. Many interesting materials have been prepared with improved optical and mechanical properties, which can be tuned between those of glass and those of polymers to meet a variety of application demands.<sup>10</sup> Moreover, with the versatile organic and inorganic components, as well as nanosize dependent properties, numerous novel organic-inorganic nanocomposites with unique properties, such as fast photochromic responses,<sup>11</sup> excellent laser efficiency,<sup>12</sup> pH sensibility,<sup>13</sup> and so forth, have been developed and engineered during the past few years.

### **5.1.2. Organic-Inorganic Nanocomposite Based on Core-Shell Nanoparticle Arrays**

Various synthetic routes have been developed to prepare organic-inorganic nanocomposites.<sup>14-16</sup> The organic component can be introduced as (i) a monomer, (ii) a polymer (in molten, solution, or emulsion states.), or (iii) a pre-formed organic network. The inorganic part can be introduced as (i) a monomer (e.g., a metal alkoxide), (ii) pre formed particles, fibers or plates, or (iii) an existed porous matrix.<sup>9</sup> In this study, we use a monomer (specifically, 2-hydroxyethyl methacrylate) as organic resource and a preformed vinyl modified silica nanoparticles as inorganic species to prepare nanocomposite with covalent bond between organic and inorganic phases.



We are also interested in the possibility of assembling the monodispersed organic/inorganic domains in an organized fashion. Nanocomposites with such periodic structure and modulation of mechanical, optical or magnetic properties have potential applications in display devices, microelectronics, data storage and nonlinear optics.<sup>17-20</sup> Among others, some frequently used techniques to organize nanoparticles into ordered macroscopic structure include the Langmuir-Blodgett technique,<sup>21,22</sup> self-assembly,<sup>23</sup> chemical vapor deposition,<sup>24</sup> and microcontact printing.<sup>25</sup> Recently, there have been several reports on the production of nanocomposites based on assembling of colloidal particles with a core-shell structure.<sup>26</sup> Based on a sequential adsorption method, Caruso *et al.* reported the alternating silica nanoparticles and poly(diallyldimethylammonium chloride) composite layers on polystyrene latex spheres.<sup>27</sup> The array of the modified particles exhibits hexagonally close packing. Ordered three-dimensional polymer nanocomposites have been fabricated by Kumacheva and coworkers with core-shell structured latex particles.<sup>28</sup> In their method, the particles were assembled into three-dimensional cylinder by particle sedimentation and solvent evaporation. Then a heat treatment of the particle compact was applied leading to flow of shells and formation of nanocomposite polymer. In these studies, the particles used were in submicrometer size. The nanocomposite based on array of particle with nanometer size is still under active studies.

In this study, a solution casting process and a photo-initiated polymerization were adapted to fabricate organic-inorganic nanocomposite thin films using pre-formed

organic modified silica nanoparticles. The self-assembling behavior of these particles on different substrate surface was studied. Using the same technique, the self-assembling of mesoporous silica nanoparticles was also demonstrated.

## **5.2. Experimental**

### **5.2.1. Materials**

Highlink OG100<sup>TM</sup>, silica nanoparticles with surface modification of 2-hydroxyethyl methacrylate (HEMA), was provided by Clariant Corporation. Benzil (Aldrich), butyl alcohol (BuOH, 99.8%, Aldrich), hydrogen peroxide solution (H<sub>2</sub>O<sub>2</sub>, 50 wt%, Fisher), sulfuric acid (H<sub>2</sub>SO<sub>4</sub>, 98.08%, Corco Chemical Corp.) were all used as received without further purification. Three different substrates were used for film casting: Pelco mica sheets (Ted Pella Inc.), glass micro-slides (Gold-seal<sup>®</sup>, Becton, Dickinson and Company) and graphite (Structure Probe Inc.).

Mesoporous silica particles with diameter of ~420 nm were synthesized with methods previously described in Section 3.2.2.

### **5.2.2. Treatment of Substrate Surface**

Before film casting, microscope slide, mica and graphite were pre-treated. The microscope slide was ultrasonically washed with acetone, followed with a freshly prepared mixture of H<sub>2</sub>SO<sub>4</sub> and H<sub>2</sub>O<sub>2</sub> at a volume ratio of 4:1. The pre-cleaned slide was then rinsed thoroughly with deionized distilled water and dried at room temperature. For

mica and graphite, the top layer was peeled off with scotch tape to provide a fresh and smooth surface ready for the film casting.

### **5.2.3. Arrays of Vinyl Monomer Modified Silica Nanoparticles and Preparation of Nanocomposite Thin Films**

The experimental setup was adopted from that for assembling polymer latex nanospheres by solution casting technique.<sup>29,30</sup> The nanocomposite thin films were prepared with solution casting technique. For a typical procedure to prepare thin films on mica surface, 1.00 g of silica nanoparticle/HEMA suspension (30 wt %) was diluted with distilled deionized water to a concentration of  $10^{-5}$  wt %. As photo-polymerization initiator, benzil solution containing 0.007 g benzil (1 wt % of the monomer) in 0.1 g of water was added into the nanoparticle suspension. With a variable volume micropipette, 20  $\mu$ l dilute suspension was withdrawn and spread on the pre-cleaned substrate. The substrate was set in a preparation box, which was kept in an ice bath. A low-temperature assembling environment was adopted to reduce the rate of the solvent evaporation and Brownian motion of the nanoparticles. In the preparation box, a 25 ml beaker filled with water was placed in order to maintain a constant vapor pressure in the preparation box and ensure a low evaporation rate of the solvent from nanoparticles suspension. With casting solution on it, the substrate was kept in preparation box for about 24 h without disturbance. During this time, transparent silica nanoparticle/HEMA thin film was formed by solvent evaporation and array of the vinyl modified silica particles.

To obtain nanocomposite thin film with chemical bond between organic (i.e., PHEMA) and inorganic phase (i.e., silica nanoparticles), the pre-assembled film with the substrate was placed into a photochemical reactor to initiate a free radical polymerization of HEMA monomer. Pure PHEMA thin film, a control sample polymerized from HEMA monomer, was prepared under the identical conditions. Reaction kinetics of the polymerization was monitored by means of FT-IR spectroscopy by taking out the samples from the reactor at different time intervals.

The arrays on graphite substrate were attempted with similar procedure except that BuOH was used as solvent to prepare diluted suspension.

#### **5.2.4. Arrays of Porous and Nonporous Silica Nanoparticles**

Arrays of porous and nonporous silica particles synthesized in our laboratory were studied with the similar setup and procedures. Particles were dispersed in water (0.02 wt %) and assembled on glass. The environment conditions remained the same as that described in Section 5.2.3.

#### **5.2.5. Instrumentation and Characterization**

Photo-initiated polymerization was carried out in a Rayonet<sup>TM</sup> Srinivasan-Griffin photochemical reactor. Infrared spectra of KBr powder-pressed pellets were recorded on a Perkin-Elmer Model 1600 FTIR spectrophotometer. Atomic force microscopy images were obtained with Microscope IIIa scanning probe microscope operated under tapping

mode. Scanning electron microscopy (SEM) was performed on an AMRAY 1830 microscope, with an accelerating voltage of 20 kV. The samples were gold-coated before the SEM characterization. Energy dispersive X-ray elemental (EDX) analysis was conducted with an EDX interfaced AMRAY 1830 scanning electron microscope operated at an accelerating voltage of 5 kV. The samples were deposited on aluminum sample holders with adhesive carbon tape prior to EDX analysis. Differential scanning calorimetry (DSC) thermograms were obtained on a Perkin Elmer DSC7 (Norwalk, CT) system. Sample weight was 5 mg. All samples were analyzed from 25 °C to 140 °C at a heating rate of 20 °C/min under air atmosphere.

### **5.3. Results and Discussion**

#### **5.3.1. Organic-Inorganic Nanocomposite Thin Films Based on Vinyl Modified Nanoparticle Arrays**

Using pre-formed organic-inorganic nano-phases (i.e., vinyl modified nanoparticles), composite thin films with partially organized organic-inorganic structure in nanometer scale were fabricated based on the arrays of nanoparticles followed by a post photo-polymerization process. The fabrication process was illustrated in Figure 5-1. Highlink OG100<sup>TM</sup> consists in a 30 wt % suspension of spherical silica nanoparticles with the size of about 13 nm in diameter in 2-hydroxyethyl methacrylate (HEMA). The diluted suspension was first applied on the substrate surface by solution casting. During the solvent evaporation, the capillary forces formed between neighboring particles drag

the particles together, leading to particle arrays with a relatively ordered structure. The surface of these silica nanoparticles is functionalized by HEMA, which can be copolymerized with free HEMA in the interstitial space between arrayed particles. After a post-polymerization, a covalent bond between organic and inorganic nanophases is provided, and a nanocomposite thin film with organized structure is obtained as a result.

The typical examples of AFM images of particle arrays on mica surfaces before polymerization are shown in Figure 5-2. The particle arrays spread out on the substrates as interconnected “islands” with domain size of 2-5  $\mu\text{m}$ . The particle arrays covers approximately 70 % of the total deposition area (Figure 5-2(a)). The arrays exhibit multilayer structure of low-dimensional close packing in the center region and partially short-range local ordering around the edge areas. The monolayer array coverage on the total film area is about 10 % (Figure 5-2(b)). Confirmed with depth analysis shown in Figure 5-3, the average thickness of the film in structured area is about 15 nm, which is reasonably close to the diameter of the particles, indicating a monolayer assemble achieved in this area. The formation of multilayer aggregation in the center region is believed to be a result of combined effects of convection force, integral particle force, and the increased suspension hydrophobicity along with water evaporation. After being applied on substrate surface, the particles away from the center region are transferred towards the already aggregated ones by the convection force arising from water evaporation. Due to the small size, the large surface area, and the high number of particle interactions, the integral particle forces per volume unit become very large, (e.g., van der

Waal's forces), the agglomeration occurs as a result of particle attraction. In addition, along with water evaporation, HEMA containing particle suspension becomes more hydrophobic, which may promote the particle aggregation forming multilayered island domains.

The particle arrays on glass slide surface exhibit a similar pattern as on mica surface. Particles arrayed on a hydrophobic graphite surface exhibit a strong tendency to agglomerate. As shown in Figure 5-4, the particles aggregate into strip-like clusters instead of spreading out on substrate surface. No monolayer or obvious ordered structure was observed.

In order to reduce the rate of Brownian motion of the nanoparticles during the polymerization, an *in-situ* photo-initiated polymerization was selected to prepare the covalently bonded organic-inorganic nanocomposites. After polymerization, the monolayer-edge, multilayer-center particle arrays are well retained. As shown in Figure 5-5, the surface of obtained organic-inorganic nanocomposite thin films becomes slightly featureless, indicating the formation of PHEMA nanophases, filling in the interstitial space between inorganic particles. In addition, the improved surface hardness by polymerization of the monomers between the particles results in decrease of the interaction between AFM tip and the surface, which in turn contributes to the apparent increased smoothness from AFM measurement.

The free radical photo polymerization of HEMA with benzil as initiator was monitored by FT-IR spectroscopy. The representative spectra of composite films at

different polymerization time intervals were shown in Figure 5-6. The characteristic bands at  $1720\text{ cm}^{-1}$  and  $1635\text{ cm}^{-1}$  can be attributed to the C=O and C=C stretching, respectively. The peaks at  $1100\text{-}1200\text{ cm}^{-1}$  can be assigned to the Si-O bond. Upon polymerization, the intensity of the C=C double bond peak at  $1635\text{ cm}^{-1}$  should decrease significantly while the carbonyl absorption at  $1720\text{ cm}^{-1}$  should not be affected. Therefore, the relative intensity of C=C band to C=O band can be used to qualitatively evaluate the extent of the polymerization as a function of time. As observed from the spectra, with reaction time increasing, the intensity ratio of these two peaks is decreased. At polymerization time of 12 h, C=C band almost disappears, which indicates a high conversion of polymerization.

After being calcined at  $500\text{ }^{\circ}\text{C}$ , the obtained composite exhibits 20 % weight loss, which provides a good estimation of the organic and inorganic composition in the final composite thin films. This increased inorganic content in the composite film (i.e., 80 wt %), in comparison with that in the casting solution (i.e., 30 wt %), is most likely due to the evaporation of monomer with solvent during assembling process. For the purpose of investigating particle arrays, the suspension is diluted with solvent in this study. Instead, preparation of thin films with higher organic contents is feasible by adding HEMA monomer into the particle suspension. The composition of the nanocomposite sample was analyzed with EDX. A typical spectrum is shown in Figure 5-7 revealing the 1:2 molar ratio of silicon to oxygen as it in  $\text{SiO}_2$ .



A single glass transition temperature ( $T_g$ ) at  $\sim 110$  °C has been detected for PHEMA control sample. However, no well-defined calorimetric glass transitions are observed in the nanocomposite thin films. Absence of  $T_g$  in similar situations has been reported for several composite systems, which has been attributed to the confinement of polymer chains in a small phase domain, thus restricting the large scale cooperative chain segmental motions which is required for glass transition.<sup>31,32</sup> Specifically, DSC measurement may not detect any phase separation at a phase domain smaller than 15 nm.<sup>33</sup> Such absence of well-defined  $T_g$  for PHEMA in the transparent nanocomposites film confirms the formation of nanosized polymer phases confined by closely arranged silica nanoparticles.

### **5.3.2. An Extended Study: Assembly of Monolayer Mesoporous Nanospheres**

Using the similar solvent casting technique and experimental setup, thin films of mesoporous nanospheres prepared with our nonsurfactant templated pathway have been fabricated on glass slide substrate surface.

The representative SEM images are shown in Figure 5-8. The particle assembly exhibits a two-dimensional monolayer structure with relatively large domain size with randomly occurring round voids of submicrometer size. The coverage of monolayers on the total deposition areas is reasonably good ( $\sim 85$  %). The particle arrays display apparently good local order. As revealed by a high magnification SEM image (Figure 5-8(b)), the arrays show small domains of perfect hexagonal order. Based on the image

analysis, the degree of ordering appears to depend mainly on the size distribution of the particles. The order defects occur when the size of particles in the near neighbor region becomes incompatible. The monolayer of mesoporous silica nanoparticles was found quite stable without agglomeration even after storage under ambient conditions for a long period of time (> 60 days).

#### **5.4. Conclusions**

Organic-inorganic nanocomposite thin films have been fabricated on mica, glass slide and graphite surfaces by solution casting and self-assembly of vinyl modified silica nanoparticles followed by an in-situ photo-initiated free radical polymerization. Most areas of the nanocomposite films have multilayer structure of low-dimensional close packing of silica particles, while a portion of the thin films display monolayer particle arrays with short-range local ordering. With this method, nanocomposite thin films can be prepared with high inorganic species (e.g., silicon dioxide) content up to 80 wt %. The obtained transparent films are composed of covalently bonded nanophases of polymer and inorganic particles.

As an extended study, thin films of mesoporous nanoparticles prepared with our nonsurfactant templated pathway have been fabricated. Monolayer self-assembly of particles with short range of well-defined hexagonal order was obtained. The order of particle arrays was found to be size distribution dependent. The thin films fabricated with porous particle are potentially useful for gas sensing applications among others.

## 5.5. Acknowledgments

I want to thank Dr. Guoliang Yang at Department of Physics at Drexel University for his help and valuable discussions with AFM measurements. I thank Ms. Gwenaelle Proust of Department of Materials Engineering at Drexel University for her assistance with DSC measurements. I also thank Clariant Corporation for providing Highlink™ products.

## 5.6. References

1. Denisyuk, I. Y.; Meshkov, A. M. *J. Opti.Tech.* **2001**, *68*, 841.
2. Sayari, A.; Hamoudi, S. *Chem. of Mater.* **2001**, *13*, 3151.
3. Mark, J. E. *Mater. Res. Soc. Sym. Proc.* **2001**, *661*, 1.
4. Sanchez, C.; Lebeau, B. *MRS Bull.* **2001**, *26*, 377.
5. Tsukruk, V. V. *Prog. Polym. Sci.* **1997**, *22*, 247.
6. Okada, A.; Usuki, A. *Mater. Sci. Eng.* **1995**, *C3*, 109.
7. (a) Fredrickson, G. H.; Bicerano, J. *J. Chem. Phys.* **1999**, *110*, 2181. (b) Chang, J.-H.; Park, D.-K.; Ihn, K. *J. Appl. Poly. Sci.* **2002**, *84*, 2294.
8. (a) Ohtsuki, C.; Miyazaki, T.; Tanihara, M. *Mater. Sci. Eng.*, **2002**, *22*, 27. (b) Naik, N. K.; Ramasimha, R.; Arya, H.; Prabhu, S. V.; ShamaRao, N. *Composites* **2001**, *32B*, 565.
9. Hajji, P.; David, L.; Gerard, J. F.; Kaddami, H.; Pascault, J. P.; Vigier, G. *Mater. Res. Soc. Symp. Proc.* **1999**, *576*, 357.
10. Sanchez, C.; Soler-Illia, G. J.; Ribot, F.; Lalot, T.; Mayer, C. R.; Cabuil, V. *Chem. Mater.* **2001**, *13*, 3061.
11. Schaudel, B.; Guerneur, C.; Sanchez, C.; Nakatani, K.; Delaire, J. A. *J. Mater.Chem.* **1997**, *7*, 61.

12. Faloss, M.; Canca, M.; Geoges, P.; Brun, A.; Chaput, F.; Boilot, J. P. *Appl. Opt.* **1997**, *36*, 6760.
13. Rottman, C.; Grader, G.; De Hazan, Y.; Melchior, S.; Avnir, D. *J. Am. Chem. Soc.* **1999**, *121*, 8533.
14. Gomez-Romero, P. *Adv. Mater.* **2001**, *13*, 163.
15. Sanchez, C.; de Soler-Illia, G. J.; Ribot, F.; Lalot, T.; Mayer, C. R.; Cabuil, V. *Chem. Mater.* **2001**, *13*, 3061.
16. Sanchez, C.; Ribot, F.; Lebeau, B. *J. Mater. Chem.* **1999**, *9*, 35.
17. Ozin, G., *Adv. Mater.* **1992**, *4*, 612.
18. Murry, C. *Science* **1995**, *270*, 1335.
19. Lin, S. Y.; Chow, E.; Hietala, V.; Villeneuve, P. R.; Jonnopoulos, J. D. *Science* **1998**, *282*, 274.
20. Kin, S. Y.; Fleming, J. G.; Hetherington, D. L.; Smith, B. K.; Briswas, R.; Ho, K. M.; Sigalas, M. M.; Zubrzycki, W.; Kurtz, S. R.; Bur, J. *Nature* **1998**, *394*, 251.
21. Knobler, Charles M.; Schwartz, Daniel K. *Curr. Opin. Collo. & Inter. Sci.* **1999**, *4*, 46.
22. Motschmann, H.; Mohwald, H. *Handbook App. Sur. Coll. Chem.* **2002**, *2*, 79.
23. Rossignol, F.; Nakata, Y.; Nagai, H.; Okutani, T.; Suzuki, M. *Chem. Mater.* **1999**, *11*, 358.
24. Eastman, J. A.; Choi, U. S.; Soyez, G.; Thompson, L. J.; DiMelfi, R. *J. Mater. Sci. Forum* **1999**, *312*, 629.
25. Gates, B.; Zhong, Z.; Xia, Y. *Mat. Res. Soc. Symp. Proc.* **2000**, *571*, 115.
26. Chainey, M.; Wilkinson, M. C.; Hearn, J. *Makromol. Chem. Suppl.* **1985**, *10*, 435.
27. Caruso, F.; Möhwald, H. *Langmuir* **1999**, *15*, 8276.
28. (a) Kalinina, Olga; Kumacheva, Eugenia. *Macromolecules* **1999**, *32*, 4122. (b) Kumacheva, Eugenia; Kalinina, Olga; Lilge, Lothar. *Adv. Mater.* **1999**, *11*, 231.
29. Rakers, S.; Chi, L. F.; Fuchs, H. *Langmuir* **1997**, *13*, 7121.

30. Dimitrov, A. S.; Nagayama, K. *Langmuir* **1996**, *12*, 1303.
31. Hajji, P.; David, L.; Gerard, J. F.; Pascault, J. P.; Vigier, G. *J. Polym. Sci., B: Polym. Phys.* **1999**, *37*, 3172.
32. Motomatsu, M.; Takahashi, T.; Nie, H.; Mizutani, W.; Tokumoto, H. *Polymer* **1997**, *38*, 177.
33. Schultz, A. R.; Young, A. L. *Macromolecules* **1980**, *13*, 663.

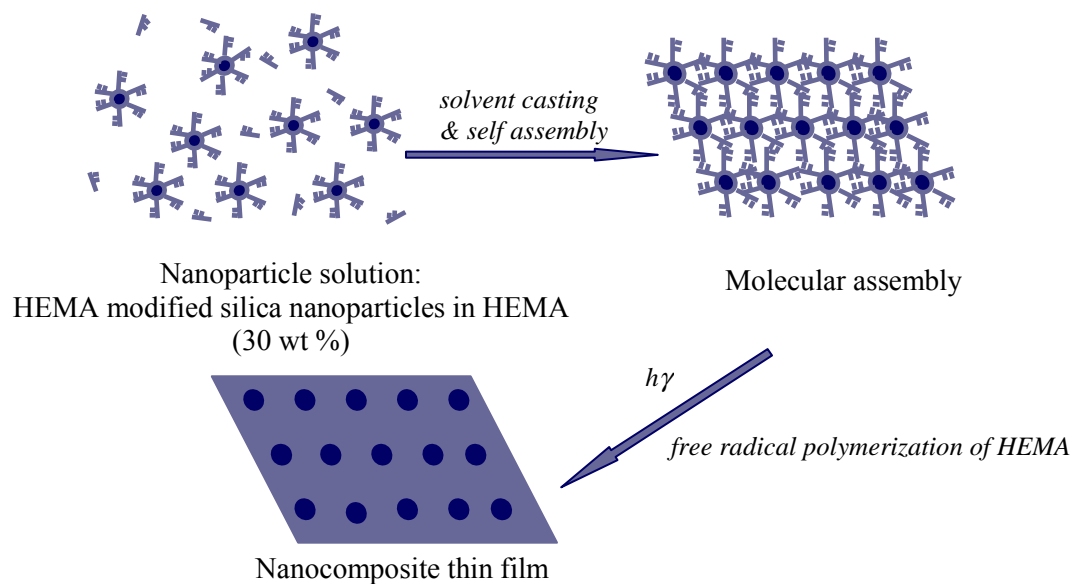
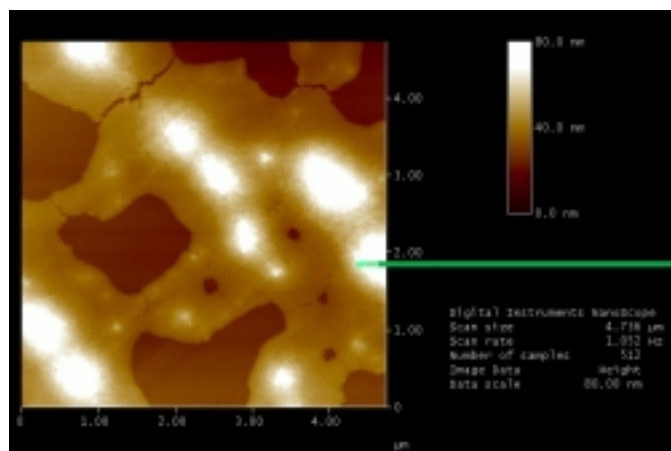
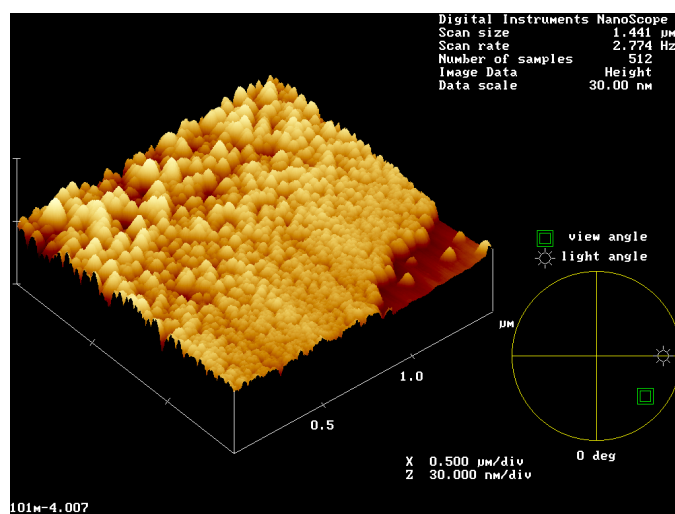


Figure 5-1. Fabrication schematics of organic-inorganic nanocomposite based on self-array of vinyl modified silica nanoparticles.



(a)



(b)

Figure 5-2. Representative AFM images of vinyl modified nanoparticles assembled on mica surface. (a) Interconnected island domains. (b) An edge area with monolayer particle arrays.

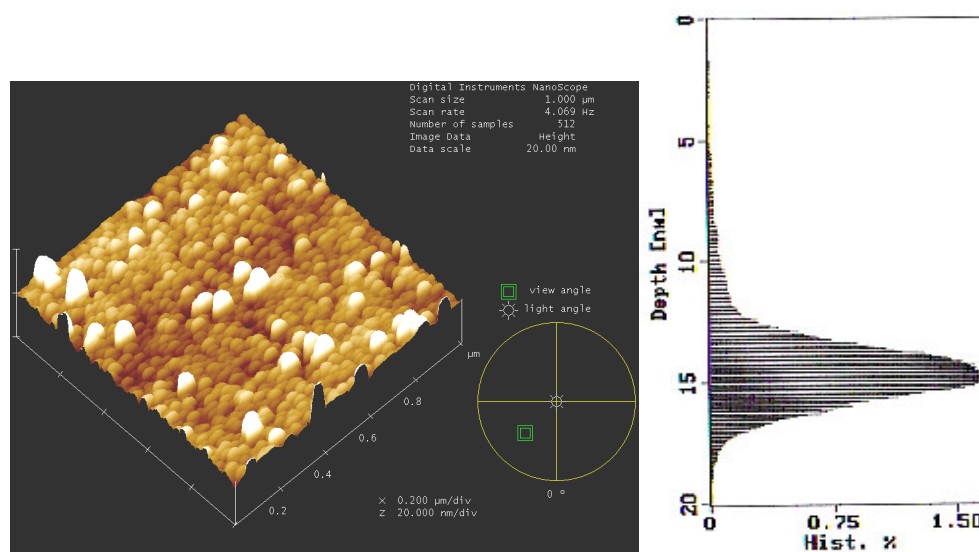


Figure 5-3. Representative AFM image of thin film of monolayer array of vinyl modified silica nanoparticles with short range ordering and the corresponding depth analysis plot.



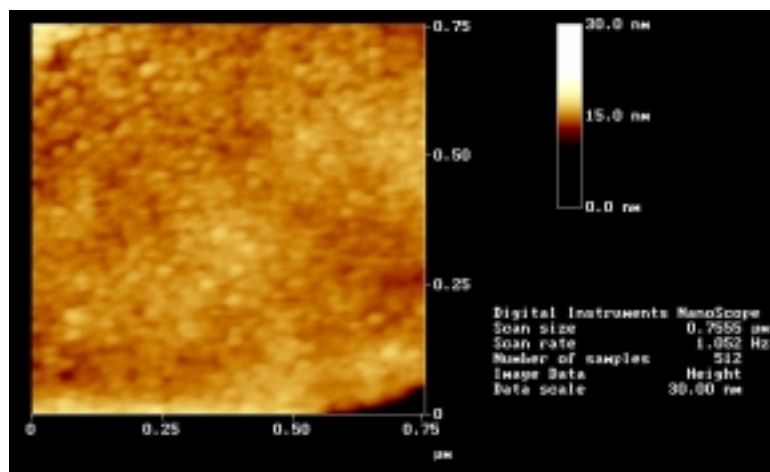


Figure 5-4. Representative AFM image of PHEMA-silica nanocomposite thin film obtained after a photo-initiated polymerization of pre-arrayed vinyl modified silica nanoparticles in HEMA suspension on mica surface.

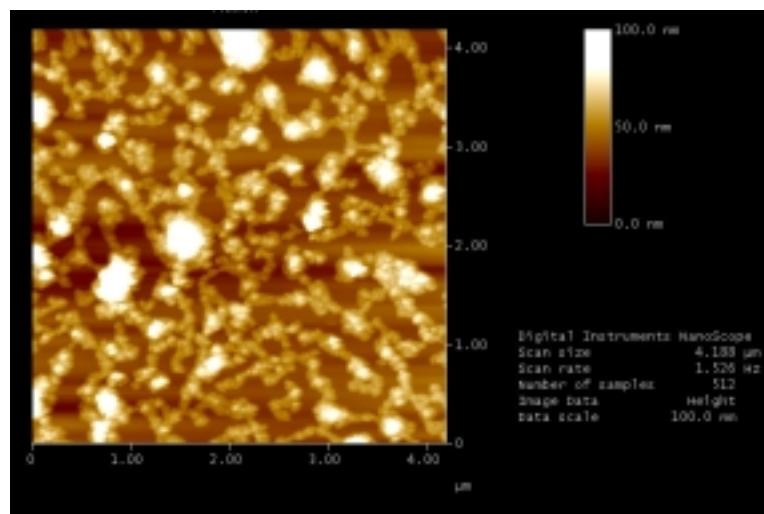


Figure 5-5. Representative AFM images of vinyl-modified silica nanoparticles arrayed on hydrophobic graphite surface.

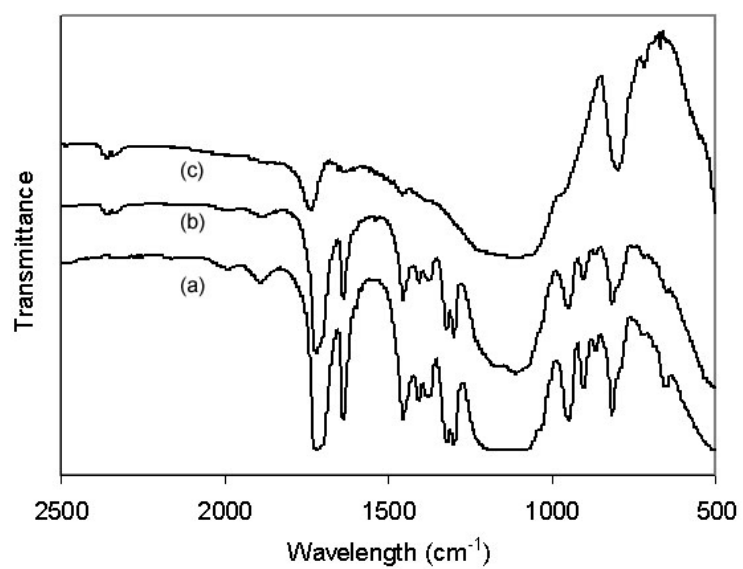


Figure 5-6. Representative IR spectra of nanocomposite thin films polymerized at different time interval: (a) 0 h, (b) 6 h, and (c) 12 h.

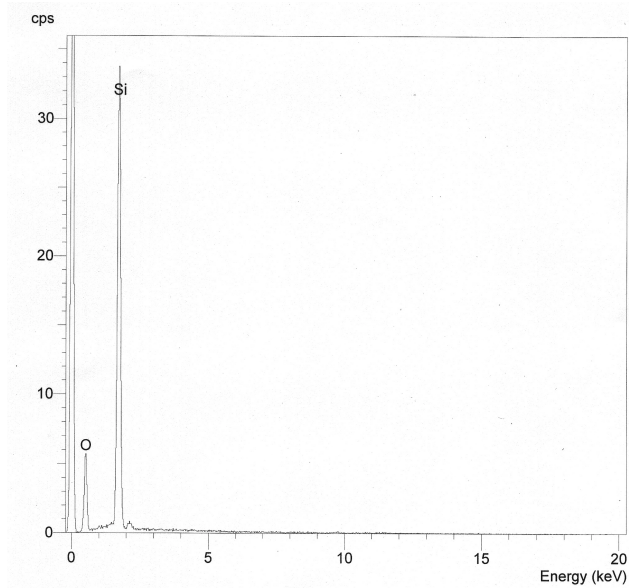
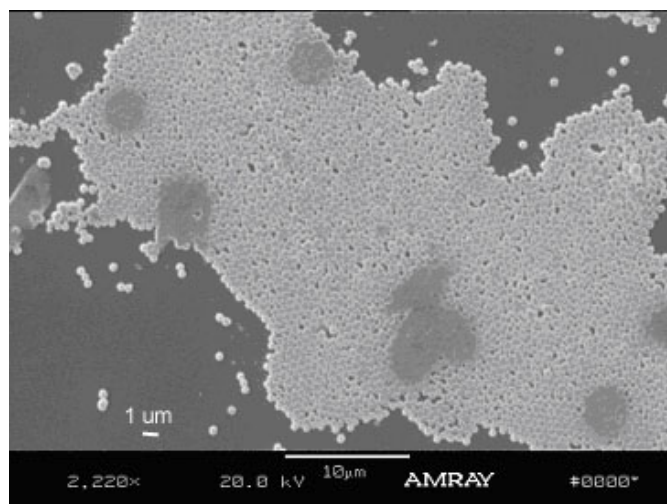
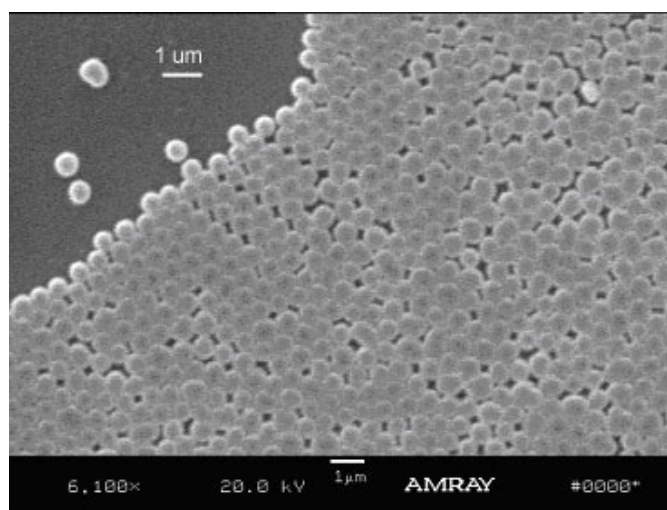


Figure 5-7. Representative energy dispersive X-ray spectrum for organic-inorganic nanocomposite thin film.



(a)



(b)

Figure 5-8. Representative SEM images of mesoporous nanoparticles arrayed on glass slide by solvent casting at (a) a low magnification, and (b) a high magnification.

## Chapter 6. Bioapplicable Conducting Polymers based on a Biological Template Guided Synthesis

### 6.1. Introduction

Since 1970s electronically conductive and electroactive polymers, such as polyaniline, polythiophene, polypyrrole, and so forth, have emerged as a new class of advanced materials,<sup>1-4</sup> holding tremendous promise for a variety of technological applications including microelectronics,<sup>5,6</sup> photonic devices,<sup>2,7,8</sup> electrostatic dissipation,<sup>9-11</sup> anti-corrosion coatings,<sup>12-15</sup> light-weight battery,<sup>16-19</sup> and chemical sensors.<sup>20-22</sup> This field of research has received a highest scientific recognition recently: three pioneers of conducting polymers, A. MacDiarmid, A. Heeger and T. Shirakawa, were awarded 2000 Nobel Prize in Chemistry.<sup>23,24</sup>

More recently, conducting polymers have also been studied for a wide range of promising applications in biotechnology.<sup>25-27</sup> Based on the alternation in their electroactivity in response to changes in the biological microenvironment, advanced biosensors have been fabricated with conducting polymers. The sensors have been principally developed to mimic the biological functions such as smelling and tasting,<sup>28</sup> or to monitor the biological processes, for example, metabolism of biocomponents, enzymes activity variation, and so forth.<sup>29,30</sup> Conducting polymers have been used as carriers for controlled drug and biomacromolecule release applications.<sup>31-33</sup> By applying programmed electrical pulses, release of bioactive species with controlled amount and rate has been demonstrated. Moreover, some recent studies in tissues engineering application showed

the possibility of utilizing conducting polymers as substrate scaffolds for growth and differentiation of different types of cells.<sup>34</sup> For example, when cultured on electrically conductive polypyrrole films, in the presence of a nerve growth factor (NGF), neuronal precursor cells differentiate into neuronal phenotype more readily than cells cultured on conventional tissue culture polystyrene surface. It would be especially interesting to further explore the possibility to control over cell growth with electrical signals, with the hope of ultimately using electrical signal to stimulate cell differentiation and neural regeneration. All these biotechnological applications greatly rely on the availability of conducting biomaterials that are biocompatible and electronically active.<sup>35</sup> In addition, lack of aqueous solubility due to their conjugated backbone structure also challenges the usefulness of conducting polymers for bioapplications, where organic solvent is not desired. In this study we have developed new bioapplicable conducting polymers with improved biocompatibility and water solubility aiming at promising applications such as bioelectronics, biosensor and intelligent scaffold materials.

### **6.1.1. Conducting Polymers with Improved Biocompatibility and Solubility**

To address the biocompatibility and solubility problems, structure modified conducting polymers have been developed based on syntheses of substituted, grafted and copolymerized materials.<sup>36-41</sup> Covalently bonded hydrophilic and/or biofriendly functional groups/chain fragments, confer improved water solubility and biocompatibility upon materials. The structure modification methods are limited by the availability of the

starting materials as well as the necessary chemistry. In some cases, the modified polymers exhibit decreased electrical activity due to a restrained conjugation structure.<sup>42,43</sup>

As a major improvement in synthesis of water soluble conductive polymer, especially polyaniline (PANI), a template assisted synthetic route was developed by Yang *et al.* in early 1990s.<sup>44-46</sup> In this approach, the molecular template such as polyelectrolyte (polyanion-) binds the aniline monomers (AN or H+AN) to form TEMP-(AN)<sub>n</sub> molecular complexes. Upon polymerization, the aniline monomers are polymerized to PANI and stay attached with the template to form TEMP-PANI. The properties and conformations of the obtained complex are greatly affected by properties of the template and the interaction between the template and polyaniline. The complexes are either water soluble or stable colloidal suspension. It is believed that electrostatic force plays a key role in the formation of polymer complexes. This synthesis route has been expanded to various template compounds including polyelectrolytes, surfactants and biomacromolecules.<sup>47-50</sup> The template guided synthesis offers opportunities to adjust the morphology and other properties of conducting polymers. So far, this method has been mainly adapted to prepare water soluble conductive polymers. More recently, through an enzyme catalyzed template guided synthesis, polyaniline/DAN intertwined complex has been prepared and used to probe the controllability over DNA conformation.<sup>51</sup>

Based on template guided method, we developed a synthetic route using a biocompatible material (i.e., type I collagen) to simultaneously improve both



biocompatibility and water solubility of conductive polymers. The schematics of this biological templated polymerization are illustrated in Figure 6-1. Prior to polymerization, fibrillar collagen functions as a backbone to pre-align aniline monomers. The attractive force between aniline monomer and collagen is mainly hydrogen bonding due to the –OH side groups presented along collagen fibril. Other forces, such as electrostatic interactions, van der Waals attractions, and hydrophobic interactions may also contribute to form aniline-collagen complexes. The polymerization was chemically initiated under an acidic condition. Aniline monomers are polymerized into long chain of polyaniline intertwining and wrapping the fibril collagen forming a polyaniline-collagen (PANI-Colla) complex. The incorporation with collagen renders PANI water solubility under acidic conditions while retaining its electrical and optical properties to a certain extent. The electronic absorption spectroscopy and atomic force microscopy are used to study the characteristics of water soluble PANI-Colla complex. The biocompatibility of the new material was examined with cell growth studies.

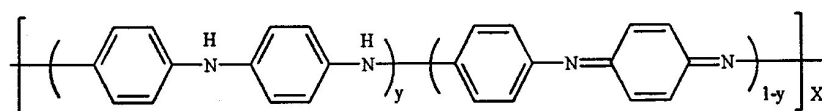
Parallel to this study, we have also explored another strategy to improve biocompatibility of conducting polymer, in which the polymer is modified with biocompatible functional groups or side chains by covalently bonding such groups or side chains onto the pre-fabricated polymer substrates or into the conducting polymer structures during the synthesis. We have been successfully modified both polyaniline backbone and polyaniline films with chloromethyl groups, through which amino acids and peptide chains are covalently bonded to polymer surfaces. The improved

biocompatibility of these materials has been verified with cell growth studies on various amino acid modified polyaniline surfaces. The detailed results of this study will be reported by Ms. Elizabeth Guterman in our group.<sup>52</sup>

Some background information on the two important materials involved in this studies, polyaniline and collagen, will be briefly introduced as follows.

### 6.1.2. Conducting Polymer: Polyaniline

Known as a blue dye a century ago, polyaniline nowadays is likely among the most useful conducting polymers because of its interesting electrical conductivity, electrochemical activity, photochemical stability, multi-color electrochromic effect and optical properties.<sup>53-55</sup> Polyaniline can be prepared by either electrochemical or chemical oxidation of aniline.<sup>56-58</sup> Consisting of two main structure units, the benzoid diamine and quinoid diimine, the generalized formula of polyaniline is shown as follows.<sup>59-61</sup>



Depending on the y value, the polymer exists at different oxidation states, which are interconvertible chemically or electrochemically. Pernigranline is the completely oxidized form (y=0), while leucoemeradine is the fully reduced form (y=1). Emeraldine, the common stable base form, contains an equal fraction of both benzoid and quinoid forms (y=0.5). Upon being doped with protonic acid, emeraldine base can be converted to

emeraldine salt, the unique conducting form of polyaniline. In emeraldine salts, imine sites ( $=N-$ ) are protonated to give bipolarons. Bipolarons further dissociate to form delocalized polarons, which function as charge carriers rendering high conductivity in polyaniline. The conductivity of polyaniline depends not only on the degree of protonation, but also the oxidation state. Illustrated in Figure 6-2,<sup>62</sup> polyaniline at different forms can be converted to the same conducting material by addition of acids that protonate the base sites within the polymer. It is noticed that these doping processes are reversible by adding bases to deprotonate. The controllable conductivity makes polyaniline one of the most useful conducting polymers.

### **6.1.3. Biological Template: Collagen**

The word “collagen” is derived from Greek word for “glue”. In the past the collagen of bones and tendons was used in industry to produce glue. Collagen is a type of protein that enwraps the organs to hold specialized cells together in discrete units. It prevents organs/tissues from tearing or losing their functional shape when they are exposed to sudden and strong movements. Besides its structural function in mature tissue, collagen plays a regulating role in developing tissue as well. It has a key function in the regulation of the proliferation and differentiation of unspecialized cells. Collagen is often used as substrate material for tissue engineering applications. In addition, many other applications have been developed for collagen proteins. The most popular uses are found in cosmetics, nutrition and medical applications such as surgery stitch cotton.<sup>63</sup>

Collagen proteins are composed of a triple helix formed by three polypeptide chains. Each chain has a large number of repetitive sequences of Gly-X-Y, where X is often proline and Y is often hydroxyproline.<sup>64</sup> As a major component of skin and bone, collagens are the most abundant proteins in mammals, constituting 25 % of the total protein mass.<sup>65</sup> Accounting for about one third of total protein mass, collagens are also a large diverse family of proteins in vertebrates, as well as in invertebrates' phyla. To date, nineteen different vertebrates collagens referred to type I-XIX have been identified. Each type has a special secondary structure formed from three polypeptide segments aligned in parallel.<sup>66</sup> The most important types are the fibrillar types I, II, III, IV and V, among which 90 % is type I collagen. Type I collagen forms the largest and strongest fibrillar component that provides tensile strength to bones, skin, tendons and ligaments. Most of structure research has been done for type I collagen, especially that extracted from rat tail tendon.<sup>67</sup> This type of collagen is soluble in water under acidic conditions. In our study, we use type I collagen as a biological template in synthesis of conducting polymers, to improve their water solubility and biocompatibility.

## **6.2 Experimental**

### **6.2.1. Materials**

Aniline (99.8%, Janssen Chimica) was distilled under a reduced pressure before use. Collagen (Type 1, from rat tail, Sigma), acetic acid (99.7%, Corco), hydrochloric

acid (HCl, 37.3%, Fisher), hydrogen peroxide (H<sub>2</sub>O<sub>2</sub>, 50%, Fisher), were all used as received without further purification.

Rat PC-12 cells (America Type Culture Collection) were used for biocompatibility studies. Cells were cultured on Lab-Tek 8 well Permanox chamber slides (Nalgen Nunc). Nerve Growth Factor (NGF, Sigma Aldrich) was used to stimulate the cell differentiation.

### **6.2.2. Synthesis of Polyaniline-Collagen (PANI-Colla) Complex Materials**

In the presence of type I collagen, PANI-Collagen (PANI-Colla) complex materials were prepared through a low temperature chemical polymerization of aniline under acidic conditions. As a typical procedure, in a 50 ml round bottom flask, collagen (10 mg) was dissolved in acetic acid solution (0.1 M, 10 ml) under magnetic stirring. Aniline monomer (11.9  $\mu$ l, 0.125 mmol) was added and the mixture was continuously stirred at room temperature for 24 h. Before the polymerization, the resultant clear solution was cooled down in an ice bath. HCl (3.0 M, 5.0 ml) was added followed by the addition of H<sub>2</sub>O<sub>2</sub> (50 wt %, 17.0  $\mu$ l, 0.250 mmol). The reaction mixture was stirred for about 3 h and then kept in a freezer at -15 °C. In about 7 days, green PANI-Colla complex colloidal solution gradually formed and was visualized as dark green solution followed by fibril precipitation. The reaction was quenched with oxalic acid aqueous solution (saturated, 1.0 ml) After centrifugation and decantation, PANI-Colla complex was separated from the reaction mixture. The product was washed with deionized

distilled water. Upon drying in a vacuum oven at room temperature for 72 h, PANI-Colla complex was obtained as dark green solid with the gravimetric yield of 87 %. As control sample, PANI was synthesized in the absence of collagen under otherwise identical conditions.

### **6.2.3. Cell Growth Studies on PANI-Colla Films**

To examine the biocompatibility of the new complex materials, thin layer of PANI-Colla co-polymer films were cast on a culture slide surface for cell growth studies. About 5 mg of PANI-Colla was dispersed in 2 ml distilled deionized water under sonicating for 20 min. Approximately 0.2 ml of solution was added into each well. The plates were then placed in the vacuum oven under ambient temperature overnight. Prior to cell-seeding the polymer coated plates were sterilized by exposing to UV light under the hood for 10 min. The control PANI-coated culture plates were also prepared with PANI dispersion in distilled deionized water.

In order to assess biocompatibility of the newly synthesized polymer, attachment, proliferation and differentiation was studied on a cellular model for neuronal differentiation PC12 pheocromacytoma cells. PC-12 cells were cultured in medium composed of 85 % high-glucose DMEM, 10 % heat-inactivated horse serum, and 5 % fetal bovine serum supplemented with L-glutamine, penstrep and fungizone. Cells were maintained in a humid and 5 % CO<sub>2</sub> incubator. Prior to being seeded on PANI-Colla films, cells were mechanically dislodged from the tissue culture flasks and seeded onto

the surface of polymer coated culture plates. In all experiments, 3 ml of medium containing 50,000 cells was used in each well. Cells were fed by withdrawing the “old” medium and replacing it with 3 ml of fresh medium using pipet every other 3 to 4 days. After visually investigating cell attachment and spreading with microscope, cell medium was primed with 25 ng/ml of NGF. Flasks were then constantly taken to the microscope for visual observation and picture taking. Except when medium was changed and microscopic observations were taken, the culture dishes were maintained in a humid and 5 % CO<sub>2</sub> incubator.

#### **6.2.4. Instrument and Characterization**

UV-Vis absorption studies were carried out with a Perkin-Elmer Lambda 2 spectrometer. Infrared spectra of KBr powder-pressed pellets were recorded on a Perkin-Elmer Model 1600 FTIR spectrophotometer. Atomic force microscopy (AFM) images were obtained with Microscope IIIa scanning probe microscope operated under tapping mode. The AFM samples were dissolved in acidic acid solution (0.1 M) and cast on mica surface. Cell attachment and growth on PANI-Colla films were evaluated using a Nikon Diaphot inverted phase contrast microscope and a 10X phase-contrast objective.

### **6.3. Results and Discussion**

Acid soluble PANI-Colla complex has been synthesized in the presence of type I collagen in an acidic aqueous environment. During the reaction, the reaction mixture

changed the color from pale green to dark green. After 5 days, dark green precipitate was observed probably due to the increased degree of crosslinking of polymer. The polymerization was monitored with UV-Vis spectroscopy. The representative spectra of the as-synthesized PANI-Colla solution at different polymerization time were recorded and shown in Figure 6-3. With an increased reaction time, the UV-Vis spectra of the complex solution gradually developed two major absorption bands. The one around 400 nm is associated with the  $\pi$ - $\pi^*$  transition on the polyaniline chain, and the one after 650 nm is attributed to polaron of the acid doped PANI and corresponds to electron localization. The presence of these two characteristic absorptions indicates the formation of the conducting emeraldine salt form of polyaniline. The UV-Vis spectrum of the as-synthesized solution remains relatively stable after 5 days. In comparison, the polymerization carried out in the absence of collagen results in brownish solution followed by dark precipitation. After 5 days, the UV-Vis spectrum of control PANI as-synthesized suspension only shows one absorption peak at 400 nm. It is believed that the absence of a typical emeraldine salt UV absorption band was due to the poor solubility of PANI in water.

The comparison pictures of the PANI-Colla and PANI as-synthesized solution and their re-dispersions in acidic aqueous environments ( $\sim$  pH 2) are shown in Figure 6-4. The control PANI as-synthesized reaction mixture was a slightly brownish green color solution with dark green precipitate, while the PANI-Colla one was green solution with dark green precipitate. Dispersion of the precipitate resulted from both polymerizations in



acidic acid aqueous solution showed that PANI formed a suspension, which settled in a few minutes; in contrast, PANI-Colla complex formed green color solution, which was stable for months. The formation of PANI-Colla complex incorporates the characteristics of both collagen and PANI, and therefore renders the material the increased solubility.

The formation of PANI-Colla complex was confirmed with FT-IR spectroscopy studies. The comparison of IR spectra of PANI-Colla, type I collagen and the control PANI samples are shown in Figure 6-5. The spectrum of PANI-Colla exhibits the characteristic absorption bands arising from both components, i.e., PANI and collagen. In the spectrum of PANI-Colla, the typical aliphatic C-H stretching vibration resulting from the amino acids in collagen is observed as a broad absorption band at  $2910\text{ cm}^{-1}$ . The intense peak at  $1636\text{ cm}^{-1}$  is assigned to the C=O stretching arising from collagen components. The broad absorption at around  $1530\text{ cm}^{-1}$  region probably is attributed to the aromatic quinoid and benzoid ring stretching (as peaks at  $1560\text{ cm}^{-1}$  and  $1490\text{ cm}^{-1}$  in PANI, respectively) from PANI and C-N stretching from collagen. The aromatic C-H stretching absorption of polyaniline is observed as a distinctive peak centered at  $780\text{ cm}^{-1}$ .

The FT-IR spectra of PANI-Colla and a physical mixture of PANI and collagen are further compared in Figure 6-6. Besides the similarities, the spectra show considerable differences in the region of  $1100\text{--}1600\text{ cm}^{-1}$ , suggesting the existence of strong interactions between the two components in the complex. The strong absorption at  $1560\text{ cm}^{-1}$  in the mixture of polyaniline and collagen was assigned to the C=N stretch of the quinoid form of polyaniline. This peak is red shifted in PANI-Colla, observed as a

broad band centered around  $1530\text{ cm}^{-1}$ , while the absorption band of benzoid ring is blue shifted and also broadened in the spectrum of PANI-Colla. The aromatic C-H stretch at  $818\text{ cm}^{-1}$  resulting from polyaniline in the mixture is also red shifted to  $798\text{ cm}^{-1}$  in PANI-Colla. The broadening and shifting of the characteristic peaks in the FT-IR spectrum of PANI-Colla, as compared to the counterparts in their simple mixture, indicate the presence of certain intermolecular interactions between PANI and collagen in the complex, such as hydrogen bonding.

The doping/de-doping reversibility of PANI-Colla is demonstrated in Figure 6-7. Visible absorption of PANI-Colla aqueous solution at pH 4.7 shows a peak at 750 nm, which corresponds to polaron in doped emeraldine salt form of polyaniline. As dissolved in buffers with pH of 6.6 and 10.5, the peak at 750 nm is shifted to much shorter wavelength, which is attributed to de-protonation of the polyaniline backbone. Finally when dissolved in 0.1 M NaOH, the complex solution shows an absorption at 550 nm, arising from the excitation transition of the quinoid rings in emeraldine base. This behavior is similar to that of the chemically synthesized PANI. The demonstrated controllability over doping levels of the complex confirms that the polyaniline obtained with collagen as guiding template is a conducting form of polyaniline and the as-synthesized complex is electroactive.

The formation of water soluble PANI-Colla complex is strongly dependent on the synthesis conditions, especially temperature and pH. The polymerization carried out under room temperature renders a brown murky solution immediately after introducing

oxidant, indicating the formation of uncomplexed polyaniline with low molecular weight.<sup>68</sup> To obtain the conducting polyaniline, both chemical and electrochemical polymerization of aniline must be carried out in a strongly acidic media. It is expected that a low pH medium is also necessary for the synthesis of conducting polyaniline by collagen templating method. In fact, our experiments show that if the pH of reaction mixture is not adjusted to a highly acidic one with HCl prior to the polymerization, the product is obtained as brownish precipitate corresponding to low molecular weight branched polyaniline.

Figure 6-8 shows the AFM images of collagen and PANI-Colla samples deposited on mica surfaces by solvent evaporation. The obtained collagen image exhibits clearly fibrillar structure with an average diameter of  $\sim 80$  nm. This result is well compared with the reported size of type I collagen in literature.<sup>69</sup> The as-synthesized PANI-Colla presents a more aggregated while still fibrillar morphology. Estimated from AFM images, the diameter of PANI-Colla fibrils is  $\sim 170$  nm. Increased diameter is attributed to the formation of complex structure with polymer intertwined with collagen fibrils as well as possible fibrils aggregation through branched polymer chains.

To evaluate the biocompatibility of the new materials, PC-12 cells were cultured on PANI-Colla coated culture dishes. PANI coated culture dishes were employed as control. Representative phase-contrast optical micrographs of cells cultured on both polymer coated surfaces after addition of NGF for 72 h are compared in Figure 6-9. It is apparent that cells are attached and differentiated better on PANI-Colla coated surface

than on the PANI coated one. Based on image analysis, approximately 10-15 % of seeded cells are attached onto PANI coated surface. The number of cells attached to PANI-Colla surface is about 3-4 times as that on PANI surface based on image analysis. The improvement of cell attachment on PANI-Colla can be explained by the presence of collagen, a well known biofriendly substrate material for cell culture. Moreover, enhanced solubility of PANI-Colla complex makes it practically possible to coat culture dishes with a layer of uniform thin film, which is also in favor of good cell supporting capability. In addition to attachment, a better neuronal growth and differentiation were observed with the PC-12 cells on PANI-Colla surface. Upon addition of NGF for 72 h, the cell differentiation on PANI occurred but rarely. In contrast, neurons adhered on PANI-Colla surface showed vivid differentiation and neuronal network formation tendencies, evidenced by the formation of prolonged interconnected neurites. Compared with PANI, PANI-Colla shows enhanced capability of sustaining primary nerve cells and the necessary support for cells growth that are critical for regeneration. The promoted cell adhesion and differentiation on PANI-Colla surfaces suggest an improved biocompatibility of this new conducting material.

#### **6.4. Conclusions**

In order to develop new materials for a variety of biotechnology applications, research has been focused on preparing biocompatible conducting polymer materials. In this study, based on template guided chemical polymerization method, PANI-Colla

complex was synthesized by pre-aligning aniline monomers around the collagen fibrils followed with an in-situ low temperature chemical polymerization under acidic condition. PANI-Colla complex was obtained with improved biocompatibility and water solubility in comparison to PANI control sample synthesized in the absence of collagen. The intermolecular forces between PANI and collagen such as hydrogen bonding play an important role in the formation of entwined fibrillar complex structure. The existence of such interaction is confirmed with IR spectroscopy studies. Similar to most of composite materials, PANI-Colla preserves characteristics from both components. Its electroactivity is controllable through reversible doping/de-doping process, and it is water soluble under acidic conditions as is collagen. As expected, the new material shows improved biocompatibility in comparison to PANI, which has been demonstrated with attachment, variation and differentiation studies of neuron precursor cells on polymer coated surfaces.

With improved biocompatibility and controlled conductivity, PANI-Colla will be used as a scaffold material for tissue engineering application. The effect of electrical stimulus on cell variation and differentiation will be evaluated with the hope of ultimately using electrical signal to stimulate controllable neural tissue regeneration. The materials also offer some yet unexplored opportunities towards the fundamental research of structure-property relationship of biomacromolecules, as well as a variety of biotechnological applications, such as biosensors, electronics and diagnostic tools. The enhanced solubility of PANI-Colla complex in water is advantageous for material

processing and device fabrication. Electro-spinning PANI-Colla nanofibers will be explored following similar procedures for electrospinning of collagen<sup>70</sup> and PANI.<sup>71</sup>

### 6.5. Acknowledgments

I am grateful to Ms. Elizabeth Guterman for the help with PC-12 cell growth studies. Many thanks are due to Dr. Guoliang Yang of Physics Department at Drexel University for his valuable suggestions on AFM measurements. I want to thank Dr. Peter I. Lelkes of School of Biomedical Engineering, Science and Health Systems at Drexel University for providing me with cell culture facilities as well as helpful discussions on cell studies. I also thank Ms. Maryann Fitzpatrick and Mr. Wolfgang Nadler for helping me with digital images of my samples.

### 6.6. References

1. Pron, A.; Rannou, P. *Progress in Poly. Sci.* **2001**, *27*, 135.
2. *Handbook of Advanced Electronic and Photonic Materials and Devices*, eds.: Nalwa, H. S. Academic Press: San Diego. 2001, p 1.
3. Naarmann, H. *Industrial Polymers Handbook*, **2001**, *3*, 1207.
4. Gurunathan, K.; Murugan, A. Vadivel; Marimuthu, R.; Mulik, U. P.; Amalnerkar, D. *P. Mater. Chem. Phys.* **1999**, *61*, 173.
5. Angelopoulos, M. *IBM J. of Research and Development* **2001**, *45*, 57.
6. *Handbook of Advanced Electronic and Photonic Materials and Devices*, eds.: Nalwa, H. S. Academic Press: San Diego. 2001, p 355.
7. Shimidzu, T. *Pure Appl. Chem.* **1995**, *67*, 2039.

8. Epstein, A. J. *Springer Ser. Mate. Sci.* **2001**, *41*, 3.
9. Kathirgamanathan, P; Ravichandran, S.; Adams, P.; Shah, D.; Quill, K.; Underhill, A. E. *Inst. Phys. Conf. Ser.* **1995**, *143*, 113.
10. Dahman, S. J. *Annu. Tech. Conf. Soc. Plas. Eng.* **2001**, *59*, 1354.
11. Koul, S.; Chandra, R.; Dhawan, S. K. *Poly.* **2000**, *41*, 9305.
12. Sitaram, S. P.; Stoffer, J. O.; O'Keefe, T. J. *Coatings Tech.* **1997**, *69*, 65.
13. Wessling, B. *Chem. Britain* **2001**, *37*, 40.
14. (a) Tallman, D. E.; Spinks, G.; Dominis, A.; Wallace, G. G. *J. Solid State Electrochem.* **2002**, *6*, 73. (b) Spinks, G. M.; Dominis, A. J.; Wallace, G. G.; Tallman, D. E. *J. Solid State Electrochem.* **2002**, *6*, 85.
15. Wei, Y.; Jamasbi, H.; Li, S.; Cheng, S.; Jansen, S. A.; Sein, L. T., Jr. *Poly. Prep.* **2000**, *41*, 1778.
16. Nagasubramanian, G.; Boone, D. *Int. SAMPE Tech. Conf.* **1995**, *27*, 795.
17. Scrosati, B. *Poly. Int.* **1998**, *47*, 50.
18. Gray, F.; Armand, M. *New Trends Electrochem. Tech.* **2000**, *1*, 351.
19. Novak, P.; Mueller, K.; Santhanam, K. S. V.; Haas, O. P. *Chem. Rev.* **1997**, *97*, 207.
20. Teasdale, P. R.; Wallace, G. G. *Analyst* **1993**, *118*, 329.
21. Sukeerthi, S.; Contractor, A. Q. *Indian J. Chem.* **1994**, *33*, 567.
22. Adeloju, S. B.; Wallace, G. G. *Analyst* **1996**, *121*, 699.
23. MacDiarmid, A. G. *Rev. Modern Phys.* **2001**, *73*, 701.
24. Heeger, A. J. *Rev. of Modern Phys.* **2001**, *73*, 681.
25. Ikematsu, M. *FED Janaru* **1997**, *8*, 39.
26. Schuhmann, W. *Mikrochim. Acta* **1995**, *121*, 1.
27. Schmidt, H.-L.; Gutberlet, F.; Schuhmann, W. *Sens. Actuators*, **1993**, *13*, 366.

28. Baldacci, S.; Matsuno, T.; Toko, K.; Stella, R.; De Rossi, D. *Sens. Mater.* **1998**, *10*, 185.
29. Gerard, M.; Chaubey, A.; Malhotra, B. D. *Biosens. Bioelec.* **2002**, *175*, 345.
30. Pal, P. S.; Sarkar, P. *J. Indian Chem. Soc.* **2002**, *79*, 211.
31. Pyo, M.; Maeder, G.; Kennedy, R. T.; Reynolds, J. R. *J. Electroanal. Chem.* **1994**, *368*, 329.
32. Massoumi, B.; Entezami, A. *J. Bioact. Compat. Poly.* **2002**, *17*, 51.
33. Sahota, T. S.; Latham, R. J.; Linford, R. G.; Taylor, P. M. *Biomed. Health Res.* **1998**, *16*, 143.
34. Schmid, C. E.; Shastri, V. R.; Vacanti, J.; Langer, R. *Proc. Natl. Acad. Sci. USA* **1997**, *94*, 8948.
35. Kamalesh, S.; Tan, P.; Wang, J.; Lee, T.; Kang, E.-T.; Wang, C.-H. *Biomed. Mater. Res.* **2000**, *52*, 467.
36. Sudhakar, M.; Stoecker, P. W.; Viswanathan, T. *Rec. Res. Dev. Poly. Sci.* **1998**, *2*, 173.
37. Chen, S.-A.; Hwang, G.-W. *Poly.* **1997**, *38*, 3333.
38. Hany, P.; Genies, E. M.; Santier, C. *Synth. Met.* **1989**, *31*, 369.
39. Yang, S.; Tirmizi, S. A.; Burns, A.; Barney, A. A.; Risen, W. M. Jr. *Synth. Met.* **1989**, *32*, 191.
40. (a) Nguyen, M. T.; Kasai, P.; Miller, J. L.; Diaz, A. F. *Macromolecules* **1994**, *27*, 3625. (b) Nguyen, My T.; Diaz, Arthur, F. *Macromolecules* **1995**, *28*, 3411.
41. Cui, X.; Lee, V. A.; Raphael, Y.; Wiler, J. A.; Hetke, J. F.; Anderson, D. J.; Martin, D. C. *J. Biomed. Mater. Res.* **2001**, *56*, 261.
42. Yue, J.; Gordon, G.; Epstein, A. J. *Polymer* **1992**, *33*, 4410.
43. Nguyen, My T.; Diaz, Arthur F. *Macromolecules* **1995**, *28*, 3411.
44. Liu, J. M.; Sun, L.; Hwang, J. H.; Yang, S. C. *Mater. Res. Soc. Symp. Proc.* **1992**, *247*, 601.



45. Liu, J.-M.; Yang, S. *Chem. Commun.* **1991**, 1529.
46. Sun, L.; Yang, Sze C. *Mater. Res. Soc. Symp. Proc.* **1994**, 328, 209.
47. Yang, S. C.; Clark, R. L.; Liao, H.; Sun, L. *Proc. SPIE-Int. Soc. Opt. Eng.* **1995**, 2528, 198.
48. Liu, W.; Cholli, A. L.; Nagarajan, R.; Kumar, J.; Tripathy, S.; Bruno, F. F.; Samuelson, L. *J. Am. Chem. Soc.* **1999**, 121, 11345.
49. McCarthy, P. A.; Huang, J.; Yang, S. C.; Wang, H.-L. *Langmuir* **2002**, 18, 259.
50. Samuelson, L.; Liu, W.; Nagarajan, R.; Kumar, J.; Bruno, F. F.; Cholli, A.; Tripathy, S. *Synth. Met.* **2001**, 119, 271.
51. Nagarajan, R.; Liu, W.; Kumar, J.; Tripathy, S. K.; Bruno, F. F.; Samuelson, L. A. *Macromolecules* **2001**, 34, 3921.
52. Guterman, E.; Cheng, S.; Palouian, K.; Bidez, P.; Lelkes, P. I. Wei, Y. *Poly. Prep.* **2002**, 43, 767.
53. Genies, E. M.; Boyle, A.; Lapkowski, M.; Tsintavis, C. *Synth. Met.* **1990**, 36, 139.
54. Laska, J. *Adv. Plas. Tech.* **1999**, 3, 16.
55. Xia, Y. *Plas. Eng.* **1998**, 45, 359.
56. Gospodinova, N.; Terlemezyan, L. *Progress Poly. Sci.* **1998**, 23, 1443.
57. Yano, J. *Current Trends Poly. Sci.* **1998**, 3, 131.
58. Wei, Y.; Li, S.; Jia, X.; Cheng, M.-H.; Mathai, M. W.; Yeh, J.-M.; Li, W.; Jansen, S. A.; Wang, Z. Y. Yang, C. Gao, J. P.; Narkis, M.; Siegmann, A.; Hsieh, B. R. *ACS Symp. Seri.* **1999**, 735, 384.
59. MacDiarmid, A. G.; Epstein, A. J. *Faraday Discuss. Chem. Soc.* **1989**, 88, 317.
60. Focke, W. W.; Wnek, G. E.; Wei, Y. *J. Phys. Chem.* **1987**, 91, 5813.
61. Wei, Y.; Hsueh, K. F.; Jang, G. W. *Macromolecules* **1994**, 27, 518.

62. Wallace, G. G., Spinks, G. M., Teasdale, P. R. *Polyaniline*, In: *Conductive Electroactive polymers*, Technomic Publishing Co., Inc. Lancaster, Basel, 1997, p. 119.
63. Chvapi, M. *Fibrous Protiens: Scientific, Industrial and Medical Aspects*, **1979**, *1*, 247.
64. Branden, C. T., Tooze, J. *Introduction to Protein Structure*, Garland Publishing Inc.: New York, London. 1991.
65. Alberts, B. *et al. Molecular Biology of the Cell*, 3<sup>rd</sup> edition, Garland Publishing Inc.: New York, 1994.
66. Piez, K. A. *Molecular and Aggregate Strutures of Collagens*, In: *Extracellular Matrix Biochemistry*, Piez, K. A., Reddi, A. H., eds, Elsevie, New York, 1984, p. 1.
67. Seljee, F. R. <http://xraywww.chem.uva.nl/franks/collagen/>
68. Samuelson, L.; Anagnostopoulos, A.; Alva, K. S.; Kumar, J.; Tripathy, S. K. *Macromolecules* **1998**, *31*, 4376.
69. Nimni, M.; Harknee, R. *Molecular Structures and Functions of Collagen* In: *Collagen Volume I Biochemistry*, CRC Press: Boca Raton, FL, 1988, p. 3.
70. Matthews, J. A.; Wnek, G. E.; Simpson, D. G.; Bowlin, *Biomacromolecules* **2002**, *3*, 232.
71. Gregory, R. V. *Fibers from electrically conductive polymers*, In: *Structure Formation in Polymeric Fibers*, ed, Salem, D. R., Carl Hanser Verlag: Muenchen, Germany, 2001, p. 359.

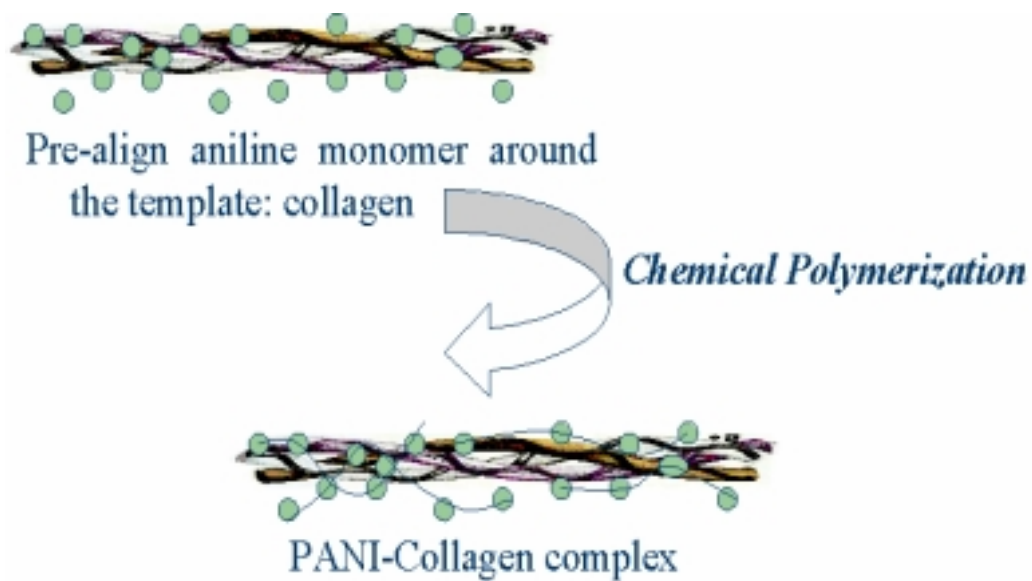


Figure 6-1. Schematics of biologically templated synthesis of PANI-Collagen complex.

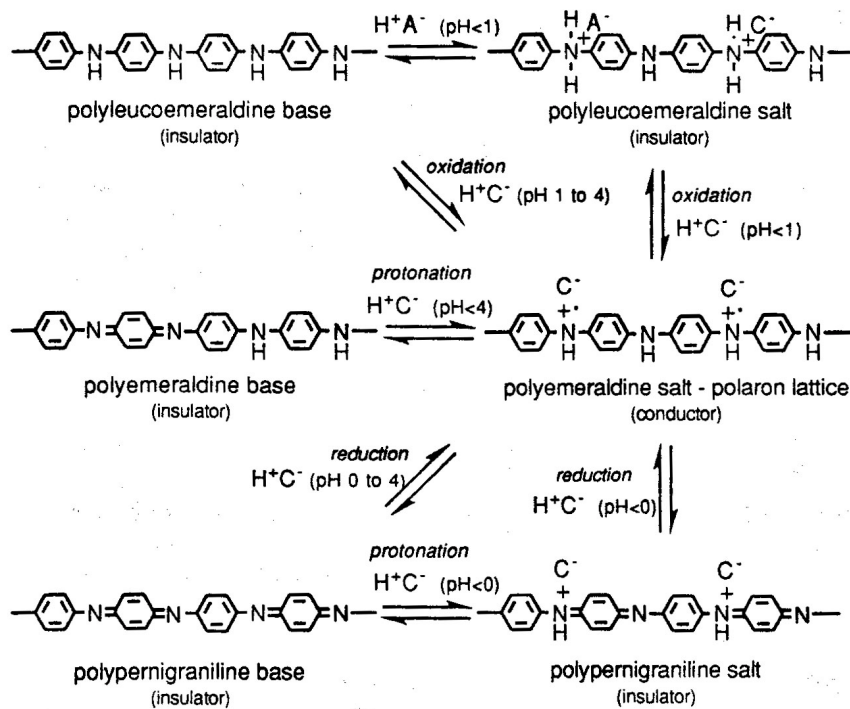


Figure 6-2. The protonation and redox reactions between the various forms of polyaniline.

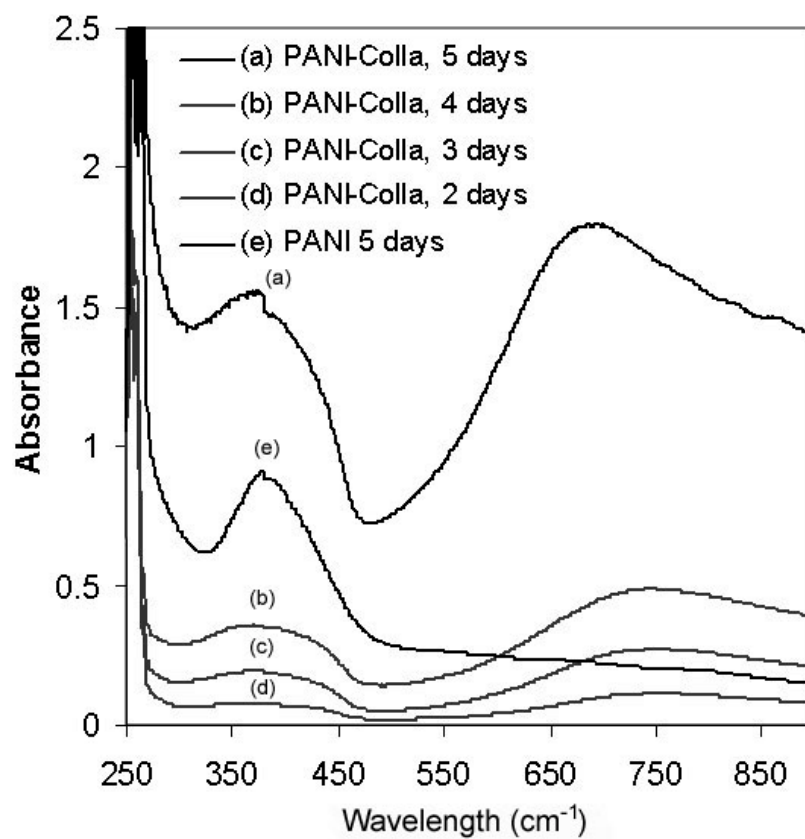


Figure 6-3. UV-Vis absorption spectra of chemical polymerized PANI-Colla complex reaction mixture at day 2 to day 5 (a)-(d), in comparison with UV-Vis absorption spectrum of PANI polymerized for 5 days (e).

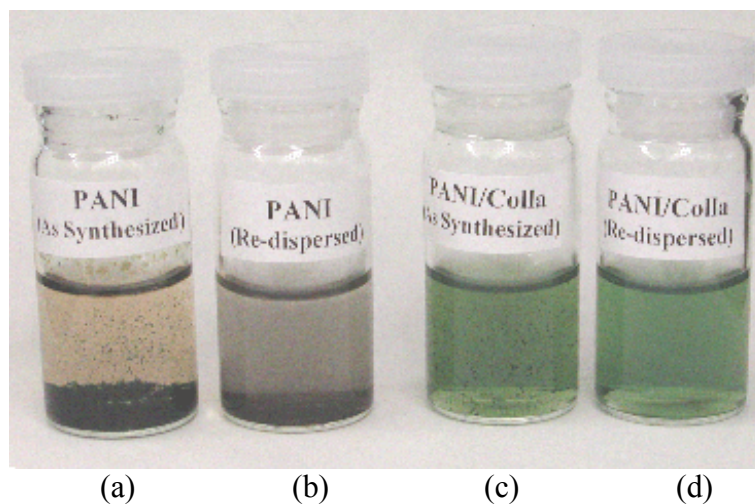


Figure 6-4. Comparison photographs of (a) PANI as-synthesized suspension and (b) Redispersed PANI in 0.01 M acidic acid vs. (c) PANI-Colla as-synthesized suspension and (d) PANI redispersed in 0.01 M acidic acid. The PANI as-synthesized reaction mixture (a) is a slightly brownish green color solution with dark green precipitate. Dispersion of precipitate of (a) in acidic acid aqueous solution forms a suspension, which settles in a few minutes. In contrast, the as-synthesized PANI-Colla (c) is green solution with dark green precipitate. Re-dispersed in acidic acid aqueous solution under sonicating, PANI-Colla complex forms green color solution (d).

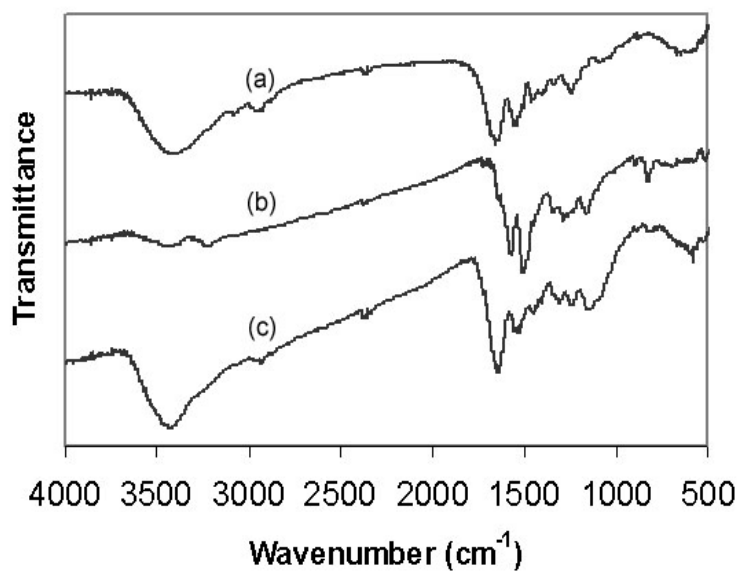


Figure 6-5. FT-IR spectra of (a) collagen, (b) PANI and (c) PANI-Colla complex.

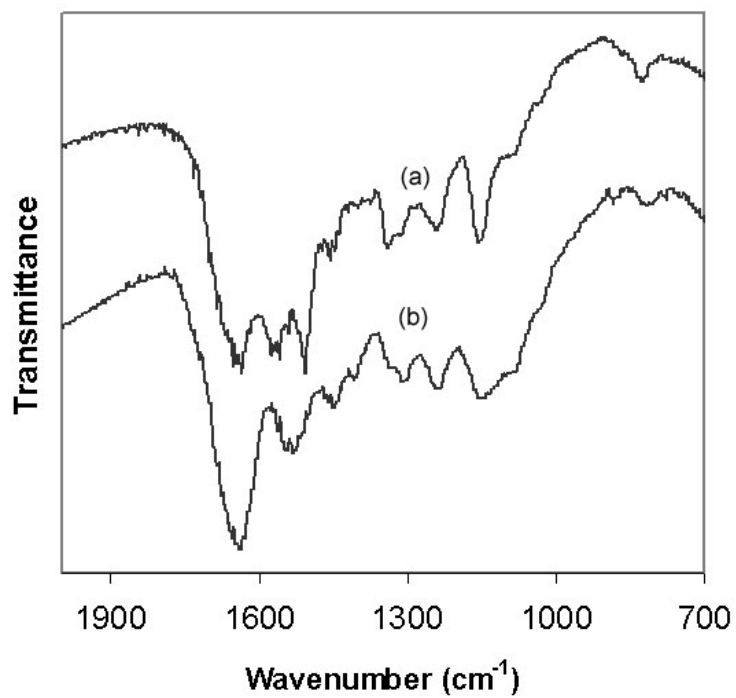


Figure 6-6. FT-IR comparison spectra of (a) a physical mixture of polyaniline and collagen vs (b) PANI-Colla complex.



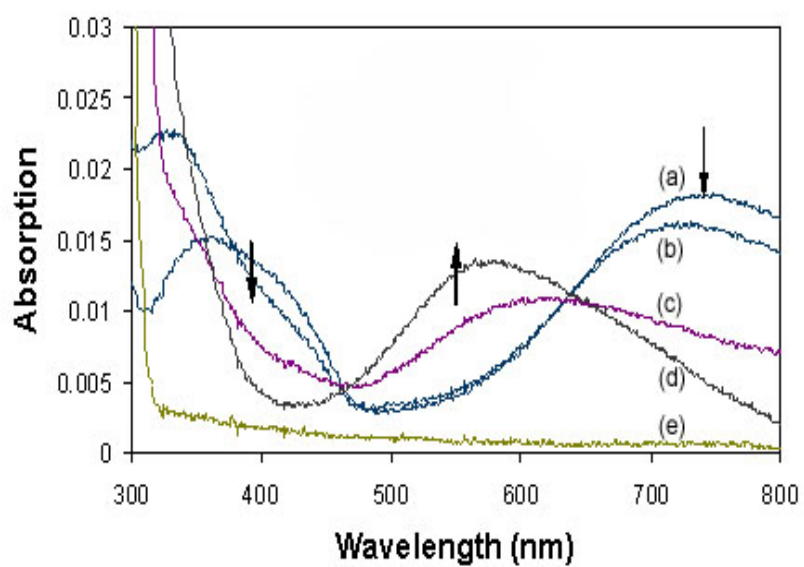
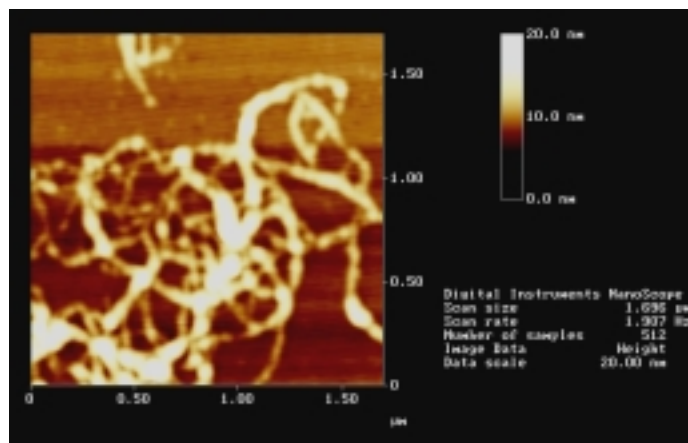
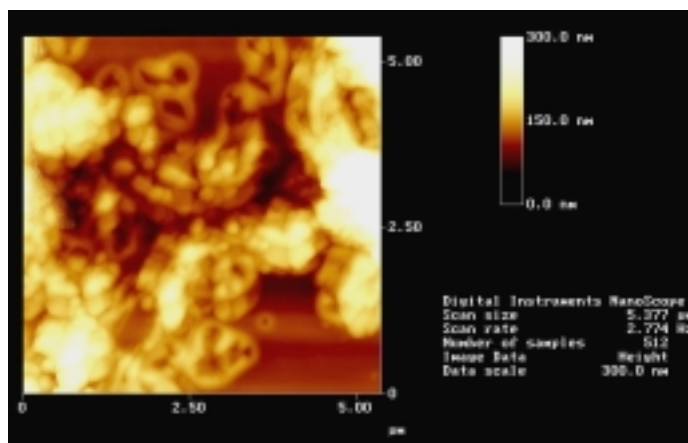


Figure 6-7. UV-Vis absorption spectra of PANI-Colla complex in aqueous solution at various pH: (a) 13.0 (b) 10.5 (c) 6.6 (d) 4.7, and (e) UV-Vis absorption spectrum of aniline collagen mixture in water at pH 4.7.

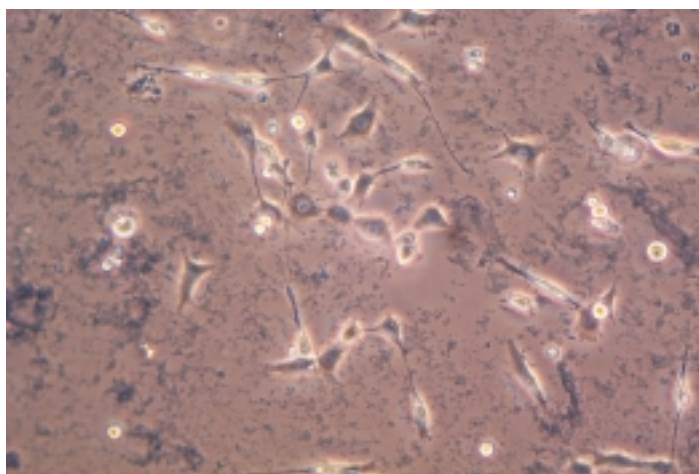


(a)

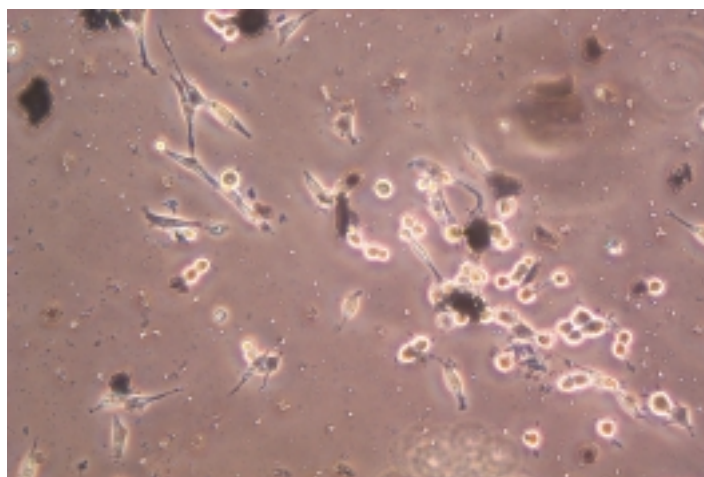


(b)

Figure 6-8. Comparison AFM images of (a) collagen and (b) PANI-Colla complex.



(a)



(b)

Figure 6-9. Comparison images of attachment and differentiation of PC-12 cells on tissue culture dishes coated with (a) PANI-Colla and (b) PANI under culturing conditions for 72 h. The bright globular features in the pictures are cells poorly attached on substrate surface and suspending in the medium. In comparison with PANI coated surface (b), PANI-Colla coated substrate (a) exhibit significantly improved cell affinitive property with less globular features observed. Precursor neuron cells adhered on PANI-Colla surface also showed vivid differentiation and network formation tendencies, evidenced by the formation of prolonged interconnected neurites after cultured for 72 h. In contrast, the cell differentiation on PANI occurred but rarely under the same conditions.

## Chapter 7. Synthesis and Characterization of Aniline Derivative Modified 8-Hydroxyquinoline Ligands and Their Metal Complexes

### 7.1. Introduction

As an attractive alternative for new generation flat panel displays, organic light emitting devices (OLEDs) have attracted a lot of research interests due to their potentially lower cost and simpler manufacturing process, along with compatibility with flexible substrates.<sup>1-3</sup> In addition, OLEDs offer excellent performance characteristics for electro-optical applications, such as high brightness and contrast, wide viewing angle, a full range of colors and low operating voltage.<sup>4-6</sup> The greatest advantage of organic light emitting materials is their ability to tailor molecular structures to serve specific functionalities.<sup>7,8</sup> Specifically, by structural modification of light emitting materials, the electroluminescent emission can be fine-tuned to a selected spectral region. Also small molecular organic compounds can be designed to preferentially transport either electrons or holes.

To obtain new metalloquinolates as potential electroluminescent materials, two aniline derivatives substituted quinoline ligand compounds, N,N'-bis(N,N-dimethyl-4'-aminophenyl)-5-imino-7-amino-8-ketoquinoline (Figure 7-1, **1a**) and N,N'-bis(4'-aminophenyl)-5-imino-7-amino-8-ketoquinoline (Figure 7-1, **2a**), were successfully synthesized with highly conjugated structure.<sup>9</sup> N,N-dimethyl-1,4-phenylenediamine and 1,4-phenylenediamine moieties were introduced, respectively, onto the 5 and 7 positions of 8-hydroxyquinoline ring through chemical oxidation reactions. The ligands were

prepared and purified as substituted 8-ketoquinolines. Prior to the coordination with metal ions, the ligands were reduced by a palladium catalytic hydrogenation. With the ligands at their reduced state, aluminum(III) and copper(II) complexes were prepared and characterized (Figure 7-1(3) and (4)).

### 7.1.1. Light Emitting Diodes

Before a detailed discussion of new materials syntheses, a brief introduction of light emitting diodes will be provided here. In some semiconducting materials, free electrons in the conduction band can recombine with free holes in the valence band and release photons in the process. This phenomenon is called electroluminescence.<sup>10-12</sup> Operated based on this process, in a light-emitting diode (LED) a great number of charge carriers (electrons and holes) are constantly injected, from two opposing directions based on their charge type, into an inorganic or organic semiconductor in the presence of an external circuit. Light is emitted as the consequence of recombination of electrons and holes along with relaxation radiative decays. The color of the light depends on the energy gap of the semiconductor materials in the active region of the LED. LEDs are widely used in displays such as digital clocks, advertising panels and digital meters.

The electroluminescence phenomenon was first discovered from inorganic materials in 1936, when Destriau *et al.* observed high field electroluminescence from a ZnS phosphor powder dispersed in an isolator and sandwiched between two electrodes.<sup>13</sup> In 1960s, inorganic semiconductors based LEDs became commercially available.<sup>14</sup>

Materials that were generally used for inorganic LEDs are semiconductor crystals from groups III and V of the periodic table such as gallium arsenide phosphide denoted as GaAsP, gallium phosphide denoted as GaP, gallium aluminum arsenide denoted as AlGaAs and so forth.<sup>15</sup> Developing highly efficient materials and technologies for devices, which can emit over the entire color range, especially blue color is a major focus of current inorganic LED research.<sup>16</sup>

Electroluminescence from organic materials was first observed for anthracene in 1963.<sup>17</sup> However, building practical LEDs from an organic electroluminescent solid remained a challenge until 1987 when Tang and coworkers successfully demonstrated an efficient and low-voltage OLED based on vacuum-deposition of thin layers of small active organic molecules.<sup>18</sup> Subsequently, Burroughes *et al.* showed that polymeric thin films could also be employed for use in efficient electroluminescent devices.<sup>19</sup> Since these early discoveries, tremendous efforts have been devoted to improve the performance of OLEDs such as life time and efficiency, and to develop new materials for flat panel display applications.<sup>20</sup> The first OLED displays based on tris(8-hydroxyquinoline)-aluminum ( $\text{Alq}_3$ )/diamine heterojunction monochrome emitting became commercially available in 1996.<sup>21,22</sup> In comparison to inorganic semiconductors, organic materials offer great advantages. OLED materials are less expensive to produce and they can be processed more conveniently. Layer thickness of less than 100 nm can be achieved through vacuum deposition or spin coating techniques. With organic materials, devices can be fabricated with large display area with lithographic pattern. One of the

greatest advantages of organic materials is the tunability of their emissive color by structural modification. Even blue and white LEDs, which were rarely achieved with inorganic materials, have been effectively developed with organic semiconducting materials.<sup>23-25</sup> In all, demonstrated with excellent performance characteristics such as high brightness and contrast, full color range, wide viewing angle and low operating voltage, OLEDs are gaining more and more acceptance in the flat panel display industry.

### **7.1.2. Structure of Organic Light Emitting Diodes**

Schematically described in Figure 7-2, an OLED consists of a series of sequentially-deposited organic thin films sandwiched between two electrodes. One of these two electrodes is transparent and usually deposited on a glass substrate in order to observe the light emission. Generally, an indium tin oxide (ITO)-coated glass is used as the anode. Electroactive metals with low work functions, such as Al, Ca, Mg and In, are used as cathodes in order to ensure an efficient electron injection. When operated under an electric field, electrons and holes are injected and migrated from the contacts toward the organic active layer, forming electron-hole pairs (excitons) that recombine radiatively to emit light.

Single organic layer device is the simplest OLED configuration, which consists of only an electron transporting or hole transporting organic layer (ETL or HTL, respectively) between an anode and a cathode. This charge transporting layer also serves as the electroluminescent layer (LL). In this type of device, the manufacturing process is

relatively simple due to the single layer structure. However most of the organic molecules exhibit different mobility of electrons and holes. Excitons usually form in the vicinity of one of the electrode-organic interfaces, where the nonradiative exciton recombination is enhanced.<sup>26</sup> As a consequence, the life time and efficiency are limited.

The luminescence efficiency can be significantly improved in heterojunction OLEDs fabricated by sequential deposition of two or more organic layers.<sup>27</sup> In single-heterojunction devices, LL functions as one transporting layer (i.e., ETL or HTL), and another transporting layer is fabricated for the carriers with opposite charge (i.e., HTL or ETL). In a double-heterojunction OLED, ETL, LL and HTL are fabricated as discrete layers. This structure renders a further control of carrier mobility. These heterojunction structures provide the opportunity to select transporting layers with proper mobility and confine the carriers in LL, where radiatively recombining excitations are formed. They also allow individually optimize the materials used for electroluminescence and carrier transport.

Another approach to shift the recombination zone toward the center of LL, is to synthesize new oligomers and polymers with proper charge affinity for a balanced charge injection.<sup>28</sup> Compared to the enormous potential variety of organic compounds, the number of luminescent molecules presently available for OLEDs is relatively small. It is also noticed that, unlike the situation for inorganic semiconductors such as silicon, controlled doping of organic molecular thin films to adjust polarity of carrier transport has not been convincingly demonstrated. Molecular structure modification therefore has



been explored as a direct and effective way to new materials with improved luminescent and conducting properties.

In this chapter, we demonstrate structure modifications of 8-hydroxyquinoline, the ligand compound of Alq<sub>3</sub> complex, through chemical substitution reactions in hoping of obtaining new luminescent materials with improved carrier mobility.

### 7.1.3. 8-Hydroxyquinoline-Metal Complexes

Being generally considered as excellent emitting and electron transporting materials, 8-hydroxyquinoline-metal complexes have been extensively studied as model compounds for practical OLED displays.<sup>29-33</sup> The first successful high-performance OLED was demonstrated using Alq<sub>3</sub>/N,N'-diphenyl-N,N'-bis(3-methylphenyl)-1,1'-biphenyl-4,4'-diamine (TPD) single heterostructures.<sup>18</sup> In a Alq<sub>3</sub>/TPD device, Alq<sub>3</sub> serves as both LL and ETL.<sup>34</sup> Holes are injected from TPD into Alq<sub>3</sub>. The hole mobility of TPD is of the order of  $\sim 10^{-3}$ ,<sup>35</sup> while in Alq<sub>3</sub> the electron mobility is  $\sim 10^{-4}$  cm<sup>2</sup>V<sup>-1</sup>s<sup>-1</sup> with hole mobility at least two orders of magnitude lower.<sup>36,37</sup> The small hole mobility of Alq<sub>3</sub> results in a short diffusion length of  $\sim 30$ -100 Å.<sup>38</sup> Therefore, excitons are formed in a region near the ETL-HTL interface known as “recombination zone”. The existence of such a working zone results in a low EL efficiency, and limits the LL thickness of optimal devices. Several groups have reported significantly increased EL efficiencies with multilayer configurations. These approaches derived benefit from either depositing a thin layer of organic hole blocking materials such as oligothiophenes<sup>39-41</sup>, or fabricating a

layer of materials such as copper phthalocyanine,<sup>42</sup> and polyaniline,<sup>43,44</sup> on to the anode surface to facilitate improving the hole injection efficiency.

As previously mentioned, structure modification also provides great opportunities to obtain new materials with improved properties. However, there have been relatively few studies on substituted metalloquinolates, which may exhibit strong photoluminescence and improved carrier mobility.<sup>45-48</sup> Metalloquinolates methyl derivatives were used as an electron transporting and hosting material in a highly efficient dye-doped multilayer OLED.<sup>49,50</sup> The synthesis of sulfonamide substituted metallo-8-hydroxyquinolines has been reported.<sup>51</sup> As compared to the unsubstituted AlQ<sub>3</sub> and ZnQ<sub>2</sub>, these materials exhibit increased solubility in nonpolar solvents, and their strong luminescence is blue-shifted.

An ideal LL material would be bipolar, allowing transporting of both holes and electrons. The recombination of charge carriers would then occur in the whole volume of the luminescent layer with high efficiency. Bipolar emitting materials not only improve the performance of OLEDs, but are likely to simplify the packing process of the device with single layer structures as well. In this study, we proposed to introduce electron-donating aromatic amine side groups such as aniline derivatives, onto 8-hydroxyquinoline ring. With highly conjugated structure, the new metalloquinolates may exhibit enhanced hole transporting ability as compared to the unsubstituted ones. Moreover, the 1-4-phenylenediamine derivative side chains offer the opportunity to chemically control the oxidation state of the molecule.<sup>52-54</sup> It would be greatly interesting

if we could fine-tune the carrier transporting by controlling the oxidation state of the materials. As to the emitting properties, these substitutes would narrow the band gap between the HOMO and LUMO, and therefore have measurable effects on the electrophotonic spectra.<sup>55</sup> It is also anticipated that the addition of bulky side chains to metalloquinolates should lead to better thin film formation by reducing the tendency of aggregation and crystallization, a philosophy which has guided the design of charge transport agents in multilayer electro-optical devices.<sup>56</sup>

## **7.2. Experimental**

Two aniline derivatives modified 8-hydroxyquinoline ligands were prepared by chemical oxidation-addition reactions of 8-hydroxyquinoline with N,N-dimethyl-1,4-phenylenediamine and 1,4-phenylenediamine, respectively, followed by hydrogenation.

### **7.2.1. Materials**

1,4-Phenylenediamine (97%, Aldrich), 8-hydroxyquinoline (99%, Aldrich), N,N-dimethyl-1,4-phenylenediamine (97%, Aldrich), aluminum isopropoxide (99.99%, Aldrich), copper (II) acetate (98%, Aldrich), palladium (10 wt%, on active carbon, Aldrich) benzene (99.8%, anhydrous, Aldrich) and potassium peroxide (99.7%, Fisher) were all used as received without further purification. Sodium phosphate (monobasic, anhydrous, Sigma) and sodium phosphate (dibasic, heptahydrate, Sigma) were used to

prepare phosphate buffer solution. Ethyl alcohol (dehydrate, Pharmco), was used as cosolvent in the synthesis of ligands.

### **7.2.2. Synthesis of N,N'-bis(N,N-dimethyl-4'-aminophenyl)-5-imino-7-amino-8-ketoquinoline (1a) and N,N'-bis(4'-aminophenyl)-5-imino-7-amino-8-ketoquinoline (2a)**

The aniline derivative modified quinoline ligands were prepared by a chemical oxidation reaction. A typical synthesis procedure to **1a** is as follows: to a 500-ml three-neck round bottom flask, 8-hydroxyquinoline (1.5 g, 0.010 mol), 300 ml phosphate buffer (pH 8.0, 0.1 M) and 30 ml ethanol were added. The flask was placed in a 75 °C oil bath. The suspension was magnetically stirred for about 30 minutes till a complete dissolution was achieved. In a 100-mL beaker, another reactant, N,N-dimethyl-1,4-phenylenediamine (2.9 g, 0.021 mol), was dissolved in 30 ml buffer (pH 8.0, 0.1 M). To ensure the homogeneity of the solution, 30 ml ethanol was added as cosolvent. The resultant reddish-purple solution was poured into the flask as one portion followed by dropwisely addition of the oxidant solution, potassium persulfate (4.1 g, 0.015 mol) in 100 ml pH 8.0 buffer. With vigorous stirring, potassium persulfate solution was added into the reaction mixture at about 1 drop/sec. The reaction mixture was kept stirred for 3 h at 75 °C. The dark blue precipitate was filtered through a Buchner funnel under a reduced pressure. Upon drying at ambient temperature for 24 h under vacuum, 2.4 g crude product was collected in the yield of 59 %. After recrystallization in toluene twice, 1.3 g target ligand compound was obtained as dark blue crystals. Mp 228-229 °C. <sup>1</sup>H

NMR (250 MHz, DCCl<sub>3</sub>)  $\delta$  (ppm): 8.95 (1H d), 8.91(1H d), 7.61(1H t), 7.11(1H d), 7.08(1H d), 7.03(1H d), 7.00(1H d), 6.86(1H s), 6.78(1H d), 6.75(1H d), 6.72(1H, d), 6.69(1H d), 3.00(6H s), 2.95(6H s). IR (neat cm<sup>-1</sup>) 3327, 1648 1593, 1518, 1352, 1295, 1244, 1165, 1139, 1080, 1011, 947, 811, 722, 686, 605. Exact Mass calcd for C<sub>25</sub>H<sub>25</sub>ON<sub>5</sub> (M<sup>+</sup>): 411.2059; found: 411.2059. Anal. Calcd for C<sub>25</sub>H<sub>25</sub>ON<sub>5</sub>: C: 72.99; H: 6.08; N: 17.03; O: 3.89; found: C: 73.42; H: 6.05; N: 16.72; O: 3.81.

Following the similar procedure, ligand **2a** was prepared by a reaction with 8-hydroxyquinoline and 1,4-phenylenediamine as starting materials. Mp 259 – 260 °C. <sup>1</sup>H NMR (250 MHz, DCCl<sub>3</sub>)  $\delta$  8.93 (1H d), 8.89(1H d), 7.63(1H t), 7.00(1H d), 6.96(1H d), 6.89(1H d), 6.85(1H d), 6.76(1H s), 6.75(1H d), 6.70(1H d), 6.69(1H, d), 6.65(1H d), 3.73(2H, br), 3.68(2H, br). IR (neat cm<sup>-1</sup>) 3430, 3350, 3202, 2200, 1657, 1599, 1518, 1340, 1284, 1164, 1086, 1012, 826, 720, 614. Exact Mass calcd for C<sub>21</sub>H<sub>18</sub>ON<sub>5</sub> (M<sup>+</sup>+H): 356.1511; found: 356.1497. Anal. Calcd for C<sub>21</sub>H<sub>17</sub>ON<sub>5</sub>: C: 70.99; H: 4.82; N: 19.71; O: 4.50; found: C: 71.43; H: 5.01; N: 18.56; O: 5.00.

### 7.2.3. Syntheses of Complexes

These ligands can be used to prepare various new complexes by reaction with different metal ions. In this study, aluminum(III) and copper(II) ions were used to demonstrate the versatility of this synthesis. To coordinate with metal ions, the keto group of the ligands was reduced to a hydroxyl group prior to the complexation reaction. A palladium catalytic hydrogenation strategy was employed to accomplish this reduction.

The reduction of ligands can be easily visualized by the color of the solution, which turned gradually from dark blue to yellow brown. As a typical procedure to prepare tris(*N,N'*-bis(*N,N*-dimethyl-4'-aminophenyl)-5,7-amino-8-hydroxyquinolato)aluminum (**3a**), ligand **1a** (0.25 g, 0.60 mmol) was dissolved in 50 ml anhydrous benzene in a 100-ml round-bottom flask under hydrogen atmosphere. As catalyst, 0.030 g palladium on active carbon was added. With hydrogen continuously bubbled, the reaction mixture was refluxed with stirring for 4 h. The resulting solution was yellow brown. Aluminum isopropoxide (0.041 g, 0.20 mmol) was then added in one portion. A reddish color was immediately visible. The reaction mixture was kept stirred at reflux for 1 day. The resultant solution was deep reddish purple with precipitates. In a nitrogen box, reaction mixture was filtered through a Gooch crucible. Reddish purple precipitate was collected and rinsed with benzene. To remove the palladium/carbon catalyst powder, the precipitate was re-dissolved in methylene chloride and filtered. The filtrate was collected and concentrated. Powdery reddish purple solid was collected and dried under vacuum to give 0.24 g of **3a** in a yield of 85 %. Complex **3b** was prepared through the reaction of **2a** and aluminum isopropoxide with similar procedures. The product was obtained in a yield of 72 %.

Copper(II) complex was prepared by the reaction of ligand **1a** (0.082 g, 0.40 mmol) and copper(II) acetate (0.036 g, 0.20 mmol) following the similar procedures to the aluminum complexes. The reaction offers a yield of 78 %. All complexes were characterized by mass spectroscopy with satisfactory results.

#### 7.2.4. Instrumentation and Characterization

Infrared (IR) spectra of KBr powder-pressed pellets were recorded on a Perkin-Elmer 1600 FTIR spectrometer. The  $^1\text{H}$ -NMR spectra were measured on an IBM Bruker AM 250 FT-NMR spectrometer with chloroform- $\text{d}_3$  as solvent. Mass spectra were obtained with a VG ZAB-HF high resolution mass spectrometer. UV-Vis spectra were recorded on a Perkin-Elmer Lambda 2 spectrometer. Melting points were measured using a MEL-TEMP melting point apparatus and were uncorrected. Elemental analysis was carried out by Micro-Analysis Inc.

### 7.3. Results and Discussion

Two highly conjugated aniline derivatives modified quinoline ligands (i.e., **1a** and **2a**) were prepared by chemical oxidation-addition reactions of 8-hydroxyquinoline with N,N-dimethyl-1,4-phenylenediamine and 1,4-phenylenediamine, respectively. The synthesis is depicted in Figure 7-3. Potassium persulfate was used as the oxidant. The reaction was held at 75 °C for 3 h. Retaining such a relatively high reaction temperature is in favor of obtaining the product in good purity and of the additions onto both 5 and 7 positions.<sup>57</sup> The ligands were obtained as substituted 8-ketoquinolines, of which the compositions and structures were characterized by mass spectra, elemental analysis, IR, and  $^1\text{H}$  NMR spectroscopy.

Both as-synthesized ligands were blue powder. After recrystallization **1a** was obtained as blue crystals and gave apparently satisfactory elemental analysis and exact

mass measurement. While attempting to recrystallize **2a** was not very successful. The exact mass measurement is consistent with calculated molecular weight. The elemental analysis, however, exhibits slight discrepancies with theoretical values. The difficulty of purifying **2a** probably results from the relatively higher reactivity of its primary amine end groups, in comparison with the tertiary amine in **1a**.

The  $^1\text{H}$  NMR spectra of ligand **1a** and **2a** in chloroform- $d_3$  are shown in Figures 7-4 and 7-5. Apart from the aromatic multiplets at 6.69~ 6.78 ppm and 7.00~ 7.11 ppm arising from the protons in two benzene rings, two sets of multiplets can be seen at low field. The doublets at 8.91 ppm and 8.95 ppm are assigned to the protons  $\text{H}_2$  and  $\text{H}_4$ , which have similar chemical shift and are both coupled to  $\text{H}_3$  in quinoline ring. The signal at 7.61 ppm area is the triplet of  $\text{H}_3$  in quinoline ring. The positions of  $\text{H}_{2-4}$  were further confirmed by spin decoupling experiments. Decoupling spectra were shown as the insertion of Figure 7-4. When the  $\text{H}_2$  and  $\text{H}_4$  area was irradiated, the signal of  $\text{H}_3$  collapsed to the expected singlet. A similar, but mirror image situation was found in  $\text{H}_2$  and  $\text{H}_4$  area when  $\text{H}_3$  was irradiated. Decoupled  $\text{H}_2$  and  $\text{H}_4$  presented as singlet due to their similar chemical shift. The narrow singlet at 6.86 ppm is expected from the proton  $\text{H}_6$  in quinoline ring. When comparing the NMR spectrum of **1a** (Figure 7-4) with that of **2a** (Figure 7-5), there is a noticeable difference in the high field resulted from the different end groups of the side chains. In the spectrum of **1a**, the protons from  $-\text{CH}_3$  appear as two narrow singlets at 2.95 and 3.00 ppm whereas for ligand **2a** the end group protons are from  $-\text{NH}_2$  and therefore present two broad overlap singlets at 3.70 ppm area.



The absence of the proton from the -NH- in the 7 position substituting side chain is because either the proton fast exchanges with water or the signal is too broad to be observed.

The IR spectra of two ligands are compared in Figure 7-6. In general for both ligands, the characteristic band at  $1590\text{ cm}^{-1}$  arises mainly from both C=N and C=C stretching of the quinoline unit, and the band near  $1504\text{ cm}^{-1}$  is attributed to the C-C aromatic ring stretching vibration of the benzenoid diamine unit. The strong absorption at  $1650\text{ cm}^{-1}$  associates with C=O stretching vibration of keto group on quinoline ring. The aromatic C-H stretching exhibits a characteristic sharp peak at  $3320\text{ cm}^{-1}$ . The structure difference between **1a** and **2a** can be distinguished from IR absorption in high energy region. The aliphatic C-H broad band at around  $2860\text{ cm}^{-1}$  is clearly observed from the spectrum of **1a**, which has -CH<sub>3</sub> as end groups. In the contrast, the primary amine groups in **2a** exhibit the typical N-H stretches at  $3170\text{ cm}^{-1}$  and  $3400\text{ cm}^{-1}$ . The absence of the strong O-H stretching band at  $3200\text{-}3600\text{ cm}^{-1}$  further confirms the keto structures for **1a** and **2a**.

The formation of keto quinoline is anticipated due to the presence of oxidant in the synthesis. The keto form aniline derivative modified quinoline ligands can be easily reduced to hydroxyl form through hydrogenation. However, it was noticed that in the air the keto ligands (e.g., **1b**) undergo oxidation and regenerate their keto forms (e.g., **1a**). This reversible process may affect the synthesis and properties of obtained complex

compounds, since we noticed that only hydroxyl ligands can coordinate with metal ions. This re-oxidation process was in-depth studied with UV-Vis spectroscopy.

Due to the structure similarity between ligands **1a** and **2a**, the former was used as the example compound to study the re-oxidation reaction. A similar situation was also observed with **2a**. The solution of **1a** in benzene is dark blue. After hydrogenation, fully reduced **1b** in benzene exhibits a characteristic yellowish color. When exposed to air, the solution gradually changes the color back to blue which is indicative of the oxidation of **1b**. This distinctive color change from **1b** to **1a** allows us to monitor the oxidation process of **1b** with UV-Visible spectroscopy. Figure 7-7 shows a series of UV-Vis spectra of **1b** obtained at different exposing time. The spectrum of pure **1b** exhibits two strong absorption peaks at 290 and 330 nm, along with a relatively weak and broad one at 420 nm. These bands are attributed to  $\pi$ - $\pi^*$  transitions of conjugated ring system with the presence of a hydroxyl group. During oxidation, the peaks at shorter wavelength attenuated and blue shifted. A new band associated with the benzoid to quinoid excitonic transition gradually developed at around 600 nm due to the formation of **1a**. As a function of reaction time, the UV absorbance at 330 nm, 420 nm and 600 nm were recorded and shown in Figure 7-8. It can be clearly observed that the absorbance at 330 and 420 nm decreases with the oxidation time while the absorbance at 600 nm increases with time. To further study the kinetics of this re-oxidation transformation, the reaction order was evaluated based on the change of UV absorbance at 600 nm during the reaction.

The absorbance at 600 nm is the characteristic of **1a** and can be correlated with the concentration of **1a** by applying Beer's Law:  $A = \epsilon b c$ , where  $A$  is referred to the measured absorbance,  $\epsilon$  is a constant of proportionality call the molar absorptivity or molar absorption coefficient, and  $b$  is the path length.<sup>58</sup> In our measurement, we keep  $b$  constant at exactly 1.00 cm, so the expression reduces to  $A = \epsilon c$ . Table 7-1 summarizes the absorbance of a series of solutions of **1a** with different concentrations at 600 nm. Constructing a plot with the concentrations on the x-axis against the corresponding absorbance on the y-axis we can determine  $\epsilon$ , which is the slope of the best straight line through the points. The UV absorbance at 600 nm of a series of **1a** solutions at different concentration was measured and summarized at below. The Beer's Law calibration curve was shown in Figure 7-9, from which  $\epsilon$  was found to be  $12.58 \text{ mM}^{-1} \cdot \text{cm}^{-1}$ .

Once the molar absorptivity of **1a** was obtained, the concentration of **1b** during an oxidation reaction from **1b** to **1a** was derived and plotted in Figure 7-10 based on Figure 7-8(c). An assumption was made that **1b** was completely oxidized to **1a** when the absorbance at 600 nm is stabilized. The insert of Figure 7-10 shows the linearity between logarithm of concentration of **1b** and elapsed reaction time, which suggests that this reaction is first order, or most likely pseudo first order due to the excess amount  $\text{O}_2$  compared with the relatively low concentration of **1b**. It is plotted in Figure 7-10 the theoretical trace of concentration as a function of oxidation time in a first order reaction. The experimental curve reasonably approximates the theoretical one up to about 80 % conversion.

To prevent the re-oxidation of the ligand during the complexation reaction, hydrogen was continuously supplied as protection atmosphere. The ligands in the reduced form were successfully coordinated with different metal ions, such as aluminum and copper. As the result, 8-hydroxyquinoline derivative-metal complexes were obtained as inert salts, which have been defined as necessary form for complex emitting materials used in organic EL devices.<sup>59</sup> The fresh-prepared aluminum and copper complexes were all reddish-purple powder and soluble in most of organic solvent. The mass spectra of aluminum complexes of **1a** and **2a** were sampled in Figure 7-11 and 7-12. For both complexes, the mass spectrum exhibits three distinctive peaks at masses equal to ligand (L), L<sub>2</sub>Al and L<sub>3</sub>Al. In comparison with the L and L<sub>2</sub>Al peaks, the height of L<sub>3</sub>Al peak is relatively low, especially in the case of ligand **2a**. The pattern that two strong peaks at L and L<sub>2</sub>Al are of about the same height, highly suggests that these two peaks result from the fragmentation of complexes (L<sub>3</sub>Al). Similar mass spectrum pattern were observed for copper complexes.

These complexes are stable when stored under nitrogen atmosphere, while once being exposed to air, especially in solution, the complexes gradually change the color to deep blue, which is the characteristic of the keto quinoline ligands. The stability of the complexes was studied with mass spectroscopy. The mass spectrum of the sample stored under nitrogen for two weeks (Figure 7-13, bottom) resembles the same spectroscopic pattern as the fresh-prepared sample with three peaks at L, L<sub>2</sub>Al and L<sub>3</sub>Al. The complex

$L_3Al$  dissociated to free ligand (L) in 2 h when exposed to air in solution (Figure 7-13, top).

Both UV and mass spectroscopy measurements indicate that the complexes prepared with the new ligands are not stable in air, probably resulting from the instability of the hydroxyl form of substituted quinolines. Due to this unfavorable phenomenon, the electrophotonic properties of the new metaloquinolate are still under investigation at present time.

#### **7.4. Conclusions**

Two highly conjugated aniline derivative modified 8-hydroxyquinoline ligands,  $N,N'$ -bis( $N,N$ -dimethyl-4'-aminophenyl)-5-imino-7-amino-8-ketoquinoline and  $N,N'$ -bis(4'-aminophenyl)-5-imino-7-amino-8-ketoquinoline, have been synthesized and fully characterized with mass spectroscopy, elemental analysis, NMR, Infrared and UV-Visible spectroscopes. After introducing aniline derivative side groups onto quinoline ring, new ligands were obtained in their keto forms, which can be easily reduced to hydroxyl forms with platinum catalyzed hydrogenations. Exposed to air, the hydroxyl quinolines show strong tendency to be oxidized back to keto quinolines. The kinetics of these oxidation reactions was spectrophotometrically studied with UV-Visible spectroscopy. The reaction was found to be approximately a first order reaction.

With these new ligands, aluminum and copper complexes were prepared as potential electroluminescent materials. The structures of the complexes were confirmed

with mass spectroscopy. By introducing the highly conjugating structures to ligands, the new complexes were proposed to exhibit improved charge transporting properties in comparison with unsubstituted 8-hydroxylquinoline. The charge transporting properties may be furthermore adjusted by controlling the oxidation state of the molecules. Even though we were not able to reveal the electrophotonic properties of these complexes due to their instability in air, the feasibility of obtaining new ligands and metalloquinolates through molecular design was demonstrated.

### 7.5. Acknowledgments

I greatly appreciate Dr. Anthony Addison for his help with electrochemistry studies and insightful suggestion on the preparation of the ligands and complexes. I also want to thank Dr. Jeff Honovich of Drexel University for his help with the mass spectral measurement I thank Dr. Shuxi Li of Drexel University, Dr. Bing Hsieh of Xerox Corporation, Dr. Fotios Papadimitrakopoulos of University of Connecticut for valuable discussions in the early stage of this study.

### 7.6. References

1. Matters, M.; De Leeuw, D. M.; Vissenberg, M. J. C. M.; Hart, C. M.; Herwig, P. T.; Geuns, T.; Mutsaers, C. M. J.; Drury, C. J. *Opt. Mater.* **1999**, *12*, 189.
2. Drury, C. J.; Mutsaers, C. M. J.; Hart, C. M.; Matters, M.; de Leeuw, D. M. *Appl. Phys. Lett.* **1998**, *73*, 108.
3. Recent reviews: (a) Pribat, D.; Plais, F. *Diffusion and Defect Data--Solid State Data, Pt. B: Solid State Phenomena* **2001**, *80*, 385. (b) Hung, L. S. *Proc. Int. Conf. Solid-*

- State and Integrated Circuit Technology* **2001**, 2, 1228. (c) Cropper, A. D.; Cok, R. S.; Feldman, R. D. *Proce. SPIE-Int. Soc. Opti. Eng.* **2001**, 4105, 18. (d) Kowalsky, W.; Benstem, T.; Bohler, A.; Dirr, S.; Johannes, H.-H.; Metzdorf, D.; Neuner, H.; Schobel, J. *Adv. Solid State Phys.* **1999**, 39, 9.
4. Bulović, V.; Burrows, P. E.; Forrest, S. R. *Semiconductors and Semimetals* **2000**, 64, 255.
  5. Mahon, J. K.; Zhou, T. X.; Burrows, P. E.; Forrest, S. R.; Thompson, M. E.; *Proc. SPIE-Int. Soc. Opt. Eng.* **1998**, 3279, 87.
  6. Wakimoto, T.; Murayama, R.; Nagayama, K.; Okuda, Y.; Nakada, H. *Appl. Surf. Sci.* **1997**, 113, 698.
  7. Mitchke, U.; Bauerle, P. *J. Mater. Chem.* **2000**, 10, 1471.
  8. Segura, J. L. *Acta Polym.* **1998**, 49, 319.
  9. Cheng, S.; S. Li; A. W. Addison; F. Papadimitrakopoulos; B. R. Hsieh; Y. Wei. *Polym. Mater. Sci. Eng.* **2000**, 83, 274.
  10. Ono, Y. A. *Electroluminescence in Encyclopedia of Applied Physics*, Trigg, G. L.; ed. VCH, Weinheim, 1993, vol. 5, p.295.
  11. Von Gorkom, H. J. *Photosyn. Res.* **1996**, 48, 107.
  12. Gonzalez Velasco, J. *Electroanaly.* **1991**, 3, 261.
  13. Destriau, G. *J. Chim. Phys.* **1936**, 33, 587.
  14. Holonyak, N. Jr.; Bevacqua, S. F. *Appl. Phys. Lett.* **1962**, 1, 82.
  15. Bergh, A.; Craford, G.; Duggal, A.; Haitz, R. *Physics Today* **2001**, 54, 42.
  16. Graford, M. G.; Steranka, F. M. *Light-Emitting Diodes in Encyclopedia of Applied Physics*, Trigg, G. L.; ed. VCH: Weinheim, 1993, vol. 8, p.485.
  17. Pope, M.; Kalmann, H. P.; Magnante, P. *J. Chem. Phys.* **1963**, 38, 2042.
  18. Tang, C. W.; Van Slyke, S. A. *Appl. Phys. Lett.* **1987**, 51, 913.
  19. Burroughes, J. H.; Bradley, D. D. C.; Brown, A. R.; Marks, R. N.; Mackay, K.; Friend, R. H.; Burns, P. L.; Holmes, A. B. *Nature*, **1990**, 347, 539.

20. Recent reviews: (a) Friend, R. H.; Gymer, R. W.; Holmes, A. B.; Burroughes, J. H.; Marks, R. N.; Taliani, C.; Bradley, D. D. C.; Dos Santos, D. A.; Bredas, J. L.; Logdlund, M.; Salaneck, W. R. *Nature* **1999**, *397*, 121. (b) Kraft, A.; Grimsdale, A. C.; Holmes, A. B. *Angew. Chem. Int. Ed.* **1998**, *37*, 402. (c) Grell, M.; Bradley, D. D. C. *Adv. Mater.* **1999**, *11*, 895. (d) *Organic Electroluminescence Materials and Devices*, Miyata, S.; Nalwa, H. S.; ed. Gordon and Breach Publishers: Amsterdam, 1997. (e) Lüssem, G.; Wendorff, J. H. *Polym. Adv. Technol.* **1998**, *9*, 443.
21. Nakada, H.; Tohma, T. In *Inorganic and Organic Electroluminescence/EL 96*, Berlin, Mauch, R. H.; Gumlich, H.-E., eds. Wissenschaft und Technik Verl.: Berlin, 1996.
22. Wakimoto, T.; Murayama, R.; Nagayama, K.; Okuda, Y.; Nakada, H.; Tohma, T. *Society for Information Display, International Symposium, Digest of Technical Papers*, **1996**, *27*, 849.
23. Ohmori, Y.; Tsukagawa, T.; Kajii, H. *Molecular Crystals and Liquid Crystals Science and Technology, Section A: Molecular Crystals and Liquid Crystals* **2001**, *370*, 1.
24. Liu, M. W.; Zhang, X. H.; Lai, W. Y.; Lin, X. Q.; Wong, F. L.; Gao, Z. Q.; Lee, C. S.; Hung, L. S.; Lee, S. T.; Kwong, H. L. *Phys. Stat. Solid. A: Appl. Res.* **2001**, *185*, 203.
25. Fujii, H. U.S. Pat. Appl. Publ. US 20020071963, A1 20020613, 2002.
26. Scott, J. C.; Karg, S.; Carter, S. A. *J. Appl. Phys.* **1997**, *82*, 1454.
27. Adachi, C.; Tsutsui, T.; Saito, S. *Optoelectron. Devices Technol.* **1991**, *6*, 25.
28. Armstrong, Neal R.; Wightman, R. Mark; Gross, Erin M. *Annu. Rev. Phy. Chem.* **2001**, *52*, 391.
29. Tang, C. W.; VanSlyke, S. A.; Chen, C. H. *J. Appl. Phys.* **1989**, *65*, 3610.
30. Hong, Z.; Wang, D.; Ma, D.; Zhao, X.; Jing, X.; Wang, F. *Synth. Met.* **1997**, *91*, 321.
31. Inada, H.; Yonemoto, Y.; Wakimoto, T.; Imai, K.; Shirota, Y. *Mol. Cryst. Liq. Cryst.* **1996**, *280*, 331.
32. Strukelj, M.; Jordan, R. H.; Dodabalapur, A. *J. Am. Chem. Soc.* **1996**, *118*, 1213.
33. Gauvin, S.; Santerre, F.; Dodelet, J. P.; Ding, Y.; Hlil, A. R.; Hay, A. S.; Anderson, J.; Armstrong, N. R.; Gorjanc, T. C.; D'Iorio, M. *Thin Solid Films* **1999**, *353*, 218.



34. Stossel, M.; Staudigel, J.; Steuber, F.; Blassing, J.; Simmerer, J.; Winnacker, A.; Neuner, H.; Metzdorf, D.; Johannes, H.-H.; Kowalsky, W. *Synth. Met.* **2000**, *111*, 19.
35. Stolka, M.; Janus, J. F.; Pai, D. M. *J. Phys. Chem.* **1984**, *88*, 4707.
36. Chen, B.; Liu, S. *Synth. Met.* **1997**, *91*, 169.
37. Kepler, R. G.; Beeson, P. M.; Jacobs, S. J.; Anderson, R. A.; Sinclair, M. B.; Valencia, V. S.; Cahill, P. A. *Appl. Phys. Lett.* **1995**, *66*, 3618.
38. Lin, L.-B.; Jenekhe, S. A.; Young, R. H.; Borsenberger, P. M. *Appl. Phys. Lett.* **1997**, *70*, 2052.
39. Uchiyama, K.; Akimichi, H.; Hotta, S.; Noge, H.; Sakaki, H. *Synth. Met.* **1994**, *63*, 57.
40. Muccini, M.; Mahrt, R. F.; Hennig, R.; Lemmer, U.; Baessler, H.; Biscarini, F.; Zamboni, R.; Taliani, C. *Chem. Phys. Lett.* **1995**, *242*, 207.
41. Yassar, A.; Valat, P.; Wintgens, V.; Hmyene, M.; Deloffre, F.; Horowitz, G.; Srivastava, P.; Garnier, F. *Synth. Met.* **1994**, *67*, 277.
42. Tang, C. W. U.S. Pat. 4 356 429, 1982.
43. Yang, Y.; Heeger, A. *J. Appl. Phys. Lett.* **1994**, *64*, 1245.
44. Yang, Y.; Westerwheele, E.; Zhang, C.; Heeger, A. *J. Appl. Phys. Lett.* **1995**, *77*, 694.
45. Hamada, Y.; Sano, T.; Fujita, M.; Fujii, T.; Nishio, Y.; Shibata, K. *Jpn. J. Appl. Phys.* **1993**, *32*, L541.
46. (a) Chen, C. H.; Shi, J.; Tang, C. W. *Macromol. Symp.* **1998**, *125*, 1. (b) Chen, C. H.; Shi, J. *Coord. Chem. Rev.* **1998**, *171*, 161.
47. Matsumura, M.; Akai, T. *Jpn. J. Appl. Phys.* **1996**, *35*, 5357.
48. Wang, J. F.; Jabbour, G. E.; Mash, E. A.; Anderson, J.; Zhang, Y. D.; Lee, P. A.; Armstrong, N. R.; Peyghambarian, N.; Kippelen, B. *Adv. Mater.* **1999**, *11*, 1266.
49. Kido, J.; Iizumi, Y. *Appl. Phys. Lett.* **1998**, *73*, 2721.
50. Hamada, Y.; Kanno, H.; Sano, T.; Fujii, H.; Nishio, Y.; Takahashi, H.; Usuki, T.; Shibata, K. *Appl. Phys. Lett.* **1998**, *72*, 1939.

51. Hopkins, T.A.; Meerholz, K.; Shaheen, S.; Anderson, M. L.; Schmidt, A.; Kippelen, B.; Padias, A. B.; Hall, H. K.; Jr.; Peyghambarian, N.; Armstrong, N.R. *Chem. Mater.* **1996**, *8*, 344.
52. Honzi, J.; Ulbert, K.; Hadek, V.; Thustakova, M. *Chem Commun.* **1965**, 440.
53. Wei, Y.; Yang, C.; Ding, T. *Tetrahedron Lett.* **1996**, *37*, 731.
54. Wang, Z. Y.; Yang, C.; Gao, J. P.; Lin, J.; Wei, Y.; Li, S. *Macromolecules* **1998**, *31*, 2702.
55. Albright, T. A.; Burdett, J. K.; Whangbo, M.-H. *Orbital Interactions in Chemistry*, Wiley: New York, 1985.
56. Yuh, H.-J.; Pai, D. M. *Mol. Cryst. Liq. Cryst.* **1990**, *183*, 217.
57. *Quinolines, Part II*, J. Gurnos, ed. John Wiley & Sons: Chichester, New York, Brisbane, Toronto, Singapore, 1982.
58. Physical Chemistry, Alberty, R.; Silbey, R. J., John Wiley & Sons: New York, 1992.
59. Hamada, Y. *IEEE Trans. Elec. Devi.* **1997**, *44*, 1208.

Table 7-1. The UV absorbance at 600 nm of a series of **1a** solutions at different concentration.

Concentration <sup>a</sup> (mM)	Absorbance at 600 nm
0.04	0.519
0.08	1.0273
0.12	1.5049
0.16	2.0239

<sup>a</sup> The solutions were prepared using benzene as solvent.

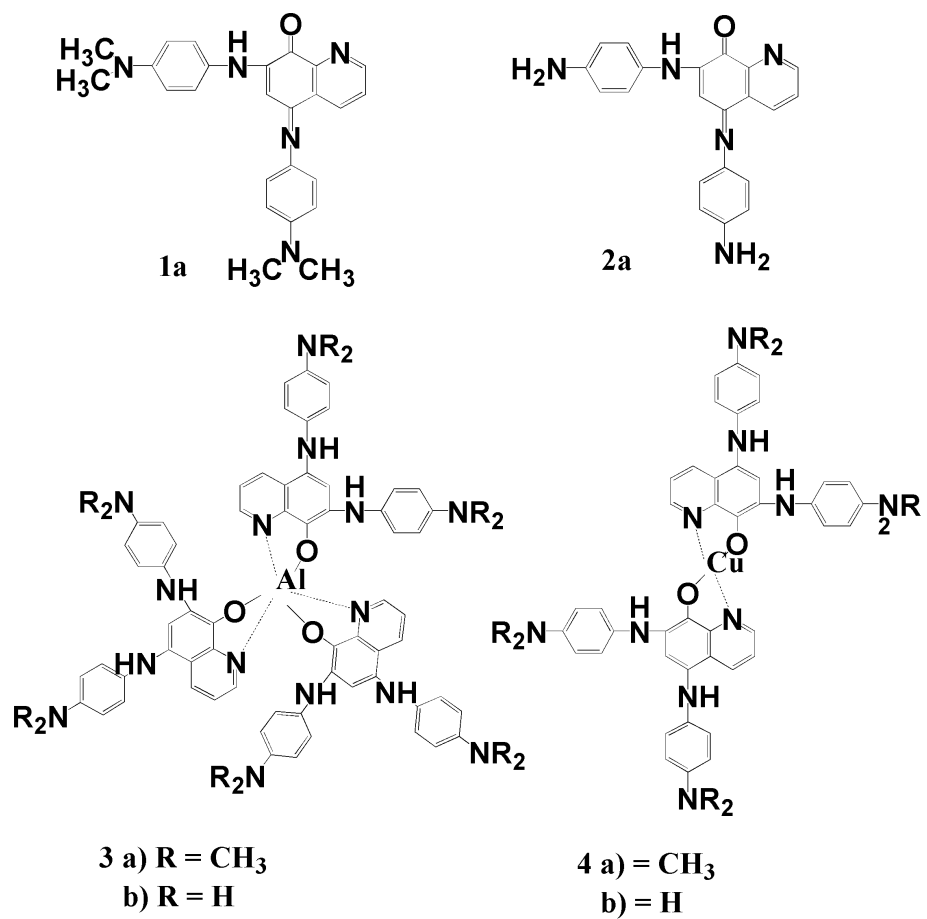


Figure 7-1. Structures of new ligands and their metal complexes.

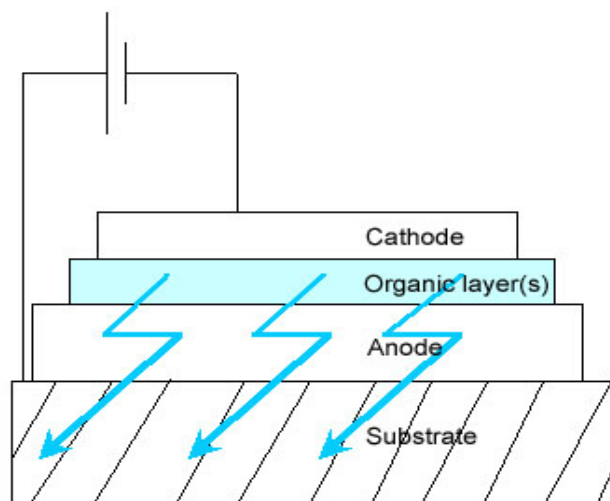


Figure 7-2. Schematic cross-sectional diagram of an OLED.

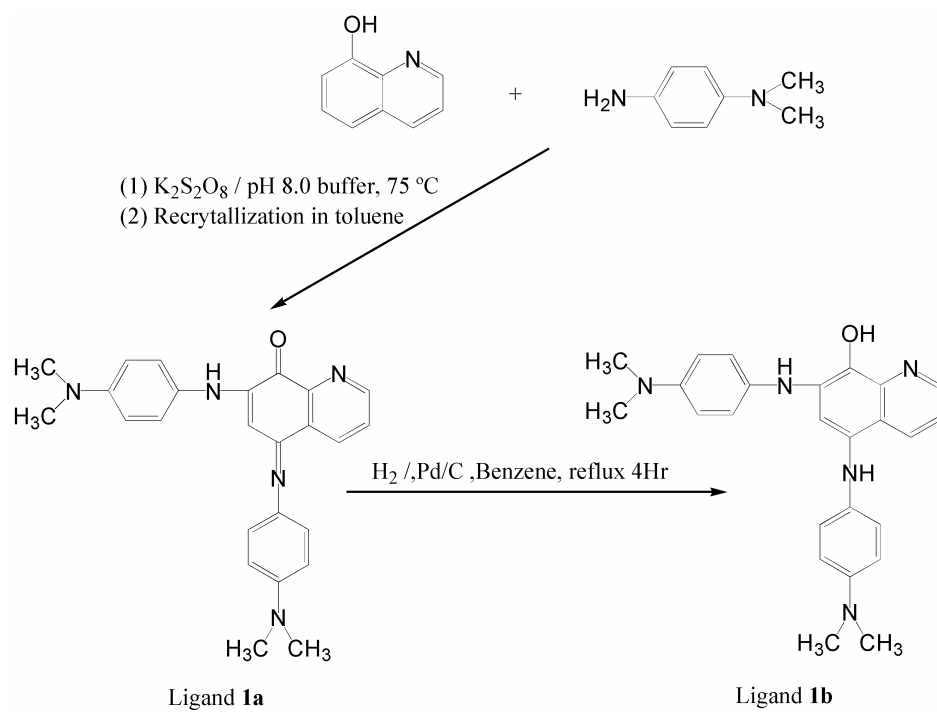


Figure 7-3. Synthetic scheme for ligand **1a** and hydrogenation reaction of ligand **1a** to ligand **1b**.

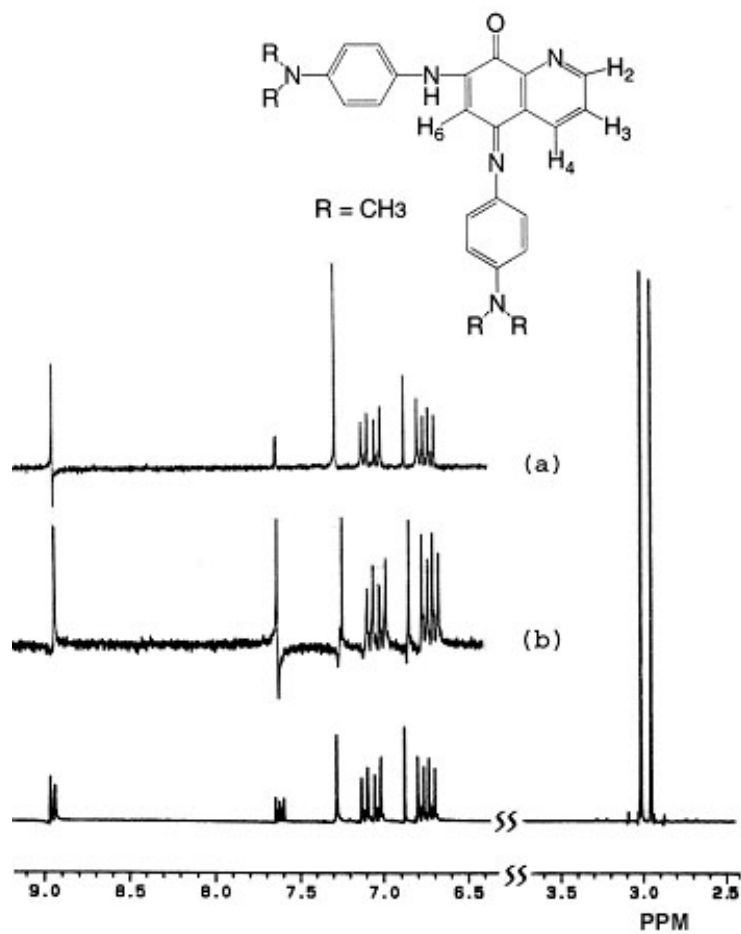


Figure 7-4. NMR Spectra of ligand **1a**. Inserts: (a) H<sub>2</sub> and H<sub>4</sub> irradiated, (b) H<sub>3</sub> irradiated.

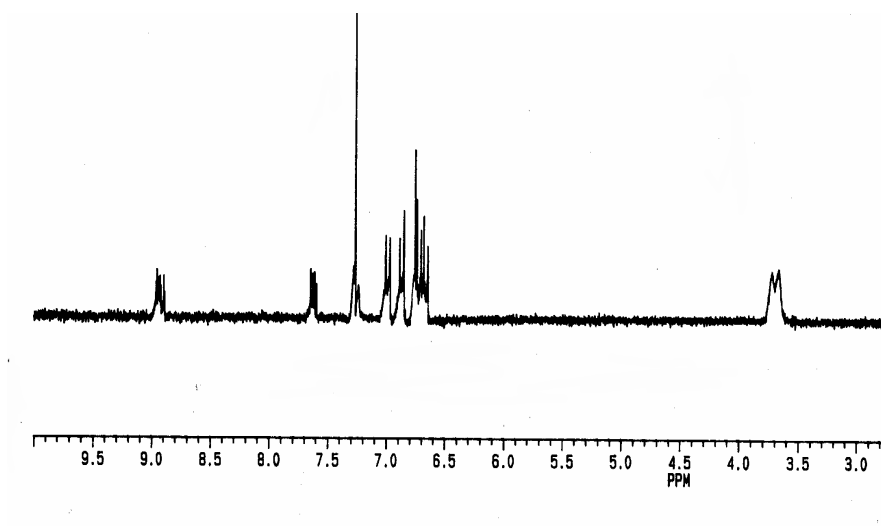


Figure 7-5. NMR Spectrum of ligand **2a**.



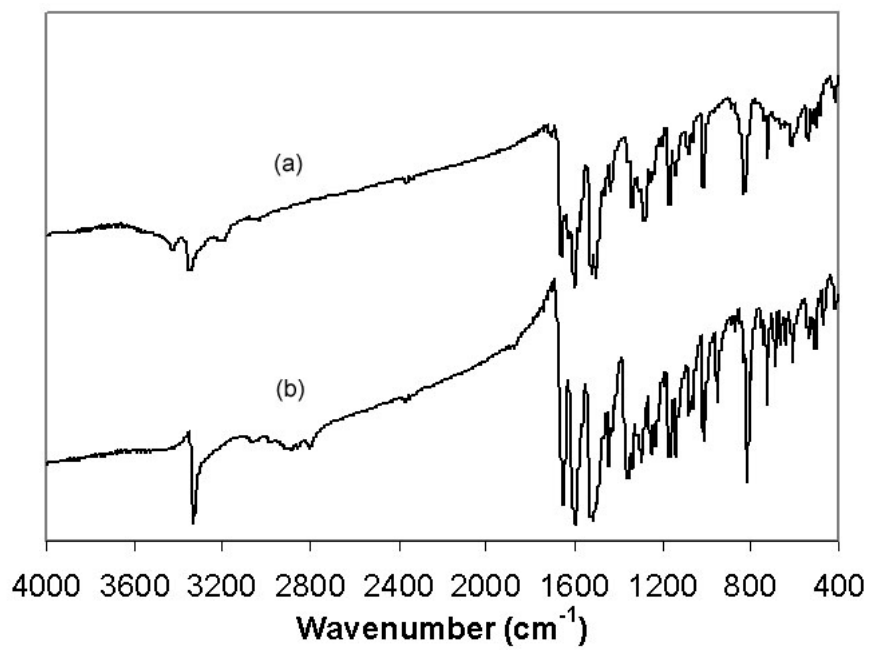


Figure 7-6. FT-IR spectra of (a) ligand **1a** and (b) ligand **2a**.

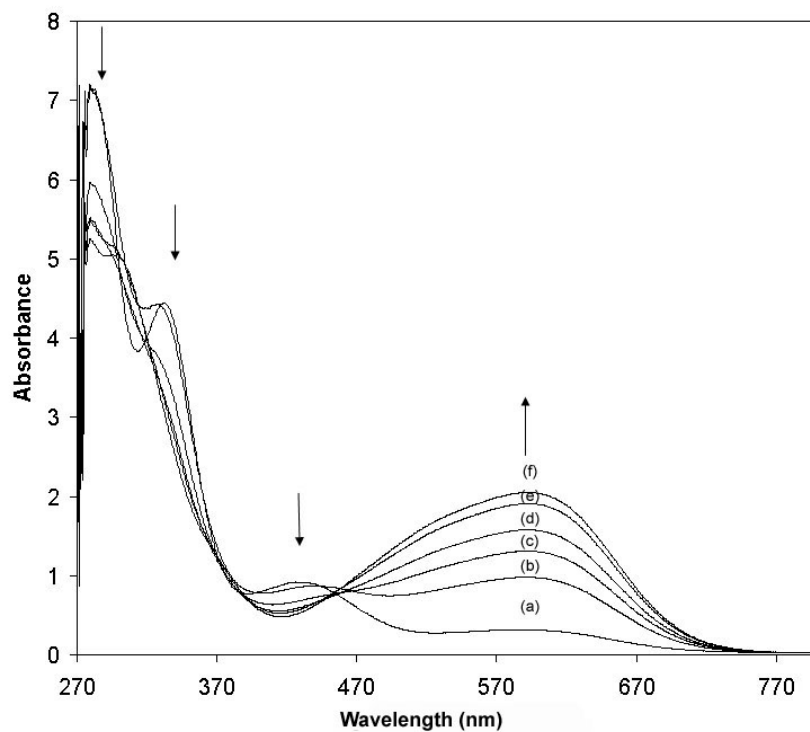


Figure 7-7. Representative UV-Vis spectra for ligand **1b** in toluene after oxidation with air for various reaction periods: (a) 1, (b) 4, (c) 7, (d) 10, (e) 13, (f) 16 min.

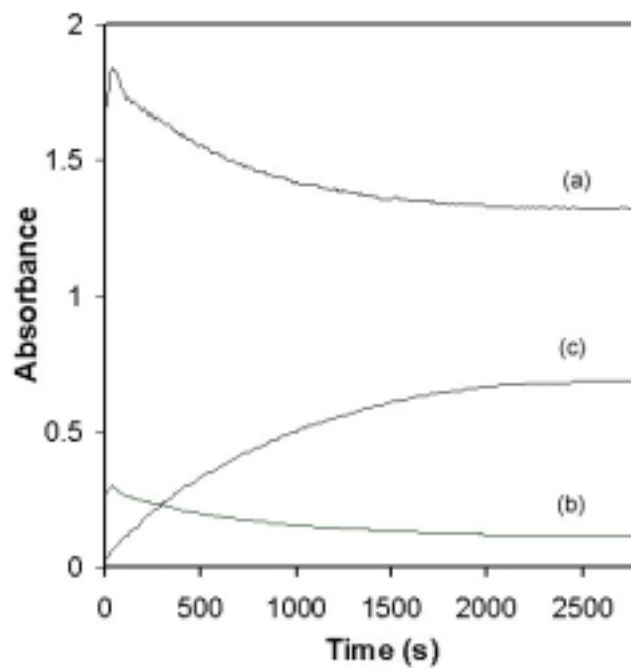


Figure 7-8. During air oxidation: **1b**  $\rightarrow$  **1a**, UV absorbance at (a) 330 nm, (b) 420 nm and (c) 600 nm measured as a function of time.

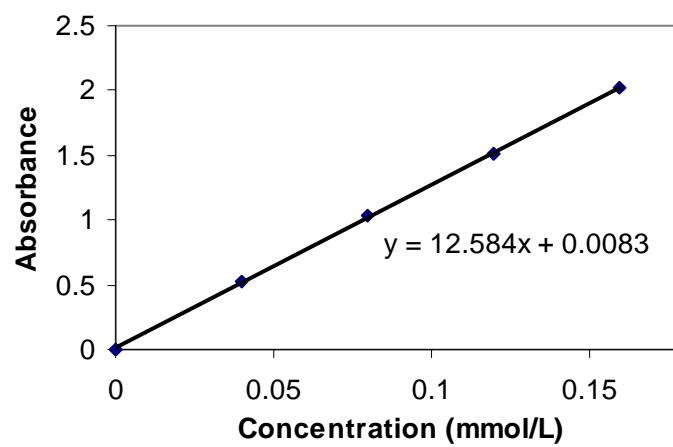


Figure 7-9. Molar absorptivity calculation curve plotted based on UV absorbance at 600 nm of ligand **1a** at different concentrations.

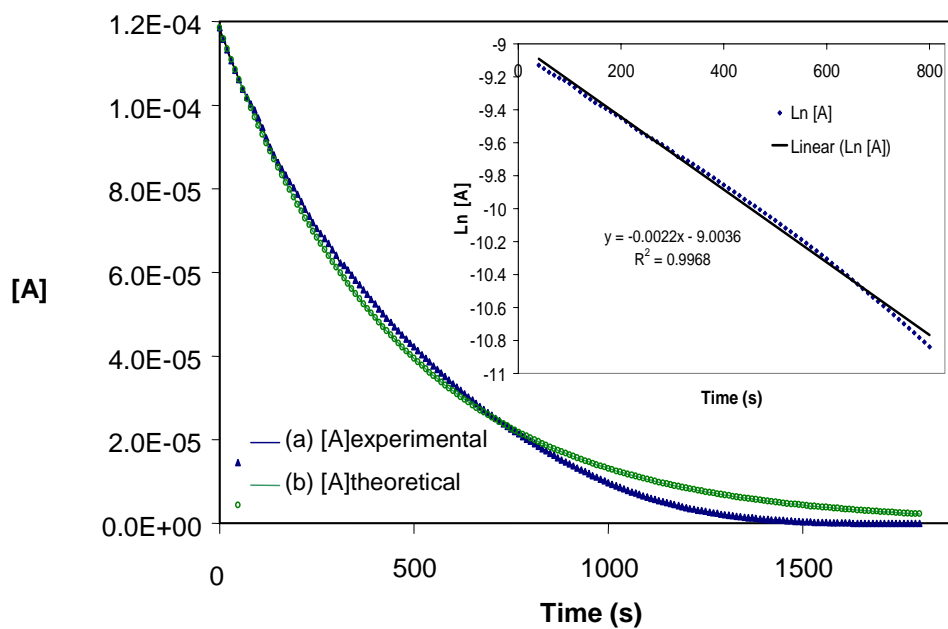


Figure 7-10. Plot of concentration of **1b** versus reaction time (a) based on UV measurement, (b) for first-order reaction with the same initial concentration. Insert: linear plot for a first-order reaction - natural logarithm of concentration of **1b** versus reaction time.

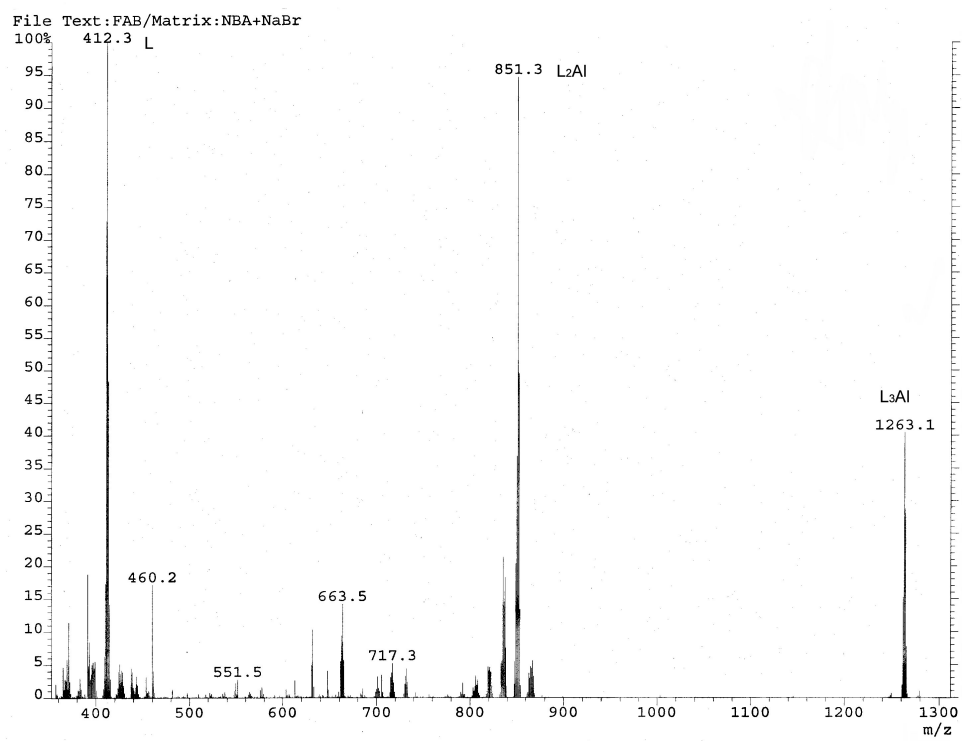


Figure 7-11. Mass spectrum of aluminum complex **3a**.

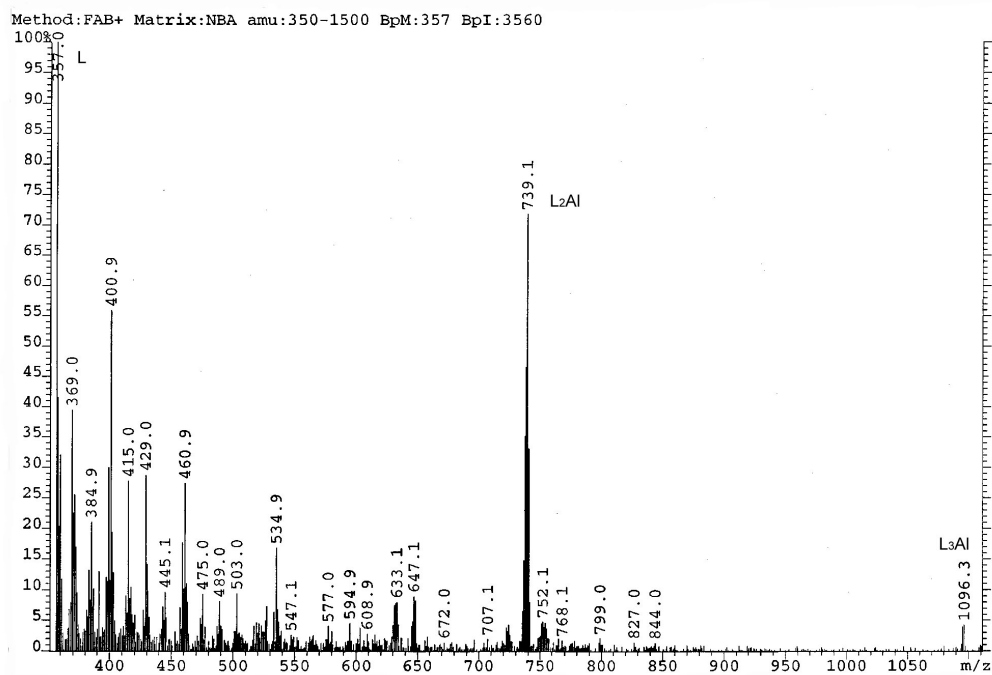


Figure 7-12. Mass spectrum of aluminum complex **3b**.

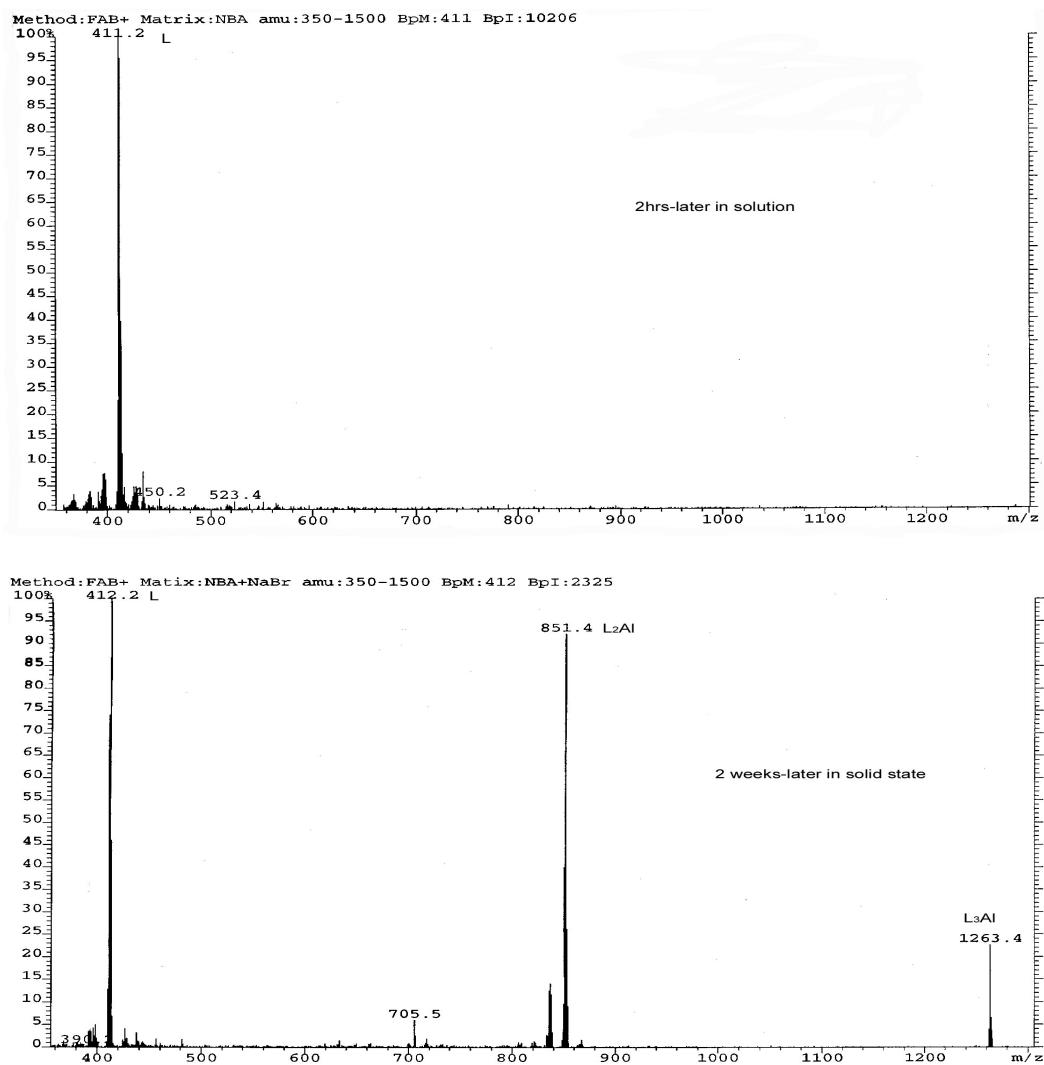


Figure 7-13. Mass spectra of aluminum complex sample, **3a**, stored under different conditions. Top: dissolved in acetone for 2 h; Bottom: powder under nitrogen for 2 weeks.



## **Chapter 8. Concluding Remarks**

This dissertation has been focused on the synthetic process development, characterization and applications of novel nanostructured, electroactive and bioapplicable materials. This work consists of two major areas. One is nanostructured porous materials. In this study, using the newly developed nonsurfactant templating sol-gel method, we have further demonstrated its outstanding versatility, including various synthetic routes using different novel templates, controllable product morphologies such as spheres and monoliths, and fine-tunable product compositions. In addition the proposed synthetic pathway and obtained products are “biofriendly”. Another theme of my research was to investigate electroactive materials and their various applications with an emphasis on biocompatible electroactive materials. The biofriendly property of these materials has been demonstrated by preliminary cell growth studies. Therefore, the objectives of this dissertation have been achieved.

These two topics are further summarized in detail in the following sections.

### **8.1. Nanostructured Materials**

Novel nanostructured sol-gel materials and composites have been developed with tailored properties, such as structure, morphology, composition and functions. The versatility of the nonsurfactant templated sol-gel method has been studied and successfully demonstrated with carefully designed synthetic conditions including

template selection, pH and composition. The convenient synthesis as well as the well defined structures and physicochemical properties render the nanostructured materials great suitability for a wide range of potential applications, such as functional coatings, chemical and biological sensors, drug delivery devices, etc.

Thermal sensitive compounds were demonstrated as a new category of nonsurfactant template functioning as pore structure directing agent as well as providing opportunities to a convenient template removal with low temperature thermal treatment. Benzoin was selected as an example of thermal sensitive compounds due to its thermal instability and good solubility in pyridine solvent. Template containing silica materials have been synthesized through acid-catalyzed sol-gel reactions of a silicon alkoxide (i.e., tetraethyl orthosilicate) in the presence of benzoin with varied concentrations from 20 to 60 wt %. Due to the characteristic thermal decomposition of benzoin, more than 90 wt % of the template can be effectively removed from the silica matrix when heated at 150 °C for 6 h under a reduced pressure (<1 mmHg). Nitrogen sorption and transmission electron microscopy (TEM) characterizations reveal that the mesoporous materials obtained after the template removal possess a three-dimensional network of interconnected wormlike mesopores. The pore parameters are adjustable by simply varying the template concentration. By controlling the heating temperature and duration, adjustable partial template removal can be achieved, which provides us necessary information to establish the insightful correlations between template distribution and pore structure.

In contrast to the conventional high temperature calcination for template removal, which usually involves temperatures of 500-600 °C, thermal sensitive compound templated method affords the possibility to obtain mesoporous materials with a thermal template removal at much lower temperature. The usefulness of the process therefore can be extended to applications wherein the materials involved are thermally instable, such as biomolecule immobilizations and coatings on metal or polymer thin film substrates, etc. It is expected that a wider range of thermal sensitive or photo sensitive compounds could be used as nonsurfactant templates aiming at the development of more convenient synthetic route under ambient conditions.

Demonstrating the versatility of the template species is just one of aspects to explore the many advantages provided by nonsurfactant template pathway. For example, it would be desirable to gain the morphology control over the porous materials. While most of the previously reported mesoporous materials prepared with nonsurfactant templated method were powders, monolithic materials or thin films, this is the first time mesoporous spheres were prepared with a nonsurfactant template. The synthesis route is closely related to the nonsurfactant template sol-gel pathway to prepare mesoporous silica monoliths. A proper amount of basic catalyst,  $\text{NH}_4\text{OH}$ , provides the necessary pH during the sol-gel reactions for the desired morphology. The obtained silica nanoparticles exhibit well-defined spherical shape and uniform size with the diameter of around 420 nm. Demonstrated with fructose, nonsurfactant templates can be easily removed from as-synthesized template-silica composites by water extraction at ambient temperature. After

the removal of template, the silica well retained the spherical shape, and similar to the monolithic materials prepared with nonsurfactant templates, exhibit mesoporous characteristics. To a certain extent, the porosity of the silica nanospheres can be fine-tuned by adjusting the template concentration in the starting sol mixture. With both the mild, convenient synthetic process and the well-defined morphology and nanostructure, the obtained mesoporous spheres are suitable for further investigation as the matrix materials for biosensor and drug delivery applications.

Besides porous materials with different morphologies, nonsurfactant templating pathway can be also used to prepare nanocomposites. With a colloidal gold sol as second sol component, mesoporous gold-silica porous nanocomposites have been prepared. The synthesis procedures are based on the nonsurfactant templated pathway by producing homogeneous sol-gel solution in the presence of templates to obtain the final dried gel monoliths. After a one-step template removal and gold annealing calcination, nanocomposites were obtained with nano-sized gold particles randomly dispersed throughout the silica matrix. The materials exhibited typical mesoporosity, which is affected by gold concentration arising from combined effects of “co-templating” and “space occupying”. While offering good confinement, the transparent silica matrix presents no appreciable effect on the optical properties of gold nanoparticles. The composites exhibit unique size-dependent characteristics of gold nanoparticles, such as plasmon resonance and Raman surface enhancement effect. Incorporating high surface area and the high porosity of the silica framework with the optical and physical/chemical

properties of gold nanoparticles makes the materials good candidates for promising sensing and catalyst applications. In collaboration with the researchers in US Army Research Laboratory, these materials are under active studies for fabricating new chemical and biological sensors to test for contamination in soldiers' water supplies. The preliminary results indicate that with surface enhanced Raman spectroscopy, the sensing of 10 ppm cyanide ion in water with our gold-silica mesoporous nanocomposites can be achieved in a timescale of minutes. A more detailed description of this study will be included in Ms. Kate Ong's Ph.D. dissertation in Dr. Yen Wei's group at Drexel University.

Nanostructured organic-inorganic thin films have been fabricated on mica and glass slide substrates by solvent casting and self-assembly of vinyl modified silica nanoparticles. Formation of covalent interactions between organic and inorganic nanophases was achieved by a photo-initiated free radical polymerization with a relatively high conversion. Most areas of the nanocomposite films have multilayer structure of low-dimensional close packing of silica particles, while a portion (about 10 %) of the thin films exhibits monolayer array of nanoparticles with short-range local ordering. The optimization of ordered structure formation of the nanocomposite thin film should be further studied. As an extended study, porous silica nanoparticles prepared via our nonsurfactant templated pathway have been assembled on glass substrate surface. The particle films exhibit monolayered structure with partial hexagonal arrangement,

which depends on size distribution. These films are of interest due to their potential in optics, barrier coating and sensor applications.

## **8.2. Electroactive, Bioapplicable Materials**

A biological templated synthetic pathway has been developed to improve the biocompatibility and processability of conducting polymers for the biological applications. The chemical initiated polymerization of aniline monomer is carried out in an acidic aqueous environment in the presence of collagen fibrils. The incorporation of polyaniline with biomaterials such as collagen renders the material significantly improved biocompatibility and water solubility in comparison to PANI control sample synthesized in the absence of collagen. Electroactivity of the complex is controllable through reversible doping/de-doping process. The attractive forces between aniline monomer and collagen, such as hydrogen bonding, electrostatic interactions, van der Waals attractions, and hydrophobic interactions, may play important roles in the formation of entwined PANI-Colla complex. The existence of such interactions is confirmed with IR spectroscopy studies. Demonstrated with attachment, variation and differentiation studies of neuron cells on PANI-Colla coated culture dishes, the new material shows improved biocompatibility, as expected, in comparison to PANI. Binding of this electroactive polymer with a biological material provides opportunities towards studying the fundamental structure-property relationship of biomacromolecules, and developing novel intelligent scaffold materials, biosensors and electronics.

In an effort to obtain new electroluminescent materials for organic light emitting diodes (OLED) applications, two highly conjugated aniline derivative modified 8-hydroxyquinoline ligands, N,N'-bis(N,N-dimethyl-4'-aminophenyl)-5-imino-7-amino-8-ketoquinoline and N,N'-bis(4'-aminophenyl)-5-imino-7-amino-8-ketoquinoline, have been synthesized. The obtained ligands exist in their keto forms, which can be concluded based on the characterization with mass spectroscopy, elemental analysis, NMR and IR spectroscopy. The compounds can be easily reduced to hydroxyl forms by hydrogenation. Upon exposure to air the hydroxyl quinolines can be oxidized back to keto quinolines. The kinetics of these oxidation reactions was spectrophotometrically studied with UV-Vis spectroscopy. The reaction was found to be approximately a first order reaction. The metal complexes were prepared with new ligands in their hydroxyl forms. It was found that these new complexes are not stable in air, especially when dissolved in solvent. With the introduction of conjugated side groups onto the 8-hydroxyquinoline ring structure, the charge transport ability of the materials should be improved. Even though we are not able to measure the electrooptical properties of the new materials so far, the feasibility of obtaining new ligands and metaloquinolates through molecular design was demonstrated. Further structure optimization is needed to improve the stability of the materials.

## **Appendix A. Stimuli-Responsive Polyphosphazenes as Controlled Drug Delivery Matrix Materials**

(An Independent Research Proposal Defended and Passed On May 03, 2001 in Partial Fulfillment of the Requirement for the Ph.D. Candidacy)

### **A.1. Abstract**

Biocompatible polymer matrix delivery system shows many advantages for controlled drug delivery, such as sustained release, effective conservation of drug activeness and adjustable controllability from various polymer architectures. Polyphosphazene, as a relatively new biodegradable polymer, has been widely studied as drug delivery matrix material. This polymer has an inorganic backbone that is biocompatible over time and able to degrade to harmless small molecule products: ammonia, phosphate, and water. Using polyphosphazene, the delivery system can be made bioerodible to avoid surgical removal of the device after use, and the degradability can be tailored to respond to different physiological environmental condition by appropriate choice of substituted side chains.

The objective of this proposed research is to investigate the modification of biodegradable polyphosphazenes with stimuli-responsive polymers and to further evaluate these materials as matrices for controlled drug delivery system, especially for pH and/or temperature sensitive drug release. In this proposed study, conformational changeable polymers as stimuli-responsive modifiers are either grafted onto polyphosphazene backbones as side chains or crosslinked to form interpenetrating polymer networks (IPN) with polyphosphazenes. Having the stimuli-responsive material



as sensor units, the biodegradable polyphosphazene matrices are to be constructed as living bodylike systems with functions of sensing the signal caused by disease, such as temperature or pH change, judging the magnitude of the signal, and then releasing the drug in direct response. These delivery systems are distinguished from the conventional polyphosphazene drug delivery systems in two ways: fast site-specific delivery and multi-pulsatile release responsive to external physical stimuli. The physical and chemical properties of stimuli-responsive polyphosphazenes are to be studied. The matrix delivery systems are to be prepared and evaluated for biodegradable controlled release.

## **A.2. Introduction**

### **A.2.1. Controlled Drug Delivery**

Controlled drug delivery and drug release systems, as the name implies, are devices designed to disseminate a drug when and where necessary, and at the proper dose. An ideally controlled drug delivery and release system should be capable of optimum response to the disease with minimum side-effects, sustained release, and prolonged efficiency. The majority of drugs used during the last few centuries for treatment of human diseases have been small molecules. Since the early 1970s, polymeric drug delivery systems have attracted much more research interests. The polymeric systems depending on their chemical basis and physical design can be classified into three categories: 1) *polymeric drugs*,<sup>1</sup> which are polymers having biological activity; 2) *polymeric prodrugs*,<sup>1</sup> which are prepared by covalently conjugate polymers to drugs; 3)

*biocompatible polymer matrices*,<sup>2</sup> which physically combine with established drug and work only as vehicles for delivering the drug to the body.

Most of the drug delivery systems currently being commercially used are produced with polymer matrices. This technique shows many advantages from the view point of *controlled* delivery. In a matrix delivery system, the drug is trapped within the polymer. There are mainly two release mechanisms, which might both be in effect in the same delivery system.<sup>2</sup> In diffusion controlled release the drug dissolves or diffuses from the polymer matrix, while in polymer erosion controlled release, the polymer has to first dissolve or disintegrate. In either case, the release of the drug is greatly affected by the chemical/physical properties of the matrix. So the control over the drug release could be achieved through appropriate selecting and designing of the polymer material. Another major advantage is that in this type of delivery system, the drug is simply encapsulated within the polymer matrix with no chemical bonding and remains in a biologically active form. As soon as being released from the polymeric matrix, the drug can immediately exert its effect upon the body. Its biological effect is the same as that when used alone and could be predicted based upon its release rate. The polymer matrix delivery approach also provides a sustained delivery. Either through a diffusion or polymer erosion mechanism, the release of the drug to the physiological environment is extended over a longer period than if the drug is used in its native form.

A variety of polymers, especially those biodegradable, are being used in the polymer matrix drug delivery system. These include aliphatic polyesters,<sup>3</sup>

polyanhydrides,<sup>4</sup> polyorthoesters,<sup>5</sup> polyaminoacid,<sup>6</sup> and polyphosphazene.<sup>7</sup> Among these materials, polyphosphazene as a novel biodegradable “inorganic polymer”, has attracted much research interests.

### **A.2.2. Polyphosphazene**

Polyphosphazenes are a class of polymers with backbones consisting of alternating phosphorus and nitrogen atoms. The repeating unit in polyphosphazenes is shown in Figure A-1,<sup>8</sup> where the side groups, R and R', can be organic, inorganic or organometallic. Interests in these polymers rely on the fact that, compared to other biodegradable polymer materials, polyphosphazenes are easier to be manipulated with different side groups. In addition, their physical and chemical properties are greatly affected by the nature of the side groups. Therefore, polymer with a wide range of properties can be obtained by appropriately choosing side chain groups.<sup>9</sup> The possibility to obtain polyorganophosphazene with different tunable properties makes those polymers potentially useful in many fields, ranging from pharmaceutical, industrial to agricultural applications.

#### **A.2.2.1. Synthesis of Polyphosphazenes**

Two different fundamental routes to synthesize substituted polyphosphazenes are shown in Figure A-2.<sup>10</sup> Method one starts from substitution reactions of the chlorine atoms on hexachlorocyclotriphosphazene to prepare phosphazene cyclic trimers with

different side groups. By ring-opening polymerization of these small cyclic trimers, polyphosphazenes with different substituents can be obtained.

Many new materials have been prepared through this direct synthesis.<sup>11</sup> However, the steric hindrance effect greatly limits the variety and the amount of the substituent on polymer chains.<sup>12</sup> To solve this problem, an alternative two-step reaction sequence was developed by Allcock and his co-workers in 1980s.<sup>13</sup> This synthesis route involves the preparation of poly(dichlorophosphazene) and a sequential substitution reaction of chlorine atoms. In the first step, poly(dichlorophosphazene) as highly reactive macromolecular intermediate, can be prepared by several different methods. The most effective route to high molecular weight poly(dichlorophosphazene) is via the ring-opening polymerization of the cyclic trimer, hexachlorocyclotriphosphazene at 250 °C in the molten phase or in solution. This reaction gives a polymer with a broad molecular weight distribution, but with an  $M_w$  near 2,000,000, which corresponds to approximately 15,000 repeating units per chain. More recently, a room-temperature, living cationic condensation polymerization of  $\text{Me}_3\text{SiN}=\text{PCl}_3$  method has also been developed through collaboration of Allcock and Manners.<sup>14</sup> This reaction yields narrow molecular weight distribution polymers, with excellent control of the molecular weight and access to block copolymers. The second step in the synthesis of Allcock's method involves the replacement of the chlorine atoms by reactions with different organic or organometallic groups. Typically, an average of 30,000 chlorine atoms per molecule could be replaced at this stage as the result of high reactivity of the P-Cl bond. Based on this macromolecular

substitution reaction, several hundred different polyorganophosphazenes have been synthesized. Most of the current industrial important polyphosphazenes are made by this method.

#### **A.2.2.2. Applications of Polyphosphazenes in Controlled Drug Delivery**

As a relatively new biodegradable polymer, polyphosphazene as drug delivery material has been widely studied. Compared with other drug delivery matrix materials, polyphosphazene shows particular advantages because it has an inorganic backbone that is biocompatible over time<sup>15</sup> and that degrades to harmless small molecule products: ammonia, phosphate, and water.<sup>16</sup> The system can be made bioerodible to avoid surgical removal of the device after use, and the degradability can be tailored to respond to different physiological environmental conditions by appropriate choice of substituted side chains. Many results show that the delivery systems designed with this material can accommodate a large variety of drugs including small drugs and macromolecules.<sup>17</sup> Release study has been explored with both hydrophobic and hydrophilic polyphosphazene.<sup>18,19</sup> The former ones are usually studied for polymer matrix erosion and diffusion release systems, while the latter ones are used to prepare hydrogel matrices after being crosslinked.

### **A.2.3. Stimuli-Responsive Polymers**

Stimuli-responsive polymers are a class of materials whose structure and properties change with external chemical and/or physical stimuli such as variation of pH, light, and temperature.<sup>20</sup> They are also called intelligent polymers. One category of the most interesting stimuli-responsive polymers is conformational changeable polymers. These materials can change their conformation from free extendable polymer chains to aggregated globule form reversibly as function of the external conditions. Some typical examples are poly(N-isopropylacrylamide) (PIPAAm),<sup>21</sup> polysilamine,<sup>22</sup> poly(acrylic acid),<sup>23</sup> and poly(N-acryloyl glycine).<sup>23</sup> These polymers usually have one or two functional end groups, through which the polymer could be grafted onto surfaces, membranes<sup>24</sup> and matrices as well as conjugated with biomolecules<sup>25</sup> to fabricate “intelligent devices” for separation, purification, chemical valve and drug delivery applications. The basic concepts for some applications are illustrated in Figure A-3.<sup>20,24</sup>

### **A.3. Proposed Research**

The objective of this proposed research is to investigate the modification of biodegradable polyphosphazenes with stimuli-responsive polymers and to further evaluate these materials as matrices for controlled drug delivery system, especially for pH and/or temperature sensitive drug release. In this proposed study intelligent materials as stimuli-responsive modifiers are either grafted onto polyphosphazene backbones as side chains or crosslinked to form interpenetrating polymer networks (IPN) with

polyphosphazenes. Obtained materials are physically mixed with therapeutic agent to fabricate the delivery systems. Having the stimuli-responsive material as sensor units, the biodegradable polyphosphazene matrices are to be constructed as living bodylike systems with functions of sensing the signal caused by disease, such as temperature or pH change, judging the magnitude of the signal, and then releasing the drug in direct response. They are distinguished from the conventional polyphosphazene drug delivery systems in two ways: fast site-specific delivery and multi-pulsatile release responsive to external physical stimuli.

### **A.3.1. Theoretical Considerations**

When designing a controlled drug delivery system, one might borrow ideas from the natural feedback systems. There exist many natural feedback systems in human body. One example is hormonal control system, which is critical to maintain regular body activities.<sup>26</sup> The release of hormones from endocrine glands is controlled by, among other factors, specific signals such as the concentration of messenger hormones, the power of biological electric current, and the body temperature. Similar to this, an ideally controlled drug delivery system should be able to sense the signal caused by disease, and correspondingly release the drug.

#### **A.3.1.1. Signal**

Temperature and pH are two of the triggering signals of the most interests for controlled drug delivery systems. The use of temperature as a signal is justified by the fact that the body temperature often deviates from the normal temperature (37 °C) as a symptom of disease accompanying by fever. This deviation can be a useful stimulus that activates the release of drugs from temperature sensitive drug delivery systems. Using pH as triggering signal, drug delivery systems could be designed to release the therapeutic agents at specific sites, because the variation in pH occurs naturally in some areas of the human body. For example, the pH in the stomach is about 2 and it goes up above 7 in small intestine through which most absorption takes place.<sup>27</sup> The pH-triggered system could also be used for tumor specific delivery due to the fact that the pH around tumor cells is lower than that around normal cells.<sup>28</sup>

#### **A.3.1.2. Proposed Intelligent Drug Delivery Systems**

In this proposed study, proper temperature or pH sensitive conformational changeable polymer is chosen according to the specific triggering signal and incorporated with polyphosphazenes as sensing unit. For example, poly(N-isopropylacrylamide) can be used to prepare temperature-sensitive polyphosphazene matrix materials and poly(acrylic acid) might be a good candidate for pH-sensitive modification. The stimuli-responsive polymer can be either grafted onto polyphosphazene main chains through various side chain reactions, or crosslinked to interpenetrate through a pre-formed



polyphosphazene network. Studies indicated that although the transition properties of the intelligent material could be modified by homo-copolymerization with other monomers,<sup>29</sup> when being grafted onto surfaces or interpenetrated with a second polymer,<sup>30,31</sup> the transition properties were not greatly affected by such structure changes. Combining tunable biodegradability and stimuli-responsiveness, the obtained novel matrix materials are to be explored for temperature and/or pH controlled drug delivery.

Different from conventional polyphosphazene drug delivery matrices, which are generally controlled by drug diffusion and polymer erosion, this proposed drug delivery system may release the drug through a different “squeezing” mechanism (Figure A-4).<sup>32</sup> In this proposed drug delivery system, the stimuli-responsive groups sense the variation of the external physiological condition (i.e., signal), and change their conformation from free extendable coils to compact globules. This change in turn stimulates the collapse of the entire polymer network. By the contraction of the polymer matrix, an outflux is caused and the drug is “squeezed” out. Through the squeezing mechanism, the system is expected to execute a more rapid release responding to the signal change. The conformational change of the grafted side chains can be achieved in a time scale of minutes.<sup>33</sup> The degradation study of polyphosphazenes with different substituents showed that varying the number of hydrophilic side groups resulted in a wide range of degradative lifetime. The polymer could degrade on the order of hours or years. Such variation in degradative characteristic provides the possibility to formulate the proposed release system based primarily on “squeezing” mechanism other than erosion. Moreover, the

conventional polyphosphazene delivery systems only respond to external conditions once, since they are usually activated by “erosion” of the polymer matrices. Once the polymer degradation is started, the releasing of the active content is rather abrupt and cannot be stopped. This is not in favor of an ideally controlled drug release. Using the proposed stimuli-responsive polyphosphazene delivery system, the drug release is induced by the reversible structural change of the sensing units. When the triggering signal changes back to the normal state, the polymer matrices regain the expandable form and the drug release is correspondingly slowed down. Thus, a feedback regulated multi-pulse drug release might be achieved due to the reversibility of the conformational change responding to the external condition. After delivery, the biodegradable polyphosphazene matrix degrades into small molecules and water-soluble side chains, which are harmless and easy to be eliminated from body.

Stimuli-responsive material modified polyphosphazenes provide a broad spectrum of possible biodegradable matrix materials for controlled drug delivery. A variety of intelligent materials sensitive to the desired triggering signal are available as sensing unit candidates. Moreover, the drug release profile could be adjusted by molecular architecture design. For a grafting modified polyphosphazene system, the more/longer graft side chains, the more quickly it responds to the environmental change.<sup>34</sup> Many factors might contribute to stronger contraction of matrices with more/longer graft side chains. Attractive force among dehydrated graft chains is enhanced for gels with many/long graft chains due to their larger molecular weight. Hydrophobic aggregation of

matrix is readily formed due to the entanglement of the long chains. In the interpenetrating network, two crosslinked sub-networks are physically entangled. Release profile could be adjusted through the rational design of the composition of polyphosphazenes and stimuli-responsive polymers. An optimum composition should be adapted for a desired release rate.

To better decipher this system, a specific temperature sensitive polyphosphazene release system to be developed base on this strategy is discussed here. As noted, poly(N-isopropylacrylamide) (PIPAAm) is one of the representative temperature sensitive polymers.<sup>35</sup> This material exhibits a lower critical solution temperature (LCST) around normal body temperature in aqueous environment. The polymer chains hydrate to form expanded structures below the LCST. However, above the LCST, they dehydrate to form compact structures. PIPAAm with various end groups, e.g., -NH<sub>2</sub> and -OH, are available for grafting. The reaction can be done through the replacement of the chlorines on the polyphosphazene main chains (Figure A-5). The obtained system delivers drugs through a temperature-controlled “squeezing” effect, as follows. As temperature increases, the PIPAAm grafted polyphosphazene matrix shrinks rapidly and expels drugs out; when the temperature drops back, the system reforms the expandable structure and suspends the drug release. This cycle is repeatable corresponding to the variation of temperature.

### **A.3.2. Experimental**

The synthesis of both polyphosphazenes and stimuli-responsive polymers has been extensively studied and is not described here in detail. Instead, modification of the polyphosphazene matrix materials, formulation of the release system, release and degradation studies are discussed below.

#### **A.3.2.1. Modification**

As noted, modification of polyphosphazenes with stimuli-responsive polymers could be realized through grafting or interpenetrating technique. Stimuli-responsive polymers with proper end groups, such as  $\text{-NH}_2$ , could be grafted onto polyphosphazene main chains by substituting chlorine atoms. Interpenetrating networks can be prepared from polymerizing the second monomer or crosslinking the second polymer in the presence of pre-crosslinked polyphosphazene network.

#### **A.3.2.2. Formulation**

Polyphosphazenes can accommodate many different drugs, from small molecules to macromolecules. For the release study purpose, a small molecule model drug, *p*-nitroaniline, is to be incorporated with the matrices to fabricate the delivery system. The release of this model drugs can be readily monitored spectrophotometrically at its absorption maximums, a wavelength of 380 nm.<sup>18</sup>

The delivery system can be made in virtually any shape or size, depending upon the physiological environment of use. The system can be shaped and sized for oral, ocular and anal insertion, for skin patches, or for parenteral insertion or injection. For the insertion and patch applications, a commonly used method is to cast the solution mixture of polymer and drug.<sup>18</sup> In an appropriate solvent, e.g., THF, drug and polymer are dissolved. The mixture is then cast in a pre-cooled mold and air dried till no detectable weight-changes.<sup>36</sup> For the injection purpose, the system would be in the form of powder in which each particle is small enough to fit through a syringe tip. In this case, the system could be prepared as microspheres by spray drying or emulsion/solvent evaporation techniques.<sup>37</sup>

#### **A.3.2.3. Degradation Study**

Degradation study is carried out in 0.1 M sodium phosphate buffer solutions at pH 7.4 under stirring. The specimens with known weight are immersed in the buffer solution at 37 °C. After each time interval with a specific length, samples are recovered and freeze dried to constant weight. Percent degradation is calculated based on weight loss of each sample.

#### **A.3.2.4. Release Study**

For the release study, samples are placed in 0.1 M sodium phosphate buffer solutions (pH 7.4) at 37 °C under stirring. Buffer solution is frequently removed and

replaced with fresh buffer using syringe in order to maintain the “sink” conditions. At preset time points, step-wise signal changes, e.g., variation of temperature and/or pH, are exerted to the release medium by replacing the buffer solution. For each signal period, the buffer solution is sampled at least 10 times. Using *p*-nitroaniline as model drug, the amount of released therapeutic agent in the sample solution can be readily evaluated with UV-visible spectrometer by observing the absorbance at 380nm. Other analysis methods, such as high performance liquid chromatography (HPLC) might also be used according to specific drugs.

#### **A.3.2.5. Instrumentation and Characterizations**

To better understand the structure-property relationship, characterization of stimuli-responsive material modified polyphosphazenes needs to be carried out.

Fourier transform infrared (FT-IR) spectroscopy is to be used to characterize the presence and chemical change of the functional groups in stimuli-responsive polyphosphazenes. For example, the absorption peak at  $3300\text{ cm}^{-1}$  due to the presence of amine groups can be used to monitor the graft reactions. FT-IR is particularly useful in studying the properties of interpenetrating network of polyphosphazenes and stimuli-responsive polymers, such as the physical interaction of the two networks.

Nuclear magnetic resonance (NMR) is an effective tool to study the chemical structures of grafted polyphosphazenes. Proton and  $^{13}\text{C}$  NMR can be used to confirm the substitution reaction since all the signals are attributable to the moieties presented on the

phosphazene main chains. Further information about the stoichiometry and sequence of different side chains bonding to phosphorous atoms can be obtained by the study of  $^{31}\text{P}$  NMR spectrum.

Light scattering technique and viscosity measurement can be employed to determine the molecular weight of grafted polyphosphazenes. The molecular weight distribution is to be measured with size exclusive chromatography (SEC), which may also be used preparatively to obtain narrow molecular weight fractions.

Differential scanning calorimetry (DSC) or differential thermal analysis (DTA) is to be used to evaluate the thermal properties/transitions of the modified polyphosphazenes. The thermodynamical and mechanical properties of polyphosphazenes, as matrix materials, can be obtained by thermal mechanical analysis (TMA).

Scanning electronic microscopy (SEM) and atomic force microscopy (AFM) are useful tools to characterize the surface morphology of the delivery system. The surface characterization and analysis are particularly valuable in evaluating how well the polymeric matrices react to the physiological environment.

#### **A.4. Ph.D. Thesis Research**

My thesis research is concentrated mainly on developing new nanocomposite and nanoparticle materials via sol-gel reactions for potential sensor and catalyst applications. Works have been focused on the synthesis and characterization of the mesoporous hybrid

materials, organic-inorganic hybrid nano-composite materials, and mesoporous nanoparticles. Other work also includes synthesis and characterization of electroactive materials and electroluminescent materials. All the works differ substantially from this proposed research.

### **A.5. Acknowledgments**

I gratefully acknowledge the members of my Ph.D. candidacy examination committee: Prof. Jean-Claude Bradley, Prof. Joe Foley, Prof. Amar Nath, Prof. Sally Solomon, Prof. Margaret Wheatley, and the chair: Prof. Anthony Addison, for their time and valuable suggestions.

### **A.6. References**

1. Ottenbrite, R. M. *ACS Symp.* **1990**, 469, 3.
2. Dun, R. L. **1990**, 469, 11.
3. Juni, K.; Nakano, M. *CRC Crit. Rev. Ther. Drug Carrier Syst.* **1987**, 3, 209.
4. Chasin, M.; Lewis, D.; Langer, R. *BioPharm Manuf.* **1988**, 1, 33.
5. Sparer, R. V.; Zentner, G. M. Process for the manufacture of bioerodible poly(ortho esters) and polyacetals. *Eur. Pat. Appl.* **1993**, 14 pp.
6. Huille, S.; Nicolas, F.; Bryson, N.; Soula, G. Delivery particles based on polyamino-acid(s) and methods for preparing same. *PCT Int. Appl.* **2000**, 30 pp. CODEN: PIXXD2 WO 0030618 A1 20000602.
7. Allcock, H. R. Biodegradable *Polymers as Drug Delivery Systems*. in: *Drugs and Pharmaceutical Sciences*. Eds, Chasin, M.; Langer, R. Macel Dekker, Inc.: New York, NY, 1990, Vol. 45, p.163.
8. Allcock, H. R. *Macromol. Symp.* **1999**, 144, 33



9. Allcock, H. R. *Adv. Mater.* **1994**, *6*, 106.
10. Qiu, L. Y.; Zhu, K. J. *J. Func. Polym.* **1999**, *12*, 115.
11. Allcock, H. R.; Schmutz, J.; Kosydar, K. M. *Macromolecules* **1978**, *11*, 179.
12. Allcock, H. R. *Polym. Prepr.* **1984**, *25*, 247.
13. Allcock, H. R. *Polym. Prepr.* **1982**, *23*, 72.
14. Honeyman, C. H.; Manners, I.; Morrissey, C. T.; Allcock, H. R. *J. Am. Chem. Soc.* **1995**, *117*, 7035.
15. Wade, C. W. R.; Gourlay, S.; Rice, R.; Hegyeli, A.; Singler, R.; White, J. *Biocompatibility of eight poly(organophosphasenes)*. in: *Organometallic Polymers*, eds, Carraher, C. E.; Sheats, J. E.; Pittman, C. U. Academic Press: New York, 1978, p 283.
16. Allcock, H. R.; Fuller, T. J. *Inorganic Chem.* **1982**, *21*, 515.
17. Ibim, S. M.; Ambrosio, A. A.; Larrier, D.; Allcock, H. R.; Laurencin, C. T. *J. Contr. Rel.* **1996**, *40*, 35.
18. Laurencin, C. T.; Langer, R. S.; Allcock H. R. Polyphosphazene matrix erosion and diffusion release systems. Int. Pat. WO 88/09664. 1988.
19. Allcock, H.R.; Ambrosio, A. M. A.; Poly(organophosphasene) hydrogels. U. S. Pat. 5,898,062. 1999.
20. Kikuchi, A.; Okano, T. *Temperature-responsive polymers as on-off switches for intelligent biointerfaces*. In: *Biorelated polymers and gels: controlled release and applications in biomedical engineering*. ed, Okano T. Academic Press: NewYork, 1998, pp. 1.
21. Fujishige, S.; Kubota, K.; Ando, I. *J. Phys. Chem.* **1989**, *93*, 3311.
22. (a) Nagasaki, Y.; Honzawa, E.; Kato, M.; Kataoka, M.; Tsuruta, T. *Macromolucules* **1994**, *27*, 4848. (b) Nagasaki, Y.; Kazama, K.; Honzawa, E.; Kato, M.; Kataoka, K.; Tsuruta, T. *Macromolecules*, **1995**, *28*, 8870.
23. Barbucci, R.; Casolaro M.; Magnani, A.; Roncolini, C.; Ferruti, P. *Polymer* **1989**, *30*, 1751.

24. Lee, Y. M.; Shim, J. K. *Polym. Mater. Sci. Eng.* **1997**, *77*, 357.
25. Hoffman, A. S.; Stayton, P. S.; Bulmus, V.; Chen, G.; Chen, J.; Cheung, C.; Chikoti, A.; Ding, Z.; Dong, L.; Fong, R.; Lackey, C.; Long, C. J.; Miura, M.; Morris, J. E.; Murthy, N.; Nabeshima, Y.; Park, T. G.; Press, O. W.; Shimoboji, T.; Shoemaker, S.; Yang, H. J.; Monji, N.; Nowinski, R. C.; Cole, C. A.; Priest, J. H.; Milton, H. J.; Nakamae, K.; Nishino, T.; Miyata, T. *J. Biomed. Mater. Res.* **2000**, *52*, 577.
26. Nason A. *Coordination: the Endocrine System*. In: *Essentials of Modern Biology*. John Wiley & Sons Inc: NewYork. 1968, p 231.
27. Nason A. *Digestion*, In: *Essentials of Modern Biology*. John Wiley & Sons Inc: NewYork, 1968, p231.
28. Van den Berg, A. P.; Wike-Hooley, J. L.; Van den Berg-Blok, A. E.; Ven den Zee, J.; Reinhold, H. S. *Eur. J. Cancer Clin. Oncol.* **1982**, *18*, 457.
29. Hoffma, A. S.; Afrassiabi, A.; Dong, L. C. *J. Contr. Rel.* **1986**, *4*, 213.
30. Gutowska, A.; Bae, Y. H.; Jacobs, H.; Feijen, J.; Kim, S. W. *Marcromolecules* **1994**, *27*, 4167.
31. Oyama, N.; Ikeda, S.; Tatsuma, T. *New Funct. Mater.* **1993**, *B*, 153.
32. Yoshida, R.; Uchida, K.; Kaneko, Y.; Sakai, K.; Kikuchi, A.; Sakurai, Y.; Okano, T. *Nature* **1995**, *374*, 240.
33. Peppas, A. N.; Lafayette, W. *Papaerback APV.* **1993**, *33*, 41.
34. Kaneko, Y.; Sakai, A.; Kikuchi, A.; Yoshida, R.; Sukurai, Y.; Okano, T. *Macromolecules* **1995**, *28*, 7717.
35. Okano, T. *Drug Delivery Syst.* **1995**, *10*, 355.
36. Rhine, W. D.; Hsieh, D. S. T.; Langer, R. *J. Pharm. Sci.*, **1980**, *69*, 265.
37. Veronese, F. M.; Marsilio, F.; Caliceti, P.; De Filippis, P.; Giunchedi, P.; Lora, S. *J. Contr. Rel.* **1998**, *52*, 227.

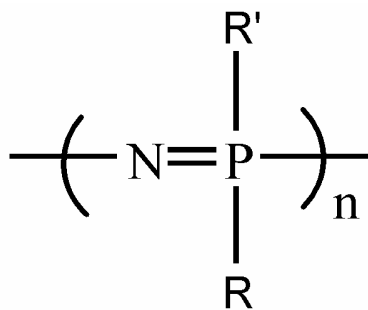


Figure A-1. Repeating unit in polyphosphazenes.

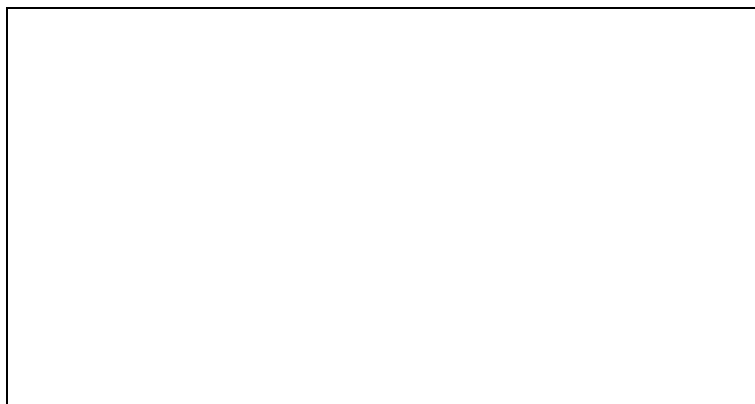


Figure A-2. Two fundamental routes to synthesize substituted polyphosphazenes.

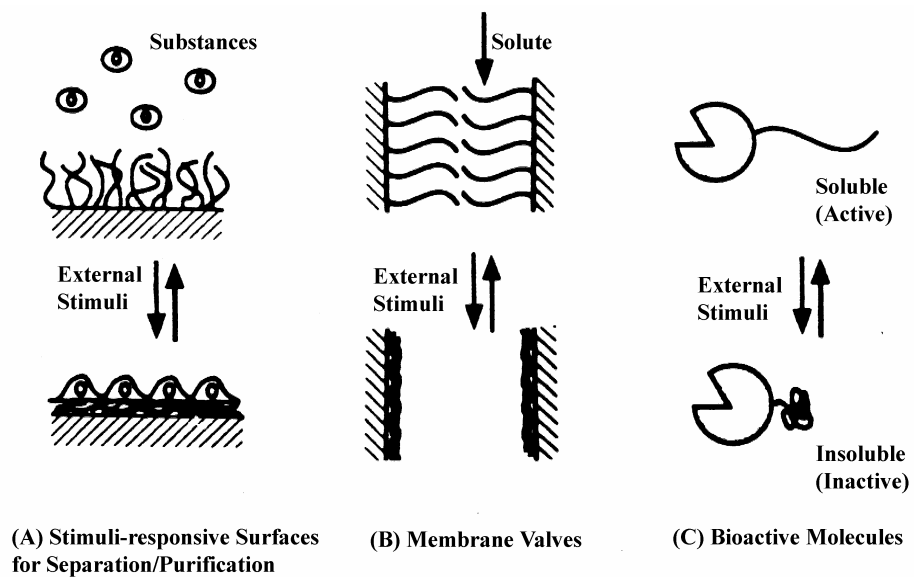


Figure A-3. Applications of materials modified with stimuli-responsive polymers for separation/purification, membrane valves, and bioactive molecules.

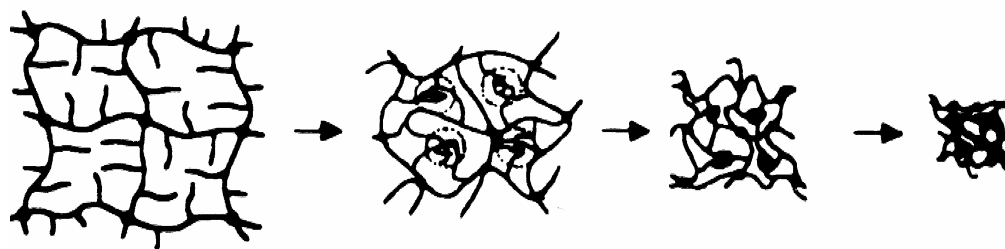


Figure A-4. Release mechanism for grafted stimuli-sensitive polyphosphazene matrices.

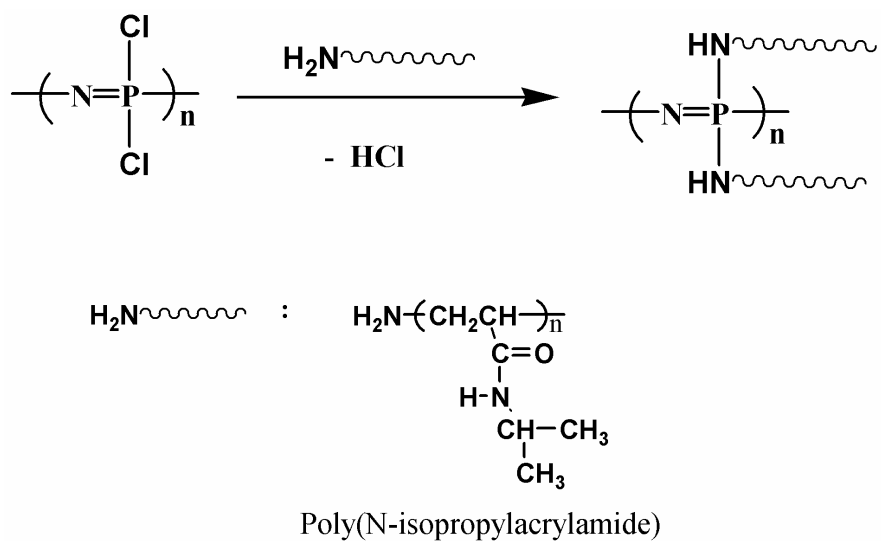


Figure A-5. Preparation of poly(N-isopropylacrylamide) modified polyphosphazene as temperature sensitive delivery matrix material.

## Appendix B Electrochemistry Measurements of Aniline Derivative Modified 8-Hydroxyquinoline Ligands

### B.1. Experimental

The electrochemical measurements were performed in acetonitrile (MeCN) solutions (thermostatted at 25 °C) with a Bioanalytical Systems (BAS-100A) electrochemical analyzer. The three-electrode assembly comprised a working electrode, an Ag<sup>+</sup> (0.01 M AgClO<sub>4</sub>, 0.1 M tetraethylammonium perchlorate, MeCN)/Ag reference electrode, and a Pt-mesh auxiliary electrode. The working electrode was a Pt wire or a Hg on Au one for voltammetry and a Pt disk for rotating electrode polarography. The supporting electrolyte was 0.1-0.2 M tetrabutylammonium hexafluorophosphate (TBAPF<sub>6</sub>). The concentration of solution of ligand **1a** and **2a** was 1.4 mM and 1.6 mM, respectively.

### B.2. Results

The electrode polarograms and cyclic voltammograms of ligands **1a** and **2a** are shown in Figures B-1 to B-8. The electrochemistry of ligand **1a** and **2a** clearly shows quasireversible reductions in MeCN with Hg on Au electrode (Figures B-2 and B-6). The oxidation of ligand **1a** contains two reversible processes (Figure B-4), while the oxidation of ligand **2a** also contains two processes with the first one irreversible (Figure B-8).



**B.3. Acknowledgments**

I am grateful to Dr. Anthony Addison for his kindly help with electrochemistry measurements. I also thank Dr. Vaidy Mathrubootham for the helpful discussion on cyclic voltammograms.

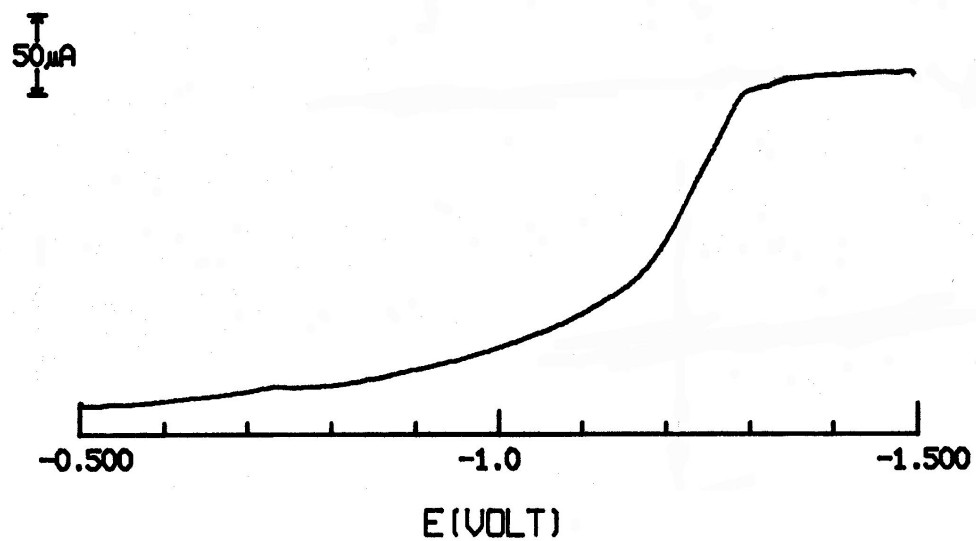


Figure B-1. Rotating disk (Hg on Au) polarogram (2400 rpm) of ligand **1a** in MeCN. Scan Rate = 50 mV/s.

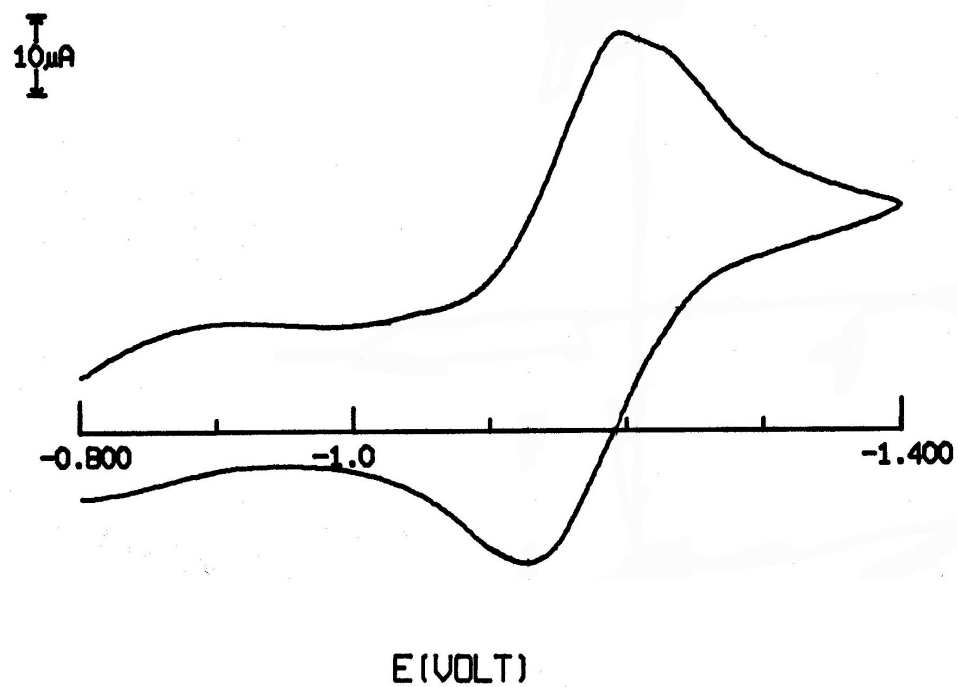


Figure B-2. Cyclic voltammogram (Hg on Au, negative potential region) vs. Ag/Ag<sup>+</sup> of ligand **1a** in MeCN. Scan Rate = 100 mV/s.

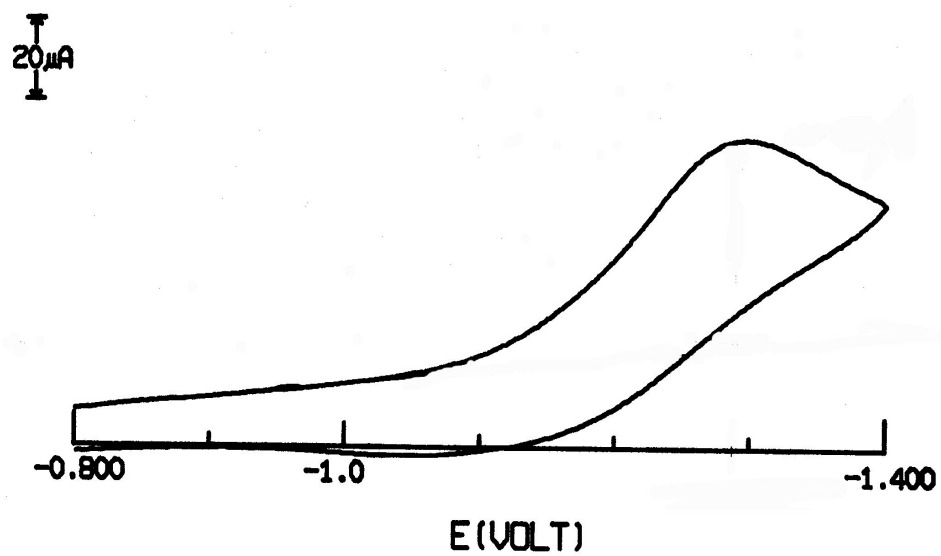


Figure B-3. Cyclic voltammogram (Pt wire, negative region) vs.  $\text{Ag}/\text{Ag}^+$  of ligand **1a** in MeCN. Scan Rate = 100 mV/s.

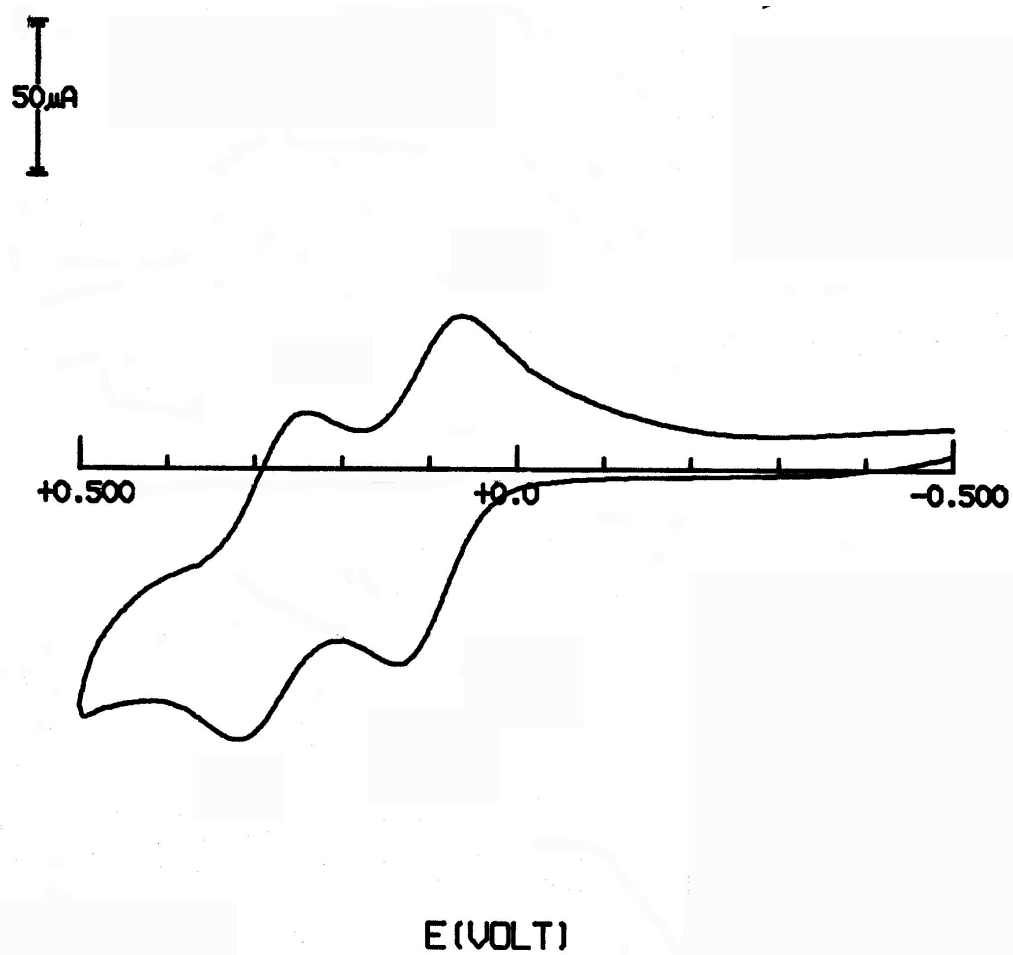


Figure B-4. Cyclic voltammogram (Pt wire, positive region) vs.  $\text{Ag}/\text{Ag}^+$  of ligand **1a** in MeCN. Scan Rate = 100 mV/s.

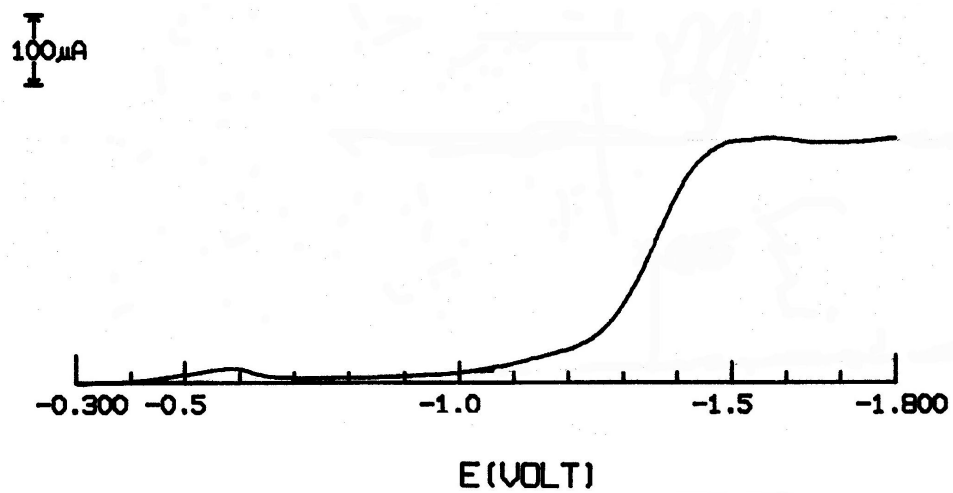


Figure B-5. Rotating disk (Hg on Au) polarogram (2400 rpm) of ligand **2a** in MeCN. Scan Rate = 40 mV/s.

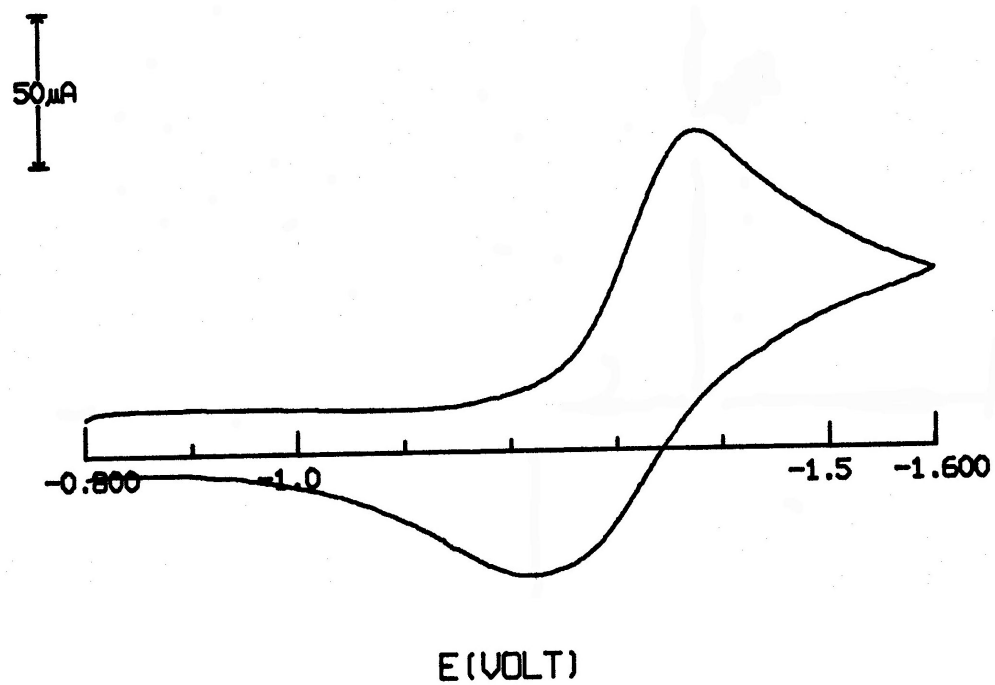


Figure B-6. Cyclic voltammogram (Hg on Au, negative region) vs.  $\text{Ag}/\text{Ag}^+$  of ligand **2a** in MeCN. Scan Rate = 100 mV/s.

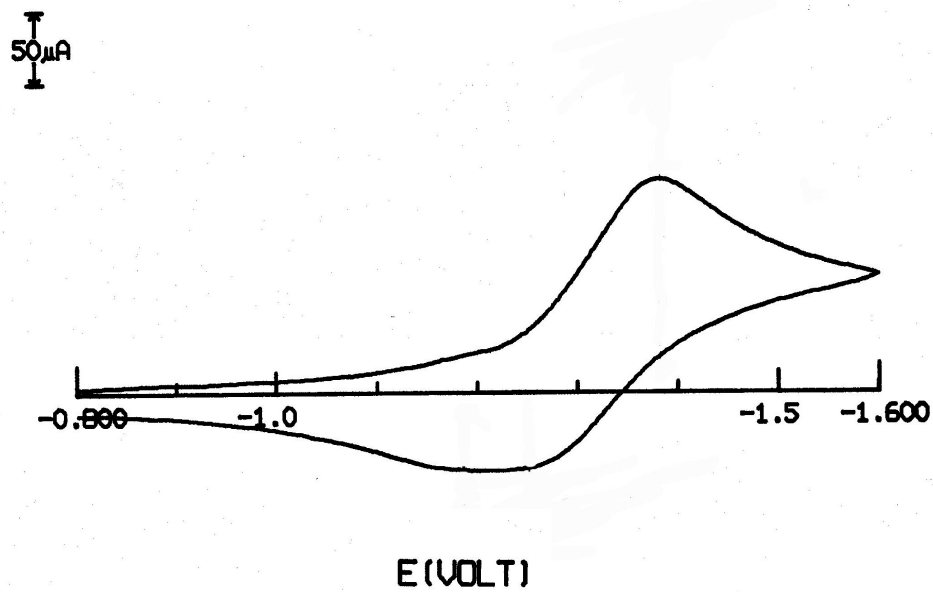


Figure B-7. Cyclic voltammogram (Pt wire, negative region) vs.  $\text{Ag}/\text{Ag}^+$  of ligand **2a** in MeCN. Scan Rate = 100 mV/s.



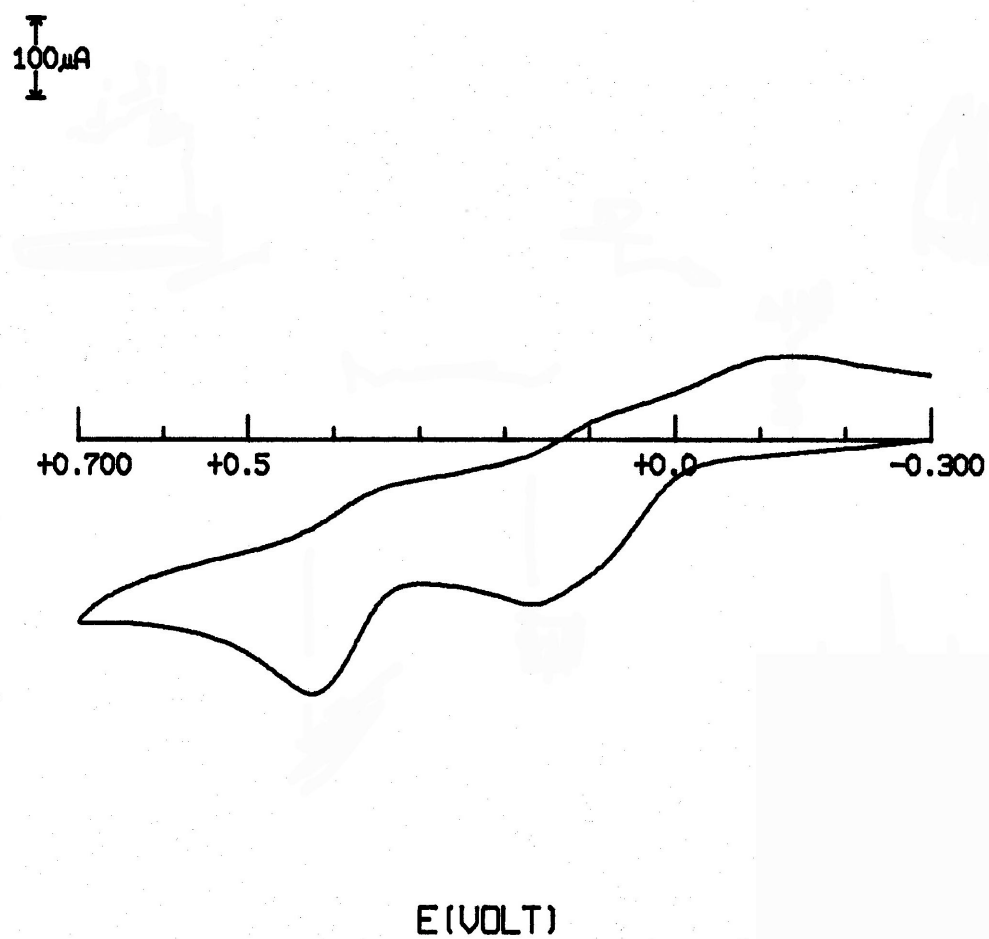


Figure B-8. Cyclic voltammogram (Pt wire, positive region) vs.  $\text{Ag}/\text{Ag}^+$  of ligand **2a** in MeCN. Scan Rate = 100 mV/s.

### Vita

Shan Cheng was born in Beijing, China on September 3<sup>rd</sup>, 1973. She is a citizen of People's Republic of China. She received B.S. in Polymer Materials Engineering from Beijing University of Chemical Technology, Beijing, China, in 1995, and M.S. in Chemistry from Drexel University, Philadelphia, PA in 1999. Since 1995 she was with BYK-Chemie in Beijing as an assistant engineer, until she joined Drexel University in 1997. From 1997 to 2002, she has been a research assistant affiliated with the Center of Advanced Polymers and Materials Chemistry and Department of Chemistry, Drexel University, under the supervision of Dr. Yen Wei. Her research interests include a wide range of fields in polymer and materials chemistry, especially nanostructured, electroactive and bio-applicable materials. She was also a teaching assistant in Department of Chemistry, Drexel University, during 1997 to 2002. Her teaching responsibilities include recitation and laboratory sessions in a number of curricular courses within chemistry fields.

Her research work has been published and presented in several national and international conferences, including ACS national and regional conferences and the Gordon Research Conference. She was the recipient of the Gordon Research Conference Graduate Student Travel Award in 2001. She was also the recipient of the Dean's Award from the College of Arts and Sciences, Drexel University, on Research Day 2002.

She will join PPG Industries in the fall of 2002.

